UNIVERSITÀ DI SIENA 1240

Dipartimento di Scienze fisiche, della Terra e dell’ambiente

Dottorato in Scienze e tecnologie ambientali, geologiche e polari

XXXV° Ciclo

Coordinatore: Prof.ssa Letizia Marsili

THE ROLE OF MINERALOGY IN CIRCULAR ECONOMY: FROM INORGANIC SPECIAL WASTES TO SECONDARY RAW MATERIALS

Settore scientifico disciplinare: *Geo 06/Geo 09*

Candidato/a
Narcisa Mihaela Marian
Università di Siena
Firma digitale del/della candidato/a

Tutore
Cecilia Viti
Università di Siena

Anno accademico di conseguimento del titolo di Dottore di ricerca
2021/2022

Università degli Studi di Siena
Dottorato in Scienze e tecnologie ambientali, geologiche e polari
XXXV° Ciclo

Data dell'esame finale
26 Giugno 2023

Commissione giudicatrice
Serena Chiara Tarantino
Mario Tribaudino
Federico Rossi

Esperto/i
Serena Chiara Tarantino
Mario Tribaudino

Supplenti

Paola Comodi

Table of Contents

ABSTRACT

In this PhD project, I have applied the traditional methodologies of mineralogical investigation (e.g., optical and electron microscopy, X-ray spectrometry, and diffraction) to the study of three different inorganic special wastes, i.e.: a) asbestos-containing wastes (in particular, cement-asbestos materials, like the well-known Eternit); b) red gypsum and c) flotation muds, deriving from TiO_2 and metallurgic industrial processing, respectively. Based on pre-existing patents, the above wastes have been suitably processed transforming them into secondary raw materials (SRM), for potential applications in the ceramic, building, and construction industries.

Different products obtained using variable amounts of the above inorganic wastes, were carefully investigated to determine their mineralogy, chemical composition, and micro/nanostructural characteristics (such as grain size and porosity). This investigation has been fundamental to understand the actual commercial potentials of the different products. The last step of my research has been done through strict collaboration with researchers from other disciplines, with two main objectives: i) obtainment of CBA cost-benefit analysis, and LCA life cycle assessment for the different waste types; and ii) obtainment of technical data on the new commercial products, through the executions of mechanical strength and chemical leaching tests, as required by current regulations. This last step has been completed only for cement asbestos wastes, whereas it is still under progress in the other cases.

Overall results aim to demonstrate the role of Mineralogy in circular economy projects, also remarking how the irreversible depletion of natural mineral resources, associated with a human waste increase, makes the circular economy target mandatory. The concrete realization of circular economy projects, such as the ones suggested in this work, often based on solid scientific evidence, requires however convincing (social, political, and economic) support by the Institutions and by involved stakeholders, in order to obtain an effective transition from the laboratory to the industrial scale.

RIASSUNTO

In questo progetto di dottorato ho applicato le tradizionali tecniche analitiche mineralogiche (ad esempio, microscopia ottica ed elettronica, spettrometria e diffrattometria a raggi X) allo studio di tre differenti rifiuti speciali inorganici: rifiuti contenenti amianto (pannelli di cemento amianto, tipo Eternit), gessi rossi e fanghi di flottazione, tutti derivanti da diversi processi industriali. Sulla base di brevetti preesistenti, i rifiuti sopra citati sono stati riciclati come materie prime seconde per la produzione di alcuni materiali ceramici in senso lato.

Lo studio di caratterizzazione ha riguardato anche i prodotti ceramici, definendo prima di tutto le loro caratteristiche mineralogiche, microstrutturali e chimiche. Successivamente, grazie alla collaborazione con ricercatori di altre discipline è stato possibile acquisire ed integrare i risultati più strettamente mineralogici con conoscenze economiche (per esempio analisi costi benefici CBA, e ciclo di vita LCA) e tecnici-commerciali (ad esempio, con l'esecuzione dei test richiesti dalla normativa, tra cui resistenza meccanica e lisciviazione chimica).

L'insieme dei risultati ottenuti in questo studio, ed opportunamente integrati con altri nello stesso campo, dimostra la fattibilità all'approccio di economia circolare, sempre più indispensabile, in un contesto di sfruttamento accelerato ed esaurimento delle risorse naturali, uniti ad una crescente produzione di rifiuti. Ovviamente, oltre all'impegno accademico, è necessario che ci sia anche un interesse ed un intervento materiale di tipo istituzionale dedicando risorse economiche affinché avvenga concretamente la transizione da economia lineare ad economia circolare, portando le sperimentazioni dal livello laboratoriale accademico alla scala degli impianti industriali.

CHAPTER I

INTRODUCTION

1.1 The depletion of not renewable natural resources and the increase of inorganic wastes

The growing exploitation of natural resources, defined by the European Environment Agency as a feature or a component of the natural environment that is of value in serving human needs (i.e., oil, gas and other fossil fuels, water, soil, rocks, and minerals), is directly related to the growing human demand for everyday goods, services, and technological devices, disregarding the fact that most of the natural resources are not renewable. Among these, minerals play a key role, since they represent the fundamental raw materials for a huge variety of applications, ranging from agriculture to infrastructure, technology, and every kind of commodity.

Mineral resources, defined as economically extractable in a foreseeable future (Winterstetter et al., 2015), are divided into different categories, based on their employment in a specific industry sector. For example, the International Resource Panel (IRP) on global material flows (report UNEP 2016a) divided raw mineral resources into three categories: metals, non-metallic, and mineral fuel. Conversely, the World Mining Data (https://www.world-mining-data.info/) divided them into iron and ferro-alloy metals, non-ferrous metals, precious metals, industrial minerals, and mineral fuels. The IRP upgraded report (2020) defines the following bullet points (see also Table 1):

Construction minerals: all raw materials and minerals used in the construction and infrastructure sectors, after potential processing of crushing, grinding, sorting, and washing. Although cement is not a naturally occurring material and it requires high-temperature processes, it is considered a construction mineral, due to its important role in the construction industry.

Industrial minerals: all minerals used for specific physical and chemical properties, such as hardness, thermal resistance, optical behavior, density, and so on. Before their commercial use, raw industrial minerals are treated following extremely variable methods, ranging from gravimetric separation in the extraction site, grinding, refining by chemicals, to heating, so as to make the material as suitable as possible for its specific industrial use.

Metals: this segment is subdivided into three others (table 1.1) and included the group of minerals called ores. Also in this case, the processing is quite complex, from extraction to the finite destination product.

Mineral fuels: raw natural resources used to supply energy. There are also metals used for nuclear energy such as uranium and thorium.

Table 1.1 Modified by the IRP 2020 report are *shown the main industry segments and the main raw materials.*

INDUSTRY SEGMENT	SUB SEGMENT	RAW MATERIALS
Construction		Sand, gravel, crushed rock, dimension stone (such as limestone, granite, syenite, marble), slate, lime, gypsum, clay (undifferentiated), cement
Industry		Asbestos, baryte, bentonite, boron minerals, bromine, diamond (industrial), diatomite, dolomite, feldspar, fluorspar, garnet, graphite, gypsum and anhydrite, helium, ilmenite, iodine, kaolin (China-clay), kyanite, lime, limestone, magnesia, magnesite, mica, nepheline syenite, olivine, perlite, phosphates (incl. guano), potash, quartz, salt, special clays, silica sand, sillimanite, soda ash, sodium sulphate, spinel, spodumene, sulphur, talc (incl. steatite and pyrophyllite), titanium oxides (rutile, anatase), vermiculite, wollastonite, zeolites, zircon
Metals	Iron and ferro-alloy metals	Iron, chromium, cobalt, manganese, molybdenum, nickel, niobium, tantalum, titanium, tungsten, vanadium
	Non-ferrous metals	Aluminium (and bauxite, its ore), antimony, arsenic, bismuth, cadmium, copper, gallium, germanium, lead, lithium, mercury, rare earth metals, rhenium, selenium, tellurium, tin, zinc
	Precious metals and minerals	Gold, platinum-group metals (iridium, osmium, palladium, platinum, rhodium, ruthenium), silver, gemstone diamonds, other precious and semi-precious minerals
Mineral fuels		Steam coal (incl. anthracite and sub-bituminous coal), coking coal, lignite, natural gas, crude petroleum, oil sands, oil shales, thorium, uranium

Figure 1.1A (UNEP 2016 report) shows the increase in global use of all categories, especially in the case of biomass and non-metallic minerals (those related to industry and construction sectors). Biomass is defined as the biodegradable fraction of products, wastes, and residues of biological origin from agriculture, forestry, and related industries including fisheries and aquaculture as well

as the biodegradable fraction of industrial and municipal waste (Sanchez et al., 2019). In an economic context, biomass comprises biological resources for the conversion of the above-mentioned resources and waste into valuable products such as food, feed, bio-based products, and bioenergy (European Commission, 2012). As regards metallic ores (figure 1B), the total demand is greater than 250% from 1970 to 2010. In the case of non-metallic minerals (figure 1C), a significant increase is observed in the extraction and demand of raw minerals for the construction sector, which is directly correlated with the problem of an unsustainable land consumption.

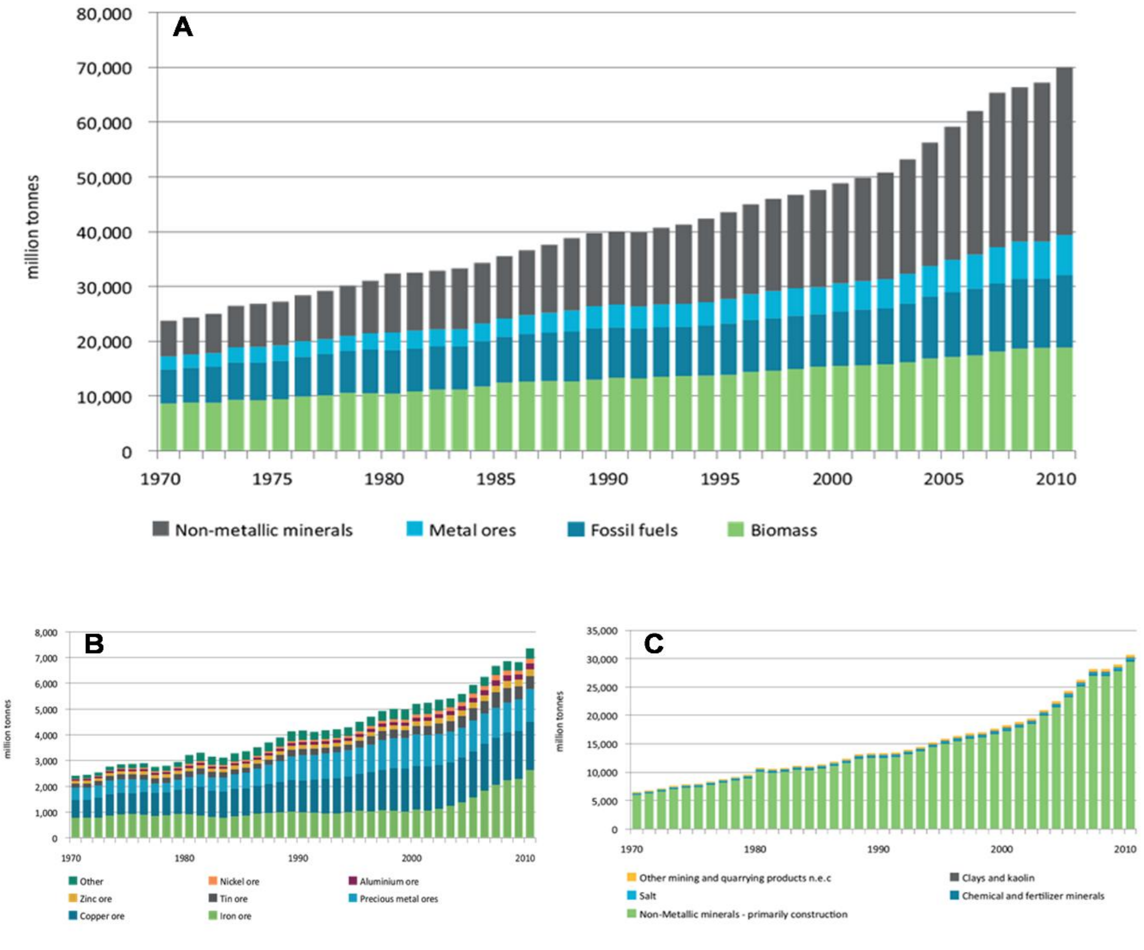

Figure 1.1 Modified by UNEP report 2016. All data refers to global extraction in millions of tonnes. A) Represents the extraction of the four categories, with an evident increase in non-metallic minerals. B) Shows the trend of extraction of metallic ores, with remarkable demand in the last 20 years for copper and precious metals. C) Indicates the trend of non-metallic minerals.

The extraction of non-renewable resources (primarily fossil fuels and metal ores) is reducing the global stocks of these materials available for the future (UNEP 2016). Mineral reserves/stocks are defined as economically mineable sites that have been measured and estimated by preliminary feasibility studies. Under this definition, the volume of the mineable portion of a resource depends on numerous indicators such as technology, economics, market trade, and geopolitical factors that are constantly evolving (Crowson, 2011; Meinert et al., 2016; Cook, 2022). Beyond this approach that focuses on politics and economics, it is important to emphasize the central role of geology and its long processes that lead to the formation of resources. These resources from a human timescale point of view can be considered finite, and what we are currently doing with the current growth rates is consuming the highest-grade deposits, leaving the next generations with increasingly poorer deposits (Northey et al., 2018). The grade of a mineral deposit is its tenor, which is the average concentration of the mineral in the volume mined. The larger the volume that can be mined with available tools and technologies, the higher the grade/tenor of the deposit is (Misra, 2012).

An example that perfectly fits in this context is the scarcity of metals and REEs (Rare Earth Elements) in recent years, which has led many countries, including Europe to draw up a list of critical raw materials defined as those that have high economic importance and high supply risk (European Commission, Study on the EU's list of Critical Raw Materials (2020). Figure 1.2, modified by the SGU Geological Survey of Sweden (A) and European Commission (B), shows the global production of critical raw materials (A), according to the European list, and the Countries and CRMs that account for most of the supply in the EU. It is remarkable that China represents both the major producer (worldwide) and supplier (in this case referred to EU).

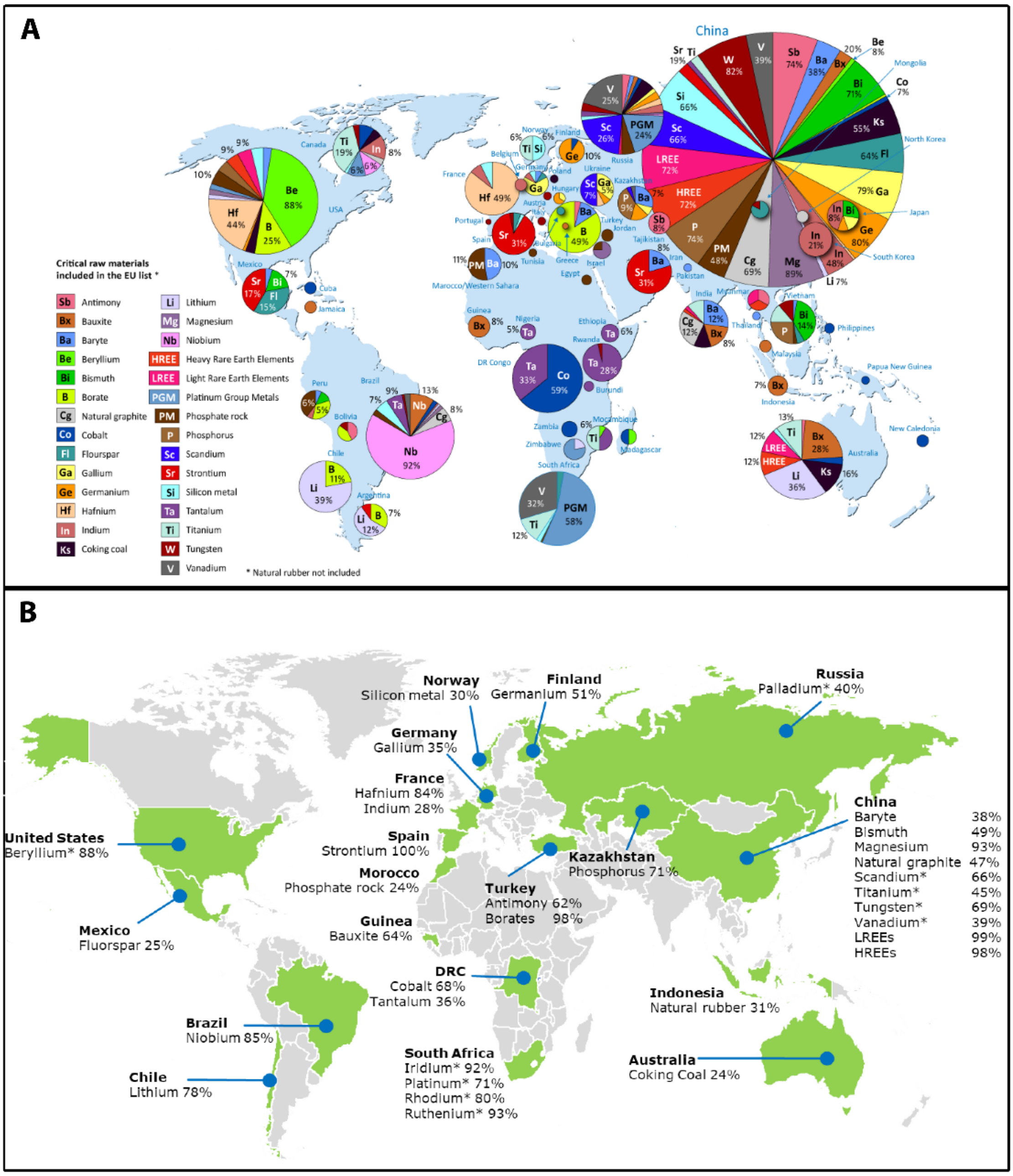

Figure 1.2 The global production of critical raw materials in 2020.

Together with natural resource exhaustion, the other consequence of mineral over-exploitation is the increasing production of inorganic wastes (both due to the industrial processing and the ever-shorter life of the “objects” we use every day). As an example, the diagram in Figure 1.3 of the World Bank (What a waste, report) highlights the solid waste production in 2016 and the projection for 2030 and 2050, distinguishing by world regional areas.

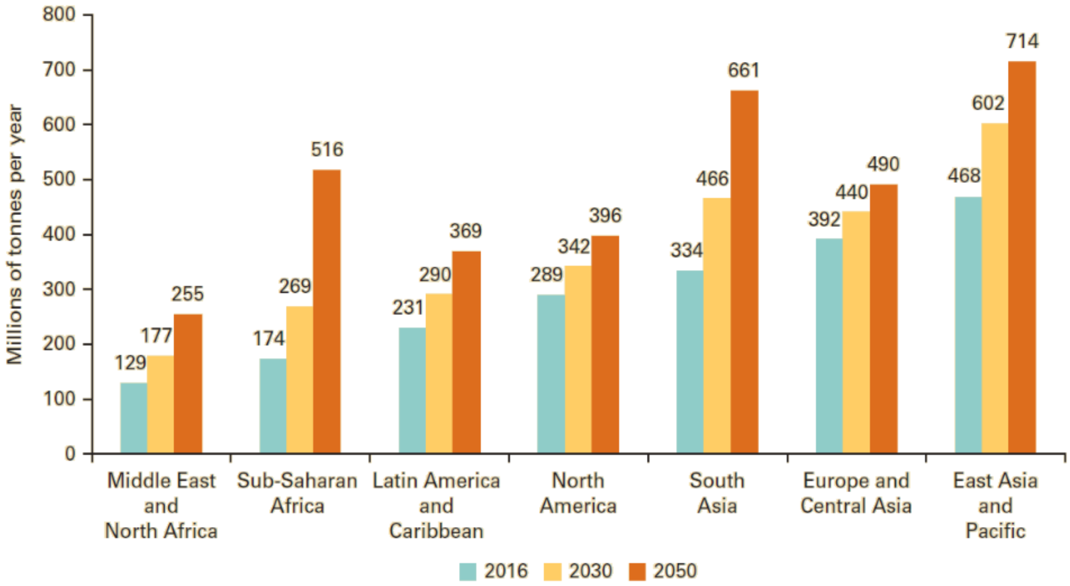

Figure 1.3 Trends in solid waste production around the world

The transformation of raw minerals into consumer goods (finished products or finished products' parts) requires in most cases industrial treatment and processing. Processing typically implies chemical, biological and/or thermal treatments, often resulting in the production of high-volume by-product wastes that can be toxic, environmentally hazardous, and must be adequately managed. A modified image from IRP 2017, figure 1.4 shows a simplified life cycle of resources from the extraction to the end of their life, following the typical path of the linear economy.

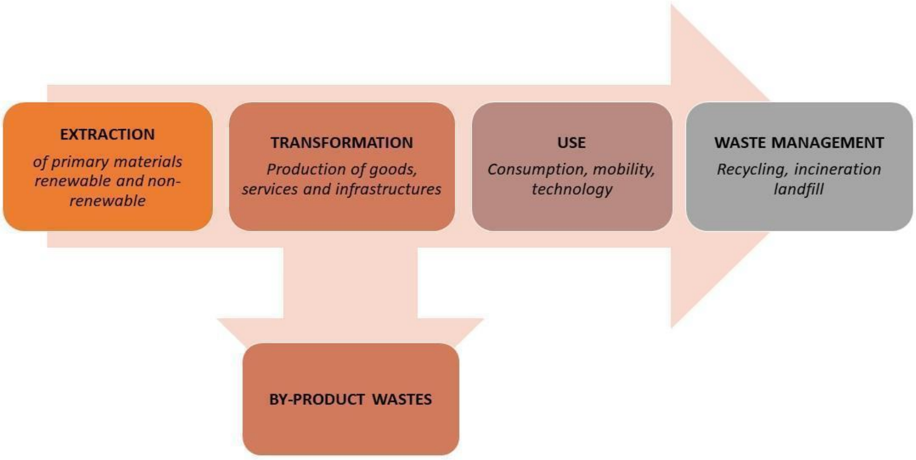

Figure 1.4 The life cycle of mineral resources.

Mineral waste can be defined as the residual material from exploration, mining, and quarrying operation which does not have productive use. Generally, is a high-volume geological material that traditionally has been used just to backfill mines. In 2020 about 100 billion tonnes of solid waste were generated by mine waste facilities activity worldwide, and two third of the total amount was generated by the EU nations. These waste deposits are urged to be considered the new orebodies for the future because they potentially are a source of valuable minerals or elements, such as iron, aluminum, and REEs (Scoble et al., 2003; Tayebi-Khorami et al., 2019; Jawadand & Randive, 2021). In other words, the linear flow shown in figure 1.4 must urgently become a circular flow, to recover essential minerals/elements from the wastes we generate, and to save, at the same time, our natural non-renewable resources.

1.2 Circular economy and waste generation

Natural resource depletion and waste production could be partially mitigated and solved by applying the good practice of circular economy and more efficient use of raw materials. The strict definition of “circular economy” is not univocal, as testified by the review of Kirchherr et al. (2017), reporting up to 114 different definitions. The authors report that, in most cases, the terminology refers to the 4R, **reduce, reuse, recycle, recover**, which is the base of every European law regarding waste. The definition given by the European Commission is *“the maintenance of the value of products, materials, and resources for as long as possible by returning them into the product cycle at the end of their use, while minimising the generation of waste”.* In this regard, the European Commission has adopted the “Circular Economy Action Plan'' which is part of the European Green Deal.

This definition has been recently updated by the Bellagio Declaration (2020), for which circular economy implies the full re-circulation of wastes with the formation of new products and maintenance of their commercial and technical performance for as long as possible. The Bellagio Declaration consists of 7 principles, reported below, aiming to help the EU member states in monitoring the transition to the circular economy:

- Monitoring the circular economy transition.
- Define indicator groups, such as material and waste flow, environmental footprint, economic and social impact, policy process, and behavior.

- Follow the indicator **RACER** which states that the circular economy must be **R**elevant, **A**ccepted, **C**redible, **E**asy to monitor and **R**obust.
- Exploit a wide range of data and information sources.
- Ensure multilevel monitoring.
- Allow for measuring progress toward targets.
- Ensure visibility and clarity.

The Directive 2008/98/EC of the European Parliament and Council (2008) deals with the definition of waste, the classification of the different types of waste, and the various strategies of waste management. Some usual definitions are summarized below:

- *Waste* is any substance or object that the holder discarded or is required to discard.
- *Hazardous waste* is any waste that displays hazardous properties.
- *Waste management* means the collection, transport recovery, and disposal of waste.
- *Prevention measures* taken before a substance material or product has become waste which reduces the quantity of waste, adverse impacts, and the content of harmful substances.
- *Re-use*, any operation that leads to the use of that product before it becomes a waste.
- *Treatment*, recovery, or disposal operation, including preparation prior to recovery or disposal.
- *Recycling* means any recovery operation by which waste materials are reprocessed into products, materials, or substances.

The same directive introduced the well-known waste hierarchy, reported in Figure 1.5. Waste prevention and reuse are the preferred options, followed by recycling (including composting) and energy recovery, while landfill disposal is the least desirable solution.

Figure 1.5 Waste hierarchy framework (https://environment.ec.europa.eu/topics/waste-and-recycling/waste-framework-directive_en)

In upcycling processes, the new product maintains or improves its technical and commercial properties. In other words, upcycling is the practice of taking something considered waste and transforming it into something of equivalent or greater value with a reduction in environmental impact (Wegener, 2016). The most fruitful studies have been done mainly on plastic waste and biofuel, transforming them into valuable products through efficient processes (Pol, 2010; Martin & Eklund, 2011; Kyungeun Sung, 2015).

However, the use of waste as secondary raw material very often results in a downcycling process (Allwood, 2014) because the processing required to transform wastes in SRM may imply: i) reduction in overall quality (i.e., mechanical or physical properties could be less valuable in respect of natural raw material); ii) possible problems in sustainability, that is satisfied only for less demanding applications and less valuable products; iii) unsatisfactory recovery of alloying elements; iv) addition of other raw materials, both to reduce contaminant content and to increase the quality of the material (see Helbig et al., 2022 for a review). Based on what was reported above, mineral recycling is not as simple as we might suppose.

Referring only to recycling as a general definition, the sector in which this practice is very easy to implement is that of municipal solid waste. In this sector, waste is better managed compared to industrial waste for several reasons: i) wastes are differentiated directly in people's homes; ii) upon arrival at collection and recycling facilities, there is more effective separation of waste, resulting in quantities of plastics, aluminum, glass, paper, and organic waste (ready for composting and subsequent production of soil amendments and fertilizers).

The sector where recycling is more difficult is that of inorganic hazardous and special wastes. First, there isn't always proper management and separation of these wastes, both because of incorrect practices and because of the material composition itself (i.e., it's difficult to separate all construction and demolition wastes into a predefined segment). In addition, some hazardous components may be present in the materials, making them complicated to recycle. An example of this is special glasses that contain elements such as arsenic, antimony, and lead, which are essential to their primary engineering use but become obstacles for special glass recycling.

In the What a Waste 2.0 report (2018), where data from 250 nations regarding waste generation are collected, 2.01 billion tonnes of municipal solid waste (MSW) was produced in 2016; the largest producers are the high-income countries. Industrial waste is 18 times higher than MSW. For these wastes, landfill is still the most used solution, disregarding the un-doubtful evidence that landfill is not sustainable for long, due to the progressively decreasing availability of free land, landfill, and open dumps, as well as to their environmental impact. The total waste generated in the EU in 2020, according to Eurostat (the European gateway on statistics), by all economic activities and households amounted to 2151 million tonnes or 4 808 kg/year per capita. The sectors that contribute most to waste generation are: construction (37.1%), mining and quarrying (23.4%), and manufacturing (10.9%). Among the total waste generated in 2020, 95.5 million tonnes are classified as hazardous wastes. According to the Circular Economy Gap Report (2022), an estimation of the global economy recycling the entire world is just 8.9% circular in 2020, with a downward trend compared with the previous estimates for 2018 (figure 1.6).

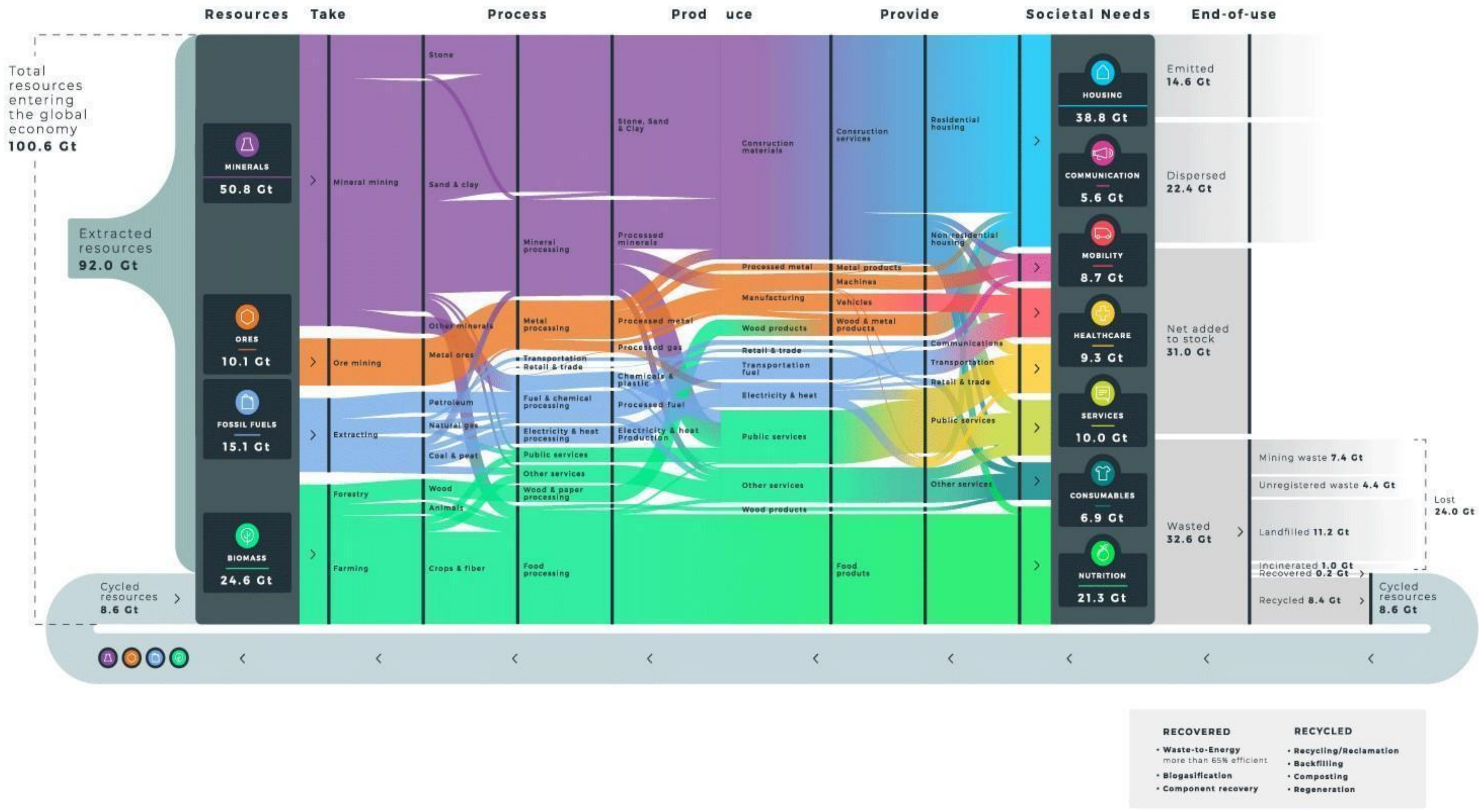

Figure 1.6 The flow diagram of the Circular economy gap report (2022), shows the total resources entering in the global economy, divided by different sectors and all the different steps until the end of use.

The report reveals that minerals contribute to all the societal needs but just a little part is recovered. As regards Europe, the total recycling percentage is about 48% (data related to 2019), without taking into account the different categories of waste and the differences among the EU member states; Italy over the years, increased its recycling from 18% in 2004, to 51% in 2019 (https://www.eea.europa.eu/ims/waste-recycling-in-europe).

1.3 Italy, raw material flow, waste generation and circular economy

In Italy, raw material flow and the percentage of circularity are calculated according to the Bellagio Declaration principles. In 2020, Italy registered a consumption of 444 million/tonnes of raw materials (biomass, fossil fuel, metals and minerals) and the most contributing sector is that of minerals, with 44% of the total.

In Italy, the utilization rate of material from recycling was 21.6 percent in 2020 demonstrating a continuous growth trend since 2011 (year when data monitoring began) with 11.%. The contribution of recycled materials to satisfy the demand for raw materials is represented by the rate of use of material from recycling and the total use (from virgin raw materials and recycled materials). Instead, when we talk about mineral reuse rate, we mean an indicator that represents the contribution of recycled minerals to meeting total demand and itis defined as the ratio of circular use to total mineral use. Circular use of minerals is given by the amount of waste recycled at recovery facilities within the country from which imported waste destined for recycling is subtracted and the amount of exported waste destined for recycling abroad is added. Total mineral use is given by the sum of virgin raw materials and recycled minerals. In Italy, the utilization rate of minerals from recycling in 2019 reached 23.7%, an increase of +10% compared to 2013 (the year when values were first monitored) (4°Circular Economy Report, 2022).

According to the ISPRA report (2022), Italy has produced in the same year about 147 million tonnes of special waste (figure 1.7A). As in the rest of Europe and the world, the sector that has mostly contributed to the formation of waste is construction and demolition (45.1 %), followed by activities of waste treatment and environmental remediation (26.3 %) and manufacturing sector (18.2 %). ISPRA data highlights a slight decrease in waste production in 2020 compared to previous years, but this feature may be related to the global pandemic situation. A more accurate analysis will be done in the next reports, confirming or not the trend in waste generation during and after the Covid crisis. Only a small fraction of overall wastes falls into the special hazardous waste group (about 7 million tons) (Figure 1.7B). The manufacturing sector generated 35.2 % of total special hazardous waste. The 33.8 % is ascribed to waste treatment activities and environmental remediation, followed by the services sector, trade, and transport with 20.2% waste production.

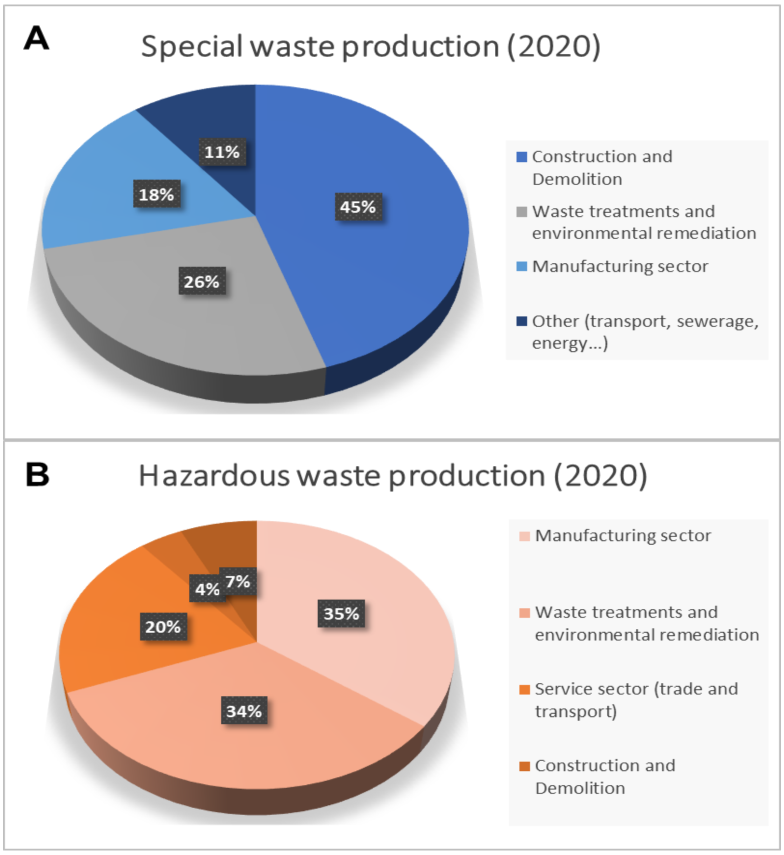

Figure 1.7. The diagram shows the production of special waste (A) and hazardous waste (B) in Italy, referred to 2020.

The total special waste managed in Italy is 159.8 million tonnes, 94.1% of which are non-hazardous, while 5.9% are hazardous. In 2020, 131.3 million tonnes of waste have undergone a recovery process, while waste submitted to disposal operations is 28.5 million tonnes.

The special hazardous waste managed in 2020 is about 9.4 million tonnes and 3.9 million tonnes, which are designated for material recovery, particularly metals or metal compounds. The total percentage of waste, both hazardous and non-hazardous, going to landfill is about 20 %.

1.4 Research purpose and thesis outline

This PhD study deals with the possible recycling of different kinds of special inorganic wastes, characterized by different mineralogical and chemical compositions and deriving from different industrial contexts. I focused my research on the following wastes: 1) asbestos-bearing wastes (such as the well-known fiber-cement Eternit) deriving from roofing removal of contaminated sites; 2) red gypsum muds, deriving from TiO_2 production plants; and 3) flotation muds from precious metals recovery in metallurgic slags.

In all the above cases, the research was carried out following 3 main steps: a) waste mineralogical, chemical, and microstructural characterization, b) execution of recycling tests (based on pre-existing patents) using variable amounts of waste to produce different kinds of new products (e.g., ceramic, construction and building materials; c) mineralogical, chemical and microstructural characterization of the new products. The collaboration with other research groups allowed the obtainment of further fundamental data, in particular leaching and mechanical tests, and economic analysis (such as cost-benefits analysis CBA and life cycle assessment LCA).

The structure of the thesis follows the different kinds of wastes that have been analyzed, with chapters III, IV, and V dedicated to Eternit, red gypsum, and flotation muds, respectively, whereas chapter II will report a summary of experimental methodologies that have been used. Most of the results of my thesis are reported in papers (already published or under revision), that have been incorporated in the corresponding chapters.

As a note to this thesis, I specify that terms such as "mineralogical analysis" and "mineralogical characterization" have been used in a very broad sense, indicating the kind of experimental and methodological approach, disregarding the sample origin (natural vs. synthetic). In fact, strictly speaking, the use of the term "minerals" (and related expressions) should be limited to natural minerals, and it could not apply to synthetic phases derived by anthropic and industrial processes, as in the present cases. However, the use of mineralogical terms would highlight the fundamental role of mineralogy and mineralogical methods in material sciences, and specifically in the study of inorganic wastes and/or products in the circular economy perspective.

CHAPTER II

EXPERIMENTAL METHODS

This chapter summarizes the main experimental techniques used in this PhD thesis to investigate the different types of inorganic wastes (i.e., cement asbestos, red gypsum, and floatation muds) and the different types of products obtained by waste processing and recycling.

2.1 X-ray powder diffraction

X-ray diffraction is the most used analytical technique for the univocal identification of any crystalline phase. In my PhD research, I have mainly used X-ray powder diffraction methods, possibly associated with Rietveld analysis, to obtain bulk qualitative and semiquantitative mineralogical compositions.

Red gypsum and floatation muds have been analyzed without any sample preparation, whereas in the case of cement asbestos tiles, representative fragments of each sample have been selected and grounded in an agate mortar in a fume cupboard with FFP3 mask and single-use material following all normative safety procedures. In this last case, I have also picked out selected bundles of fibers (e.g., white chrysotile and blue crocidolite), for specific X-ray diffraction collection.

XRPD patterns have been collected in the XRD laboratory of the DSFTA, using a Philips X'Pert PROPW3040 (Figure 2.1A) with a Bragg-Brentano geometry (Figure 2.1B), equipped with PW3015 detector X'Celerator, with Cu X-ray tube working at 40 kV accelerating voltage and 30 mA of filament current. A Cu anode was used to obtain an incident CuKα radiation of 1.54060 Å.

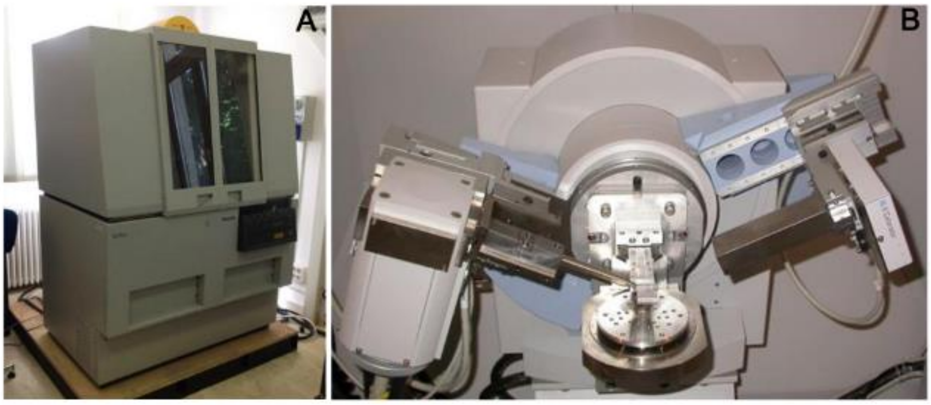

Figure 2. 1 A and B) the XRPD instrument

In some cases (as detailed in next Chapters, and specifically in Chapter III), Rietveld analyses have been performed at the University of Milano Bicocca laboratories and only in specific cases, to determine the semiquantitative amounts of amorphous and crystalline phases using a given amount of internal standard as corundum. The data were obtained through the GSAS Package and the graphical interface EXPGUI.

2.2 Energy dispersive X-ray fluorescence spectroscopy (ED-XRF)

Bulk chemistry of the investigated material through energy dispersive X-ray fluorescence spectrometry (ED-XRF) have been done at the University of Milano Bicocca, using a Panalytical Epsilon 3X with a metal-ceramic thin-window type X-ray tube (50 mµ), Rhodium anode with a power of up to 9 W. The voltage is programmable from 4 to 50 kV in 0.01 kV steps, while the current is programmable from 1 to 1000 µA in 1 µA steps. The spectrometric chamber can be maintained in a helium atmosphere, to analyze light elements, or in air for heavy elements. The sample holder is an automatic 10-bay with spinner movement. All emission lines of the elements in the sample are counted simultaneously by a multichannel analyzer (MCA) having 4096 channels. The detector is a "Drift Chamber'' type silicon semiconductor with dual-stage Peltier cooling and an 8-µm Be ultrathin window.

The collected data were analyzed with Epsilon 3 Software using the Omnian - standardless model, which allows qualitative and quantitative analysis (via mathematical algorithms) of unknown materials, without the need to use calibration lines through standards with a similar matrix to those of the samples under analysis. The content of volatile elements in the sample was determined by the difference in weight before and after the calcination of 0.5g of powder.

All waste samples have been grounded and about 10-15 g were mixed with 5 g of boric acid and a few drops of polyvinyl alcohol, which functions as a glue and does not interfere with the analyses. The resulting powders were put in an aluminum cup and pressed under a laboratory press (ca 15000 kg/cm2) for about 1 minute. Then the samples were put in a desiccator at room temperature for 24 hours to lose the moisture introduced in samples with the polyvinyl addition.

2.3 Scanning electron microscopy (SEM) and energy dispersive spectrometry (EDS)

SEM analyses, coupled with EDS microchemical determinations, have been done at the DSFTA laboratories and obtained using the following microscopes:

- Philips XL30 (Figure 2.2 A) working at 20 kV accelerating voltage, equipped with an EDS system EDAX-DX4 with ZAF correction method.
- TESCAN VEGA 3 (Figure 2.2 B) working at 20 kV accelerating voltage, 15 µA of emission current, equipped with an EDS Bruker Quantax 200EDX for chemical microanalysis with P/B - ZAF correction.
- FEI QUANTA 400 (Figure 2.2 C) equipped with EDS Pathfinder ThermoFisher X-ray (Figure 2.2 D) microanalysis for chemical microanalysis.

Figure 2. 3 The wide range of electron microscopes available during my research work.

Secondary electron images (SE), back-scattered electron images (BSE), and EDS microanalyses were collected in all microscopes I used. As regards sample preparation, two different methods have been used, depending on the nature of the sample: a) deposition of loose grains (e.g., gypsum crystals), powders (e.g. floatation muds), fiber bundles, and small fragments (e.g. from cement asbestos samples) on adhesive carbon tape covering Al stubs and b) cutting, thinning and polishing of solid coherent samples, thus obtaining polished petrographic sections (i.e., the Eternit-like tiles and the various ceramic products formed by waste processing). In both cases, samples were carbon coated using a Rotary-Pumped BALZERS UNION CED 020 Sputter Coater to make the sample conductive. Of course, SE and BSE images were mostly recorded in the first and in the second case, respectively. This is because SE images are suitable for obtaining accurate 3D information about crystal/grain size, habit, and other features, such as twinning (especially in the case of RG samples). In BSE images, polished surfaces of the sample display a sharp chemical contrast, due to the correlation between the BSE coefficient and the average atomic weight of the different mineralogical phases. BSE images are therefore suitable for overall mineralogical and microstructural characterization of solid coherent samples.

2.4 Transmission electron microscope (TEM)

Transmission electron microscopy has been performed, at DSFTA laboratories (Figure 2.4), using a JEOL JEM 2010 with a LaB_6 electron source, working at 200 kV of accelerating voltage with ultra-high resolution (UHR) pole piece and point-to-point resolution of 0.19 nm. The TEM is equipped with an Oxford ISIS EDS for nano-chemical analyses and an Olympus Tengra CCD camera (2k x 2k x 14 bit) for image acquisition. High vacuum conditions (10^{-5} Pa) are obtained by three pumps system (i.e., rotary, diffusive, and ionic pumps).

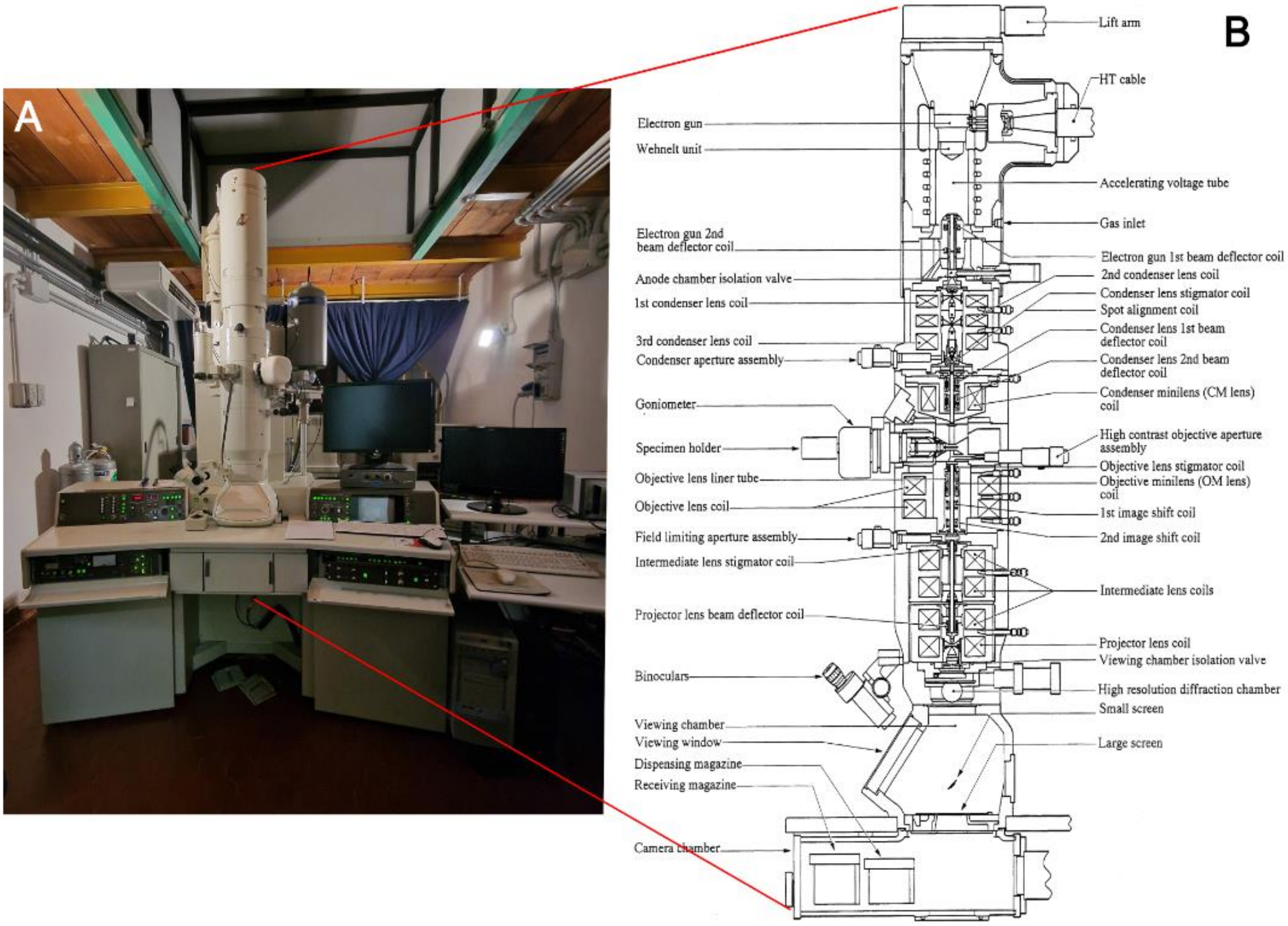

Figure 2. 4 Images of the TEM lab and the optical scheme of the column

As regards sample preparation, a small representative amount of the sample has been finely powdered in a mortar agate, dispersed in deionized water, and treated by bath-type ultrasonic method to facilitate the disaggregation of large grains. Two – three drops of the solution were then deposited over copper grids, 200 mesh in dimension, with carbon lacey support film. Samples were then carbon coated with a turbo high vacuum Emitech 950 Carbon Evaporate Sputter, to make them conductive.

2.5 Thermal analyses

Thermal analyses were performed using an SDT Q600 (Figure 2.5 A and B) in DSFTA laboratories. The maximum temperature reached is 1300 °C, starting from room temperature, with a heating rate of 10°C/min, and an airflow of 20ml/min. Some samples ranged from 15 µm to 40 µm, i.e., asbestos-containing materials (ACM), Crocidolite, Chrysotile, red gypsum, and flotation muds were put in an alumina ceramic cup of 40 µl. Some samples were finely powdered under a fume cupboard with adequate protection (in the case of asbestos-containing materials), while others were placed in the holders as they were without any special preparation.

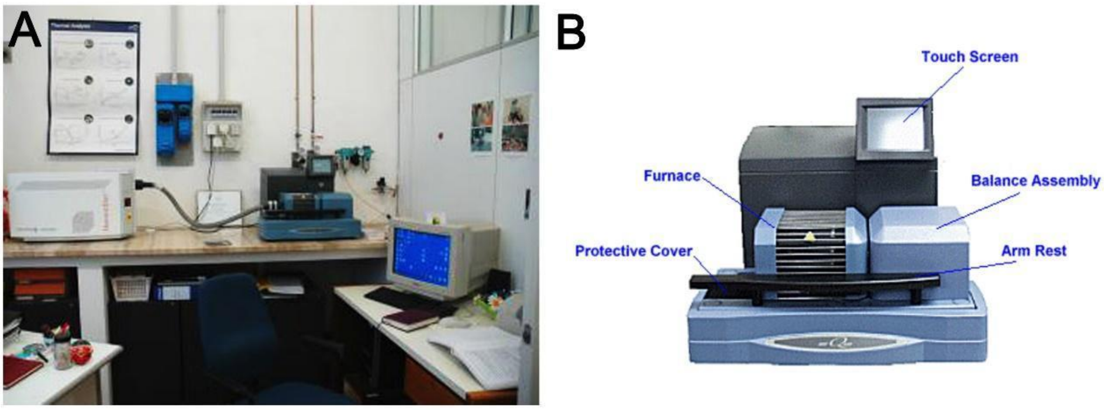

Figure 2. 5 A) Thermal analyses DSFTA laboratory and B) the SDT Q600.

The instrument provided the following curves: i) TG thermogravimetry, showing the sample weight change as a function of heating; ii) DTG, which is the derivative curve of the TG, useful to emphasize the temperature of the maximum rate of weight loss (temperature in °C in X-axis, weight in wt % Y-axis); iii) DTA differential thermal analysis, where the T difference between the sample under investigation and a reference sample (usually alumina) is measured, resulting in upward and downward signals, exo- and endothermic transformations, respectively (temperature °C in X-axis and derivate of weight in %/°C); iii) DSC differential scanning calorimetry, measuring the heat flow provided to the sample and the reference sample, to be both maintained at the same temperature. The latter two methods are particularly useful for studying endothermic (dehydration, dehydroxylation, decompositions, phase transition) and exothermic (recrystallization, structural transformation, oxidation, organic matter combustion) transformations. The data were collected and interpreted with the TA Universal Analyses open-source software.

CHAPTER III

THE EXAMPLE OF A TOXIC SPECIAL WASTE: ASBESTOS CONTAINING MATERIALS (ACM) AND WASTES (ACW)

3.1 Research overview, main objectives, and related scientific production

After 30 years from Law 257/92, which banned the use of asbestos due to its dangerousness for human health, the occurrence of asbestos-containing materials and wastes (ACM and ACW, respectively) is still surprisingly abundant in the Italian territory. Until the 1990s, Italy was one of Europe's main producers of Chrysotile, specifically from the Balangero mine (Western Alps, Piedmont). Many cement-asbestos plants were active in all the Italian territory, e.g., Casale Monferrato (Alessandria), Rubiera (Reggio Emilia), Cavagnolo (Turin), Broni (Pavia), Bari and Priolo (Sicily). These plants produced different kinds of cement-asbestos products, among which the well-known Eternit and Fibronit tiles, mostly used for plant and building roofing. This active industrial production resulted in a widespread and uncontrolled diffusion of asbestos-bearing products, leading now to an impellent management strategy. Three main solutions currently adopted in ACM management are: i) encapsulation, consisting of a resin coating over the exposed surface, thus avoiding fibres release; ii) confinement, consisting of a solid barrier (such as a wall) between the contaminated surface and the environment; iii) removal and disposal in dedicated landfills.

According to the 2022 ISPRA report, 387,000 tonnes of ACW were produced in 2020, mainly from construction and demolition material (97.6% of the total) and insulation material (1.9% of the total), respectively 170605 and 170605 (European Waste Code). The operative landfills for hazardous special waste in 2020 amounted to 18, but only 4 of these are specifically designed for hazardous waste (with a single-dedicated storage cell). Moreover, they are not evenly distributed throughout the Italian territory. In 2020, a total of 391,000 tonnes were disposed of in those dedicated landfills, 88.8% of which were in northern Italy. Smaller amounts, 8,000 ACW tonnes, were exported to Germany, Spain, and France, with a downward trend with respect to previous years.

Considering the huge volumes of ACM and ACW still occurring in Italy and the limited number of dedicated landfills, it is obvious that landfill disposal cannot be considered as a definitive and sustainable solution. The alternative could be asbestos waste inertization, thus transforming a dangerous carcinogenic waste in a safe inorganic material, potentially re-cyclable as a secondary raw material.

This topic has been the first subject of my Ph.D. work. The results I've obtained have been reported in a paper published in 2021 by Marian et. al. in the Journal of Hazardous Material (Volume 413, July 5, digital object identifier https://doi.org/10.1016/j.jhazmat.2021.125419; IF 14.20). The research started with a collaboration with Dr. P.Tuccitto & Dr. S. Grillo, owners of a new patent for an efficient and fast inertization of asbestos fibers in ACW (such as Eternit). The study has been done in collaboration with the University of Milano Bicocca and the Centro di Geotecnologie of the University of Siena, whereas the realization of the various step of waste collection, waste treatment and ceramic synthesis has been done through collaboration with private companies such as Tecneco, which provided the asbestos-containing waste from removal operations, Scame Forni Industriali and Petroceramics, for ACW thermal inertization, Ideal Standard, Graftonica and PMG, which enthusiastically pursued strategies for the recycling of inert materials. The research project was also financially supported by two grant projects, in particular "Deattivazione efficace dell'amianto e riutilizzo DEAR" (2020-2022), founded by Ministero della Transizione Ecologica; and "Asbestos Fast Inertization and Recycling A- FIRE" (2021-2024), founded by the Fondazione Cariplo.

In the following paragraph (3.2), I reported the paper of Marian et al. (2021), whereas, in paragraph 3.3, I report a short summary of two other papers, mostly focused on the characterization of the SRM deriving from Eternit inertization and on the possible application in different industrial productions. In these two last papers, I mostly contributed for what concerns the discussion and the preliminary check of material after the inertization process to verify the complete decomposition of asbestos fibers, whereas the data have been collected by the researchers of the University of Milano Bicocca and Ideal Standard company.

3.2 From hazardous asbestos-containing wastes (ACW) to new secondary raw material through a new sustainable inertization process: A multimethodological mineralogical study

Marian Narcisa Mihaela[a], Giorgetti Giovanna[a], Magrini Claudia[a], Capitani Giancarlo[b], Galimberti Lucia[b],Cavallo Alessandro[b], Salvini Riccardo[a], Vanneschi Claudio[a], Viti Cecilia[a]

[a] *Department of Physical Science, Earth and Environment DSFTA (UniSi) V. Laterina 8, I-53100, Siena, Italy*

[b] *Department of Earth and Environmental Sciences DISAT (UniMIB) Piazza della Scienza, 4 – 20126, Milano, Italy*

[c] *Department of Environment, Earth and Physical Sciences and Centre for GeoTechnologies CGT (UniSi) Via Vetri Vecchi 34, 52027, San Giovanni Valdarno (AREZZO) Italy*

ABSTRACT

Nowadays, asbestos-containing wastes (ACW) still represent an important environmental problem and a severe health hazard due to the well-known pulmonary diseases derived from asbestos fibers inhalation. Except for a very few cases, ACW are currently confined in controlled landfills, giving rise to increasingly high amounts of still hazardous wastes. A promising alternative to landfill confinement is represented by ACW inertization, but the high cost of the inertization processes so far proposed by the scientific community have hampered the creation of actually operative plants. In this paper, we explore the possibility to use an innovative process that ensures the obtainment of asbestos-free inert material in an exceptionally short processing time, thus greatly reducing cost-related problems. The efficacy of the inertization process has been verified through accurate mineralogical investigations on both chrysotile and crocidolite de-activated fibers, through X-ray diffraction, scanning and transmission electron microscopy. Overall mineralogical, microstructural and granulometric characteristics of the inert bulk material suggest that it could be successfully re-used as a secondary raw material in ceramic industries. This innovative inertization procedure could therefore provide an effective and economically sustainable solution for ACW management.

INTRODUCTION

The term “asbestos” refers to a group of natural fibrous minerals with specific habit and size requirements (i.e., fiber diameter < 3 µm, length > 5 µm and an aspect ratio > 3:1). Based on current regulations, asbestos minerals are Chrysotile $Mg_3Si_2O_5(OH)_4$ (i.e., the fibrous variety of serpentine layer silicate) and five chain silicates belonging to the amphibole group: Mg-riebeckite $Na_2(Fe,Mg)_5Si_8O_{22}(OH)_2$ (the blue asbestos known as Crocidolite), Grunerite $(Fe,Mg)_7Si_8O_{22}(OH)_2$ (commercially known as Amosite), Actinolite $Ca_2(Mg,Fe)_5Si_8O_{22}(OH)_2$, Tremolite $Ca_2Mg_5Si_8O_{22}(OH)_2$ and Anthophyllite $(Mg,Fe)_7Si_8O_{22}(OH)_2$. Due to their outstanding properties in terms of mechanical, chemical, thermal, and physical resistance, asbestos fibers have been broadly used in many different applications and materials during the last century (Ross & Nolan, 2003; Strohmeier et al., 2010). Asbestos containing materials (ACMs) can be divided into friable and compact materials: friable asbestos designates any ACM that can be crumbled easily when dry, with loose asbestos fibers that can be scratched effortlessly by hand, whereas compact ACMs are composite materials (e.g., cement – asbestos) with asbestos fibers (generally from 4 to 15 wt%).

The discovery of the relationship between asbestos fibers inhalation and lung diseases such as asbestosis and mesothelioma (e.g., Wagner et al., 1960; Selikoff et al., 1965; Skinner et al., 1988; Guthrie & Mossman, 1993; Dela Cruz et al., 2011; Gualtieri, 2017) has led to many national and international laws, that banned the use, extraction, import, export, marketing and production of ACM (Aryal & Morley, 2020). There is an universal ban on amphibole asbestos whereas chrysotile asbestos, despite its inclusion by the International Agency for Research on Cancer (IARC) in Group 1 “substance carcinogenic to humans” (Yarborough, 2007; IARC, 2012), can still be used “in a safe mode”. In Italy, asbestos ban is defined by Italian Law 257 (1992) (Norme relative alla cessazione dell’impiego dell’amianto) after which dozens of other regulations (national or regional) have been formulated, including the Italian Decree Minister 06/09 (1994) (Normative e metodologie tecniche di applicazione dell’art. 6, comma 3, e dell’art. 12, comma 2, della legge 27 marzo 1992, n. 257, relativa alla cessazione dell’impiego dell’amianto), regarding the procedures for risk assessment and remediation procedures, the Italian Decree Minister 29/07 (2004) (Regolamento relativo alla determinazione e disciplina delle attività di recupero dei prodotti e beni di amianto e contenenti amianto), which establishes the guidelines for thermal inertization of asbestos-containing materials and recycling of the inert material, and the Italian Decree Minister 27/09 (2010) (Definizione dei criteri di ammissibilita’ dei rifiuti in discarica) that rules for landfill of asbestos containing wastes, ACW.

The presence of asbestos-containing materials, such as the widespread Eternit asbestos-cement roofing slates, is still massive in Italy and in many other European countries. Based on a recent dossier by (Legambiente, 2018) "Are we free from Asbestos? The delays of regional plans, land reclamation and alternatives to landfills", there are approximately 370,000 structures in Italy where asbestos is still present (based on regional surveys), for a total of almost 58 million square meters of roofing in industrial sites, as well as in public and private buildings. The survey activities were completed by 6 Regions out of 20, while for 9 of them the survey is still in progress (Legambiente, 2018; Paglietti et al., 2016).

Based on current legislation, possible remediation strategies are essentially three: confinement, encapsulation and removal (with storage in controlled landfills or with possible waste inertization). Unfortunately, asbestos removal procedures in Italy are still lagging behind. According to ISPRA (2020) Italy produced 296,000 tons of ACW in 2018, which required adequate management. Currently, in Italy there are more than 300 storages sites (i.e., sites where the ACW is temporary located before its definitive placement in national or foreign landfills), but only 19 active landfills (only 4 specifically for hazardous materials) where the ACW is permanently placed and buried. According to the ISPRA (2020) survey, 69,000 of 296,000 tons produced in 2018 were transferred abroad. The choice of export rather than storage in national landfills is most dictated by cost reasons and by the limited available volumes in national operative sites. Actually, the amount of ACW to be disposed per year is expected to increase, given to the incomplete data reveled from for the delays in regional survey, mapping and removal activities. The limited number of operating national landfills (19), together with their limited residual storage capacity, suggest that the asbestos waste management is going to be, in the next future, a progressively growing and impelling problem.

The solution currently adopted, i.e., storage/landfill on national or foreign soil, does not represent a long-term sustainable one. A possible alternative is ACW inertization. Scientific research has been successfully involved in this topic (Gualtieri et al., 2011; Iwaszko et al., 2018; Ruiz et al., 2018) leading to many excellent scientific papers and to hundreds of patents (35 of which in Italy) dedicated to ACW inertization through thermal, thermochemical and/or mechanical treatments, also providing possible solutions for the inert material reuse.

In the concrete, operating plants for the ACW inertization are very rare, pointing out an unresolved gap between theory (the huge amount of valid and efficient processes/patents proposed so far) and practice (the realization of dedicated ACW inertization plants). What is the reason for this yet unsolved gap? Almost all processes/patents proposed so far involve heating at high temperatures, which seems a trustable way for a complete inertization of asbestos fibers. Chrysotile and amphibole fibers are decomposed and transformed into non-fibrous crystalline phases or amorphous/glassy material. Chrysotile decomposes around 600–700 °C (e.g., Viti, 2010; Gualtieri, et al., 2012a; Gualtieri et al., 2012b), while amphibole decomposition usually requires higher temperature (variable for each amphibole) although crocidolite samples heated at 800 °C display crystallization of Hematite, Aegirine and Cristobalite (Pacella et al., 2020 and reference therein). Thermal treatments described in previous patents and scientific studies require high energy consumption, due to the time needed to achieve high temperatures and keep them constant up to the complete inertization. That time is never shorter than 1 h, with an average inertization rate of 1–2ton/day or less, for different typology of material, ranging from intact asbestos slates to mixtures of grinding ACW with other materials (Paolini et al., 2019), therefore not economically sustainable. This is the reason why only one inertization plant is currently operating throughout Europe, i.e., INERTAM (Europlasma Group) at Morcenx (France). In the Morcenx plant, the use of plasma torches allows the achievement of 1400–1600 °C, with an almost complete melting of ACW. The amorphous or partially vitreous inert material (called "cofalit") is currently reused as road ballasts.

In this paper, we explore the possibility to use a new innovative patent (UIBM: Invenzione Industriale n°25588/’17, by Tuccitto & Grillo, Owners and Inventors) that allows irreversible and complete de-activation of asbestos fibers in exceptionally short processing time (15 min in temperature), thus providing a viable and sustainable solution for ACW management. This paper reports a detailed mineralogical characterization, based on a multimethodological approach, of: (a) pristine ACW samples (i.e., widespread roofing fiber-cement) and (b) the inert material obtained by thermal inertization process.

SAMPLE DESCRIPTION AND EXPERIMENTAL DETAILS

The samples investigated in this study correspond to fiber-cement roofing panels which have been provided by two Italian companies specialized in ACW removal and disposal (i.e., Tecneco srl and Isambiente snc). Samples come from 26 different industrial and civil buildings in Tuscany, Italy (Figure. 3.1a, where "TEC" and "ISA" labels refer to the samples provided by the two companies above, respectively). Figure. 3.1b shows the relative abundance of the different types of fiber-cement panels. Based on scanning electron microscope and energy-dispersive X-ray spectroscopy, SEM/EDS investigations, most common fiber-cement panels contain both chrysotile and crocidolite fibers (as typical of Eternit products), but we also observed panels with chrysotile alone or with chrysotile + man made vitreous fibers (MMVF). Finally, we remark that in 4 cases (i.e., TEC17-TEC20-ISA2-ISA4), the removal operations were unnecessary since they regarded asbestos-free roofing panels, where only MMVF have been detected.

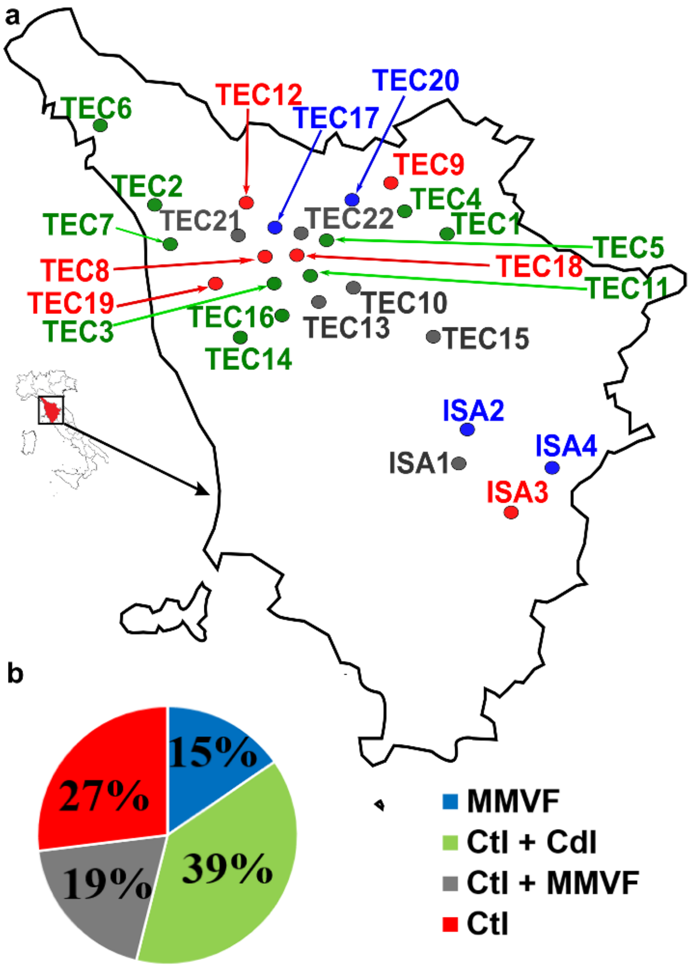

Figure 3. 1. (a) Schematic image showing samples provenance. (b) Relative amount of the different types of fiber-cement panels (based on SEM/EDS analyses on selected fiber bundles from each of the 26 samples). Eternit-like panels (with both Chrysotile and Crocidolite ctl+cdl) are the most commonly employed (39%), followed by panels with Chrysotile (ctl) alone (27%) and with Chrysotile + man made vitreous fibers (ctl+mmvf) (19%). We remark that in 4 cases (15%) (MMVF), the removal operation has involved asbestos-free roofing panels TEC20-TEC17-ISA2-ISA4.

Inertization tests have been performed on four selected panels (in particular, samples TEC1, TEC2, TEC3 and TEC4), all characterized by the widespread presence of both Chrysotile white and Crocidolite blue fibers. The inertization of the four Eternit-like panels was made at a pilot plant of the Scame Forni Industriali S.p.a. (Treviso, Italy), and was realized following the procedures of the new patent UIBM: Invenzione Industriale n°25588/'17 (Tuccitto & Grillo, Owners and Inventors). Operating details of the furnace and inertization conditions are reported in Table 3.1 and it is extremely important to underline that this process is one of the few that not required a preliminary stage of grinding. Eternit slates are brought to 1100 °C in a very short time, keeping them in temperature for circa 15 min and cooling them quickly. The main operating steps are: (1) increase the temperature to 900 °C in three fast steps; (2) enter a controlled atmosphere; (3) increase the temperature to 1100 °C; (4) place the ACW on the conveyor belt; (5) start the conveyor belt and let asbestos slates move at constant velocity throughout the thermal cycle under controlled atmosphere; (6) collect the slates at oven exit after 15 min of treatment. Furthermore, the patent is the only one that take place in an operative industrial site. The post-inertization samples have been labeled as INERT1, INERT2, INERT3 and INERT4 (after TEC1, TEC2, TEC3 and TEC4, respectively).

Table 3. 1 Technical data of the inertization facility at the Scame Forni Industriali pilot plant

TECHNICAL DATA – FURNACE INERTIZATION LINE 130-15-100+350 GI	
conveyor belt width	1.300 mm
effective height above the belt	150 mm
heating zone length	1.000+3.500 mm
working maximum temperature	1120 °C
furnace maximum temperature	1150 °C
control zones	n. 5 SCR
electric voltage	3 x 400 V 50 Hz
installed power	166 kW
consumption at maximum production	125 kW
pressure of CH_4	30 – 40 mbar
consumption of CH_4 during production	20,0 Nm^3/h
pressure of H_2O	2 bar minimum
consumption of H_2O during production	3,5 – 4,5 m^3/h; starting T of 20°C
WORKING CONDITIONS AT THE INERTIZATION LINE 130-15-100+350 GI	
type of material to be treated	Cement-asbestos slates
estimated hourly production	up to 500 kg/h
speed of conveyor belt	up to 400mm/min
weight on the conveyor belt	up to 30 kg/m
thermal treatment	asbestos inertization

Mineralogical, chemical and micro/nanostructural investigations have been performed using the following experimental techniques:

X-Ray Powder Diffraction (XRPD)

Samples were grinded in agate mortar, adding 10% wt. of α-alumina (NIST SRM 676a, internal standard), and back loaded into an Al sample holder. The XRPD study was conducted using a Bragg–Brentano PANanalytical X'Pert-Pro PW3060 diffractometer with θ–θ geometry and CuKα radiation, in the 5–80º 2Ɵ range with step size of 0.02°, at room temperature and operating conditions of 40 mA and 40 kV. Qualitative phase analysis was carried out with the PANalytical X'Pert High Score Plus® software, using the ICSD PDF2-2004 database. Quantitative phase analysis (QPA) was performed with the Rietveld method (Rietveld, 1969) using the GSAS package (Larson & Dreele, 2004) and the graphical interface EXPGUI (Toby, 2001).

The weight fraction of each crystalline phase (W_{α}') in the studied samples was quantified according to the following equation:$W\alpha'=W\alpha Wc'Wc(11-Wc')$where W_{α} and W_{c} are the refined weight fractions of phase α and of the internal corundum standard, respectively, W_{c}' is the actual added weight of the internal standard (10 wt%). The actual weight fraction of the amorphous material (W_{g}') is then calculated as $Wg' = 1-\Sigma_{i} W_{\alpha i}'$. According to Gualtieri (2000), the relative error in glass content quantification is around 10% for fractions of the amorphous phase greater than 10 wt% and increases with decreasing weight fraction of the glass.

X-Ray Fluorescence spectrometry (XRF)

Bulk chemical analyses of inert samples were obtained with a PANalytical Epsilon 3X energy dispersive X-ray fluorescence (EDXRF) instrument. The Omnian-standardless method was used for quantitative analyses. Volatile components (H_2O plus CO_2) were determined through the weight loss on ignition (LOI). The Fe^{3+}/Fe^{2+} ratio was determined through $KMnO_4$ redox titration.

Scanning Electron Microscope (SEM)

The instrument, Philips XL30 working at 20 kV accelerating voltage, equipped with an energy dispersive system (EDS) EDAX-DX4 for microanalysis with ZAF correction method. The backscattered electron (BSE) images and EDS analysis were collected on two different kinds of sample: a) stubs with separate types of fibers, picked off from pristine asbestos panels; b) four polished petrographic section made on carefully selected inertized material.

Transmission Electron Microscope (TEM)

The analyses were performed with JEOL 2010, working at 200 kV, with a point-to-point resolution of 1.9 Å and LaB6 gun. The microscope is equipped with an Oxford ISIS energy dispersive system (EDS) and with an Olympus Tengra CCD camera (2k x 2k x 14 bit) for image acquisition. Treated chrysotile and crocidolite have been dispersed on carbon coated, 200 mesh Cu-grids (2 grids for each INERT sample). Additional TEM mounts were prepared by ion milling 3 mm wide disks cut out around decomposed chrysotile and crocidolite sites selected on polished petrographic thin sections.

Thermal analyses

The analysis was made on 18,058 mg of asbestos panel grinded (specifically on TEC4) performed with a Simultaneous DSC/TGA Thermal analyzer Q600 TA instruments (heating rate 10 °C/min, from room temperature to 1000 °C, in 20 ml/min airflow).

After preliminary observations on the 26 roofing slates by stereomicroscopy and SEM/EDS, further detailed analyses have been carried out on the following samples: (1) bulk pristine Eternit panels (TEC1–2–3–4) before thermal treatment; (2) chrysotile and crocidolite asbestos fibers picked off from pristine TEC1–2–3–4 panels; (3) bulk INERT1–2–3–4 panels after thermal treatment; (4) pseudomorphic bundles corresponding to the original asbestos fibers picked off from INERT1–2–3–4 panels.

RESULTS

Mineralogical characterization of pristine Eternit-like panels

The 26 fiber-cement panels have been preliminary observed at the stereomicroscope and subsequently checked by SEM/EDS to determine the nature of the fibers occurring in the different samples (Figure 3.2). Based on these preliminary observations, we selected four representative Eternit-like samples, containing both Chrysotile and Crocidolite fibers and characterized by similar mineralogical, chemical, and microstructural features (TEC1–2–3–4). At the stereomicroscope, the two types of fibers are easily distinguishable due to their different color (e.g., Figures 3.2a and b). Blue Crocidolite fibers are usually longer than white Chrysotile and exhibit a lower compressive and traction resistance. SEM back-scattered electron (BSE) images confirm the occurrence of Chrysotile and Crocidolite, in long fibers with sub-micrometric diameters (Figures 3.2c and d). Representative EDS spectra are shown in Figurers 2e and f, and provide quantitative analyses close to the end member composition Chrysotile $Mg_3Si_2O_5(OH)_4$ and Crocidolite $Na_2(Fe,Mg)_5Si_8O_{22}(OH)$, respectively.

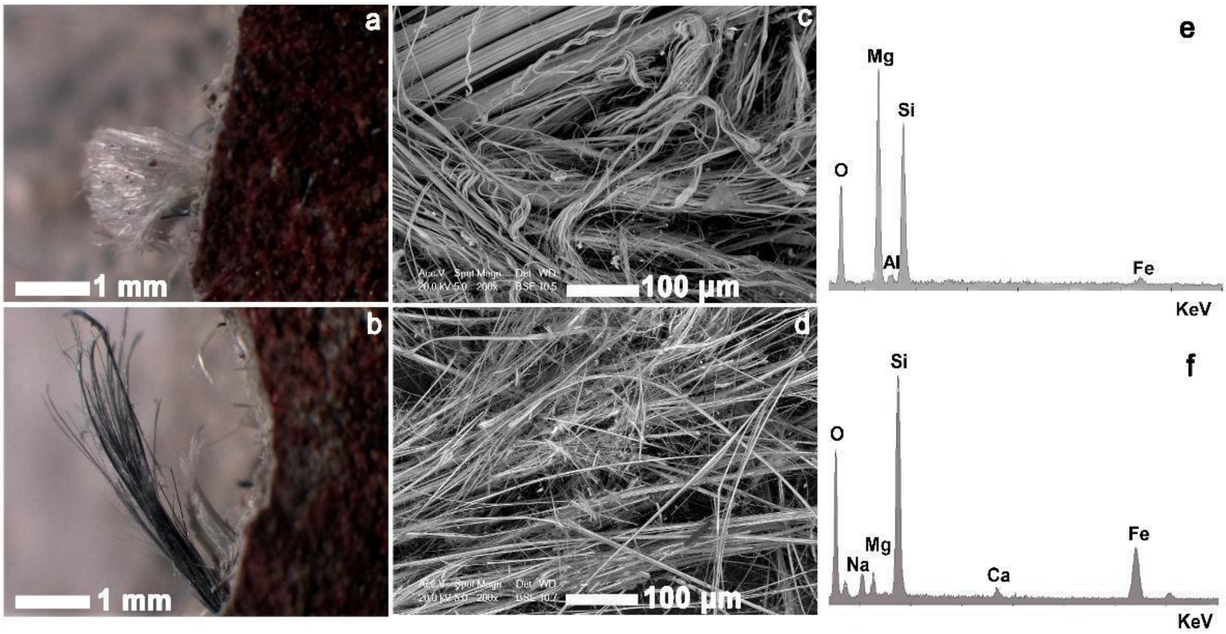

Figure 3.2(a) Chrysotile (white) and (b) Crocidolite (blue) fiber bundles at the stereomicroscope. (c and d) Representative SEM backscattered (BSE) images of Chrysotile and Crocidolite, respectively. (e and f) Corresponding Chrysotile and Crocidolite EDS spectra. All data refer to sample TEC4.

Bulk XRPD has been collected for sample TEC4, revealing the occurrence of Calcite, Quartz, Mica, Chrysotile and Riebeckite (as main crystalline phases), with minor Portlandite and Gypsum. XRPD has been also performed on selected white and blue fibers occurring in TEC4, confirming the occurrence of pure Chrysotile and Riebeckite (Crocidolite), respectively.

Figure 3.3 shows thermogravimetric (TG, in green), derivative thermogravimetric (DTG, in blue) and differential thermal analysis (DTA, in red) curves for sample TEC4. Total weight loss (wt% in TG curve) at 1000 °C is about 31%, following the subsequent steps: (a) loss of 2.7 wt% from room T to 110 °C, due to bulk sample adsorbed water; (b) loss of 2.1 wt% from 110° to 220 °C, probably due to Gypsum transformation from Dihydrate to Hemihydrate (e.g., West & Sutton, 1954; Ramachandran et al., 2002; Kuntze, 2009); (c) loss of 3.4 wt% from 220° to 410°C, probably due to cement phases dehydration (Ramachandran et al., 2002; Torréns-Martín et al., 2015) and Crocidolite dehydroxylation (Kusiorowski, Zaremba, Gerle, et al., 2015); (d) loss of 16 wt% from 410 °C to 690 °C, corresponding to Crocidolite and Chrysotile dehydroxylation (Viti, 2010; Bloise et al., 2016); and (e) loss of 6.2 wt% from 690° to 770°C, due to Calcite decarbonation, producing DTG and DTA endothermic signals around 712 °C.

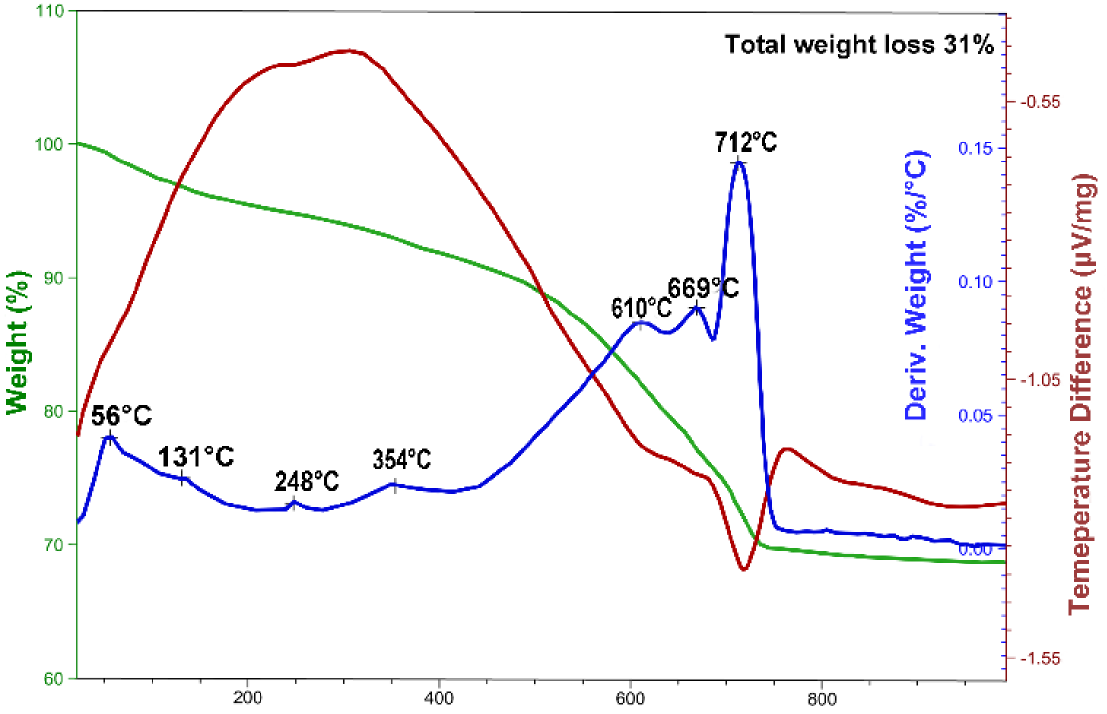

Figure 3. 3 TG, DTG and DTA curves for representative sample TEC4.

After thermal analyses, the samples were further checked by XRPD, to determine the main crystalline anhydrous phases occurring after thermal treatment at 1000 °C. Main detected crystalline phases are Larnite Ca_2SiO_4, Quartz SiO_2 and Brownmillerite $Ca_2Fe^{3+}AlO_5$.

Bulk mineralogical and chemical characterization of post-inertization panels: XRPD and XRF results

Table 3.2 reports the quantitative phase analysis obtained by Rietveld refinement of XRPD data of samples INERT1–2–3–4. For all samples the dominant phase is represented by amorphous material (glass), which ranges from ~55 wt% to ~78 wt%. Regarding crystalline phases, all samples contain abundant calcium silicate (Larnite Ca_2SiO_4), ranging from ~15 to ~31 wt%. Other phases always present in all samples, although in small amounts, are Calcite (0.8–4.9 wt%), Quartz (0.4–3.0 wt%) and Mayenite ($Ca_{12}Al_{14}O_{33}$), which ranges from 1.2 to 7.7 wt%. Gehlenite $Ca_2Al(AlSi)O_7$ was detected at significant level in all sample but INERT1, with amount ranging from 2.4 to 4.8 wt%. Brownmillerite (Ca_2AlFeO_5) was detected only in sample INERT1 (1.8 wt%). Portland cement phases, i.e., Larnite, Brownmillerite, Gehlenite and Mayenite, which probably represent newly formed high-T products of the inertization process, dominate among crystalline phases and all together range from ~18 wt% (INERT1) to ~44 wt% (INERT4). Olivine, Clinopyroxene, and Orthopyroxene, identified by XRPD, SEM and TEM on selected asbestos fibers after inertization (see 3.3, 3.4, 3.5 paragraphs), and therefore representing direct reaction products of Chrysotile and Crocidolite breakdown, could not be refined at significant level in these powdered bulk mixtures. A representative XRPD spectrum of the bulk sample is reported in Figure 3.4.

Table 3. 2. Bulk XRPD quantitative phase analysis of the four studied samples after inertization

Sample	INERT1		INERT2		INERT3		INERT4	
	Wt%	σ	Wt%	σ	Wt%	σ	Wt%	σ
C_2S	15.3	0.3	31.2	0.2	23.8	0.2	28.3	0.2
Cal	4.9	0.2	0.8	0.1	0.8	0.1	1.4	0.1
C_4AF	1.8	0.2	-	-	-	-	-	-
Qtz	0.4	0.2	0.8	0.1	1.4	0.1	3	0.1
Geh	-	-	4.8	0.3	3.4	0.3	2.4	0.3
May	1.2	0.3	7.7	0.3	5.8	0.4	5.1	0.3
Glass	77.6		54.7		64.9		67.3	
GOF	6.5		7.8		0.5		6.6	
R%	6.2		6.7		8		6.2	
wR%	8.2		9.4		11		8.4	

C_2S = Larnite; C_4AF = Brownmillerite (cement chemist notation CCN, Taylor, 1997); Cal = Calcite; Qtz = Quartz (Kertz, 1983); Geh = Gehlenite; May = Mayenite.

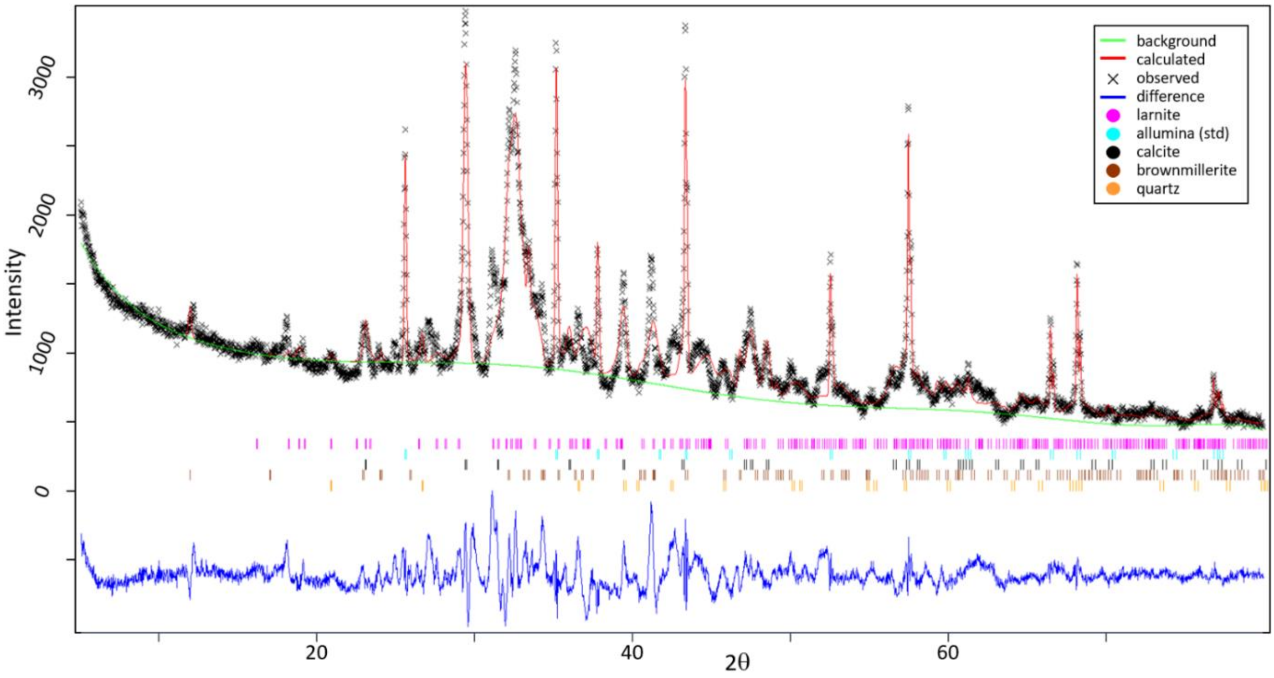

Figure 3. 4 Example of Rietveld refinement of the INERT4 sample. Observed (crosses), calculated (continuous line), and difference (bottom line) curves are reported. Vertical bars mark Bragg reflection positions corresponding to the main crystalline phases.

Table 3.3 reports XRF bulk composition of the post-inertization panels, revealing that they are mostly formed by CaO (46–52 wt%) and SiO_2 (23–28 wt%), with minor MgO, Al_2O_3, Fe_2O_3 and SO_3. Loss on ignition (LOI) is below 3%, as expected for heated samples, except for INERT1, which shows a surprisingly high loss of 10.67%. The explanation of this anomalously high value in the sample first tested at the Scame Forni (approximately, one year ago) is probably an "aging" effect and may reflect possible post-treatment transformations such as the CaO hydration.

Table 3. 3 XRF bulk data (wt. % oxides) for post-inertization samples.

WT. %	**INERT1**	**INERT2**	**INERT3**	**INERT4**
MgO	5.63	5.88	7.69	6.62
Al_2O_3	4.27	3.78	3.54	4.26
SiO_2	23.61	27.13	23.87	28.70
SO_3	3.07	4.05	5.42	2.55
Cl	0.02	0.14	0.19	0.12
K_2O	0.61	0.30	0.26	0.34
CaO	46.39	51.13	52.02	49.00
TiO_2	0.24	0.37	0.22	0.23
Cr_2O_3	0.05	0.03	0.03	0.04
MnO	0.48	1.04	0.59	0.36
Fe_2O_3	4.58	4.00	3.14	4.53
SrO	0.09	0.12	0.10	0.09
BaO	0.07	0.05	0.07	0.03
H_2O	10.67	1.76	2.64	2.82
Total	99.76	99.78	99.78	99.66

Microstructures and microchemical data of post-inertization panels: SEM/EDS observations

SEM observations have been done on polished petrographic Section (5 cm length, insets on Figure 3.5) of INERT1–2–3–4 (Figure 3.5).

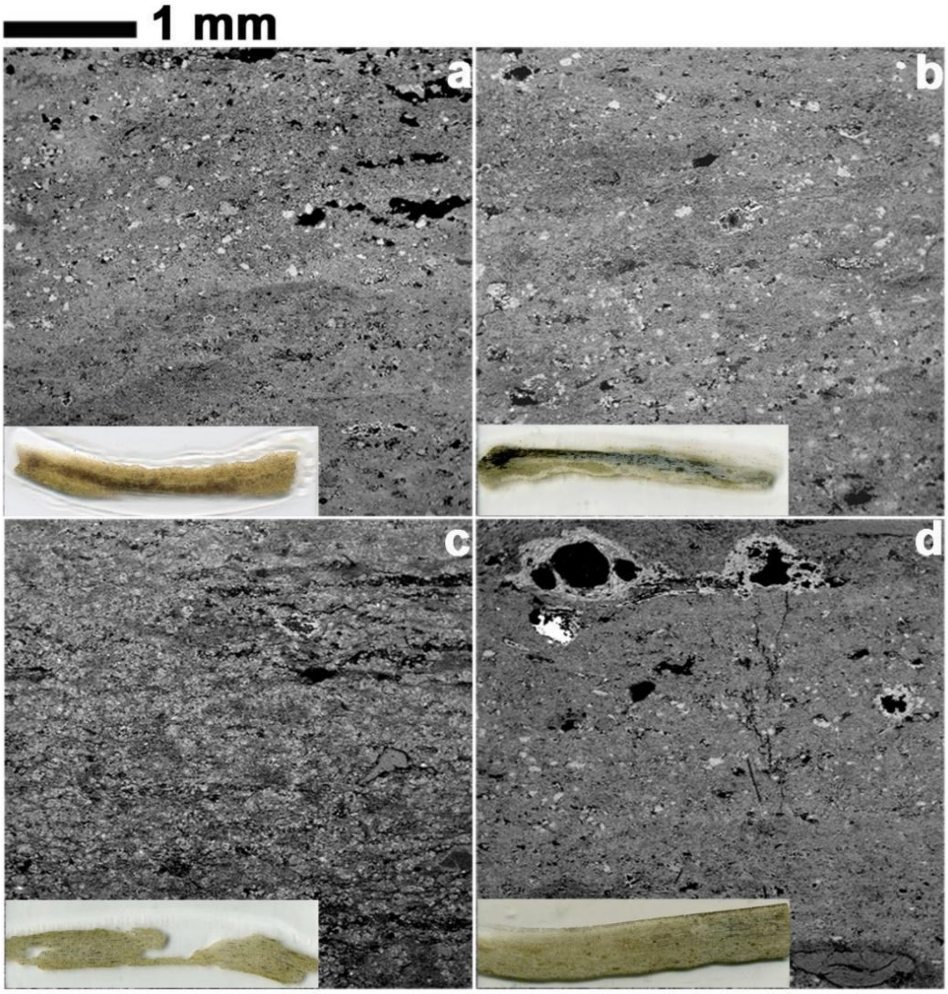

Figure 3.5(a–b–c–d) SEM/BSE low-magnification images and corresponding thin petrographic sections (insets, which length dimension is 5 cm) of treated panels (INERT 1–2–3–4, respectively), pointing out overall microstructural features such as grain size distribution, porosity, possible anisotropic arrangements. The scale bar is the same for all SEM/BSE images since they were made with the same magnification (20X). Coarser grains correspond to the pristine clinker aggregates, whereas black sites correspond to pores. Light-grey lens-shaped bodies with peculiar black central pores (e.g., upper side in d) correspond to decomposed crocidolite fiber bundles (see below for details).

Figure 3.5 shows low-magnification SEM/BSE images of INERT1–2–3–4, pointing out some broad differences in terms of grain/matrix ratio, overall grain size distribution, porosity, and anisotropy, reasonably inherited from pristine, pre-treatment panels. This is particularly evident for sample INERT3 showing a definitely higher grain/matrix ratio, more homogeneous grain size distribution and slight anisotropy, parallel to the panel surface (e.g., Figure 3.5c). Disregarding these broad differences, all samples share the same microstructural features, being formed by a fine to ultrafine matrix hosting grains and aggregates up to 500 µm in size (Figure 3.6). Most common grains/aggregates are: (1) clinker-like aggregates (e.g., Figure 3.6a and d); (2) single crystals of

Quartz (e.g., Figure 3.6a and b) and Feldspars (both K-feldspar and plagioclase); (3) apparently fibrous pseudomorphic bodies, always characterized by inner large cavities and light-grey BSE contrast (decomposed crocidolite sites d-cdl; e.g., Figure 3.6a and b); and (4) apparently fibrous pseudomorphic bodies, characterized by an homogeneous dark-grey BSE contrast (decomposed Chrysotile sites d-ctl; e.g., Figure 3.6b).

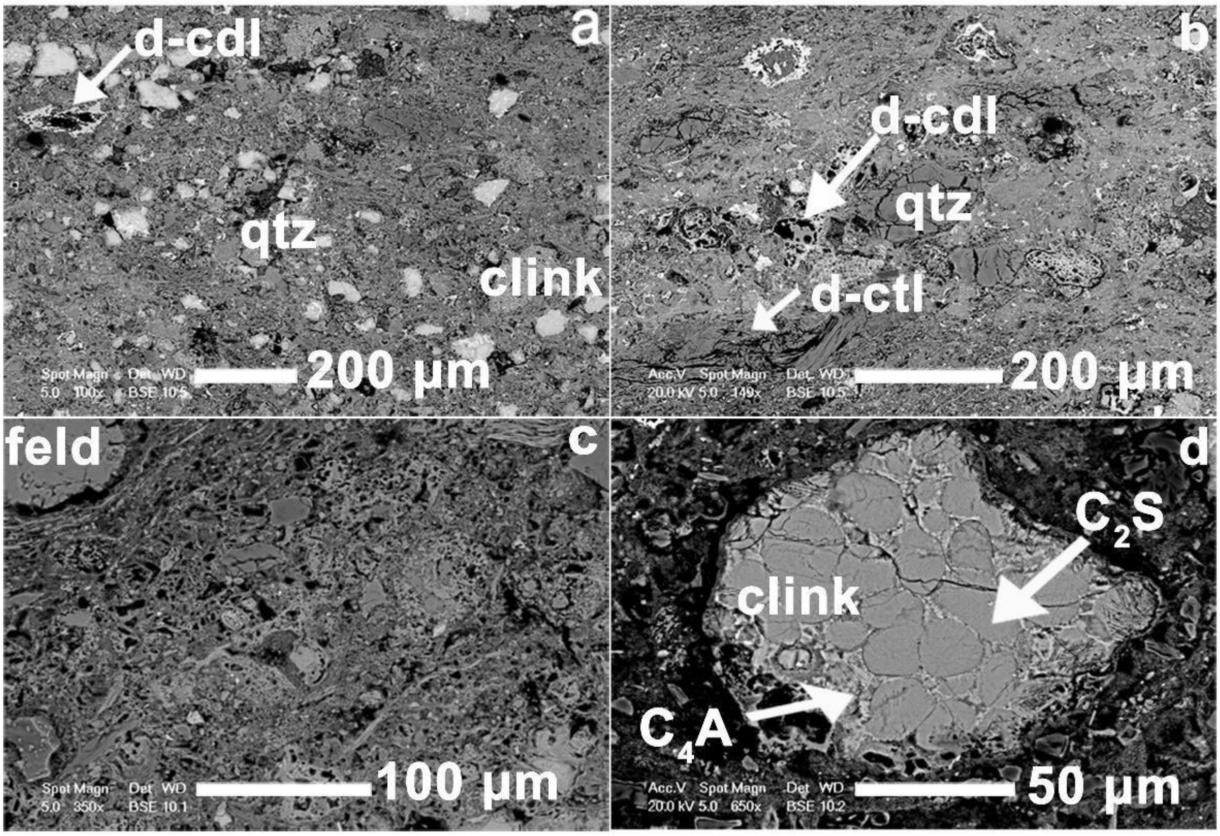

Figure 3. 6(a−b−c−d) Representative SEM/BSE images of the most recurring grains and aggregates in inert samples (INERT1−2−3−4, respectively), i.e., Quartz (qtz), clinker aggregates (clink), Feldspars (feld), decomposed crocidolite (d-cdl) and decomposed Chrysotile (d-ctl). The size of single-crystal grains and aggregates ranges from 10 to 200 µm and are homogeneously distributed in an ultrafine matrix. Figure. d shows the typical microstructure of clinker-like aggregate, here mostly consisting of light-grey one calcium alluminoferrite C_4AF and dark grey larnite C_2S.

The fine to ultrafine matrix is highly porous, with interconnected irregular pores, and displays a very complex microstructure where different kinds of micro and nanograins are associated with an apparently amorphous compact material (e.g., Figure 3.6c).

Clinker-like aggregates are ubiquitous in all inert samples and show variable size (ranging between 20 and 100 µm) and shape. They typically display lobate boundaries, characterized by reaction rims with the embedding matrix, probably inherited from pristine cement reactions. Clinker aggregates are internally heterogeneous, with grey rounded grains surrounded by a light-grey material (Figure 3.6d). EDS data revealed that they correspond to larnite and calcium alluminoferrite C4AF, respectively, in agreement with XRD results.

Chrysotile and crocidolite breakdown products: XRPD, SEM/EDS results

We collected XRPD data on the apparently fibrous pseudomorphic bundles, picked off from the bulk inert samples; these analyses aim to verify the complete decomposition of Chrysotile and Crocidolite, therefore proving the efficacy of the inertization process. Remarkably, the “pseudofibres” showed a strangely lower mechanical resistance with respect to pristine asbestos fibers, when handled with the tweezers at the stereomicroscope. In particular, decomposed chrysotile is brittle and disaggregate very easily, while decomposed crocidolite is also brittle, but tough and more difficult to be extracted from the bulk sample (possibly due to the wide presence of glassy material which works as cement; see below). Table 3.4 shows main crystalline phases resulting from chrysotile and crocidolite decomposition, based on XRPD results. The main crystalline phase replacing chrysotile fibers is olivine. Olivine was systematically detected in all samples, minor Quartz, Calcite, Akermanite $Ca_2MgSi_2O_7$ (belonging to the Melilite group) and Oldhamite (Ca,Mg,Fe)S may also occur. Main crystalline phases resulting from crocidolite decomposition are Clino- and Orthopyroxenes, Olivine and Kirschsteinite $CaFeSiO_4$, together with minor Quartz and an Akermanite-like phase. As shown below, these crystalline products are associated with an abundant amorphous phase.

Table 3. 4 Main crystalline phases replacing chrysotile and crocidolite fibers after thermal inertization, based on XRPD data (ol=Olivine, ak=Akermanite, cpx=Clinopyroxene opx=Orthopyroxene, qtz=Quartz, kir=Kirschsteinite, ol=Oldhamite).

XRD RESULTS	D-CTL	D-CDL
INERT1	ol, ak qtz,	cpx, kir, ak,
INERT2	ol, qtz, cal	ol, opx, qtz
INERT3	ol, qtz, cal	ol, opx, qtz
INERT4	ol, qtz, old	ol, qtz

SEM BSE images show that pristine Chrysotile fibrous bundles are replaced by pseudomorphic aggregates, rounded to irregular in cross sections (Figure 3.7a) and highly elongated in parallel sections (Figure 3.7b), based on the original orientation of fibers axes. Pseudomorphic bundles display constant features in all the inert samples, with a relatively homogeneous dark-grey contrast in BSE images and pervasive brittle fracturing, both parallel and perpendicular with respect to the original fiber axis (e.g., Figure 3.7c and d). Whereas separation parallel to the fiber axis was typical also of untreated chrysotile bundles, we remark that fracturing perpendicular to pristine fiber axis was observed only in treated samples and testify the sharp drop in mechanical resistance, due to crystal structural modifications and to the replacement of strong elongated chrysotile single crystals with nanosized aggregates (as detailed in TEM Section 3.5).

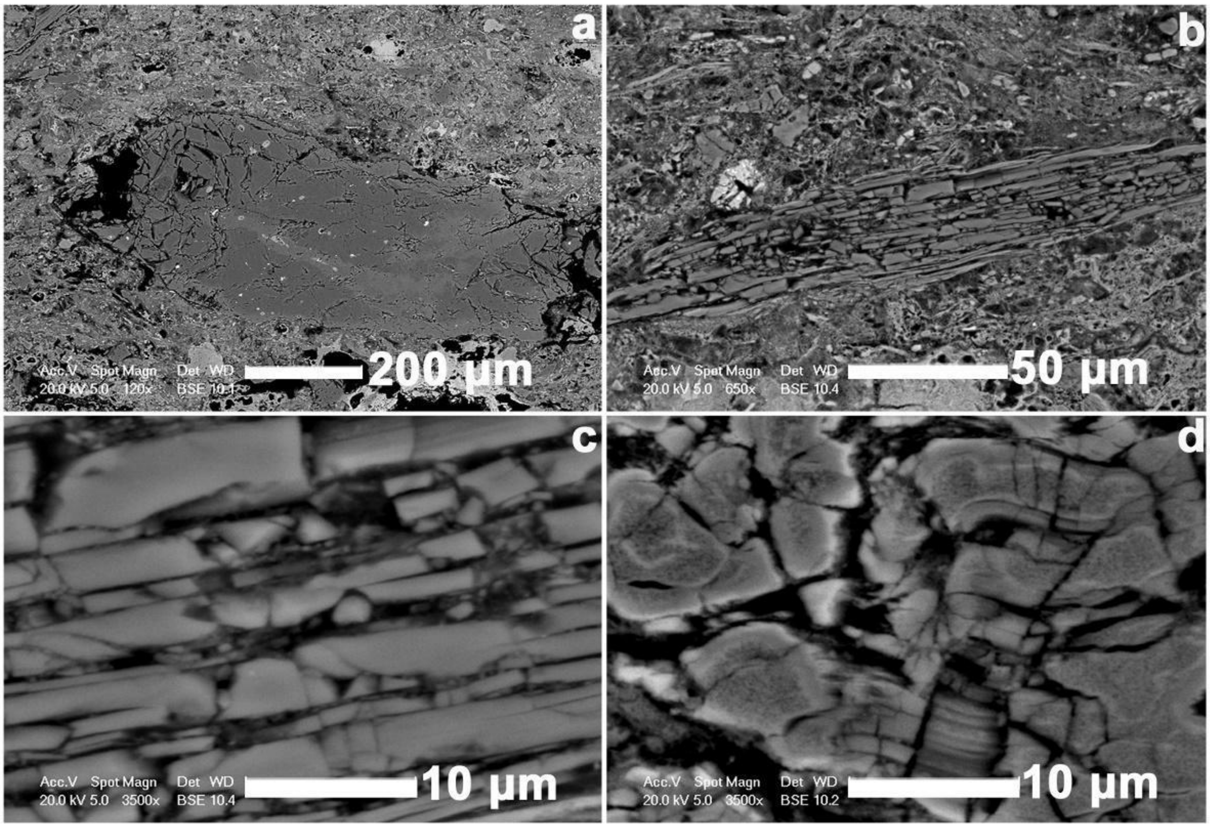

Figure 3. 7 SEM/BSE images displaying pseudomorphic bundles corresponding to Chrysotile breakdown. The most significant microstructural features are represented by pervasive fracturing perpendicular to the original fiber axis. (a) Irregular and rounded aggregate. (b) Elongated aggregates. (c and d) details of the pervasive fracturing of the pseudomorphic bundles, actually formed by nanosized grains (see TEM results below).

Due to the ultrafine size of the breakdown products of Chrysotile (see TEM data reported in Section), the volume analysed by EDS always affected assemblages of different phases, therefore resulting in mixed data with average composition close to that of the original serpentine (usually, with an excess Mg).

The sites of the original crocidolite bundles are easily recognizable, due to their BSE contrast, always brighter with respect to the fine-ultrafine cement matrix, and to the systematic occurrence of a relatively large central cavity (Figure 3.8a and b). As observed in the case of Chrysotile breakdown, the pseudomorphic bundles may display sub-rounded cross sections or elongated habits, depending on the orientation (arrows in Figure 3.8a), and show a distinctive large central cavity (rounded or elongated in shape, respectively, Figure 3.8a and b).

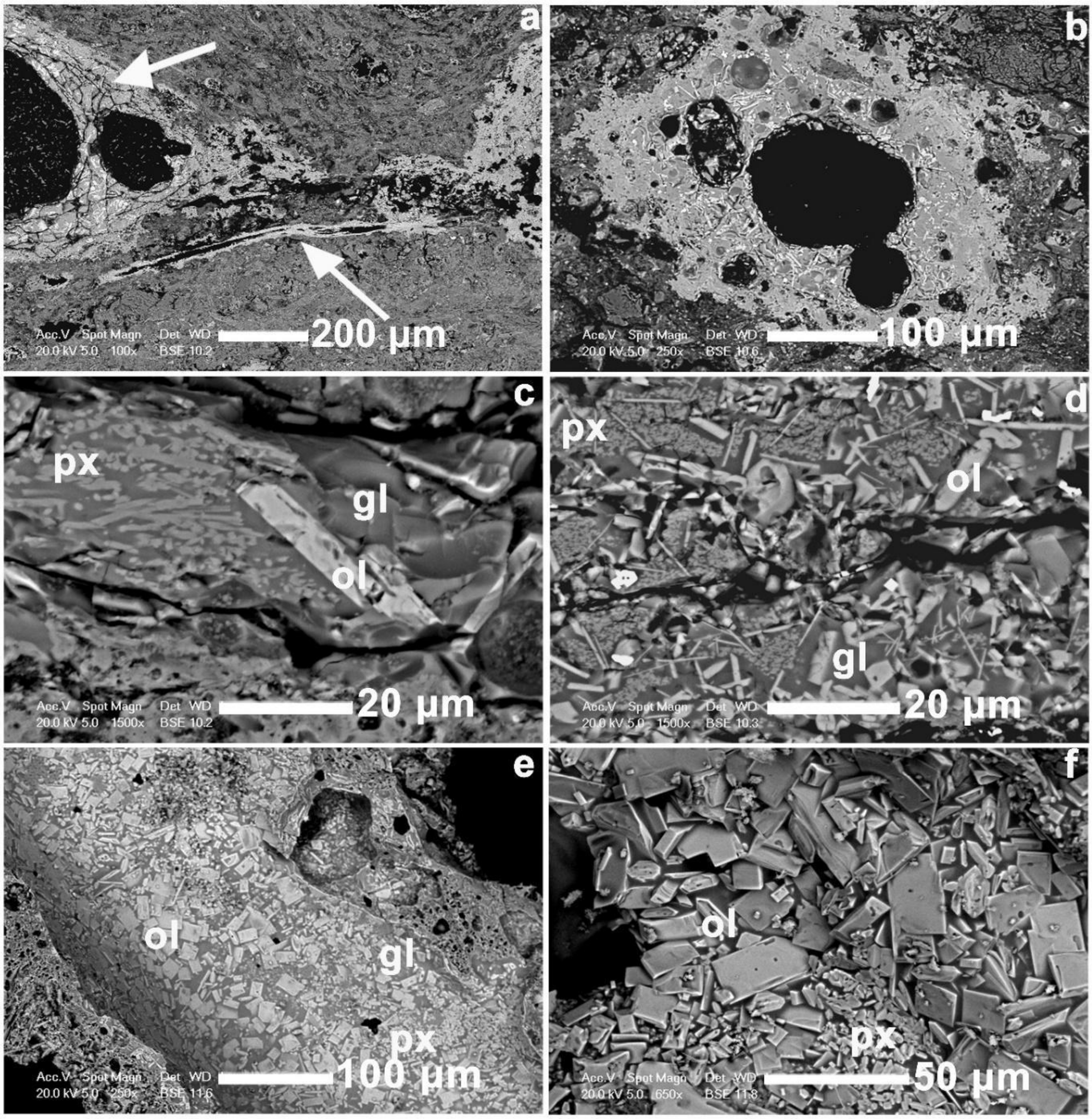

Figure 3. 8 SEM/BSE images of main phases of Crocidolite breakdown: ol=Olivine, px=Pyroxenes, gl=Glassy groundmass. (a) Two pseudomorphic bundles (arrow) corresponding to parallel and cross sections (elongated and rounded, respectively); note the systematic occurrence of the central cavities. (b) Wide central cavity surrounded by light-grey BSE contrast material. c-d-e-f) Details

of olivine and pyroxene crystals, enclosed in the amorphous groundmass. Olivines have euhedral and skeletal habit, crystal size between 10 and 50 µm and typically occur close to the central cavities. Pyroxenes occur in the outer portions of pseudomorphic bundles and have smaller grain size between 1 and 10 µm.

Decomposed Crocidolite bundles consist of a glassy groundmass, that protrudes within the surrounding ultrafine cement matrix, thus giving rise to irregular, lobate boundaries (Figure. 8b). This peculiar microstructure explains why decomposed crocidolite products are strongly bonded to the matrix, and hard to be removed from their original sites.

The glassy groundmass reveals a silicatic composition, with a significantly high content in Fe and Na (Table 3.5, where overall EDS data ranges are reported, expressed as oxides wt%).

Table 3. 5 Compositional ranges of the glassy groundmass occurring in decomposed crocidolite (SEM EDS data).

Oxides	Wt. % ranges
Na_2O	1.99-12.17
MgO	1.88-3.82
Al_2O_3	0.76-2.15
SiO_2	45.26-63.08
K_2O	0.38-11.93
CaO	1.37-30.69
MnO	0.19-2.12
FeO	14.33-24.24
Total	100

The glassy groundmass hosts different crystalline phases (Figure 3.8c and d), in particular Olivine, Ortho and Clinopyroxes, and minor metallic Fe. Olivine crystals are up to 50 µm in size, with euhedral (prismatic-acicular) to skeletal habits, and preferentially occur close to the central cavity. The composition is variable in terms of Mg/Fe ratio and Ca substitution, giving rise to both ferromagnesian and calcic olivines. Figures 3.9a and b report two representative spectra of ferromagnesian and calcic, kirschtenite-like olivines, respectively, in agreement with XRD results.

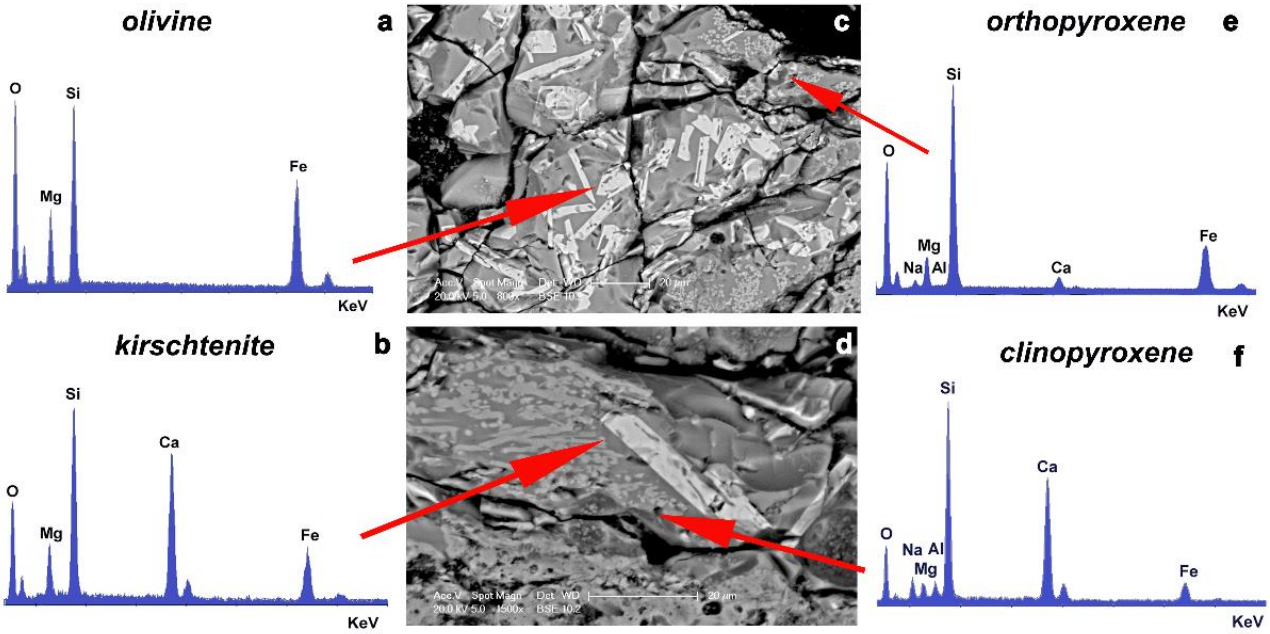

Figure 3. 9 Representative EDS spectra of Fe-Mg and calcic olivines (a and b) and ortho- and clinopyroxenes (e and f), resulting from crocidolite decomposition.

Ortho and Clinopyroxenes are characterized by a lower grain size with respect to olivine (up to 10 µm in size) and preferentially occur in the outer portions of the pseudomorphic aggregate, close to the cement matrix boundary (e.g., Figures 3.8e and f). Representative EDS spectra for ortho- and clinopyroxene are reported in Figure 3.9e and f.

TEM investigation

TEM investigations have been performed to accurately determine the nanostructural characteristics of the high-temperature products of asbestos breakdown and to ensure the definitive absence of Chrysotile and Crocidolite fibers.

The treated bulk material (i.e., the cement-derived matrix) reveal a very complex nanostructure (Figure 3.10). The matrix shows recurrent features, among which: (a) occurrence of crystalline to weakly crystalline nanograins or nanolamellar grains with Ca-Al silicatic composition, as typically of clinker phases; (b) abundant amorphous material hosting the different nanocrystals; (c) abundant nanopores.

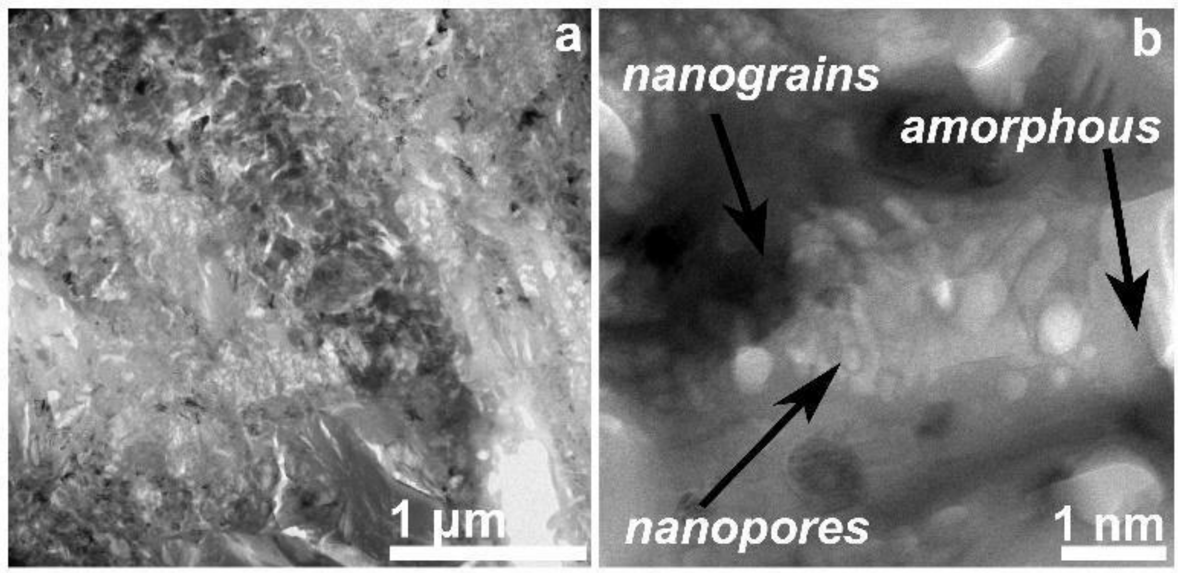

Figure 3. 10 TEM bright-field images, showing the typical nanostructure of cement-derived matrix. (b) Arrows indicates nanopores and nanograins of calcium and aluminium silicates (darker contrast) hosted in low-contrast amorphous material.

Based on SAED and EDS data, chrysotile is replaced by a close association of Olivine and Pyroxene nanocrystals, 10–150 nm in size, hosted in an amorphous material. The original fibrous habit is maintained (Figure 3.11a), giving rise to an elongated pseudomorph where Olivine and Pyroxenes nanocrystals and amorphous material are closely associated (Figure 3.11b). Figures 3.11 c and d show representative high-resolution images of enstatite and forsterite, respectively, characterized by regularly spaced lattice fringes. We remark that the "size" of this nanostructure (i.e., Olivine + Pyroxene + amorphous association) is responsible for the mixed analyses obtained at the SEM-EDS micron scale.

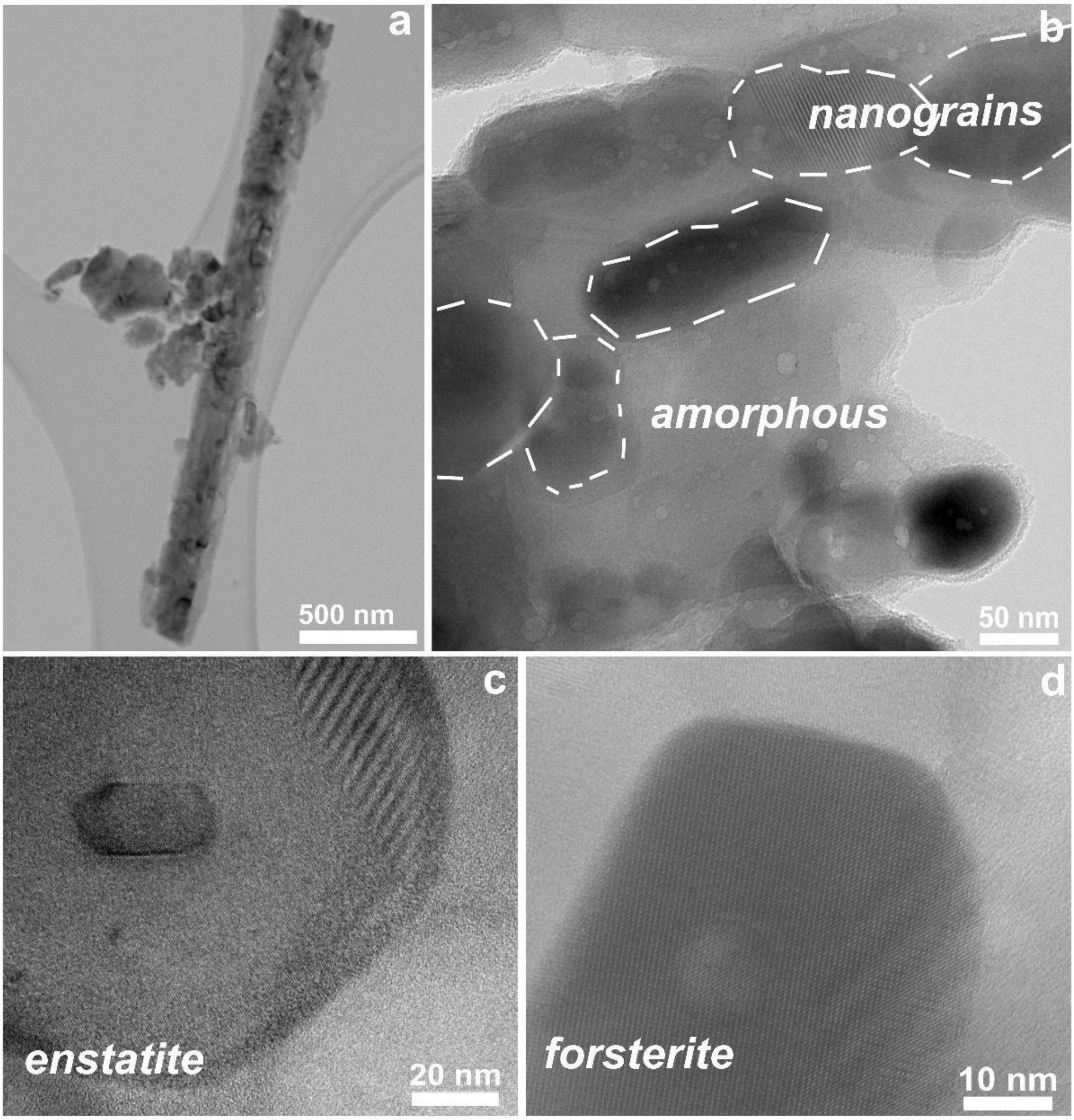

Figure 3. 11TEM images of chrysotile breakdown products. (a) Low magnification bright-field, showing a pseudomorphic bundles, formed by round-shaped nanograins, characterized by variable TEM contrast due to the variable crystal orientation of the different nanograins. (b) Detail of the pseudomorph showing the ultrafine association of amorphous material and rounded nanocrystals with different size (from 10 to 60 nm). (c and d) Representative high-resolution images of enstatite and forsterite nanocrystals.

SAED and EDS data confirm that Crocidolite is replaced by fayalitic Olivine, Pyroxenes and silica-rich amorphous material (e.g., Figure 3.12). Olivine and Pyroxenes crystals have a well-defined habit and are coarser than chrysotile breakdown products, being typically larger than 500 nm (Figure 3.12).

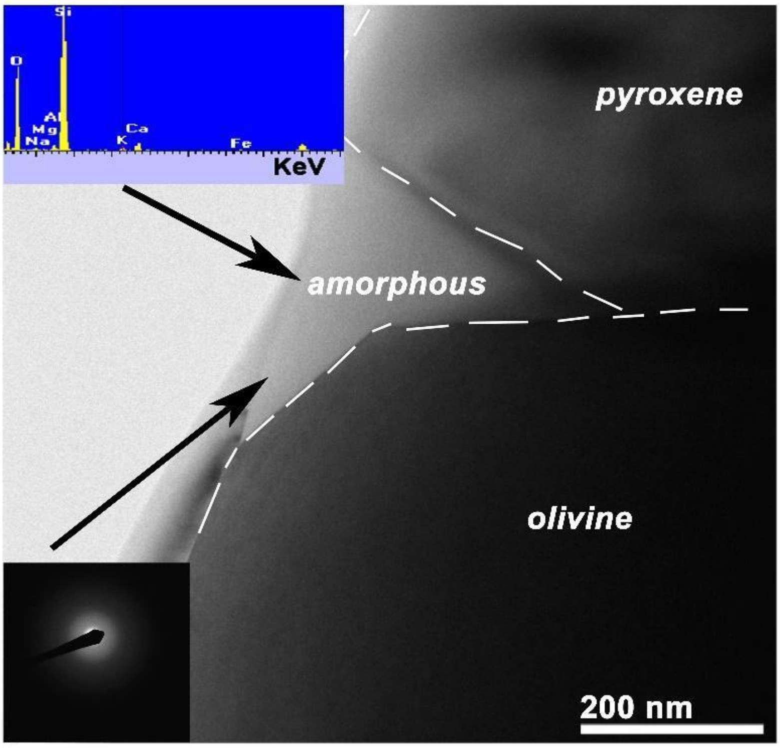

Figure 3. 12 Bright-field TEM image showing micron-sized Olivine and Pyroxene crystals resulting from Crocidolite decomposition. The insets report the selected area electron diffraction (SAED) and EDS analysis for the amorphous material.

DISCUSSION

Economic and environmental implications of the study

The solid waste production due to booming economy is of great concern as it can cause human health problems, pollution of the ecosystems, extensive land occupation for landfills, increased cost for waste collection and disposal. This is particularly true for ACW, since declared toxic and banned. Adopting environmentally sustainable green technologies for the management of solid waste would reduce these problems. Most notably, the traditional concept of waste regarded as pollution is progressively moving towards the new perspective of a waste regarded as resource (e.g., Gualtieri & Boccaletti, 2011; Gualtieri, Giacobbe, et al., 2012; Gualtieri, Veratti, et al., 2012; De Carvalho Gomes et al., 2019; Ligabue et al., 2020; Tang et al., 2020; Zhang et al., 2020).

Recycling ACW into a sustainable secondary raw material would be therefore a viable approach to eliminate a toxic waste from the environment, reduce related health risk, and conserve natural resources for the next generation at once. However, there are some barriers to overcome, namely the high costs and energy consumption demanded by thermal treatments, typically required in asbestos decomposition processes (Spasiano & Pirozzi, 2017). The results of this study meant to represent the scientific background for the realization of a future inertization plant where large volumes of harmful wastes, such as those containing asbestos fibers, can be de-activated by short-time thermal processing. The short inertization time, 15 min in temperature compared to 1–50 h of other patents, actually represents the most promising feature to ensure the economic sustainability of a future industrial-scale plant.

The sustainability of the entire process is a complex and primary topic, which requires in-depth economic analysis of the many items involved, among which the environmental advantages resulting from ACW volume reduction, the inertization costs per ACW ton vs. the cost of disposal, either in national or foreign landfills. Even though a detailed and comprehensive economic analysis is in progress and will be presented elsewhere (in particular, costs-benefits analysis and Life Cycle Assessment, LCA), broad preliminary estimates demonstrate the competitiveness of the Tuccitto & Grillo patent. Other patents describe vitrification, lithification and ceramization processes using tunnel kilns for ceramics, therefore systems longer than 100 linear meters, with deactivation times up to 50 h, and no experiment has been ever conducted or authorized at the moment. Even for patents using batch kilns, the treatment time exceeds 20 h. The long time spent in the kiln at high temperature results into high-energy costs that make any industrial start-up economically unsustainable. As an example, the Italian patent by ENEL describes a process leading to vitrification of ACW materials with asbestos content between 40% and 60%, through thermal cycles at temperatures between 1000 °C and 1300 °C. The energy consumption necessary to vitrify one kg of ACW is approximately 1.55 kWh (Paglionico, 2017). The energy consumption for the INERTAM plant at Moncenx can be easily envisaged much higher since operating at 1400–1600 °C, and the estimated cost is between 1000 and 2500 € per ton, depending on the ACW composition and water content (Spasiano and Pirozzi, 2017). According to Tuccitto & Grillo, owners and inventors, the estimated energy consumption of the patent "UIBM: Invenzione Industriale n°25588/'17" is only 0.25 kWh per kg of ACW treated, more than 6 times lower than the ENEL patent, with an energy cost as low as 60–70 € per ton of ACW treated. This estimated cost is competitive even if compared with the cost of landfill disposal, 199 € per ton in average (Paglietti & Conestabile della Staffa INAIL, 2013).

A comprehensive economic analysis of the overall process should also consider the possible re-use of the inert ACW as a secondary raw material (SRM) to be re-employed in several industrial fields. To date, the recycling of deactivated ACW as SRM has been largely exploited in several different fields, in particular for the production of clay bricks, glass, glass-ceramics, ceramic frits, ceramic pigments, cement products, geopolymers (Gualtieri et al., 2008, 2011; 2012a and 2012b; Yvon & Sharrock, 2011; Kusiorowski, et al., 2015; Ligabue et al., 2020). Comparatively fewer studies exist for applications in the plastic and rubber sectors.

Samples used for our inertization tests correspond to the widespread fiber-cement roofing panels (Eternit-like), that represent one of the main sources of large ACW volumes (ISPRA, 2020), that need to be adequately managed through safe (and expensive) disposal in carefully designed landfills. It is worth of mention that, based on our observations, in some cases removal operations were not strictly necessary, since they involved asbestos-free materials containing only man-made vitreous fibers admixed to common cement mortars. This feature points out that a relatively simple mineralogical study before any treatment or removal operation could avoid unnecessary expensive operations. In this respect, our research group is involved in the realization on a portable multi-analytical tool for in situ asbestos detection. We are also exploring the potentiality of special cameras, as Digital Cameras and Multi- and Hyper spectral sensors, carried by drones and /or Unmanned Aerial Vehicle and a remote sensing approach in detecting asbestos minerals in Eternit-like roofing panels that, if successful, would result into an even faster and simpler preventive screening of hazardous materials, allowing to direct the removal operations where required.

Asbestos irreversible decomposition and health concerns

Our investigations have proven the absolute efficacy of the proposed inertization process, showing the complete and irreversible decomposition of asbestos fibers, both chrysotile and crocidolite, i.e., the most common asbestos varieties in commercial products, with processing times definitely shorter than in all procedures suggested so far. Asbestos fibers transform into other crystalline phases and amorphous material, none of which has been recognized as a potentially hazardous mineralogical phase. Furthermore, we have shown that original asbestiform minerals, when preserving their original habit, actually decompose into pseudomorphic nanophase aggregates, where single nanocrystals have rounded to irregular habit. In other words, none of the new phases replacing asbestos fibers (mostly olivines, pyroxenes and Fe oxides) shows fibrous or acicular shapes. The micro/nanostructure of decomposed fibers also explains the exceptional drop in mechanical resistance of the pseudomorphs, that exhibit very easy brittle fracturing.

Cement-asbestos roofing slates are only a part of the man-made products where asbestos has been used in the past. Among these, there are other building materials such as water pipelines, water storage thanks and chimneys, whose mineralogical formulation is close to that of Eternit-like slates. It is therefore very probable that the inertization route described in the Tuccitto & Grillo patent will be affective also in these other types of ACWs. The inertization process, therefore, leads to a recrystallization into microscopic and submicroscopic particles, some of them in the nanoparticle range, which by definition refers to particles with all the three dimensions smaller than 100 nm (ISO/TC 229, Nanotechnologies, 2017). These nanoparticles can penetrate the alveolar-capillary membrane and reach the bloodstream (Brown et al., 2013). The liver is the primary organ of detoxification and is one of the tissues that is most exposed to nanoparticles (Cornu et al., 2020). The question about the safety of these nanomaterials and cement dust exposure (Rahmani et al., 2018; Shanshal & Al-Qazaz, 2020) and their impact on human health is therefore a legitimate concern. In this respect, within the frame of the present project, we are planning in vitro experiments aiming at ascertaining the biological effects of the deactivated cement-asbestos material. In a previous comparative cytotoxicity study on human alveolar epithelial cells, (Giantomassi et al., 2010) have reported that thermal transformed ACW has considerably lower cytotoxic than the original asbestos material.

Routes of possible reuse of the SRM

Composite materials, for instance, are constituted by mixing materials of different nature, such as organic polymers (rubber, plastics or resins) and inorganic natural or artificial components (mine or industrial processing wastes). The goal of combining such different components is to obtain products that retain the best properties of both or the emergence of new desirable properties together with cost benefits. Commonly desired final properties include mechanical reinforcement, anti-scratch toughening, flammability reduction, as well as special optical, dielectric, magnetic or bioactive properties. The main issue in the production of such materials is that the different components tend to be incompatible from a chemo-physical point of view and separate at the microscopic level like oil and water mixtures. This produces aggregation of the filler, macroscopic separation, formation of point or stripe defects, and ultimately a loss of the desired properties.

Our investigation has proven that the inertization process creates an extensive recrystallization of the original minerals into silica glass, Ca-Al silicates and minor ferromagnesian silicates with grain size down to the nanometer scale. The nanometer scale, therefore, represent the ultimate grain size into which the SRM can be reduced. The latter let us envisage a profitable strategy to compatibilize the organic matrix and the inorganic filler, that relays on the possibility to form chemical bonds between the inorganic nanoparticles surface and polymer chains. This can be achieved by the "grafting to" method, that is the attachment of previously prepared polymer chains to the surface via a reactive chain end (Selli et al., 2019) or by the "grafting from" one, that is growing directly the polymer on reactive sites present on the surface (Crippa et al., 2013).

From the above discussion it follows that the SRM, in view of its peculiar nanostructure, may have a high value, especially if technologically advanced applications can be assured. On the other hand, also for applications in more traditional industrial processes, such as ceramics and cement industries, the economic balance must include a comparison with the costs of the raw materials used in these sectors. The deactivated ACW has a composition that in principle could replace, in a given percentage and after variable admixing with other components, raw materials such as silica, feldspar, talc, kaolin clay, etc. These raw materials are costly. For example, the cost of feldspar of quality grade for the ceramic industry are around 100 €/ton, and that of kaolin clay 120–130 €/ton (source Ideal Standard S.r.L.). The reuse of deactivated ACW as SRM may therefore promote reduction of industrial production costs and, more importantly, may reduce raw material exploitation that typically causes environmental concern, pollution, destruction of the countryside and depletion of natural resources.

CONCLUSIONS

The present study provides a viable and sustainable way for asbestos-bearing waste management and represents the scientific groundwork for the realization of a future industrial-scale plant for ACW treatment, thus contributing to reduce the impellent problems related to these hazardous materials. Our process allows asbestos decomposition and deactivation by thermal treatment in an extremely short time, with a substantial drop in the inertization cost. The accurate mineralogical, chemical, and micro/nanostructural investigations on deactivated waste demonstrate and certify the effectiveness of the inertization processes and the irreversible disappearance of all asbestos fibers. Moreover, the deactivated wastes revealed chemical, mineralogical and micro/nanostructural characteristics that appear to be very promising for their re-cycling in several industrial sectors as secondary raw materials, in a perspective that is fully compatible with the principles of sustainability, natural resources protection and circular economy.

3.3 OTHER RELATED STUDIES FOCUSED ON THE CHARACTERIZATION AND REUSE OF SRM DERIVING FROM INERTIZED ACW

- Thermal decomposition of cement–asbestos at 1100° C: how much "safe" is "safe"? Fabrizio Vergani, Lucia Galimberti, **Narcisa Mihaela Marian**, Giovanna Giorgetti, Cecilia Viti, Giancarlo Capitani. Journal of Material Cycles and Waste Management 24 (1), 297-310. https://doi.org/10.1007/s10163-021-01320-6.
- Recycling detoxified cement asbestos slates in the production of ceramic sanitary wares. Andrea Bernasconi, Luca Pellegrino, Fabrizio Vergani, Fabrizio Campanale, **Narcisa Mihaela Marian**, Lucia Galimberti, Matteo Perotti, Cecilia Viti, Giancarlo Capitani. https://doi.org/10.1016/j.ceramint.2022.09.147.
- Recycling of the inert material as an inorganic filler in epoxy resins for flooring is almost ready. In preparation. The application in this case is quite different from the others and reflects the wide variety of areas in which the deactivated cement asbestos material could be reused.

Here below I report the abstracts of the two papers and the working paper on resins.

Thermal decomposition of cement-asbestos at 1100°C: how much "safe" is "safe"?

The products of cement–asbestos treated in air at 1100 °C were characterized by a multi-methodological approach to determine: (i) the effective deactivation of harmful asbestos fibers; (ii) the mineralogy and microstructure of the inert product and its possible use as a secondary raw material (SRM); and (iii) any potential health hazard of the SRM. For this purpose, energy-dispersive X-ray fluorescence spectrometry (EDXRF), X-ray powder diffraction (XRPD), scanning, and transmission electron microscopy (SEM and TEM) analyses were performed. The powdered SRM was also analyzed by dynamic laser scattering and solution leaching experiments, to determine grain size distribution and possible elements release. Our results confirm the deactivation of crocidolite and chrysotile asbestos fibers, but at the same time evidence a significant fraction of nanoparticles in the SRM and some critical releases of SO_4^{2-}, F^- and Cr^{6+} in solution. Both the nanoparticle fraction and the critical elemental release may pose human health concern and adversely affect potential applications of the SRM. Strategies to control the grain size distribution through adjusted thermal treatment conditions and microwave-assisted grinding operations are discussed. Possible routes to safely reuse the SRM are indicated.

Recycling detoxified cement asbestos slates in the production of ceramic sanitary wares

The recycling of cement asbestos slates (CASs) thermally treated in air at 1100 °C as secondary raw material in the production of Vitreous China (VC) sanitary wares has been investigated. Deactivated cement asbestos powder (DCAP) has been used in individual substitutions (5 wt%) of Quartz and Feldspar. The single raw materials, the ceramic technological properties before and after firing, and the phases and microstructure evolution during firing have been investigated with a variety of techniques, including those commonly used for production quality checks and instrumental methods for mineralogical analyses. DCAP acts as flux rather than as inert in the firing process, promoting greification. Although the substituted samples have some critical aspects that need to be addressed before processing, such as the presence of sulphate salts that increase the dispersant demand and the colour of the fired ceramic body, the overall technological properties are comparable to those of normal production, suggesting the possible reuse of DCAP powder in the production of sanitary wares.

Recycling of deactivated cement asbestos as inorganic filler in epoxy resins for flooring applications

Cement asbestos slates, commonly known as Eternit® and still abundant in private and public building, were deactivated through a thermal process. The resulting deactivated cement asbestos powder (DCAP), a mixture of Ca-Mg-Al silicates and glass, was used as filler in PT and PF, two different epoxy resins (bisphenol A epichlorohydrin) for flooring applications. The addition of the DCAP filler to the PF samples causes a slight (but still acceptable) decrease of the main mechanical properties (compressive, tensile and flexural strengths) with increasing DCAP content. The addition of DCAP filler to pure epoxy (PT resin) causes a slight decrease of the tensile and flexural strengths with increasing DCAP content, while the compressive strength is almost unaffected, and the Shore hardness increases. The main mechanical properties of the PT samples are significantly better than those of the filler-bearing sample of normal production. Overall, these results suggest that DCAP can be advantageously used as filler in substitution of commercial barite. In particular, the sample with 20 wt% of DCAP is the best performing in terms of compressive, tensile, and flexural strengths, whereas the sample with 30 wt% of DCAP shows the highest Shore hardness, which is an important property to be considered in flooring applications.

CHAPTER IV

RED GYPSUM WASTE FROM TiO_2 INDUSTRIAL PRODUCTION AND ITS POSSIBLE USE AS SRM IN CERAMICS

Chapter overview

In this chapter, I report the research on red gypsum muds deriving from a local plant for TiO_2 production and representing the most abundant special inorganic waste in Tuscany. Overall data and main conclusions have been presented in a manuscript, that has been submitted the 13 of September 2022 in Ceramics International (currently sent back to the Editor after major revision). This paper is the result of the collaboration between the University of Siena and the GRINN srl Start Up, which realized patents for the reuse of different kind of wastes to produce new ceramic-like products (https://grinn.it/).

Here below, I report the manuscript after revision (December 2022). For the realization of the manuscript, I specifically investigated both the waste and the new ceramic products using the mineralogical techniques described in Chapter II. All the authors have contributed to data interpretation, discussion, and conclusions.

4.2 From high-volume industrial waste to new ceramic material: the case of red gypsum muds in the TiO_2 industry

Narcisa Mihaela Marian[a], Matteo Perotti[a], Carlo Indelicato[a], Claudia Magrini[a], Giovanna Giorgetti[a], Giancarlo Capitani[b], Cecilia Viti[a]

[a] *Department of Physical Science, Earth and Environment DSFTA (UniSi) V. Laterina 8, I-53100, Siena, Italy*

[b] *Department of Earth and Environmental Sciences DISAT (UniMIB) Piazza della Scienza, 4 – 20126, Milano, Italy*

ABSTRACT

The present study aims to apply the principles of circular economy, using special inorganic waste (in particular, red gypsum muds from a TiO_2 plant in Tuscany, Italy) to produce ceramic materials for the construction and building industries. Red Gypsum (RG) muds produced during more than 10 years of industrial processing were chemically and mineralogically characterized by X-ray fluorescence spectrometry (XRF), X-ray powder diffraction (XRPD), scanning electron microscopy with energy dispersive X-ray spectrometer (SEM/EDS), and thermal analyses (TA). The analyses testify that RG waste production is chemically and mineralogically constant over time, and therefore suitable to be used as a secondary raw material in industrial ceramic production. Ceramic specimens have been realized using an extremely high amount of the RG waste (up to 70%) and characterized using the same chemical-mineralogical techniques, revealing that Anhydrite, Pyroxene, and Fe/Ti oxides are the main crystalline phases, embedded in a glassy compact matrix. Overall results indicate that the production of ceramic materials could represent a definitive and sustainable solution for the problematic management of the large volumes of RG waste deriving from TiO_2 plants.

INTRODUCTION

Mineral resources are essential raw materials of everyday commodities, from the most basic ceramics and building materials to high-tech and nanotechnologies devices. Most significant mineral resources are not renewable, at least on the human time scale. In other words, there is a time-scale gap between the human exploitation/consumption of natural resources and the geological times required by our planet to restore what is consumed. This poses severe problems for the future availability of natural raw materials, and strategies alternative to the massive exploitation of natural resources until their exhaustion is immediately needed (Rees, 2017; Commission et al., 2018).

The industrial processes that transform raw mineral resources into various industrial products typically require physical and/or chemical treatments of the raw material. In most cases, this implies chemical reactions with the consequent production of highly polluting, acid wastewater. In other words, the use of natural resources and the realization of commercial products are inevitably associated with the production of waste at any stage of the product life cycle, therefore requiring an adequate management strategy (OECD, 2015).

Gypsum waste is commonly produced in the construction and demolition industry, but huge amounts also arise from TiO2 production plants (Mohd Tadza et al., 2019; Jiménez-Rivero & García-Navarro, 2020; Ju et al., 2022). The industrial process involves acid chemical treatment to extract Ti from ilmenite ($FeTiO_3$), the ore mineral (McNulty, 2007; Ginsberg et al., 2011; Gázquez et al., 2014, 2021), resulting in the formation of acid wastewater, which can be successfully neutralized with $CaCO_3$ powder (Gázquez et al., 2009). The neutralization reaction of acid wastewater with Calcite powder represents a step in environmental protection, despite inevitably resulting in another environmental issue. In fact, the neutralization reaction H_2SO_4 (aq) + $CaCO_3 \rightarrow CaSO_4{\cdot}2H_2O + CO_2$ results in the production of a considerable volume of Gypsum mud (7/8 tons of gypsum waste for 1 ton of TiO_2 production), characterized by a red color due to the occurrence of minor Fe-bearing phases deriving from the raw mineral Ilmenite. Although red Gypsum (hereafter RG) (in accordance with European Waste Catalogue code 061101) mud is a non-hazardous waste, it is classified as industrial waste that needs to be managed and adequately relocated (Mohd Tadza et al., 2019; Protano et al., 2020; Rosli et al., 2020).

Managing large volumes of gypsum waste is an environmental, social, and political problem that needs to be addressed soon. Currently, the most adopted solution is the environmental restoration of abandoned quarries, mines, and landfills where RG is used as inert material to restore the original morphology of the area. Unfortunately, social communities do not always appreciate environmental restoration due to possible geochemical and hydrogeological concerns, despite scientific data supporting this solution's safety (Protano et al., 2020; Rosli et al., 2021).

A promising alternative, in agreement with environmental protection issues, sustainable exploitation of natural resources and circular economy, is to reuse RG wastes as secondary raw material. Many previous studies (Gazquez et al., 2013; J. Zhang et al., 2016; Y. Zhang et al., 2018; Cai et al., 2021) explored the possible reuse of Gypsum wastes in the cement and building materials industry. It was demonstrated that using RG instead of natural Gypsum in Portland cement manufacture maintains the physico-mechanical properties and the leaching behaviour of the final product. Zhang et al., (2018) also studied the use of RG to produce foamed Portland Cement with good compressive strength and thermal insulation properties. Cai et al., (2021) demonstrated the possible use of up to 20% RG as raw material to partially replace fly ash, generally composed of mullite and quartz, for the manufacturing of autoclaved aerated concrete, obtaining good physical and mechanical properties. Moreover, RG by-products have been also tested as to raw materials in gypsum blocks manufactured for the building and construction industry (Zhang et al., 2016). Fauziah et al., (2011) investigated the possibility of using RG in combination with sewage sludge and soil in different proportions in the agricultural environment as an amendment and a source of Ca for plants.

The present study fits into this context. RG wastes deriving from a TiO2 industrial plant (Tuscany, Italy) have been investigated to confirm their chemical and mineralogical homogeneity over more than 10 years of industrial production and to verify the possible occurrence of toxic elements above normative limits. Subsequently, the investigated RG wastes have been used as a secondary raw material to produce an innovative thermoformed ceramic material, following the procedures described in patent n. 0001369219, released by the Italian Patent and Trademark Office in 11/01/2010 (owner GRINN Solutions s.r.l.). The resulting ceramics realized using a high quantity of gypsum waste from 60 to 70% and characterized by excellent aesthetic, mechanical, and physical properties, may represent a competitive material in the ceramic trade, thus representing a promising example of the circular economy.

SAMPLES AND ANALYTICAL METHOD

Four representative samples of RG wastes (RG1-RG2-RG3-RG4), produced in an industrial plant located in Tuscany (Italy) for more than 10 years of production (Table 1S) were analyzed. Samples RG1 (the oldest: 2010) and RG4 (the youngest: July 2021) have been used to produce 2 ceramic tiles (hereafter, samples CRG1 and CRG4, respectively; Fig. 1S), following the procedures described in the patent and summarized below (paragraph 4 RG WASTE PROCESSING). CRG1 has a size of 4 cm length x 2 cm width x 0.7 cm height, while CRG4 one is round shape with 6 cm in diameter and 1 cm high. Both RG untreated samples and CRG resulting ceramic products have been analyzed with different mineralogical techniques.

X-ray powder diffraction (XRPD) analyses were carried out with a Bragg-Brentano Philips X'Pert PRO PW3050/60 diffractometer (CuKα radiation, operating conditions of 40 kV and 30 mA), equipped with PW3071 X'Celerator detector, 3-80° 2θ range, allowing the accurate determination of the bulk mineralogical composition of both RG samples and CRG samples. Before the analyses, small quantities (few mg) of RG and CRG samples were finely grounded in an agate mortar.

Energy dispersive X-ray fluorescence spectrometry (EDXRF) for chemical bulk analysis was performed on samples prepared by mixing approximately 15 g of powdered material with 5 g of boric acid and a few drops of polyvinyl alcohol. Powders were then pressed under a laboratory press (20t/cm2) compacted into pellets of 40 mm of diameter and finally analyzed with the PANalytical Epsilon 3XL instrument. The Omnian-standardless method was used for quantitative analyses. Volatile components (H_2O plus CO_2) were determined through the weight loss on ignition (LOI). The Fe^{3+}/Fe^{2+} ratio was determined through KMnO4 redox titration.

Thermal analyses (thermogravimetry, TG, differential thermogravimetry DTG, and differential thermal analysis, DTA) were obtained by a simultaneous DSC/TGA Thermal analyzer Q600 TA instruments, applying a heating rate of 10°C/min, from room temperature to 1000°C, in 20 ml/min airflow. Analyses were carried out on a few mg (17-37) starting untreated RG wastes to check their thermal behavior during heating.

Scanning Electron Microscope (SEM) analyses were carried out with a TESCAN VEGA 3 working at 20 kV of accelerating voltage, 15 µA of emission current. The microscope is equipped with an energy dispersive X-ray spectrometer (EDS) Bruker Quantax 200EDX for chemical microanalysis with P/B - ZAF correction method. Natural minerals were used as standards for EDS calibration. RG powders have been dispersed on adhesive carbon tape installed above SEM aluminum stubs, whereas CRG tiles were cut to realize polished petrographic sections, 33 mm length x 20 mm width x 30 µm thickness; both powders and polished sections were carbon-coated before SEM observations. SEM images of CRG samples were analyzed with the particle image analysis software (FIJI/ImageJ, (Schindelin et al., 2012)), focusing on 2D porosity determination. The applied methodology is shown as flows. Five representative back-scattered electrons (BSE) images were collected for each sample at low magnification (150x), and then smoothed, filtered and thresholded. Binarization aims to obtain a two colour image to elaborate successive segmentation, to determine areas occupied by the ceramic material and the areas occupied by 2D pores. Once binarized and segmented, images were processed with the particle analyses tool of Image/J. A minimum threshold of 1µm was chosen to analyze particles. The obtained porosity value is then the average ratio (%) between the area occupied by pores and the total area of each image.

The research methodology showing the main analyses made on RG and CRG samples, is summarized in the flowchart in Figure 4.1.

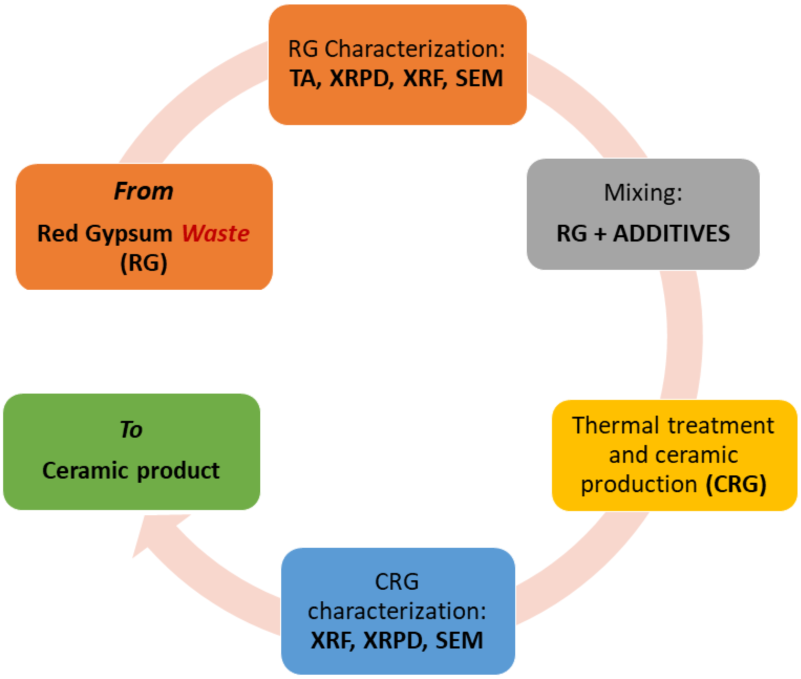

Figure 4.1 Flowchart diagram, are reported the samples and the main analyses performed

THE RED GYPSUM WASTE: CHEMICAL, MINERALOGICAL AND MICROSTRUCTURAL CHARACTERIZATION

RG samples are macroscopically comparable, with homogeneous color and grain size. Table 1 reports the XRF bulk composition of the four samples revealing that they are constantly formed by SO_3 (37 - 38 wt. %) and CaO (27 – 30 wt. %) with minor Fe_2O_3, TiO_2, SiO_2, Al_2O_3, and MgO. We also remark on the occurrence of trace elements Cr and V (here expressed as wt. % oxides Cr_2O_3 and

V_2O_5), reasonably resulting from the original raw mineral ilmenite and important for possible environmental concerns. The volatile content, ranging from ~19 to ~21 wt.%, was estimated through thermal analyses to better discriminate the loss between hygroscopic water (humidity) and structural water of Gypsum which led to mineralogical transformation first to Hemihydrate and then to Anhydrite.

Table 4. 1 EDXRF bulk data (wt.% oxides) for the four RG samples and two ceramic samples CRG1 and CRG4.

wt%	**RG1**	**RG2**	**RG3**	**RG4**	**CRG1**	**CRG4**
Na_2O	0.74	0.46	0.36	0.51	1.243	1.156
MgO	2.46	1.06	2.17	3.91	1.22	0.931
Al_2O_3	1.25	1.18	1.24	0.80	4.657	4.61
SiO_2	2.31	1.94	2.16	1.46	19.649	19.78
P_2O_5	0.03	0.03	0.03	0.03	*n.d.*	*n.d.*
SO_3	38.45	38.53	37.25	38.76	35.487	35.798
Cl	0.67	0.03	0.10	0.34	*n.d.*	*n.d.*
K_2O	0.12	0.09	0.06	0.05	0.405	0.328
CaO	29.30	30.23	29.11	27.48	28.353	25.484
TiO_2	1.29	1.14	1.43	1.38	1.217	1.134
V_2O_5	0.18	0.13	0.16	0.13	0.144	0.117
Cr_2O_3	0.06	0.05	0.05	0.04	0.132	0.053
MnO	0.08	0.11	0.11	0.15	0.08	0.109
Fe_2O_3	3.97	3.52	4.57	3.90	3.971	3.58
CuO	*n.d.*	*n.d.*	*n.d.*	*n.d.*	*tr*	*tr*
ZnO	*n.d.*	*n.d.*	*n.d.*	*n.d.*	0.061	0.063
SrO	0.02	0.02	0.03	0.02	*tr*	*tr*
ZrO_2	*n.d.*	*n.d.*	*n.d.*	*n.d.*	0.183	0.191
SnO_2	0.02	0.02	0.02	0.02	0.46	0.414
BaO	0.00	0.01	0.01	0.01	0.487	0.494
NiO	0.01	n.d.	n.d.	n.d.	*n.d.*	*tr*
PbO	*n.d.*	*n.d.*	*n.d.*	*n.d.*	0.174	0.127
LOI	19.05	21.46	21.15	21.01	1.87	5.42
Total	100.00	100.00	100.00	100.00	99.793	99.789

Note: LOI= loss on ignition, n.d.= not detected, tr=trace

Thermal analyses allowed us to investigate the transformation of Gypsum into Anhydride, with a theoretical overall weight loss of approximately 20-21 wt%. Gypsum dehydration occurs in two separate steps: i) in the first step, Gypsum transforms to Hemihydrate, close to 128°C, with a weight loss of 13-14 wt%; ii) in the second step, Hemihydrate transforms to Anhydrite, close to 158/160°C, with a weight loss of 6-7 wt% (Hudson-Lamb et al., 1996; Freyer & Voigt, 2003; Charola et al., 2007; Smykatz-Kloss, 2012).

TG, DTG and DTA results for our gypsum samples are reported in Figure 4.2 (green, red and blue lines, respectively), whereas main TG losses and temperatures of main DTG and DTA signals are summarized in Table 2. TG data and LOI indicate a highly variable weight loss from room temperature to 100°C (from 1.60 wt% up to 17.11 wt%), associated with endothermic signals in the range 55-84°C. The observed differences in weight loss below 100°C are probably due to samples conservation conditions and, consequently, to variable contents in atmospheric adsorbed water. Primary weight loss occurs in the range of 100-180°C (from 15.00 wt% to 17.60 wt. %), due to the progressive dehydration from Gypsum to Hemihydrate and lastly into Anhydrite. The width and asymmetric shape of DTG and DTA peaks in the 100-180°C range (especially evident for samples RG1-RG2 and RG3; figures 2S in appendix 2) reflect the two-step dehydration of Gypsum (e.g., the wide and asymmetric endothermic signal in the 141-158°C range). At higher temperatures (range 180-600°C), weight loss is very low (2.00-3.30 wt.%), whereas we remark the occurrence of a weak exothermic peak (360-403°C) that has been interpreted as due to the transformation of soluble Anhydrite (γ) to insoluble Anhydrite (β) (West & Sutton, 1954; Ramachandran & Paroli, 2002; Ballirano & Melis, 2007; Javangula & Lineberry, 2014). Weight loss in the 600-1000°C range is negligible (0.84-2.00), whereas is visible a weak endothermic signal at 673-683 °C, possibly caused by dehydration of minor Fe-bearing phases (Smykatz-Kloss, 2012).

Total weight losses for the four Gypsum wastes in the range 100-1000°C range from 19.05 to 21.46, in agreement with the expected loss for pure gypsum samples.

Table 4. 2 Main TG, DTG, and DTA data for the samples RG1, RG2, RG3, RG4. The abbreviations w (weak), s (strong) and vs (very strong, main peak) are arbitrary and are based on a qualitative observation of the peak's height.

TG data							
RG1		**RG2**		**RG3**		**RG4**	
T range (°C)	TG loss %	T range (°C)	TG loss %	T range (°C)	TG loss %	T range (°C)	TG loss %
RT-100	17.11	RT-100	1.60	RT-100	2.06	RT-100	11.86
100-180	15.00	100-180	17.60	100-180	17.15	100-180	15.87
180-600	2.71	180-600	2.16	180-600	2.00	180-600	3.30
600-1000	1.34	600-1000	1.70	600-1000	2.00	600-1000	0.84
total weight loss 100 - 1000	19.05	total weight loss 100 - 1000	21.46	total weight loss 100 - 1000	21.15	total weight loss 100 - 1000	20.01

DTG peak temperature in DTG curves (°C)			
RG1	**RG2**	**RG3**	**RG4**
75 s	52 w	52 w	62 s

140 vs	138 vs	134 vs	142 vs
155 sh	151 sh	147 sh	
672 w	675 w	672 w	
DTA peak temperature in DTA curves (°C)			
RG1	**RG2**	**RG3**	**RG4**
84 s endo	58 w endo	55 w endo	70 s endo
148 vs endo	145 vs endo	141 vs endo	
158 sh endo	152 sh endo	149 sh endo	153 vs endo
399 w exo	376 w exo	360 w exo	403 w exo
683 w endo	675 w endo	673 endo	

Note: RT= room temperature, w=weak, s= strong, vs=very strong (main peak), sh=shoulder endo=endothermic, exo=exothermic

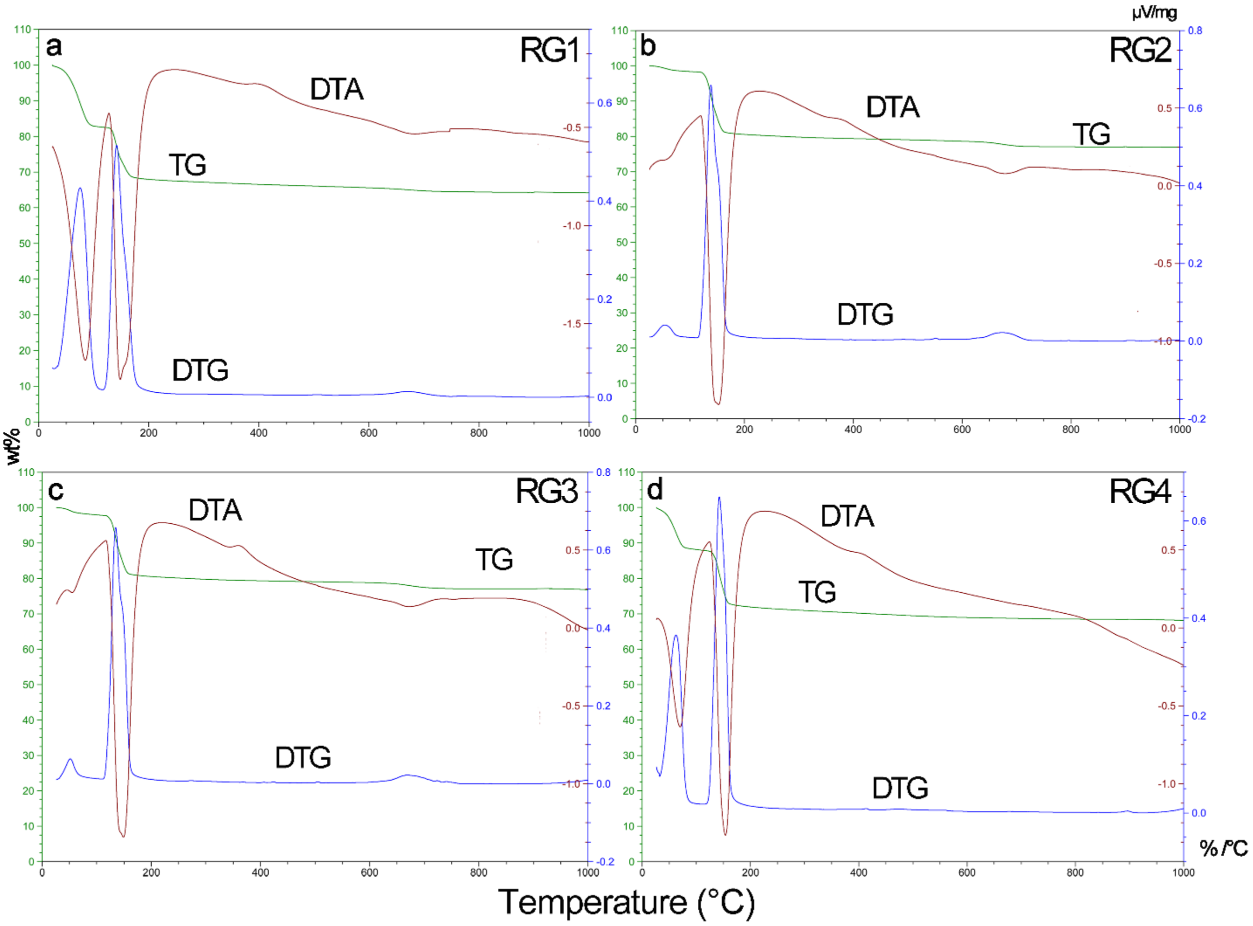

Figure 4.2 Thermal analysis of the four RG samples, in air, heating rate of 10°C/min, in the range 0 -1000 °C; DTA exothermal signals are upwards. Green curve: thermogravimetric analysis (TG); blue curve: differential thermogravimetry (DTG); red curve: differential thermal analysis (DTA).

XRPD patterns confirm that RG wastes are almost exclusively formed by gypsum, with rare occurrence of quartz (Figure 4.3). Figure 4.3 reports gypsum main reflections, with *hkl* lattice planes (brackets) and corresponding interplanar distance (d). Red arrows indicate some minor peaks belonging to Gypsum, particularly evident in samples RG1, RG2, and RG3, with interplanar distances of 2.87Å, 2.79Å, and 2.68Å, corresponding respectively to 200, 112, 220 *hkl* lattice planes. The grey arrows identify the main peak of Quartz corresponding to the 3.35 Å-spaced (101) lattice planes (Bayless, 1986; Follner et al., 2002). XRD data, therefore, confirm that wastes deriving from more than 10 years of TiO_2 production are almost exclusively formed by Gypsum.

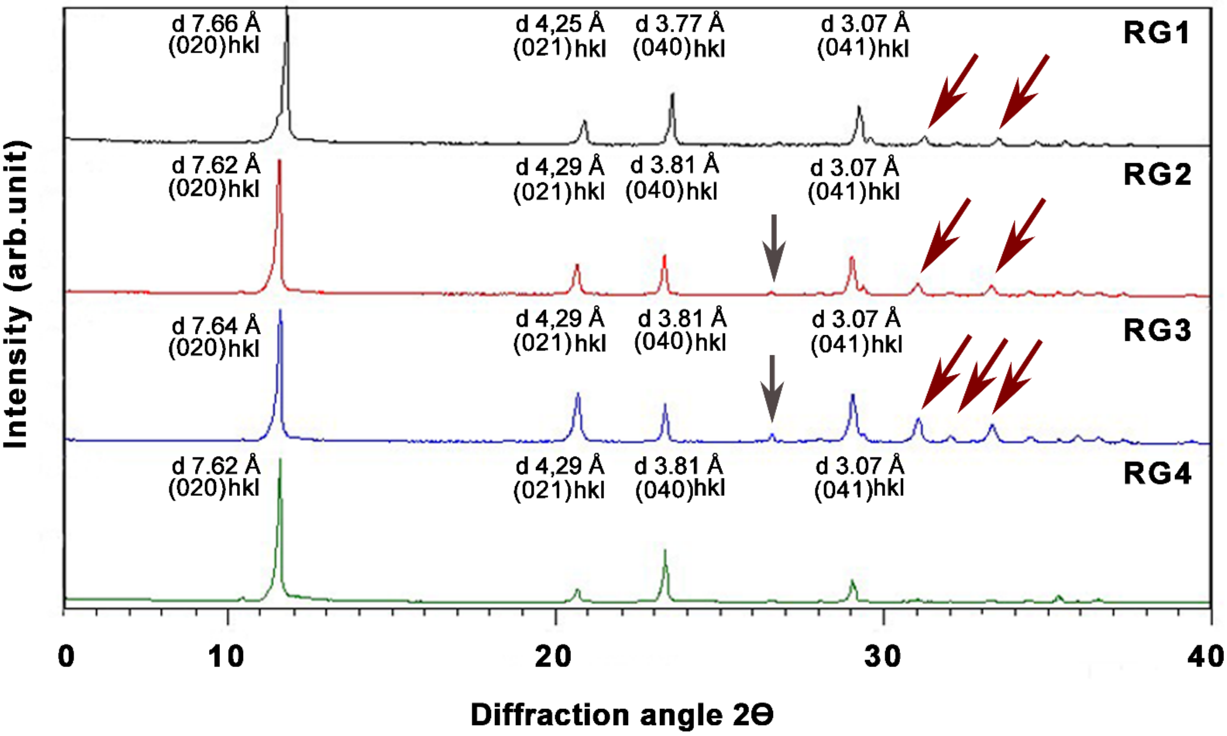

Figure 4.3 XRPD patterns of untreated RG wastes, with main (hkl) reflections and corresponding d-spacings (Å); red arrows indicate some minor peaks always belonging to gypsum, whereas grey arrow identifies the main peak of quartz corresponding to 3.35 Å-spaced (101) lattice planes.

SEM observations reveal minor microstructural differences between the RG samples, as observed in Figure 4.4, where the four samples are compared at the same magnification (300X Figure 4.4 A: RG1; B: B RG2; C: RG3; D: RG4). Figures 4.4 A and C show euhedral crystals (highlighted with the line drawing) with the typical Gypsum twinning (“fishtail” or “swallowtail” twinned crystals), whereas Figures 4.4 B and D highlight not-twinned euhedral crystals with a tabular prismatic habit (line drawing). The crystal size of the four Gypsum samples is comparable, ranging from ~ 20 µm to ~ 200 µm.

The images E and F in Figure 4.4 are representative of two common minor phases, that were not detected by XRPD due to their extremely low amount, in particular, Ti- and Fe-oxides. The Ti- and Fe-oxide grains, bright in BSE images, have grain sizes below 20-30 µm and exhibit subhedral habits, suggesting that they arise from the primary raw material rather than from the acid waste de-activation process leading to Gypsum formation. Careful SEM/EDS analyses also allowed for the detection of rare Fe and Ti oxide grains slightly enriched in Cr and V, coherently with XRF results. The above heavy elements do not occur in the gypsum crystal structure, as confirmed by EDS analyses.

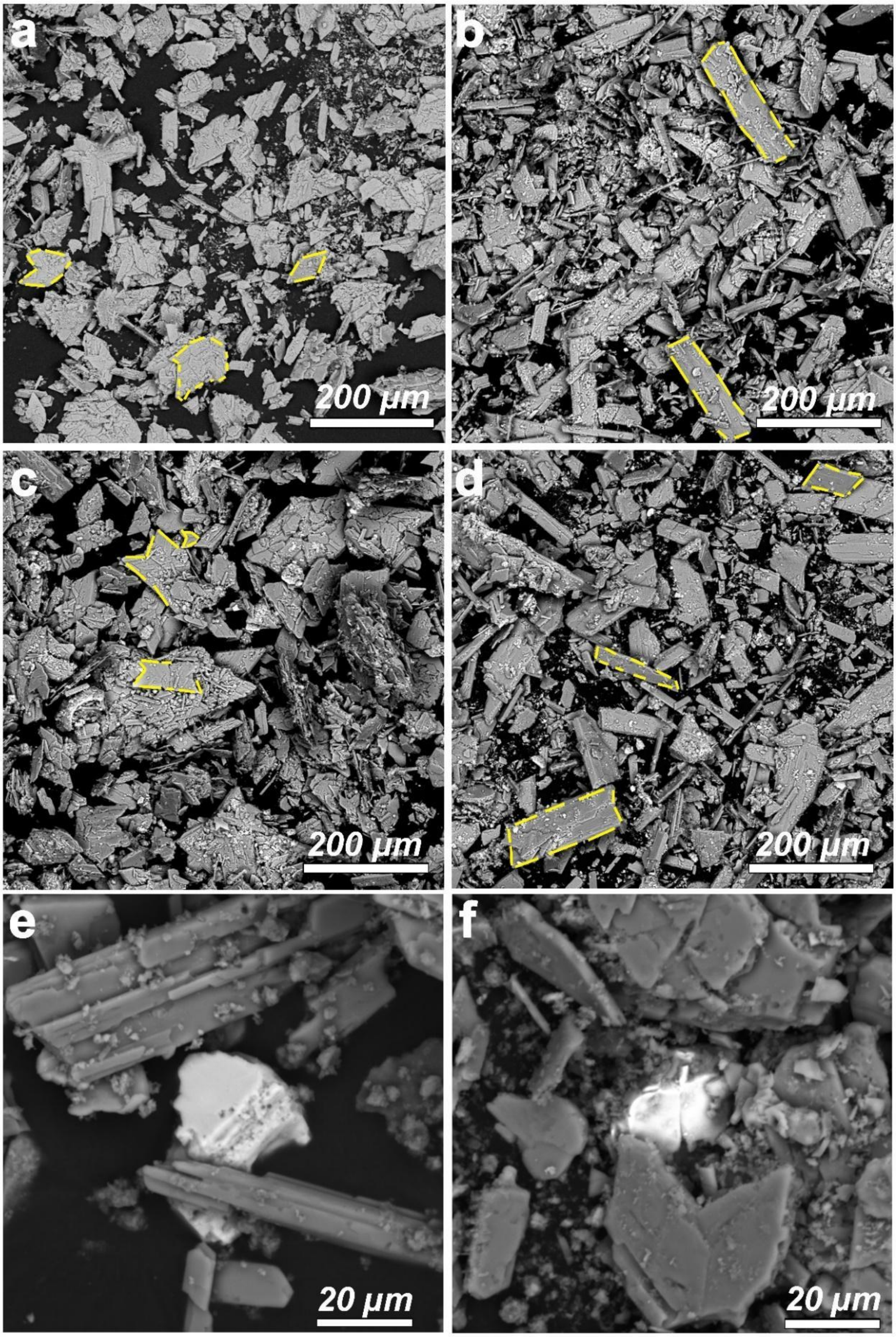

Figure 4.4 BSE SEM images of the RG samples. a) Gypsum in RG1 sample, with common twinned crystals; b) Gypsum in RG2 sample with predominant not-twinned euhedral tabular crystals; c) Gypsum in RG3 sample, with common twinning; d) Gypsum in RG4

samples, with predominant tabular habit and rare twinned crystals; e and f) Representative images of Fe and Ti – oxides respectively occurring in gypsum samples

RG WASTE PROCESSING

Ceramic tests CRG1 and CRG4 have been realized using approximately 70% of unaltered red Gypsum (no grinding process was done), mixed with variable additives, predominantly i) amorphous silica; ii) Na- silicates, in variable proportions. The samples were pressed and formed under wet conditions (about 20-30 % of humidity), and then treated in a furnace at slightly different conditions, i.e., at 920 °C and 1000°C, for 60 and 30 minutes, respectively. Both samples' heating rate was set up at 100 °C/h. Further technical details cannot be disclosed due to the patent trade secret.

THE CERAMIC PRODUCTS: CHEMICAL, MINERALOGICAL AND MICROSTRUCTURAL PROPERTIES

The two analyzed ceramic products are quite different at a macroscopic observation (Figures 2S a and b for CRG1 and CRG4, respectively appendix II), particularly for the different color (variable with the used additives). In Figure 3S (Appendix II) it is possible to observe other ceramic products, analogous to those studied, realized with the above patent and with red Gypsum. The two samples have been in part powdered (for XRF and XRD analyses) and cut to realize thin polished petrographic sections (for optical microscopy and SEM/EDS observations).

Table 4.1 reports, in the last two columns, XRF bulk data for CRG samples. The ceramic products are mainly composed of SO_3 (~ 35-36 wt.%), CaO (~ 25-28 wt.%), and SiO_2 (~ 20 wt. %) with minor Al_2O_3, Fe_2O_3 Na_2O, TiO_2 and MgO.

Minor differences between the two ceramic products are reasonably due to slight variation in the starting ceramic batch, particularly for what concerns the CaO content and LOI values. It is remarkable that undesired heavy elements, such as Cr and V, occur in limited amounts.

Figure 4.5 reports XRPD patterns of the two samples, showing a good reproducibility of the ceramic production process (black and red lines for CRG1 and CRG4, respectively). The main crystalline phase is Anhydrite (blu line), deriving from gypsum dehydration, with minor Augite-like pyroxene (green line), which represents the new high-T crystalline phase formed from the silicatic flux. Arrows correspond to the main peaks of Hematite (Fe_2O_3), probably resulting from the raw starting material, and Cassiterite (SnO_2), which conversely has been added to the ceramic batch, probably to improve the aesthetic properties of the ceramic product.

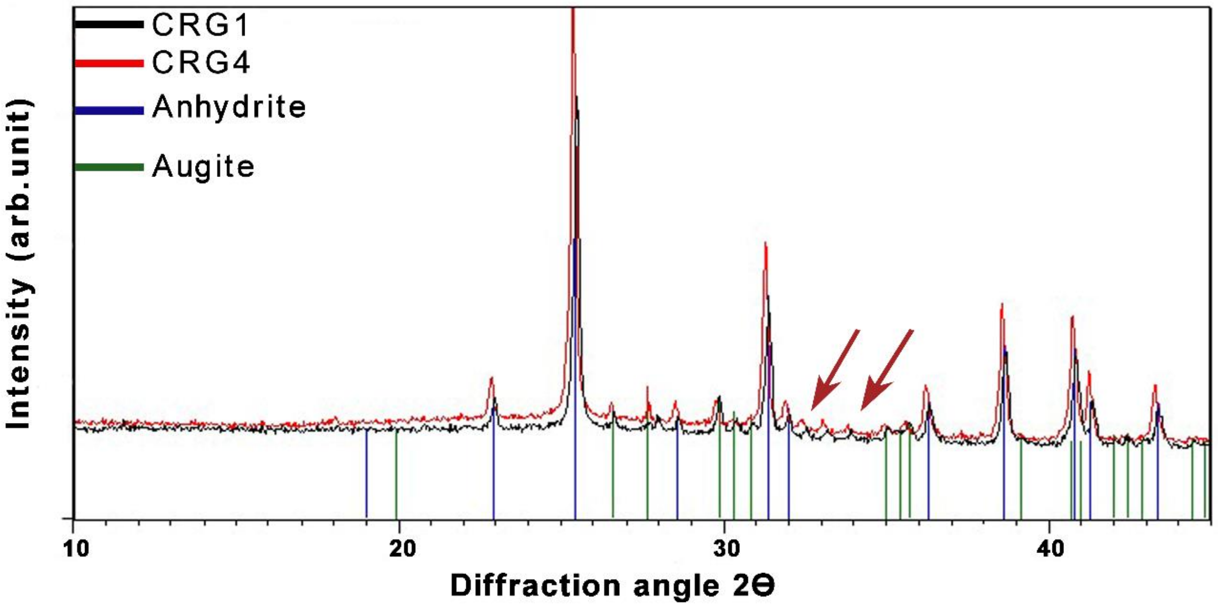

Figure 4.5 XRPD patterns of the CRG1 (red line) and CRG4 (black line); blue lines correspond to anhydrite peaks, whereas the green ones correspond to the silicatic phase, pyroxene. Minor hematite and cassiterite are pointed out by the arrows.

SEM/BSE observations on the two polished petrographic sections reveal broadly similar microstructures, even if significant differences can be observed for what concerns Pyroxene crystal size, pore size and distribution (e.g., Figures 4.6).

The average apparent porosity of the two investigated samples obtained from image analysis is quite different, reflecting the ceramic oven's slightly different temperature and time conditions. CRG1 has an average porosity value of 22%, while CRG4 is less porous (12%), evident in figures 4.6 A and D and in Figure 4S A and B where are reported the two pore size distribution histograms. Pore size ranges from 8 µm to 450 µm for CRG1 and from 8 µm to 330 for CRG4. In both samples, pore shape is variable, from rounded to irregular (e.g., arrows in figs. 6A and D), whereas the aspect ratio (i.e., the ellipticity of pores) shows greater variability in sample CRG4. Full image analysis data are available in table 2S and figure 3S in the supplementary materials.

The ceramic products comprise a glassy and compact matrix, hosting the different crystalline phases (Figures 4.6 B-C and 4.6 E-F for CRG1 and CRG4, respectively). The observed crystalline phases are (from the more to the less abundant): 1) Anhydrite (pale gray) which is the most abundant crystalline phase in both samples (e.g., anh in Figures 4.6C and F). Anhydrite is characterized by an evident parallel fissure system (“shrunk structure”), consequent to the significant volume reduction during the Gypsum-to-Anhydrite phase transition; 2) Augitic pyroxenes (pale grey), in elongated and skeletal crystals, up to 10 x 2 µm and 50 x 10 µm in CRG1 and CRG4, respectively (px and yellow line drawing in Figures 4.6C and F); 3) Cassiterite SnO_2, characterized by the highest BSE coefficient, in rounded sub-euhedral crystals, 5-10 µm in size (e.g., cst in Figures 4.6 C and F); 4) Ti-rich iron oxides, typically occurring in tiny (up to 5 x1 µm) acicular crystals (e.g., Ox Fe and Ti in Figure 4.6F) 5) Fe oxides, in euhedral crystals with high BSE coefficient, 5-10 µm in size (Ox-Fe in Figures 4.6C and F).

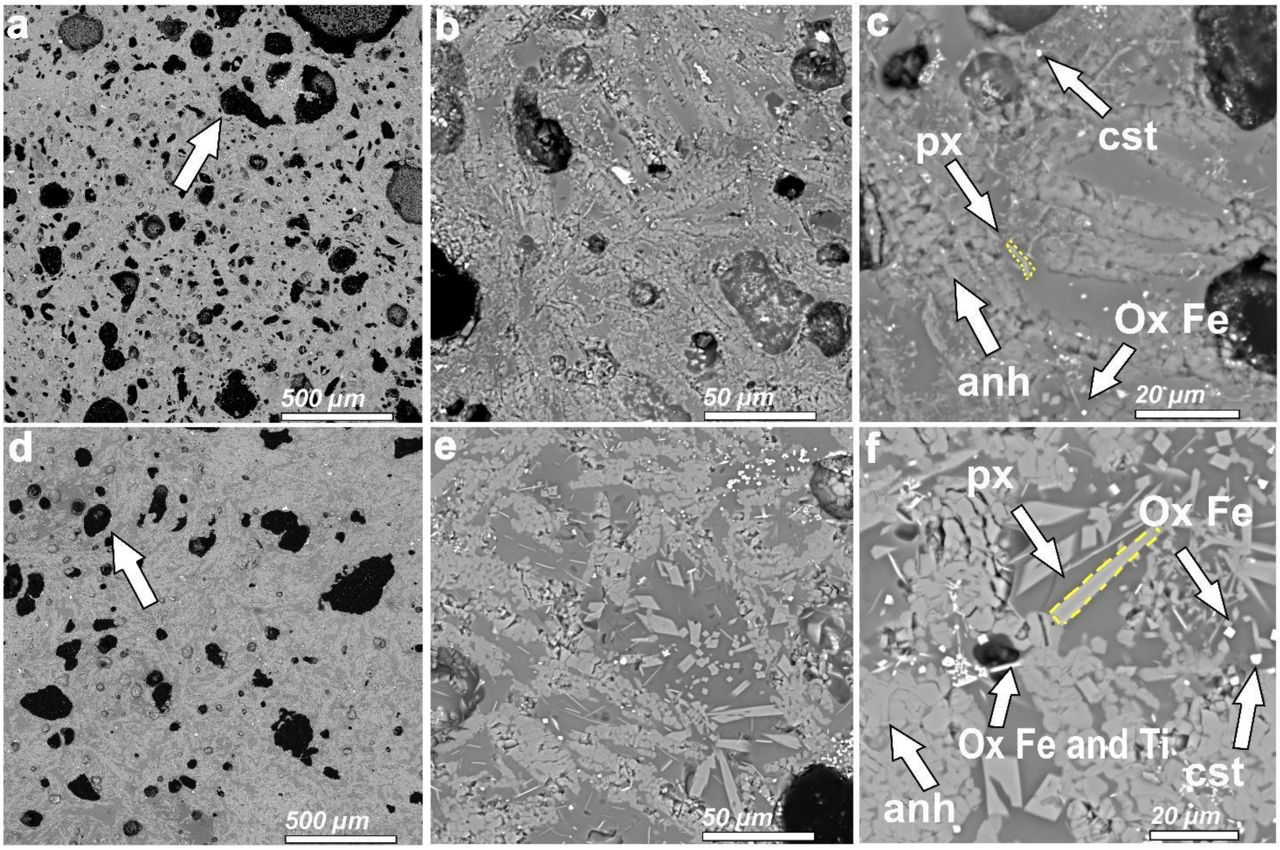

Figure 4.6 SEM BSE images of the two CRG samples (upper row: sample CRG1; lower row: sample CRG4; images in column have been collected at the same magnification). Images a and d have highlighted the relevant differences in pore size and pore distribution in the two ceramic products. Images b and e allow remarking the significantly different crystal size (especially for pyroxene), which is larger in CRG4. Images c and f show the main crystalline phases detected by SEM/EDS.

The grain size of anhydrite crystals is equivalent in the two samples and are substantially inherited by the size of starting gypsum crystals. Conversely, the size of augitic crystals and pore distribution, clearly indicate a more evolved annealing in CRG4 with respect to CRG1. This is probably due to slightly different processing and heating conditions, in particular, the maximum temperature reached, 1000 °C, and the stationing heating time, 30 minutes, for CRG4 (Dondi et al., 1998; Khater et al., 2019 Gliozzo, 2020). As regards minor phases, such as cassiterite, Fe and Ti-rich Fe oxides, microstructural features do not allow to understand if crystals are the same as the original starting batch or if they have experienced high-T re-crystallization in the ceramic kiln.

Table 4.3 reports EDS representative chemical analyses for glass matrix, Anhydrite, Pyroxene, Fe oxides and Cassiterite (see also Table 3S, in appendix 2, reporting the maximum, minimum and mean value for each phase of ceramic materials, expressed in wt% oxides). Some point analyses are reported in figures 5S and 6S of appendix 2.

Table 4. 3 EDS average compositions of glass, anhydrite, pyroxene, Fe and Ti-rich Fe oxides, and cassiterite for samples CRG1 and CRG4.

	Glass		**Anhydrite**		**Pyroxene**		**Ox Fe and Ti**		**Cassiterite**	
Wt%	**CRG1**	**CRG4**	**CRG1**	**CRG4**	**CRG1**	**CRG4**	**CRG1**	**CRG4**	**CRG1**	**CRG4**
SiO_2	57.90	57.41	1.73	1.85	52.17	47.77	7.99	12.17	9.38	4.90
Al_2O_3	11.88	13.42	0.44	0.36	8.39	7.53	2.66	3.38	2.69	1.14
MgO	4.63	2.98	0.12	0.07	9.57	8.96	1.91	4.20	0.63	0.20
FeO (tot)	4.60	4.24	0.24	0.14	6.58	10.00	70.67	55.79	0.79	0.29
Na_2O	5.66	6.16	0.43	0.12	3.89	2.94	1.89	1.61	2.11	0.72
K_2O	1.19	1.04	0.04	0.02	0.48	0.36	0.16	0.14	0.35	0.27
CaO	8.88	9.29	34.16	35.57	16.70	17.33	2.42	3.54	2.48	0.76
TiO_2	1.96	2.10	0.18	0.10	2.01	4.76	8.46	15.21	0.34	0.08
Cr_2O_3	0.01	0.01	0.00	0.01	0.04	0.03	0.29	0.23	0.01	0.01
MnO	0.09	0.25	0.08	0.04	0.17	0.33	0.42	0.58	0.00	0.02
SO_3	2.38	2.11	62.55	61.69	-	-	2.60	2.40	3.60	0.57
SnO_2	0.49	0.59	0.04	0.02	-	-	0.18	0.62	77.61	91.02
V_2O_3	0.36	0.39	0.00	0.00	-	-	0.33	0.12	0.01	0.01

The glassy matrix has a similar composition in both samples and is mostly composed of SiO_2, Al_2O_3, Na_2O and CaO, together with minor FeO and MgO, deriving from the additives used in the starting ceramic batch. The measured TiO_2, SnO_2 and SO_3 contents could be due to the large volume analysis, possibly resulting from contamination (i.e., the occurrence of tiny grains of Ti-rich oxide, Cassiterite and Gypsum in the analyzed matrix volume). Conversely, EDS data suggest that V_2O_5 is preferentially partitioned in the matrix glass, showing the highest detected values.

Ca-pyroxenes reveal composition intermediate between Augite and Diopside, with representative atoms per formula units (a.p.f.u.) of Si 1.98, $^{[IV]}$Al 0.02, $^{[VI]}$Al 0.09, Ti 0.02, Fe^{2+} 0.09, Mg 1.01, Ca 0.68, Na 0.10, K 0.01. However, also Ca-pyroxenes enriched in Na have been detected by EDS spectrometer, with a representative composition of (a.p.f.u.) of Si 1.90, $^{[VI]}$Al 0.10, $^{[VI]}$ Al0.30, Ti 0.06, Fe^{2+} 0.22, Mn 0.01, Mg 0.46, Ca 0.65, Na 0.28, K 0.03. The latter belongs to Ca-Na pyroxenes according to the classification of Morimoto, (1988).

EDS data for micrometric crystals, such as those of Fe oxides, Ti-rich Fe oxides and Cassiterite, are typically affected by contamination drawbacks. It is however remarkable that they may host up 0.23 and 0.29 wt.% in Cr_2O_3, not detected in the surrounding glassy matrix.

DISCUSSION

THE ENVIRONMENTAL CONCERN OF RG WASTES

The environmental concern of RG wastes is directly related to the growing worldwide demand for TiO_2. The uses of TiO_2 range from the most traditional ones, i.e., paintings and pigments, to many different applications, such as special and bio-ceramics, cosmetics, gas sensing and medical devices, particularly when TiO2 is synthesized in nanosized crystals e.g., (Weir et al., 2012; Shakeel et al., 2016; Haider et al., 2019; Jafari et al., 2020; Tian et al., 2021). The primary waste of TiO_2 industrial production are acid solutions produced during raw material ($FeTiO_3$) processing and subsequent Ti extraction (Liang et al., 2005; Wang et al., 2020). Acid solutions pose a more significant environmental concern with respect to RG waste, due to soil acidification and groundwater pollution. Therefore, RG, i.e., secondary waste deriving from acid solution neutralization, should be considered the “best solution” to reduce the overall environmental impact of TiO_2 industrial production. At the same time, RG production “neutralizes” another kind of waste that also has a huge environmental and landscape impact, i.e., the $CaCO_3$ powders deriving from extraction and processing of carbonatic lithologies (as in the case of the nearby Calcare Massiccio and Carrara Marble quarries).

The main problem in RG waste management is represented by their volumes. In Italy about 500.000 tons/year are produced, similarly to the Terengganu Malaysia plant production (400.000 tons/year) (Fauziah et al., 1996; Amirul Hakim Sidek et al., 2019). The Huelva’s Spanish plant has a RG production of ~ 70.000 tons/year (Gázquez et al., 2009; Gazquez et al., 2013), whereas the Taicang plant in China has the highest impact with 15.000.000 tons/year (J. Zhang et al., 2018; Chen et al., 2021). One of the commonly adopted solutions for RG waste management is the environmental restoration of dismissed quarries and landfills (Kim et al., 2016; Muralikrishna & Manickam, 2017). As regards the studied case from 2004, Tuscan RG wastes have been disposed in a dismissed quarry (Poggio Speranzona, nearby the TiO_2 industrial plant) after an agreement among the industrial counterpart, the Tuscany Region Council, and the municipalities where the quarry is located (ARPAT, 2010). RG disposal was monitored by periodic geochemical analyses of soil, groundwater, and aquifer, done by ARPAT (Regional Agency for Environmental Protection of Tuscany; reports available at http://www.arpat.toscana.it/), as well as by the scientific community (e.g., (Protano et al., 2020)). The comparison of chemical results obtained before RG disposal, during their disposal and at the end of site restoration, demonstrated that soil, groundwater, and aquifer chemistry was constant, without significant trends of increasing or decreasing of the major ions and trace elements concentration. This indicates that RG was substantially inert, and they did not release undesired elements in the environment above normative limits (Martins & Castro, 2020; Protano et al., 2020).

Nevertheless, the social community did not appreciate this kind of solution for future disposal, raising doubts about Cr and V concentrations in water eluates and possible water sulphation. Currently, no other environmental restoration project has been approved. This implies that an alternative solution for RG waste disposal must be rapidly found. The study fits this aim, proposing a viable reuse of RG as a secondary raw material, in agreement with the European directive (Directive 2008/98/EC of the European Parliament and of the Council, 2008), waste valorization (Leder, 2020) and circular economy principle. The reuse of RG waste in the ceramic industry has another important environmental implication, since it provides a low-cost secondary raw material (SRM) that substitutes a raw natural resource (i.e., clay minerals), contributing to the reduction of non-renewable resources exploitation.

THE CHARACTERISTICS OF SRM AND CORRESPONDING CERAMIC PRODUCTS

The production of ceramics, both traditional and advanced, is one of the most investigated solutions for inorganic waste recycling (Hossain & Roy, 2020; Zanelli et al., 2021 for a review), often offering high-quality products (Sung, 2015). RG waste has a constant chemical composition, comparable over the years, thus providing a chemically and mineralogically reproducible secondary raw material, that is a fundamental requirement for possible industrial production. By comparing with previous RG chemical data from other industrial productions (e.g., Gázquez et al., 2009, 2021; Mohd Tadza et al., 2019; Chen et al., 2021), the investigated samples reveal higher SO_3 and CaO and lower Fe_2O_3 and TiO_2 contents, suggesting that RG waste produced in Tuscany plant are purer than that of the Chinese, Malaysian, and Spanish plants. XRD bulk analysis demonstrated that the only crystalline phase in our RG waste is gypsum and sporadic quartz.

Ceramic specimens experimentally produced in this study display comparable chemical and mineralogical compositions but show slightly different microstructures. Indeed, CRG4 sample consists of coarser and more euhedral crystals than CRG1 sample, consistently to the higher processing temperature. As expected, the different temperature also affects porosity size and distribution. CRG1 has a total porosity of 22% compared to the 11% of samples CRG4; the equivalent diameter is higher in CRG4 than in CRG1; the pore size distribution for CRG1 shows a higher frequency in the 10-40 µm size range designing a finer porosity, whereas the pore size distribution of CRG4 shows a dominant frequency in the range 10-20 µm, but with a greater proportion of larger pores (up to 90-100 µm), thus showing a less sorted porosity (table 2S and figure 4S). The data shown here support the feasibility of a reproducible industrial production deriving from the fixedness of the starting SRM. The main crystalline phases in ceramic products are anhydride, Ca-pyroxene with minor Fe-oxides and cassiterite (added in the ceramic mixture), finely intermixed to an amorphous silicatic matrix. Anhydride derives from gypsum de-hydration below 200 °C (Table 4.2 and Figure 4.2). It is worth noting that, based on DTA results, anhydrite transforms from a soluble to an insoluble phase, as testified by the occurrence of an exothermic signal in the range of 350-410 °C. The occurrence of insoluble anhydrite is a fundamental prerequisite for obtaining relatively low sulfate ion release in leaching tests (in progress). The anhydrous composition of starting gypsum and anhydrite is the same, except for Mg which is more abundant in RG than in the resulting anhydrite (Tables 4.1 and 4.3). The analyzed pyroxenes correspond to solid solutions between Ca- and Ca-Na pyroxenes, with variable Mg/Fe ratios, closer to augite and diopside in CRG1 and CRG4, respectively (Morimoto, 1988). Most of the analyzed pyroxenes revealed variable Na and Al contents (Table 3), thus corresponding to the augite/aegirine-augite field. The crystallization of augite/aegirine pyroxenes clearly reflects the use of Na-silicatic fluxes in the ceramic mixture. EDS analyses do not allow the distinction between Fe^{2+} and Fe^{3+}, but it is possible to assume that the majority of Fe is in the form of 3+ oxidation state considering the sample storage conservation at open air and the oxidizing atmosphere during the heating process. These features further support that Pyroxenes in the ceramic products have Augite/Aegirine composition. Further, the observed chemical variability of pyroxenes is reasonably caused by locally variable equilibria during the heating process, as already observed for other Ca-rich silicatic ceramics (Dondi et al., 1998). The amorphous matrix has a prevalent aluminosilicate composition with relatively low alkali content compared to standard glasses.

The main concern in the ceramic tests is represented by the occurrence of heavy elements, such as V and Cr, even if in low amounts, as revealed by XRF and EDS results. It is worth noting that based on SEM/EDS data, Cr is associated to Fe oxides, probably in the form of Cr^{3+} substituting Fe^{3+} in the oxide crystal structure (Burke et al., 2012), whereas V is preferentially partitioned in the glass matrix, probably in the 5+ oxidation state due to the ceramic kiln oxidizing atmosphere. This distribution may suggest an easier release of V from the amorphous matrix compared to Cr, which is fixed within the crystal structure of the Fe oxide. However, the limited number of analyses carried out and the impossibility to determine with certainty the oxidation state of Cr and V only allow for speculative hypotheses. The mobility and solubility of these two elements depend on several physical and chemical factors, among which pH of the leaching agent, mineralogical composition of raw materials and firing temperatures at which ceramics are fired. Cr and V are often related to thermally unstable minerals that may breakdown during the ceramic firing process, leading to the formation of newly formed compounds. So, firing temperature could influence the mobilization and consequently the solubilization of these two elements to a great extent (Dondi et al., 1997). As detailed below, leaching tests on these ceramic products are in progress to determine the nature and the amount of possible released elements.

FUTURE INVESTIGATIONS REQUIRED FOR THE LAB-TO-PLANT TRANSITION

This paper represents the scientific background for further analyses that will be necessary to move from the lab experimental scale to an actual industrial plant. First, the ceramic material must be tested to determine its chemical and mechanical behavior. Leaching tests are in progress to determine the concentrations of the different chemical elements in the eluate, on the basis of the Italian law that defines the allowed limits for each element (*Individuazione Dei Rifiuti Non Pericolosi Sottoposti Alle Procedure Semplificate Di Recupero Ai Sensi Degli Articoli 31 e 33 Del Decreto Legislativo n. 22. GU Serie Generale n.88 Del 16-04-1998 - Suppl. Ordinario n. 72*, 1998; *152. Norme in Materia Ambientale. GU Serie Generale n. 88 Del 14 Aprile 2006 - Supplemento Ordinario n. 96*, 2006). Moreover, we have performed preliminary test on resistance, tensile strength, and abrasion through Los Angeles and MicroDeval tests, according to EN-1097 and EN-1097-2 procedures to compare the mechanical properties of our products with those of traditional ceramics.

Another fundamental contribution to this work and future projects, include a careful economic analysis, such as cost/benefit analysis (CBA) to determine the economic advantages and disadvantages of the overall industrial process, pointing out possible criticisms and improving actions. Life cycle assessment (LCA) analysis will further support CBA, showing the details of the whole process, from the raw materials to the end products. LCA is a concrete and comprehensive tool to assess the environmental impacts of products from the cradle to the gate, the treatments, and the economies (the production of goodies) at a society level (Haupt & Zschokke, 2017; Tóth Szita, 2017; Z. Chen & Huang, 2019).

CONCLUSIONS

The management of huge volumes of RG waste represents an impelling problem with significant environmental, economic and social implications. The investigated RG industrial waste denotes constancy over the time. The data, covering approximately 10 years production, are also in complete agreement with previous data reported in bibliography as well as by periodic surveys done by the Regional Agency of Environmental protection of Tuscany (ARPAT). Other features of this research are represented by: 1) the large availability and the reproducibility of RG waste, that may be used as a low-cost secondary raw material; 2) the extraordinarily high % of RG waste used as SRM, replacing natural not renewable resources; 3) the relatively low T required to convert RG waste into a new ceramic product (never exceeding 1000°C). This supports the hypothesis of the economic and environmental sustainability of the process, which could be further refined through other future tests with slightly different mixtures of RG waste and additives in order to realize the most suitable eutectic mixtures at even lower temperatures.

CHAPTER V

FLOTATION MUDS

5.1 Chapter overview

This chapter deals with the last kind of special inorganic waste investigated in my PhD work, i.e., flotation muds, obtained from precious metals recovery process. The muds (mostly silicatic amorphous ultrafine powders) were used as SRM to realize new ceramic products. Both flotation muds and ceramic samples were provided by the GRINN Start Up (https://grinn.it/).

As in previous chapters, mineralogical data, overall results, and main conclusions are presented in the form of a scientific manuscript, that is currently in preparation and will be soon submitted.

I specifically performed all mineralogical investigations, such as XRPD, SEM/BSE and EDS analyses on both waste and new product and contributed to general discussion. Other kinds of investigations, such as the determination of mechanical properties and 3D X-ray tomographic imaging, have been obtained thanks to the collaboration with the Centro di Geotecnologie of University of Siena (Prof. Salvini) and the Electrochemical Innovation Lab of University College of London (Dr. Iacoviello), respectively.

5.2 Flotation sludges from precious metals recovery processes: from waste to secondary raw material in ceramics

INTRODUCTION

Recovering and recycling valuable materials from industrial wastes is one of the main targets of present society. Most natural resources are non-renewable (at least at the human time scale), and their availability is running out. Other problems arise from the global impacts of resource exploitation and extraction in terms of economic costs, political and social impacts, and environmental and landscape protection. In this context, the circular economy (reuse and recycling of used materials and waste) becomes an irrevocable solution. The reuse of industrial wastes, consisting of either hazardous or non-hazardous phases, has the further advantage of limiting landfill disposal (Ponomarenko et al., 2021).

Only in 2019, the Italian metallurgic industry (code 24 and 25 according to the Italian economic classification, ATECO), produced more than 10 million ton of special wastes, accounting for the 37.5 % of the overall national production of special wastes, placing the sector at the third place after the construction/demolition and treatment/remediation wastes (ISPRA 2021).

Recovery of precious metals (hereafter PM) from metallurgic wastes is of primary interest not only in jewellery industry, but also in electronics and catalysts industrial sectors (Ding et al., 2019). Because of their excellent corrosion resistance, good electrical conductivity and high catalytic activity, PM are widely applied in many fields. For instance, gold and silver make up parts of switches, bonding wires, and contacts in electronic industry, while palladium is mainly used in hard disks production (Diaz et al., 2016; Ding et al., 2019). Other widespread applications of these elements are as activation components in various types of catalysts, from automotive to chemical engineering to oil-refining processes (Ding et al. 2019). The need for recovery is primarily due to the extremely low natural amount of PM and REE (Rare Earth Elements a set of 17 elements, the lanthanides, scandium and yttrium which are essential for high-tech devices, electronics, lasers, industrials processes), in Earth’s crust (globally below 0.01 ppm), that can be exploited only in the few sites/countries, where they are geochemically concentrated (S. Zhang et al., 2017). The increasing demand for these rare and limited natural resources makes the recovery from end-of-life products necessary, also in agreement with the 2030 sustainable development goals. PM recovery is cheaper than exploitation and has several environmental advantages, since emitted CO_2 and energy consumption are lower than those deriving from traditional mining exploitation (Ciabatti et al., 2019; Saidani et al., 2019).

Recovery of PM from existing end-of-life products (typically wastes from electronics, namely E-wastes, and spent catalysts) is typically carried out through pyrometallurgical (i.e., smelting in furnaces and successive refinements) and hydrometallurgical techniques (i.e., leaching with cyanide, aqua regia, thiourea, thiosulfate, halide reagents; (Ding et al., 2019; Trinh et al., 2020; Yousif, 2019). Waste treatment allows PM to be separated from the "inert" material and concentrated at a rate high enough to allow PM recovery. A considerable amount of both gold and silversmith wastes and E-wastes are also recovered through physical and physico-chemical procedures such as froth flotation (Wills 2013; Ciabatti 2018; Jeon et al. 2018; Burat et al., 2019). Froth flotation is a separation technique widely applied in mineral processing to concentrate minerals (e.g., copper sulfides, lead, zinc, platinum, tin minerals), which takes advantage of the different physico-chemical properties of PM after the addition of various flotation chemical reagents (Burat et al. 2019; Jeon et al. 2018). Flotation wastes are typically represented by PM-free, "inert" muds, that can be reused as well (e.g., as secondary raw materials for asphalt production; Ciabatti 2018). According to the Environmental Protection Agency (EPA) and the European Waste Catalogue (EWC), flotation muds of secondary production from PM recovery industry are classified as non-dangerous wastes, but they still have to face storage problems.

Different types of wastes have been extensively recycled in the production of glass-ceramic, since it is versatile enough to accommodate various kinds of waste, such as coal fly ash (Kumar et al. 2000, Erol et al. 2001), slag from the steel industry (Khater 2002), ash and slag from waste incinerators (Boccaccini et al. 1997, Andreola et al. 2001), mud from zinc hydrometallurgy (Montanaro et al. 2001), red mud from alumina production (Peixin and Jiaqiang 2000) and other types of waste (see Rawlings et al. 2006 and Sarrigani and Amiri 2019 for comprehensive reviews). Ceramic products have been manufactured by using treated silver mine tailings after flotation (Drif et al. 2021), iron ore tailings (Silva et al. 2014), coal mine wastes (Taha et al. 2017), phosphate rock wastes (Loutou et al. 2019), lithium tailings (Lemougna et al. 2019), red mud waste from alumina processing (Liu et al. 2017).

The work deals with flotation muds derived from PM recovery processes and investigates their use as a secondary raw material (SRM) in the production of a thermoformed ceramic product, following the procedures described in patent n. 0001369219 "*Procedimento per realizzare manufatti termoformati, specialmente utilizzando materiali riciclati o di recupero*", released by the Italian Patent and Trademark Office in 11/01/2010 (owner GRINN Solutions s.r.l.). The results of this investigation confirm that this kind of waste can be successfully re-used in the ceramic industry, resulting in products with high technological performances, competitive with respect to traditional ceramics.

MATERIALS AND METHODS

Two different flotation mud samples (FM1 and FM2) have been used as secondary raw materials to produce ceramic materials (CFM1 and CFM2, respectively). Details on the ceramic starting mixtures, as well as on the furnace conditions (e.g., sintering temperature, heating rate and atmosphere), are reported in the Italian patent 0001369219 by GRINN S.r.l..

Chemical, mineralogical and microstructural characteristics of both secondary raw materials (the two flotation mud wastes, FM) and new products (the ceramic tiles, CFM) have been determined using the following techniques:

Energy-dispersive X-ray fluorescence (EDXRF) spectrometry for bulk chemical analyses were obtained with the Panalytical Epsilon 3XL instrument. The Omnian-standardless method was used for quantitative analyses. Volatile components (H_2O plus CO_2) were determined through the weight loss on ignition (LOI). The Fe^{3+}/Fe^{2+} ratio was determined through KMnO4 redox titration.

X-ray powder diffraction (XRPD) analyses were carried out with a Bragg-Brentano Philips X'Pert PRO PW3050/60 diffractometer equipped with PW3071 X'Celerator detector and CuKa detector in the 0-60 2ϴ range, and operation condition of 40 kV and 30 mA, for the determination of the bulk mineralogical composition of both starting raw materials (FM) and the final ceramic products (CFM).

Scanning Electron Microscope (SEM) analyses were carried out with a TESCAN VEGA 3 working at 20 kV of accelerating voltage, 15 µA of emission current, 0.1 nA of beam current, equipped with an energy dispersive X-ray spectrometer (EDS) Bruker Quantax 200EDX for chemical microanalysis. Data reduction was done with the P/B - ZAF correction method and natural minerals were used as standards for EDS calibration. Estimation of Fe^{3+} was evaluated following the procedure described in Droop (1987). SEM analyses were carried out on untreated FM samples and polished thin sections of the CFM products. Samples were carbon-coated before SEM observations. Backscattered electron (BSE) images of CFM samples were analyzed by the ©Particles software to determine average apparent porosity, aspect ratio, roundness, and equivalent diameter of pores. For this analysis, five low magnification (150x) images, representative of each CFM sample, were collected and treated by smoothing, filtering and thresholding processes.

Due to its microstructural characteristics (see below), CFM2 has been selected for further specific analyses, in particular, mechanical tests, detailed porosity and 3D microstructure study, using the following facilities:

X-ray computed tomography (micro-CT) using two microscopes: a Nikon XTH 225 (Nikon Metrology, Tring UK) scanner and a micron-scale ZEISS Xradia 620 Versa (Carl Zeiss, Pleasanton, CA, US). The samples were mounted on a rotating stage that allows a 360° rotation with the sample in between the X-ray source and the detector. The Nikon scan was collected with a tube voltage of 80 kV and 93 µA. 3185 projections were acquired with 1 second per projection acquisition time. After reconstruction with the proprietary Nikon reconstruction software CT Pro 3D (Nikon, Tring, UK), resulting images for all datasets had a voxel size of 8.5 µm. Instead, 1601 projections (2 seconds exposure time) were acquired with the ZEISS Xradia 620 Versa microscope. For an optimal transmission a tube voltage of 120kV and 146 µA was set. The raw projections have been reconstructed with the proprietary ZEISS XMReconstructor software package, achieving a voxel size of 1 µm.

Mechanical tests were carried out on 6 specimen cubes (50x50x50 mm) and 6 joists (300 x 50 x 50 mm), derived from CFM2 sample tiles: i) uniaxial compressive strength test (UNI EN 1926), ii) determination of the flexural strength under concentrated load (UNI EN 12372). In addition, a sample of aggregate (about 2Kg weight) was reduced to the size suitable for the “Microdeval” test (UNI EN 1097-1) aimed to determine the wear resistance.

FLOTATION MUD WASTES: CHEMICAL COMPOSITION AND MICROSTRUCTURE

Table 5.1 shows the bulk chemical composition of both starting raw materials and ceramic products. The flotation muds essentially consist of Si, Al, and Ca oxides, with less amount of Fe (here expressed as Fe_2O_3 wt.%), Mg and Na. Other elements are present in minor amounts such as Ce, Zr, Zn, Cu, Ni, Cr, Sn below 1 wt% of their relative oxide, probably coming from the original material before the PM recovery.

Table 5. 1 XRF data of FM and CF samples

	FM1	**FM2**	**CFM1**	**CFM2**
Na_2O	5.06	1.99	4.38	3.33
MgO	5.13	2.88	3.59	4.00
Al_2O_3	18.39	25.95	15.49	21.12
SiO_2	39.16	30.31	38.60	35.43
P_2O_5	0.81	0.39	1.00	0.65
SO_3	0.76	0.42	0.97	0.63
Cl	0.48	0.79	0.15	0.01
K_2O	0.29	0.27	0.44	0.67
CaO	16.78	23.65	23.46	21.18
TiO_2	1.24	0.96	1.12	0.89
Cr_2O_3	0.54	0.41	0.45	0.39
MnO	0.12	0.16	0.11	0.11
Fe_2O_3	6.51	4.91	5.67	6.11
NiO	0.37	0.30	0.33	0.36
CuO	0.29	0.30	0.24	0.22
ZnO	0.44	0.19	0.39	0.25
SrO	0.08	0.12	0.09	0.10
ZrO_2	1.14	2.57	1.03	1.87
SnO_2	0.24	0.27	0.41	0.32
Sb_2O_3	0.02	*n.d*	0.02	*n.d*
BaO	0.59	0.55	0.66	0.43
CeO_2	0.84	1.25	0.73	1.20
PbO	0.15	0.10	0.18	0.07
WO_3	*n.d*	0.29	n.d	0.27
SeO_2	*n.d*	0.07	*n.d*	*n.d*
Y_2O_3	*n.d*	0.05	0.02	0.04
LOI	0.57	0.87	0.48	0.38
Total	100.00	100.00	100.00	100.00

XRPD analysis carried out on both FM samples revealed a completely amorphous structure, (figure 1S, Appendix III).

At the SEM, the untreated flotation muds (FM1, Figure 5.1 A and B; FM2 Figure 5.1 C and D) are composed of grains with variable shape and size (from a few micrometers to ~ 200 µm). Figures 5.1

B and D highlight the conchoidal fracture typical of glass, in agreement with XRPD results where no crystalline phase was detected. Based on BSE contrast, the glass fragments appear to be homogeneous, and no evident heavy minor phase can be detected, except for some rare tiny grains made up by Fe-oxides and Ni-sulphate. EDS data (Table 5.2) carried out on some grains confirm the composition of a Ca and Al-rich silicatic material, with a certain amount of Na_2O and MgO, as revealed by XRF bulk chemical analyses, and with minor amounts of Ce, Zr, Sn, and Cr.

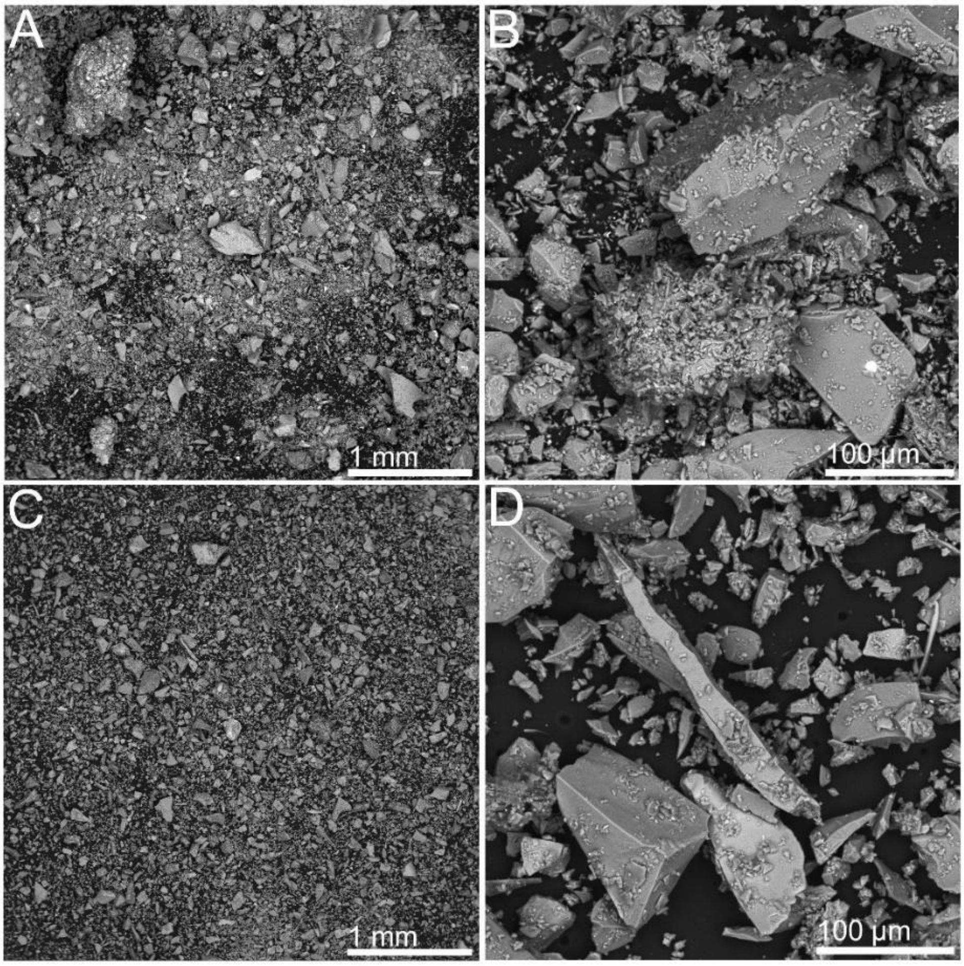

Figure 5. 1 SEM BSE images of FM1 (A and B) and FM2 (C and D).

Figure 5. 2 SEM EDS chemical data (expressed as oxides) on FM1 and FM2

	FM1					**FM2**							
Wt% oxides	***An-1***	***An-2***	***An-3***	***An-4***	***An-5***	***An-1***	***An-2***	***An-3***	***An-4***	***An-5***	***An-6***	***An-7***	***An-8***
Cl	1.76	*n.d.*	*n.d.*	1.23	*n.d.*	*n.d.*	*n.d.*	*n.d.*	1.68	*n.d.*	*n.d.*	*n.d.*	0.88
Cu	*n.d.*	*n.d.*	*n.d.*	1.88	*n.d.*	*n.d.*	*n.d.*	*n.d.*	*n.d.*	8.31	*n.d.*	*n.d.*	*n.d.*
Ag	*n.d.*	*n.d.*	*n.d.*	*n.d.*	*n.d.*	*n.d.*	*n.d.*	*n.d.*	*n.d.*	2.15	*n.d.*	*n.d.*	*n.d.*
MgO	2.84	0.96	5.05	2.86	2.59	2.87	2.92	2.36	3.37	*n.d.*	2.53	0.59	3.21

Al_2O_3	18.42	3.45	21.93	13.64	42.56	20.66	16.78	14.69	28.48	1.97	20.36	4.68	27.57
SiO_2	44.08	5.57	42.09	31.26	33.04	45.56	43.56	35.50	32.72	*n.d.*	44.00	6.65	33.74
FeO	1.03	86.54	*n.d.*	19.80	*n.d.*	8.54	6.58	26.28	1.83	*n.d.*	9.80	79.50	7.98
CaO	18.93	1.71	21.51	11.17	18.80	11.22	12.58	12.55	23.93	*n.d.*	12.18	3.70	19.73
TiO_2	0.89	*n.d.*	1.08	4.34	*n.d.*	*n.d.*	0.85	*n.d.*	0.73	*n.d.*	*n.d.*	*n.d.*	0.66
SO_3	0.79	*n.d.*	*n.d.*	*n.d.*	*n.d.*	*n.d.*	0.59	*n.d.*	*n.d.*	39.83	*n.d.*	*n.d.*	*n.d.*
Na_2O	11.25	0.77	1.51	6.37	1.81	5.13	5.36	3.08	4.01	*n.d.*	3.80	0.62	2.62
MnO	*n.d.*	0.85	*n.d.*	*n.d.*	*n.d.*	*n.d.*	0.05	*n.d.*	*n.d.*	*n.d.*	*n.d.*	0.91	*n.d.*
Cr_2O_3	*n.d.*	0.14	*n.d.*	*n.d.*	*n.d.*	*n.d.*	0.01	*n.d.*	*n.d.*	*n.d.*	*n.d.*	3.36	0.29
ZrO_2	*n.d.*	*n.d.*	1.92	2.27	1.21	2.76	4.75	3.31	2.62	*n.d.*	2.91	*n.d.*	2.98
Ce_2O_3	*n.d.*	*n.d.*	4.59	3.27	*n.d.*	*n.d.*	*n.d.*	*n.d.*	*n.d.*	*n.d.*	*n.d.*	*n.d.*	*n.d.*
K_2O	*n.d.*	*n.d.*	0.32	*n.d.*	*n.d.*	0.61	0.73	0.68	0.62	*n.d.*	0.63	*n.d.*	0.33
NiO	*n.d.*	*n.d.*	*n.d.*	1.91	*n.d.*	2.63	2.38	1.54	*n.d.*	44.71	3.78	*n.d.*	*n.d.*
SnO_2	*n.d.*	*n.d.*	*n.d.*	*n.d.*	*n.d.*	*n.d.*	2.87	*n.d.*	*n.d.*	3.03	*n.d.*	*n.d.*	*n.d.*
V_2O_3	*n.d.*	*n.d.*	*n.d.*	*n.d.*	*n.d.*	*n.d.*	0.00	*n.d.*	*n.d.*	*n.d.*	*n.d.*	*n.d.*	*n.d.*

CERAMIC TILES PROCESSING

The overall details of the process are covered by confidential restrictions of the patent, so here are reported only general information. As detailed below, the two ceramic tests were performed by slightly changing the starting mixture and/or the heating/cooling conditions in the ceramic furnace. In the case of test CFM1, the starting mixture was formed by up to 70-75 % of the flotation mud waste together with three different additives: i) Aluminum-silicate of Ca, Mg, Fe (≈ 5-15 %); ii) amorphous silica and Na-silicate (≈ 5-15 %); iii) Ca-sulfate, Fe-sulfate and B-oxide (1-5%). Powdered sample was pressed and formed under wet conditions (by adding 25% H_2O), dried in a pre-furnace (humidity reduction of 10%), and then heated in a furnace in oxidizing atmosphere at 930 °C for 30 minutes (50 °C/h heating rate), followed by cooling at 80°C/h rate.

CFM2 ceramic test was produced with up to 80-85 % of flotation mud waste and three additives: i) aluminum-silicates of Ca, Mg, Fe (≈ 1-8 %); ii) amorphous silica and Na-silicate (≈ 5-15 %) iii) Ca-sulfate, Fe-sulfate, B-oxide (B_2O_3), Na_2O, SnO_2, ZnO (≈ 1-8 %). The sample was powdered, pressed, and formed under wet conditions (with 15% H_2O), combined with ultrasonic treatment and dried in the pre-furnace environment (humidity reduction of 5%). Heating occurred in an oxidizing atmosphere at 1000 °C for about 30 minutes (heating rate 80 °C/h), followed by cooling at 100°C/h rate.

CHEMICAL, MINERALOGICAL AND MICROSTRUCTURAL CHARACTERISTICS OF CFM1 AND CFM2

The two investigated ceramic products are tiles with variable dimensions. CFM1 has size of 6 cm length x 4.5 cm width and 1.5 cm height while CFM2 has size of 3 cm length x 2 cm x 1 cm height. The two ceramic tiles are light brown in colour, with evident porosity (figure 5.2).

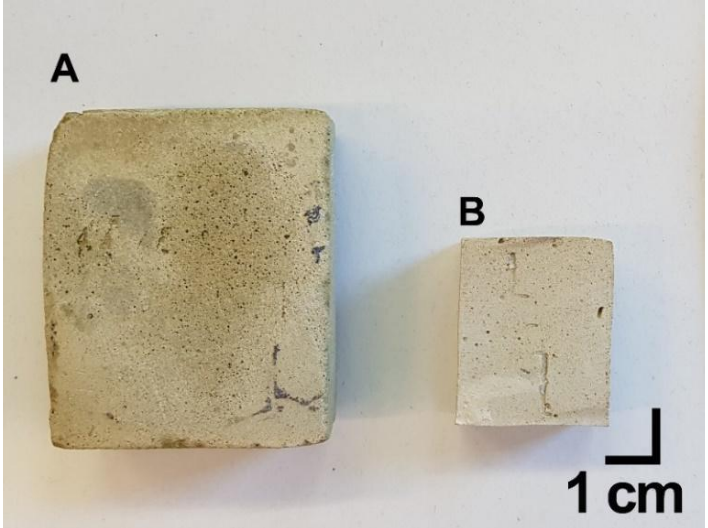

Figure 5. 2. Ceramic products, respectively CFM1 A and CFM2 B.

Bulk XRF chemical analyses of the ceramic products are reported in Table 5.1, showing almost equivalent chemical compositions, except for Si and Al concentrations, that exhibit reverse amounts in the two samples (i.e., higher SiO_2 and lower Al_2O_3 in CFM1; and the inverse trend in CFM2). Major components are SiO_2, CaO and Al_2O_3, followed by Fe, Na and Mg oxides. Minor components are constituted by some metal oxides (Ti, Cr, Mn, Cu, Ni, Zn, Sn), together with very low amounts of Ce and Zr oxides, also present in the flotation muds.

Figure 5.3 shows the XRPD data of the two investigated ceramic samples, which are significantly different from each other, due to the differences in starting additives and processing conditions. Main crystalline phases, resulting from the high-temperature ceramic processing, are calcium-silicate Gehlenite $Ca_2Al(AlSi)O_7$, Anorthite $CaAl_2Si_2O_8$ and Augite $(Ca,Mg,Fe^{2+},Fe^{3+},Ti,Al)_2(Si,Al)_2O_6$ for CFM1 sample, while diopside $CaMgSi_2O_6$, anorthite and the feldspathoid Nepheline $(Na,K)AlSiO_4$ are the main crystalline phases in CFM2 sample. The occurrence of a feldspathoid in CFM2 indicates SiO_2 undersaturation conditions that represent a relatively unusual composition in traditional ceramic material, as discussed below.

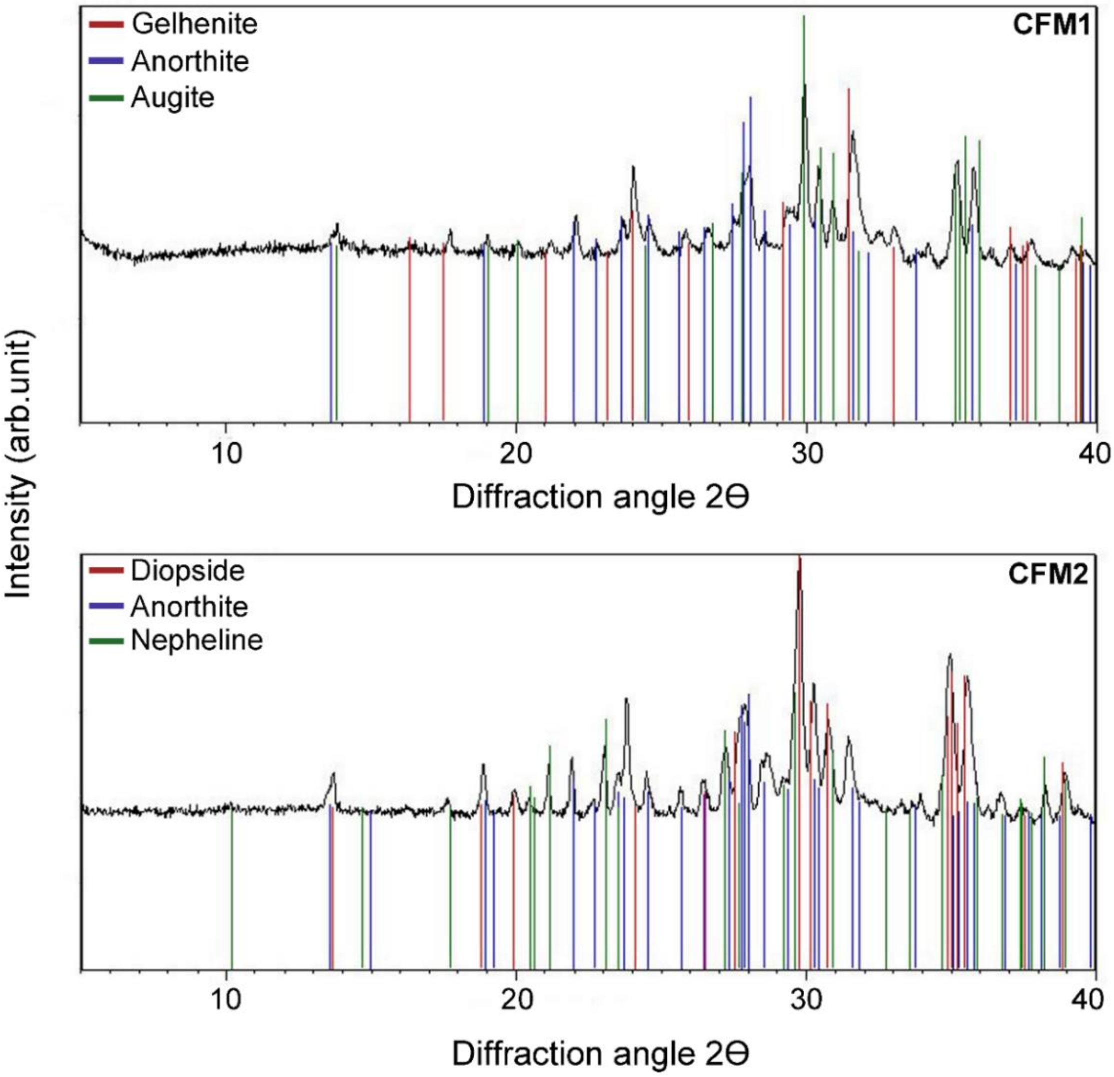

Figure 5. 3 XRPD patterns of the two CFM1 and CFM2 derived respectively from FM1 and FM2

From a microstructural point of view, the two products CFM1 and CFM2 are significantly different, as shown in Figure 5.4 and 5.5 respectively.

At low magnification (Figures 5.4 A and B) CFM1 is compact and quite homogeneous. It is possible to observe pores with rounded to sub-rounded shape and extremely variable size (10 - 390 µm in diameter). In 2-dimensional BSE images, they appear to be isolated, with no evident interconnected microstructure. At higher magnification, it is possible to detect the occurrence of a microcrystalline groundmass hosting different crystalline phases, as indicated in figure 5.4 with arrows and mineral abbreviations. The groundmass consists of major Ca-plagioclase (darkest grey colours in BSE, figure 5.4C) and other Ca-silicates such as clinopyroxenes (figure 5.4C), in agreement with XRPD results.

The distribution of the two minerals is not homogeneous, showing some regions in which Ca-plagioclase is the dominant phase, while in other portions clinopyroxenes prevails. In some cases, the above crystalline phases are bordered by individuals of Ca-Al silicates which have the composition of Melilite (general chemical formula $(Ca, Na)_2(Al, Mg, Fe^{2+})$ $[(Al, Si)SiO_7]$). This group of minerals belongs to the solid solution between Akermanite ($Ca_2MgSi_20_7$) and Gehlenite ($Ca_2Al_2SiO_7$), which are common constituents of ceramic materials (Swainson et al. 1992, Dondi et al. 2004, Rathossi and Pontikes 2010). In figure 5.4. is possible to observe Gehlenite as bright grey subrounded crystals which form a perimeter around a portion of a bigger aggregate, a microstructure, similar to pseudomorphic crystals. Moreover, in some cases, Larnite (Ca_2SiO_4) and Wollastonite ($CaSiO_3$) have been also detected; the latter is widespread in some localized regions of the sample, where it forms very fine-grained elongated crystals alternating with anhedral Ca-plagioclase (figure 5.4D); the brighter, smaller, sub-euhedral to anhedral crystals are instead Fe-(Cr) oxides (figure 5.4B-C) and, rarely, Cassiterite (SnO_2) grains.

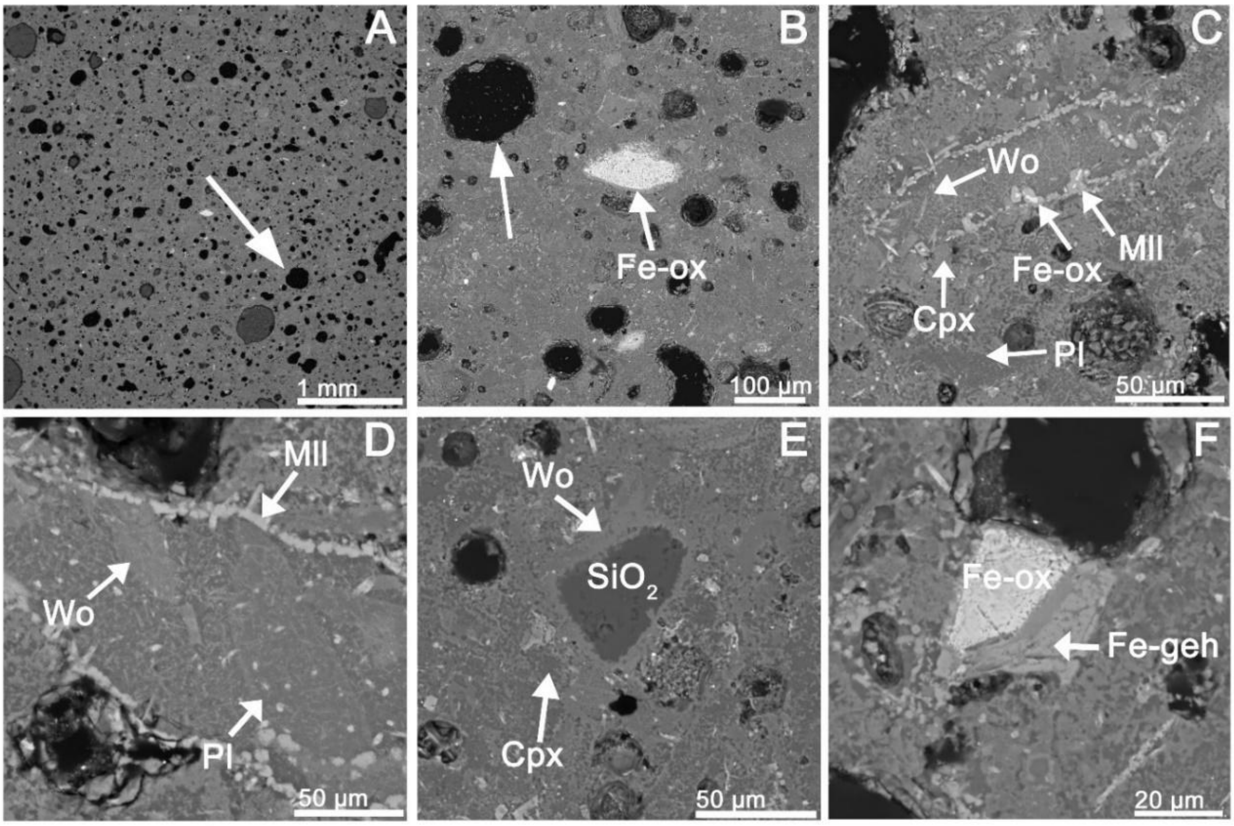

Figure 5. 4 Figure 4-SEM images (BSE mode) of the CFM1 specimen, showing both microstructure and mineralogy. A: large view with distribution of porosity (arrow) and groundmass; B: magnification of the groundmass with highlighted rounded pores and a Fe-oxide crystal; C: distribution of the main mineralogical phases within the groundmass composed of Ca-plagioclase, Clinopyroxene and elongated Wollastonite crystals. Melilite individuals form a perimeter around a portion of the groundmass. D: Another region similar

to C, with Wollastonite and Plagioclase forming the groundmass, bordered by subrounded Melilite crystals. E: A silica grain surrounded by Wollastonite and Clinopyroxene groundmass. F) Iron oxide rimmed by Fe-Gehlenite (abbreviations are cpx=Clinopyroxene, Pl=Plagioclase; Fe-Ox=iron oxide; Mll=Melilite; Wo=Wollastonite; Fe-Geh=Fe-gehlenite).

Sample CFM2 shows an apparently more compact microstructure, but it is characterized by a higher total apparent average porosity (26%). Pores are definitely smaller than in previous sample CFM1 (2-115 µm in diameter) and display an elongated and irregular shape (Figure 5.5 D-E-F), often evolving in an interconnected pattern. The ceramic material is more crystalline than the previous sample, showing crystals and grains of different phases, up to 300-400 µm in size (e.g., Figure 5.5 C-D). The overall microstructure is characterized by an apparent "grain-supported" texture composed by single grains or aggregates which are often in contact with each other, set up in a glassy and variably porous matrix, alternating with areas composed almost exclusively by a fine grained, less porous, groundmass. Based on EDS analyses, main mineralogical phases are Ca-bearing Nepheline (light grey colours in fig. 5.5 C-D) and Wollastonite ($CaSiO_3$). Wollastonite may form rims around bigger grains or aggregates, whereas in other cases it makes up needle-like, skeletal elongated micro phenocrystals set in a glassy homogeneous groundmass (Figure 5.5 F). The latter has an irregular distribution, with some areas characterized by a compact, not porous, glassy microstructure with dispersed elongated micro phenocrystals of Wollastonite (Figure 5.5 E-F), and other areas with a crystalline porous texture (Figure 5.5 C-D). Microstructure is characterized also by the presence of dispersed aggregate grains of amorphous silica and some minor iron oxides crystals (the grains with highest contrast in fig. 5D). Moreover, Melilite crystals are common within the aggregates.

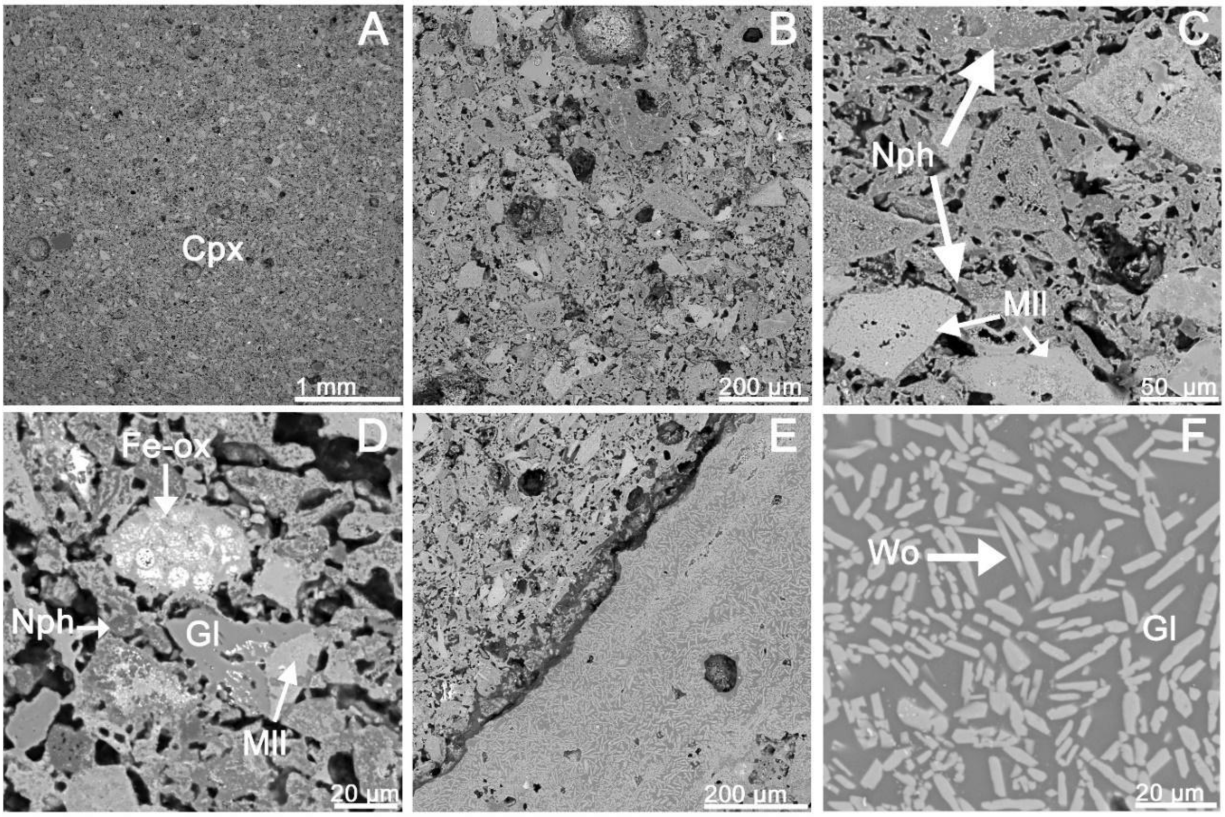

Figure 5. 5 SEM images (BSE mode) of the CFM2 specimen, showing both microstructure and mineralogy. A: large view. B: magnification of the area in A with distribution of pseudomorphic phases within an interconnected porosity pattern. C: detail of aggregates unevenly composed of Melilite, Clinopyroxenes and Nepheline. D: detail of an aggregate mainly composed of Fe-oxides and distribution of Melilite, Nepheline and portions of silicate glass. E: to the left the microstructure shown A, B and C. To the right an area with glass and elongated skeletal wollastonite micro-phenocrystals (enlarged view in F). Abbreviations Cpx=Clinopyroxene, Mll=Melilite; Nph=Nepheline; Gl=glass; Fe-ox: Fe-oxides.

Some representative EDS analyses for both CFM are reported in table 5.3.

Table 5. 3 SEM/ EDS analyses on the two investigated ceramic samples CFM1 and CFM

								CFM1							
	An12	**An14**	**An29**	**Fe-Geh8**	**Fe-Geh9**	**Fe-Geh24**	**Wo41**	**Wo43**	**Wo8**	**Cpx4**	**Cpx30**	**Mll12**	**Mll22**	**Mll1**	**Fe-Ox21**	**Fe-Ox26**
SiO_2	46.85	46.02	45.74	29.42	30.67	28.51	51.62	51.29	51.78	44.80	46.22	37.04	43.00	42.79		
TiO_2				6.78	6.10	6.71						1.89				0.89
Al_2O_3	34.81	34.99	35.32	4.65	6.33	5.53	3.66	3.82	3.80	28.55	23.95	12.76	12.74	15.02	7.91	8.56
Cr_2O_3				1.03								0.76			21.22	
FeO		0.66		22.05	20.05	22.46	2.69	3.07	2.14	1.38	2.76	10.54	1.40	3.62	50.91	86.14
MnO															0.76	
MgO				1.92	2.00	1.11	3.22	3.54	3.29		3.44	7.53	5.94	4.19	7.14	
CaO	16.36	16.41	16.38	31.15	30.99	34.27	37.91	37.58	38.16	22.93	19.24	28.22	30.43	27.10	0.93	
BaO																
Na_2O	1.98	1.91	2.55	1.55	2.16	1.42	0.91	0.70	0.84	2.34	4.39	1.26	6.49	6.31		0.81
NiO															5.90	
ZnO														0.98	5.23	1.64
Sn																1.96

	CFM2															
	Mll11	**Mll12**	**Mll37**	**Wo21**	**Wo5**	**Wo6**	**Ne1**	**Ne5**	**Ne6**	**Di9**	**Cpx39**	**Glass4**	**Glass10**	**Fe-ox8**	**Fe-ox9**	**Fe-ox40**
SiO_2	40.95	37.81	35.60	48.54	53.91	54.43	41.84	39.96	40.02	57.29	38.57	72.92	74.39	2.28	4.24	0.61
TiO_2											1.13					
Al_2O_3	15.58	15.78	16.15	4.10			34.28	34.50	35.54	1.25	29.11	7.17	7.81	1.82	3.32	1.57
Cr_2O_3															0.63	
FeO	8.02	8.99	7.29				0.79	0.68	0.70		1.88			94.05	86.13	96.17
MnO															0.57	
MgO	4.45	5.03	6.44	0.41		0.73				18.06	2.24	2.18	1.92		1.70	0.86
CaO	20.39	23.04	25.02	43.70	46.09	44.84	3.87	6.01	4.93	22.60	22.29	3.15	3.03	1.85	3.41	0.79
BaO	1.51	1.19	1.42													
Na_2O	4.55	2.16	2.14	1.05			15.01	14.51	14.37	0.81	3.09	7.76	6.22			
K_2O	1.92	1.67	0.51	2.20			4.21	4.34	4.44		0.29	6.82	6.63			
NiO			1.43													
SO_3											0.72					
ZrO_2	2.64	4.33	4.00													

Abbreviations: An= Anorthite; Mll= Melilite; Fe-Geh= Fe-gehlenite; Wo= Wollastonite; Fe-ox= fe oxides; Ne= Nepheline; Cpx= Clinopyroxene; Di= Diopside.

PHYSICAL AND MECHANICAL PROPERTIES

Figure 5.5 shows the samples used for the mechanical tests, i.e., uniaxial compressive strength and flexural strength. As stated above, these determinations were executed only on CFM2 sample, since it showed more critical microstructural features with respect to CFM1.

Figure 5.5. Cubic and elongated samples of CFM2for flexural and compressive strength determinations.

Table 5.4 reports both compressive strength and flexural strength results. In the ceramic tiles prepared for the mechanical tests, especially the flexural strength, some joints and fractures were visible, affecting the text execution and leading to a great variability of this parameter, from 0.8 MPa to 11.1 MPa (as seen in the last column of Table 5.4). The specimen showing the lowest value of flexural strength is the B, that revealed more evident macro cracks.

Table 5. 4. Results of the uniaxial compressive (top) and flexural (bottom) tests carried out on specimens derived from CFM2 sample.

Sample	Length (mm)	Thickness (mm)	Height (mm)	Weight (g)	Dry Density (t/m³)	Point load (kN)	Compressive strength (MPa)
A	53.4	49.7	54.5	269.1	1.860	150.0	55.3
B	53.3	49.3	54.1	266.2	1.873	190.0	73.9
C	53.3	49.2	53.9	265.1	1.876	140.0	53.2
D	53.5	49.3	53.6	265.9	1.881	140.0	53.3
E	53.7	49.2	53.5	266.7	1.887	190.0	73.4
F	53.3	49.3	54.2	268.9	1.888	180.0	67.3
Sample	**Length (mm)**	**Thickness (mm)**	**Height (mm)**	**Weight (g)**	**Dry Density (t/m³)**	**Point load (kN)**	**Flexural strength (MPa)**
A	301.0	52.4	48.7	1494.6	1.946	3000.0	9.1
B	300.5	54.1	49.3	1517.2	1.893	270.0	0.8
C	301.0	53.9	49.1	1500.8	1.884	3840.0	11.1

Micro-Deval abrasion test measured the wear resistance produced on the aggregate by the friction between the particles the abrasive charge given by spheres inserted in a rotating drum. To determine the wear resistance of the coarse aggregate, the material was prepared by reducing it to a test particle size class. Table 5.5 shows the results of the tests.

Table 5. 5 Results of the wear resistance test

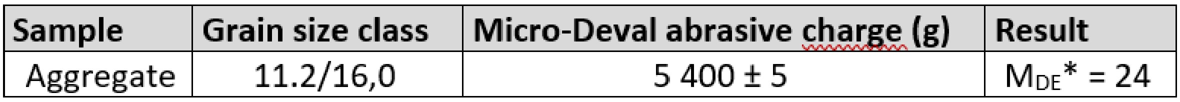

Sample	Grain size class	Micro-Deval abrasive charge (g)	Result
Aggregate	11.2/16,0	5 400 ± 5	M_{DE}* = 24

* M_{DE} = MicroDeval coefficient as computed by the following equation:

$$M_{DE} = [(M - m) / M] * 100$$

where:

M: mass, in g, of the specimen before the test;

m: mass, in g, of the retained in the 1,6 mm sieve after the test.

POROSITY

Distribution of pores in 2D SEM images was calculated for both sample CFM1 and CFM2, using the dedicated SEM image analyses ©Particle software. Main results are reported in figure 5.6. The two samples revealed different porosity classes. While in sample CFM1 the pores appear to be distributed and more frequent in the range from 0 to 40 µm, in sample CFM2 the equivalent pore diameter is smaller (class ranging from 0 to 10 µm, with extremely high frequency).

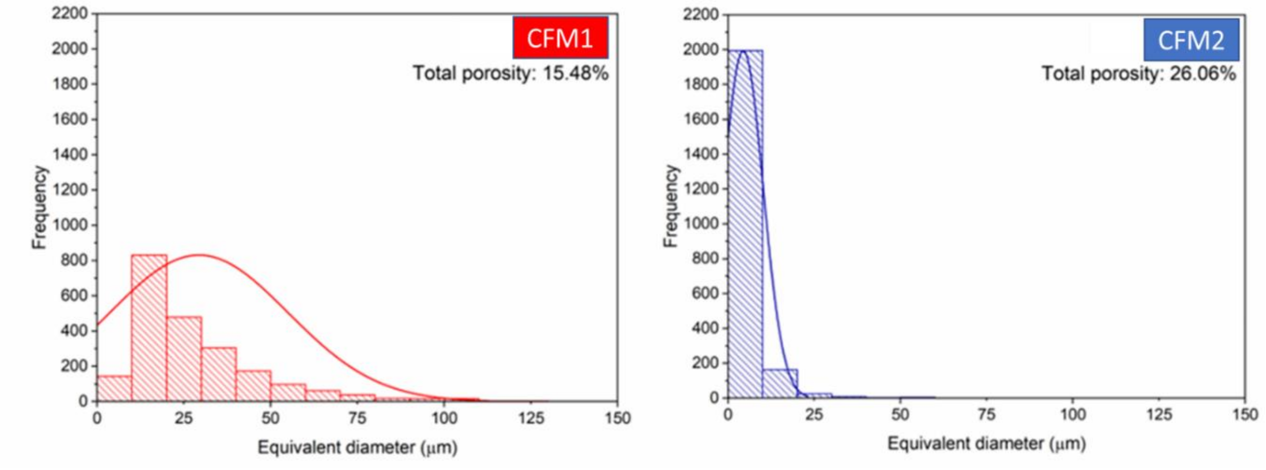

Figure 5.6 Porosity determination for CFM1 and CFM2 made with the SEM software.

For 3D analysis on porosity, a sample of approximately 11 mm by 11 mm by 14 mm was investigated by micro-CT as previously described in the materials and method section. Avizo 3D 2022.1 (ThermoFisher Scientific) was used to create volume representations and perform image segmentation. A subvolume was created for each scan (790 x 942 x 748 voxels, corresponding to 6.7 mm x 8.0 mm x 6.4 mm and 864 x 1138 x 928 voxels, corresponding to 863 x 1137 x 927 microns for Nikon and Versa scans, respectively) to avoid artifacts in the outer portion of the scan. An anisotropic diffusion filter was used to reduce noise. This improved the quality of the data to facilitate segmentation. To avoid user bias, automatic segmentation was performed using the Otsu method in the Avizo software (Figure 5.7).

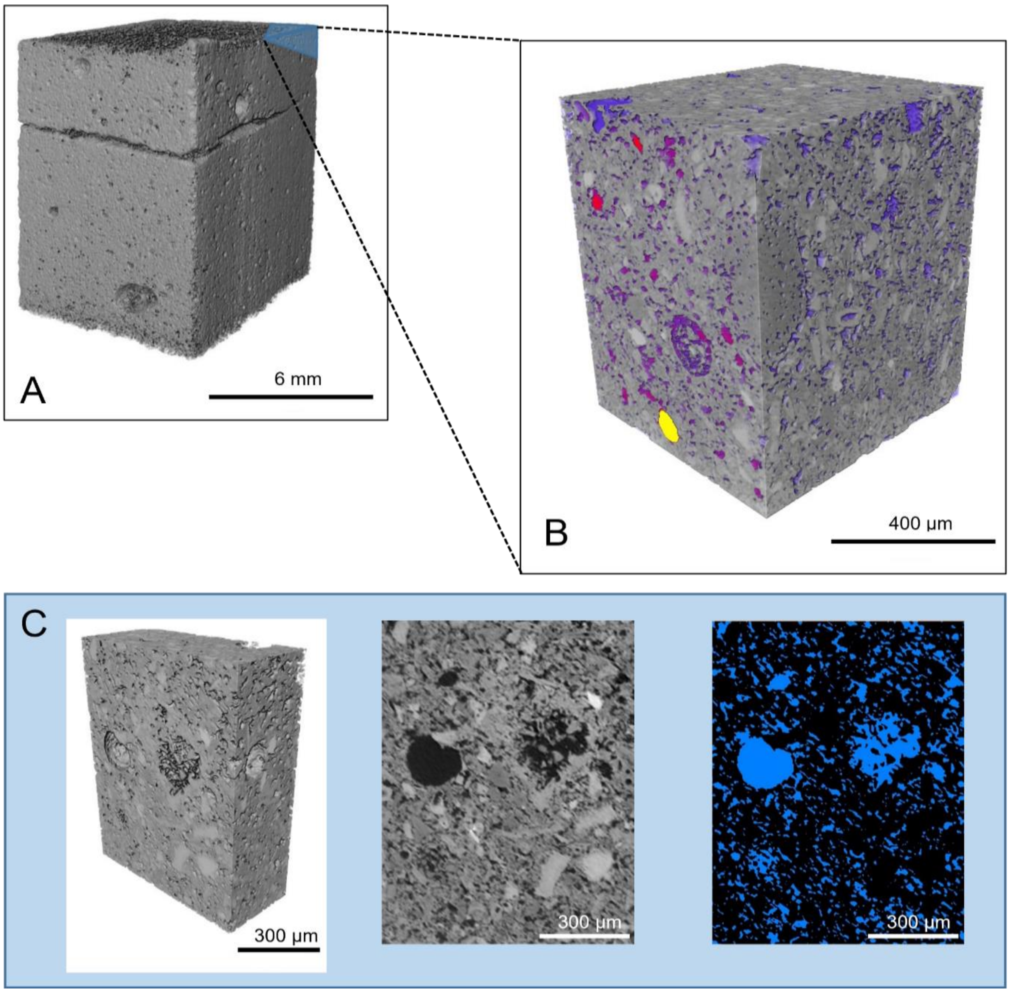

Figure 5.7 3D rendering of CFM sample obtained with Nikon micro-CT (voxel size 8.5 µm); B) 3D rendering of a subvolume of the sample shown in A taken from the edge, with an higher resolution (voxel size 1 µm) obtained with VERSA micro-CT scanner. Colours of pores represent Local Thickness computed areas with Fiji/ImageJ software. C) Representative 3D section of the subvolume shown in B along with 2D slice (raw data in the center) and its segmented version (right).

The total porosity calculated with the volume fraction modulus in Avizo gave a value of 3.4% for the Nikon scan, while a value of 21.48% was obtained with the higher resolution Versa scan. To characterize the pore diameter distribution, a local thickness approach was used for the Versa scan data using the free FiJi software (Schindelin et al. 2012). For definition, the Local Thickness algorithm defines "the diameter of the largest sphere that fits inside the object. To better investigate porosity connectivity, the tortuosity factor of the interconnected pores was calculated using the same procedure described in Backeberg et al. (2017). The tortuosity factor is a parameter that quantifies the geometric interconnections between pore spaces, considering the variation of pore cross-sectional areas through a given direction in a porous material. In particular, the TauFactor (Cooper et al. 2016) was used to model the 3D connectivity pattern of the subsample under study. This Matlab application models the tortuosity factor (τ) along the three dimensions of the diffusive (i.e., porous) phases studied. The minimum value of τ is 1, which means that along the test axis the cross-section of a pore region is constant, and the path is perfectly straight. Otherwise, if there are no connected paths along the test direction, TauFactor returns a value of infinity. Through this type of analysis, the three mutually perpendicular directions (x, y, z) of the sampled subvolume were modeled and a value of τ was calculated for each of them to test the extent of interconnectivity that would facilitate water flow, for example, and the presence of anisotropy in the porosity pattern, if any.

DISCUSSION AND CONCLUSIONS

Considering the overall results obtained recycling of flotation muds from precious metals recovery seems to be a valuable way to reduce disposal problems and environmental pollution. The first analyses were carried out on a laboratory scale to characterize the raw waste material and the resulting ceramic tiles. Flotation muds result to be mainly composed of SiO_2, CaO, Al_2O_3 with less amount of Fe and other elements such as Ce, Zr, Zn, Cu, Ni, Cr, Sn probably coming from the original material before the flotation process. The ceramics were produced by the GRINN Start Up based on patent 0001369219, using a very high percentage of flotation sludge (about 80%). Ceramic products resulted to consist of a glassy matrix embedding different mineralogical species such as anorthite, gehlenite, pyroxenes, plagioclases, nepheline, melilite-like and wollastonite. These main minerals are not homogeneously distributed in the samples (i.e., wollastonite distributed only in some areas), and are never pure but generally are solid solution testifying local phase equilibrium leading to local crystallization conditions. In the two ceramics there were also identified (from XRF and EDS) metals such as Sn, Ni, Zr, Zn, Ce in association to melilite.

Mechanical strength and flexural strength (determined for CFM2, revealing more critical microstructural features) yield good values, comparable to other ceramic products from waste recycling as we can observe in table 5.6. In addition, the good mechanical resistance of the studied material is also testified by results of wear resistance test, which yielded a micro-Deval parameter close to the limit values usually employed for aggregates in the construction field, in particular for granular underlay applications.

Table 5.6 Here are reported some characteristics of ceramics materials resulting form the reuse of wastes. The results of this work are shown in last row.

Waste raw materials	Additives	Sintering Conditions	Crystalline phases	Mechanical strength (MPa)	Flexural strength (MPa)	Reference
Blast furnace slag	Chemical reagents, such as CaO, Sb_2O_3, etc	960°C, 975 °C, 990 °C	Akermanite, Augite, Diopside, Gehlenite	-	26-89	Zhang et al. (2018)
Municipal solid waste incineration fly ash	Pure kaolin clay, soda-lime glass, water	800-1100 °C for 30 min	Wollastonite, Anorthite, Albite, Cristobalite	-	38.2 ± 5	Ponsot et al. (2015)
Municipal solid waste incineration bottom and coal fly ashes	Free of additives	850-950°C for 3h	Anorthite, Diopside	122.76 - 299.09	2.48-2.61	Zhang et al. (2020)
Silver mine tailings	Clay, barium carbonate $BaCO_3$, water	900 °C, 950 °C, 1000 °C, 1050 °C for 3 h	-	-	4.9-18.6	Drif et al. (2021)
1) Calamine mine processing tailings (CMPT) and 2) treated calamine mine process tailings (TCMPT)	Free of additives, just water	1 and 2) 950°C, 1000°C, 1050 °C for 3h	1) and 2) Anhydrite, Magnetite, Augite, Gehlenite, Hematite, Quartz (in different proportions)	-	1) 4,6-23,3 2) 3,1	Taha et al. (2016)
Blast furnace slag, Glass fiber, water glass	TiO_2, ZrO_2 and CaF_2	Crystallized at 780 °C for 90 minutes, nucleated at 920 °C for 90 minutes	Akermanite, TiO2, Diopside, Perovskite, Melilite, ,Anorthite, Labradorite, Augite	12 - 68	-	H Gao et al. (2018)
Waste marble powder	Brick clay, Waste marble powder ($CaCO_3$)	950 °C, 1050 °C for 2 h	Quartz, Hematite, Anorthite, Gehlenite, Wollastonite, Calcium Silicate	6.2-34.2		Sutcu et al. (2015)
Flotation muds	Aluminum silicates of Ca, Mg and Fe, amorphous silica, Na-silicates, B_2O_3, Na_2O, SnO_2, ZnO	1000°C for 30 min	Diopside, Anorthite, Nepheline + minor Wollastonite, Melilite and glass	53.2 - 73.4	10,1	This work

The porosity is relatively high in both CFM ceramics, and deep analyses with micro- CT also show that is interconnected. Data derived from this preliminary study can serve as a basis for the next feasibility steps. Further experiments need to be conducted to test the representativeness and homogeneity of the waste both over time and with the different extraction methods (i.e., type of e-waste treated for PM extraction). Also, higher sintering temperatures should be investigated to observe the evolution of microstructure (particularly porosity) and mineral assemblages. In addition, the leaching behavior of heavy metals originally contained in FM, such as Ce, Zr, Ni, Zn, which are predominantly contained in melilites and iron oxides in the ceramic body, should be investigated to also evaluate any possible environmental impact of this type of reuse.

CHAPTER VI

GENERAL CONCLUSIONS

This PhD dissertation deals with a new kind of “mineral resource”, i.e., our inorganic wastes. Specifically, I have studied three inorganic special wastes that are completely different for what concerned their chemical composition, mineralogy, origin, and toxicity. The first case dealt with asbestos-containing wastes that, because of their extreme danger when inhaled, required an additional processing step, i.e., thermal inertization, to make them safe for possible secondary use. Once the asbestos fibers have been irreversibly transformed into other minerals, as demonstrated in Chapter III, the inert waste may be considered as a valuable new secondary raw material. At differences from ACW, the other two wastes, i.e., red Gypsum and flotation muds are not hazardous industrial wastes, but they also represent an environmental and social problem. Red gypsum waste is a major problem in Tuscany, due to the huge volumes produced by the TiO_2 industry, it is difficult to store, and is not well accepted by local communities for landscape restoration. Flotation sludges, although less important in terms of waste volumes, can contain some important metals that must be detected and possibly recovered.

Following the organization of the present thesis, specific conclusions, potential implications, drawbacks and future works are reported at the end of previous chapters (in particular Chapter III, IV and V for the three different waste kinds, respectively), so that I here report only some general considerations.

Overall, the results of my thesis have demonstrated that the reuse of inorganic waste, sometimes even hazardous waste, is possible and that further scientific efforts must be soon devoted to this target. However, to do this, a more intense interaction between academic world and involved industrial stakeholders, social and public bodies and political community is needed. Recycling of inorganic wastes is necessary to reduce over-exploitation of non-renewable natural resources, reducing, at the same time, overuse of soil and waste volumetric increase in landfills. As described in the previous chapters, natural resources are of great concern today. Since the Industrial Revolution, we are consuming at a much-accelerated rate what the Earth system has produced over millions of years through complex geological processes, and new ways and places are needed to find the necessary resources. One of the possible solutions to the present trend of “waste increase + natural resource depletion” is provided by the circular economy approach, through the reuse/recycling of inorganic waste to realize new commercially valid products. In addition, some types of waste can compensate for the lack of key elements such as critical raw materials. These processes are certainly complex and require further studies and economic inputs but should be considered as unavoidable by the social and political communities. The final target would in fact a real transition from linear to circular economy, as suggested/imposed by national and international bodies, such as the European Union, solving the common gap between theory (what we do in academic laboratories) and practice (what can be realized in a production plant).

To conclude, this work aims also to remark the fundamental role of Mineralogy in all the above topics and in the industrial production of new competitive inorganic materials. The results reported in previous Chapters clearly demonstrated how mineral/phase assemblages, reactions, microstructures, crystal structures and compositions determine almost all properties of inorganic material, thus influencing their potential commercial uses and technical performance. This further supports the need of a closer interaction between the industrial context and “traditional academic disciplines”, like Mineralogy, to obtain the most successful results.

ACKNOWLEDGMENTS

I would like to thank Tecneco S.r.l., Isambiente S.n.c., Ideal Standard S.r.l., GRINN S.r.l., Petroceramics S.p.a, PMG S.r.l., Graftonica S.r.l, Drs. Paolo Tuccitto and Sergio Grillo, and all the partners involved in the various projects, that allowed the realization of this thesis and related scientific papers. For what concerns cement asbestos study, the research was supported by the projects DEAR (deattivazione efficiente dell'amianto e riutilizzo https://dearprogetto.it/) and A-FIRE (Asbestos fast inertization and recycling https://a-fire.it/), founded by "Ministero della transizione ecologica" in 2020 and Fondazione Cariplo in 2021, respectively.

My acknowledgments go to Professor Cecilia Viti, for all the support given me during these three years and all my educational path transmitting me the passion and curiosity for mineralogy. I would like to also thank the Drs. Claudia Magrini and Giovanna Giorgetti for their constant help and collaboration, all along the way. My great thanks to Professors Giancarlo Capitani, Riccardo Salvini and Giuseppe Protano for their contribution.

Finally, I would like to thank all my colleagues with whom I had a constant and fruitful discussions.

REFERENCES

Allwood, J. M. (2014). Squaring the Circular Economy: The Role of Recycling within a Hierarchy of Material Management Strategies. In *Handbook of Recycling: State-of-the-art for Practitioners, Analysts, and Scientists*. https://doi.org/10.1016/B978-0-12-396459-5.00030-1

Amirul Hakim Sidek, M., Yunus, R. M., Al-Nizar Khan Ahmad Khan, M., & Remanul Islam, M. (2019). Industrial Operation Feasibility for Red Gypsum-Based Brick Manufacturing. In *Asian Journal of Applied Sciences*. www.ajouronline.com

Andreola, F., Barbieri, L., Lancellotti, I., Leonelli, C., & Manfredini, T. (2016). Recycling of industrial wastes in ceramic manufacturing: State of art and glass case studies. Ceramics International, 42(12), 13333-13338.

Andreola, F., Barbieri, L., Corradi, A. et al. The possibility to recycle solid residues of the municipal waste incineration into a ceramic tile body. Journal of Materials Science 36, 4869–4873 (2001). https://doi.org/10.1023/A:1011823901409

Arganda-Carreras, I., Kaynig, V., Rueden, C., Eliceiri, K. W., Schindelin, J., Cardona, A., & Sebastian Seung, H. (2017). Trainable Weka Segmentation: a machine learning tool for microscopy pixel classification. Bioinformatics, 33(15), 2424-2426. https://doi.org/10.1093/bioinformatics/btx180

ARPAT. (2010). *ACCORDO VOLONTARIO SUL RIUTILIZZO DEI GESSI ROSSI TIOXIDE PER IL RIPRISTINO AMBIENTALE DELLA EX CAVA DI POGGIO SPERANZONA*.

Aryal, A., & Morley, C. (2020). Call for a global ban policy on and scientific management of asbestos to eliminate asbestos-related diseases. *Journal of Public Health Policy*, *41*(3), 279–285. https://doi.org/10.1057/s41271-020-00223-4

Ballirano, P., & Melis, E. (2007). Thermal behaviour of β-anhydrite $CaSO_4$ to 1,263 K. *Physics and Chemistry of Minerals*, *34*(10), 699–704. https://doi.org/10.1007/s00269-007-0186-2

Bayless, P. , D. C. Erd. , M. E. M. , A. P. S. , D. K. S. ,. (1986). *Mineral Powder Diffraction File, Data Book. International Centre for Diffraction Data. JCPDS*.

Bellagio Declaration. (n.d.).

Backeberg, N. R., Iacoviello, F., Rittner, M., Mitchell, T. M., Jones, A. P., Day, R., ... & Striolo, A. (2017). Quantifying the anisotropy and tortuosity of permeable pathways in clay-rich mudstones using models based on X-ray tomography. Scientific reports, 7(1), 1-12.

Barry, T. I., Cox, J. M., & Morrell, R. (1978). Cordierite glass-ceramics-effect of TiO2 and ZrO2 content on phase sequence during heat treatment. Journal of Materials Science, 13(3), 594-610.

Bloise, A., Catalano, M., Barrese, E., Gualtieri, A. F., Bursi Gandolfi, N., Capella, S., & Belluso, E. (2016). TG/DSC study of the thermal behaviour of hazardous mineral fibres. *Journal of Thermal Analysis and Calorimetry*, *123*(3), 2225–2239. https://doi.org/10.1007/s10973-015-4939-8

Boccaccini AR, Petitmerment M, Wintermantel E (1997). Glass – ceramics from municipal incinerator fly ash. Am. Ceram. Soc. Bull., 76(11): 75-78.

Brown, J. S., Gordon, T., Price, O., & Asgharian, B. (2013). Thoracic and respirable particle definitions for human health risk assessment. *Particle and Fibre Toxicology*, *10*(1), 12. https://doi.org/10.1186/1743-8977-10-12

Burke, I. T., Mayes, W. M., Peacock, C. L., Brown, A. P., Jarvis, A. P., & Gruiz, K. (2012). Speciation of Arsenic, Chromium, and Vanadium in Red Mud Samples from the Ajka Spill Site, Hungary. *Environmental Science & Technology*, *46*(6), 3085–3092. https://doi.org/10.1021/es3003475

Burat, F., Baştürkcü, H., & Özer, M. (2019). Gold&silver recovery from jewelry waste with combination of physical and physicochemical methods. Waste management, 89, 10-20.

Cai, Q., Ma, B., Jiang, J., Wang, J., Shao, Z., Hu, Y., Qian, B., & Wang, L. (2021). Utilization of waste red gypsum in autoclaved aerated concrete preparation. *Construction and Building Materials*, *291*, 123376. https://doi.org/10.1016/J.CONBUILDMAT.2021.123376

Charola, A. E., Pühringer, J., & Steiger, M. (2007). Gypsum: A review of its role in the deterioration of building materials. In *Environmental Geology* (Vol. 52, Issue 2, pp. 207–220). https://doi.org/10.1007/s00254-006-0566-9

Chen, Q., Ding, W., Sun, H., & Peng, T. (2021). Synthesis of anhydrite from red gypsum and acidic wastewater treatment. *Journal of Cleaner Production*, *278*, 124026. https://doi.org/10.1016/J.JCLEPRO.2020.124026

Chen, Z., & Huang, L. (2019). Application review of LCA (Life Cycle Assessment) in circular economy: From the perspective of PSS (Product Service System). *Procedia CIRP*, *83*, 210–217. https://doi.org/10.1016/J.PROCIR.2019.04.141

Ciabatti I., (2018), Il recupero dei metalli preziosi dagli scarti delle lavorazioni orafe, La chimica e l'industria, n.5, anno II, 39-43.

Ciabatti I., M. Fontani, C. Martini (2019) The Arezzo seminar on precious metals. Substantia 3(1) Suppl.: 7-10. doi: 10.13128/Substantia-599

Circle Economy. (2022). *The Circularity Gap Report 2022* (pp. 1-64, Rep.). Amsterdam: Circle Economy.

Commission, E., Directorate-General for Internal Market Entrepreneurship and SMEs, I., Bobba, S., Claudiu, P., Huygens, D., Alves Dias, P., Gawlik, B., Tzimas, E., Wittmer, D., Nuss, P., Grohol, M., Saveyn, H., Buraoui, F., Orveillon, G., Hámor, T., Slavko, S., Mathieux, F., Gislev, M., Torres De Matos, C., … Garbarino, E. (2018). *Report on critical raw materials and the circular economy*. Publications Office. https://doi.org/doi/10.2873/167813

COMMISSION OF THE EUROPEAN COMMUNITIES *Guidance on classification of waste according to EWC-Stat categories*, (2010).

European Commission, Study on the EU's list of Critical Raw Materials – Final Report (2020).

Cook, P. J. (2022). Resources and reserves in a carbon-constrained world. *Mineral Economics*, *35*(3–4), 361–371. https://doi.org/10.1007/s13563-022-00318-2

Cooper, S. J., Bertei, A., Shearing, P. R., Kilner, J. A. & Brandon, N. P. TauFactor: An open-source application for calculating tortuosity factors from tomographic data. SoftwareX (2016).

Cornu, R., Béduneau, A., & Martin, H. (2020). Influence of nanoparticles on liver tissue and hepatic functions: A review. *Toxicology*, *430*, 152344. https://doi.org/10.1016/j.tox.2019.152344

Crippa, M., Bianchi, A., Cristofori, D., Merletti, F., Morazzoni, F., Scotti, R., & Simonutti, R. (2013). High dielectric constant rutile–polystyrene composite with enhanced percolative threshold. *Journal of Materials Chemistry C*, 9.

Crowson, P. C. F. (2011). Mineral reserves and future minerals availability. *Mineral Economics*, *24*(1), 1–6. https://doi.org/10.1007/s13563-011-0002-9

Carvalho Gomes, S., Zhou, J. L., Li, W., & Long, G. (2019). Progress in manufacture and properties of construction materials incorporating water treatment sludge: A review. *Resources, Conservation and Recycling*, *145*, 148–159. https://doi.org/10.1016/j.resconrec.2019.02.032

Da Silva, F. L., Araújo, F. G. S., Teixeira, M. P., Gomes, R. C., & Von Krüger, F. L. (2014). Study of the recovery and recycling of tailings from the concentration of iron ore for the production of ceramic. Ceramics International, 40(10), 16085-16089.

Drif, B., Taha, Y., Hakkou, R., & Benzaazoua, M. (2021). Integrated valorization of silver mine tailings through silver recovery and ceramic materials production. Minerals Engineering, 170, 107060.

Dela Cruz, C. S., Tanoue, L. T., & Matthay, R. A. (2011). Lung Cancer: Epidemiology, Etiology, and Prevention. *Clinics in Chest Medicine*, *32*(4), 605–644. https://doi.org/10.1016/j.ccm.2011.09.001

Diaz, L. A., Lister, T. E., Parkman, J. A., & Clark, G. G. (2016). Comprehensive process for the recovery of value and critical materials from electronic waste. *Journal of Cleaner Production*, *125*, 236–244. https://doi.org/10.1016/J.JCLEPRO.2016.03.061

Ding, Y., Zhang, S., Liu, B., Zheng, H., Chang, C. chi, & Ekberg, C. (2019). Recovery of precious metals from electronic waste and spent catalysts: A review. *Resources, Conservation and Recycling*, *141*, 284–298. https://doi.org/10.1016/J.RESCONREC.2018.10.041

Dondi, M., Ercolani, G., Fabbri, B., & Marsigli, M. (1999). Chemical Composition of Melilite Formed during the Firing of Carbonate-Rich and Iron-Containing Ceramic Bodies. *Journal of the American Ceramic Society*, *82*(2), 465-468.

Dondi, M., Ercolani, G., Fabbri, B., & Marsigli, M. (1998). An approach to the chemistry of pyroxenes formed during the firing of Ca-rich silicate ceramics. *Clay Minerals*, *33*(3), 443–452. https://doi.org/DOI: 10.1180/000985598545741

Dondi, M., Fabbri, B., & Mingazzini, C. (1997). Mobilisation of chromium and vanadium during firing of structural clay products. *ZI International*, *50*(10), 685–696.

Directive 2008/98/EC of the European Parliament and of the Council, Official Journal of the European Union 3 (2008). https://doi.org/10.5040/9781782258674.0028

Erol, M., Küçükbayrak, S., Ersoy-Meriçboyu, A., & Öveçoğlu, M.L. (2001). Crystallization behaviour of glasses produced from fly ash. Journal of The European Ceramic Society, 21, 2835-2841.

European Commission, 2012. Innovating for sustainable growth: a bioeconomy for Europe. Off. J. Eur. Union 8 (2), 60.

Fauziah, C. I., Hanani, M. N., Zauyah, S., Samsuri, A. W., & Rosazlin, A. (2011). Co-application of Red Gypsum and Sewage Sludge on Acidic Tropical Soils. *Communications in Soil Science and Plant Analysis*, *42*(21), 2561–2571. https://doi.org/10.1080/00103624.2011.614032

Fauziah, I., Zauyah, S., & Jamal, T. (1996). Characterization and land application of red gypsum: A waste product from the titanium dioxide industry. *Science of the Total Environment*, *188*(2–3), 243–251. https://doi.org/10.1016/0048-9697(96)05179-0

Fernandes, H. R., Tulyaganov, D. U., & Ferreira, J. M. (2013). The role of P2O5, TiO2 and ZrO2 as nucleating agents on microstructure and crystallization behaviour of lithium disilicate-based glass. Journal of materials science, 48(2), 765-773.

Follner, S., Wolter, A., Helming, K., Silber, C., Bartels, H., & Follner, H. (2002). On the Real Structure of Gypsum Crystals. *Crystal Research and Technology* , *37*(2–3), 207–218. https://doi.org/10.1002/1521-4079(200202)37:2/3<207::AID-CRAT207>3.0.CO;2-L

Freyer, D., & Voigt, W. (2003). Crystallization and Phase Stability of CaSO4 and CaSO 4 - Based Salts. In *Monatshefte fur Chemie* (Vol. 134, Issue 5, pp. 693–719). https://doi.org/10.1007/s00706-003-0590-3

Gázquez, M. J., Bolívar, J. P., García-Tenorio, R., & Vaca, F. (2009). Physicochemical characterization of raw materials and co-products from the titanium dioxide industry. *Journal of Hazardous Materials*, *166*(2), 1429–1440. https://doi.org/https://doi.org/10.1016/j.jhazmat.2008.12.067

Gázquez, M. J., Bolívar, J. P., Garcia-Tenorio, R., & Vaca, F. (2014). A Review of the Production Cycle of Titanium Dioxide Pigment. *Materials Sciences and Applications*, *05*(07), 441–458. https://doi.org/10.4236/msa.2014.57048

Gazquez, M. J., Bolivar, J. P., Vaca, F., García-Tenorio, R., & Caparros, A. (2013). Evaluation of the use of TiO2 industry red gypsum waste in cement production. *Cement and Concrete Composites*, *37*(1), 76–81. https://doi.org/10.1016/J.CEMCONCOMP.2012.12.003

Gázquez, M. J., Contreras, M., Pérez-Moreno, S. M., Guerrero, J. L., Casas-Ruiz, M., & Bolívar, J. P. (2021). A Review of the Commercial Uses of Sulphate Minerals from the Titanium Dioxide Pigment Industry: The Case of Huelva (Spain). In *Minerals* (Vol. 11, Issue 6). https://doi.org/10.3390/min11060575

Giantomassi, F., Gualtieri, A. F., Santarelli, L., Tomasetti, M., Lusvardi, G., Lucarini, G., Governa, M., & Pugnaloni, A. (2010). Biological effects and comparative cytotoxicity of thermal transformed asbestos-containing materials in a human alveolar epithelial cell line. *Toxicology in Vitro*, *24*(6), 1521–1531. https://doi.org/10.1016/j.tiv.2010.07.009

Ginsberg, T., Modigell, M., & Wilsmann, W. (2011). Thermochemical characterisation of the calcination process step in the sulphate method for production of titanium dioxide. *Chemical Engineering Research and Design*, *89*(7), 990–994. https://doi.org/10.1016/J.CHERD.2010.11.006

Gliozzo, E. (2020). Ceramic technology. How to reconstruct the firing process. *Archaeological and Anthropological Sciences*, *12*, 260. https://doi.org/10.1007/s12520-020-01133-y/Published

Gualtieri, A. F. (2000). Accuracy of XRPD QPA using the combined Rietveld–RIR method. *Journal of Applied Crystallography*, *33*(2), 267–278. https://doi.org/10.1107/S002188989901643X

Gualtieri, A. F. (2017). *Mineral fibres: crystal chemistry, chemical-physical properties, biological interaction and toxicity*.

Gualtieri, A. F., & Boccaletti, M. (2011). Recycling of the product of thermal inertization of cement–asbestos for the production of concrete. *Construction and Building Materials*, *25*(8), 3561–3569. https://doi.org/10.1016/J.CONBUILDMAT.2011.03.049

Gualtieri, A. F., Cavenati, C., Zanatto, I., Meloni, M., Elmi, G., & Gualtieri, M. L. (2008). The transformation sequence of cement-asbestos slates up to 1200 °C and safe recycling of the reaction product in stoneware tile mixtures. *Journal of Hazardous Materials*, *152*(2), 563–570. https://doi.org/10.1016/j.jhazmat.2007.07.037

Gualtieri, A. F., Giacobbe, C., Sardisco, L., Saraceno, M., Lassinantti Gualtieri, M., Lusvardi, G., Cavenati, C., & Zanatto, I. (2011). Recycling of the product of thermal inertization of cement-asbestos for various industrial applications. *Waste Management*, *31*(1), 91–100. https://doi.org/10.1016/j.wasman.2010.07.006

Gualtieri, A. F., Giacobbe, C., & Viti, C. (2012). The dehydroxylation of serpentine group minerals. *American Mineralogist*, *97*(4), 666–680. https://doi.org/10.2138/am.2012.3952

Gualtieri, A. F., Veratti, L., Tucci, A., & Esposito, L. (2012). Recycling of the product of thermal inertization of cement-asbestos in geopolymers. *Construction and Building Materials*, *31*, 47–51. https://doi.org/10.1016/j.conbuildmat.2011.12.087

Guthrie, G. D., & Mossman, B. T. (1993). Health effects of mineral dust. In *Reviews in Mineralogy* (Mineralogi, Vol. 28). P.H. Ribbe Series.

Haider, A. J., Jameel, Z. N., & Al-Hussaini, I. H. M. (2019). Review on: Titanium dioxide applications. *Energy Procedia*, *157*, 17–29. https://doi.org/10.1016/j.egypro.2018.11.159

Haupt, M., & Zschokke, M. (2017). How can LCA support the circular economy?—63rd discussion forum on life cycle assessment, Zurich, Switzerland, November 30, 2016. *International Journal of Life Cycle Assessment*, *22*(5), 832–837. https://doi.org/10.1007/s11367-017-1267-1

Helbig, C., Huether, J., Joachimsthaler, C., Lehmann, C., Raatz, S., Thorenz, A., Faulstich, M., & Tuma, A. (2022). A terminology for downcycling. *Journal of Industrial Ecology*, *26*(4), 1164–1174. https://doi.org/10.1111/jiec.13289

Hossain, S. S., & Roy, P. K. (2020). Sustainable ceramics derived from solid wastes: a review. In *Journal of Asian Ceramic Societies* (Vol. 8, Issue 4, pp. 984–1009). Taylor and Francis Ltd. https://doi.org/10.1080/21870764.2020.1815348

Hudson-Lamb, D. L., Strydom, C. A., & Potgieter, J. H. (1996). The thermal dehydration of natural gypsum and pure calcium sulphate dihydrate (gypsum). *Thermochimica Acta*, *282–283*(SPEC. ISS.), 483–492. https://doi.org/10.1016/0040-6031(95)02819-6

IARC, 2012. Arsenic, metals, fibres, and dusts, IARC Monographs 100 C. International Agency for Research on Cancer, Lyon, FR.

IRP (2017). Assessing global resource use: A systems approach to resource efficiency and pollution reduction. Bringezu, S., Ramaswami, A., Schandl, H., O'Brien, M., Pelton, R., Acquatella, J., Ayuk, E., Chiu, A., Flanegin, R., Fry, J., Giljum, S., Hashimoto, S., Hellweg, S., Hosking, K., Hu, Y., Lenzen, M., Lieber, M., Lutter, S., Miatto, A., Singh Nagpure, A., Obersteiner, M., van Oers, L., Pfister, S., Pichler, P., Russell, A., Spini, L., Tanikawa, H., van der Voet, E., Weisz, H., West, J., Wiijkman, A., Zhu, B., Zivy, R. A Report of the International Resource Panel. United Nations Environment Programme. Nairobi, Kenya

IRP (2020). Mineral Resource Governance in the 21st Century: Gearing extractive industries towards sustainable development. Ayuk, E. T., Pedro, A. M., Ekins, P., Gatune, J., Milligan, B., Oberle B., Christmann, P., Ali, S., Kumar, S. V, Bringezu, S., Acquatella, J., Bernaudat, L., Bodouroglou, C., Brooks, S., Buergi Bonanomi, E., Clement, J., Collins, N., Davis, K., Davy, A., Dawkins, K., Dom, A., Eslamishoar, F., Franks, D., Hamor, T., Jensen, D., Lahiri-Dutt, K., Mancini, L., Nuss, P., Petersen, I., Sanders, A. R. D. A Report by the International Resource Panel. United NationsEnvironment Programme, Nairobi, Kenya.

ISPRA Rapporto *Rifiuti Speciali* 321/2020 ISBN: 987-88-448-1009-2

ISPRA *Rapporto Rifiuti Speciali Edizione 367*/2022 ISBN: 978-88-448-1116-7

Italian Decree Minister 06/09/ 1994, 1994. Normative e metodologie tecniche di applicazione dell'art. 6, comma 3, e dell'art. 12, comma 2, della legge 27 marzo 1992, n. 257, relativa alla cessazione dell'impiego dell'amianto. S. Ord alla G.U. N 220 Serie Generale del 20/09/1994.

Italian Decree Minister 29/07/ 2004, 2004, Regolamento relativo alla determinazione e disciplina delle attività di recupero dei prodotti e beni di amianto e contenenti amianto N.248. G.U. N.234 Serie Generale del 05/10/2004.

Italian Decree Minister 27/09/ 2010, 2010, Definizione dei criteri di ammissibilità dei rifiuti in discarica. GU N. 281 Serie Generale del 01/12/2010.

Italian Law 257, 1992, Norme relative alla cessazione dell'impiego dell'amianto. S.Ord. alla G.U. N. 087 Serie Generale Parte Prima del 13.04.92 Supplemento 064 del 13.04.92, March 27th.

IARC, 2012. Arsenic, metals, fibres, and dusts, IARC Monographs 100 C. International Agency for Research on Cancer, Lyon, FR.

INAIL, Settore ricerca, Dipartimento installazioni di produzione ed insediamenti antropici, 2013, Mappatura delle discariche che accettano in Italia i rifiuti contenenti amianto e loro capacità di smaltimento passate, presenti e future. Inail, Roma.

Individuazione dei rifiuti non pericolosi sottoposti alle procedure semplificate di recupero ai sensi degli articoli 31 e 33 del decreto legislativo n. 22. GU Serie Generale n.88 del 16-04-1998 - Suppl. Ordinario n. 72, (1998) (testimony of Italian Decree Minister).

152. Norme in materia ambientale. GU Serie Generale n. 88 del 14 aprile 2006 - Supplemento Ordinario n. 96, (2006) (testimony of Italian Decree Minister).

Iwaszko, J., Zawada, A., Przerada, I., & Lubas, M. (2018). Structural and microstructural aspects of asbestos-cement waste vitrification. *Spectrochimica Acta Part A: Molecular and Biomolecular Spectroscopy*, *195*, 95–102. https://doi.org/https://doi.org/10.1016/j.saa.2018.01.053

Jafari, S., Mahyad, B., Hashemzadeh, H., Janfaza, S., Gholikhani, T., & Tayebi, L. (2020). *Biomedical Applications of TiO 2 Nanostructures: Recent Advances*. https://doi.org/10.2147/IJN.S249441

Javangula, H., & Lineberry, Q. (2014). Comparative studies on fire-rated and standard gypsum wallboard. *Journal of Thermal Analysis and Calorimetry*, *116*(3), 1417–1433. https://doi.org/10.1007/s10973-014-3795-2

Jawadand, S., & Randive, K. (2021). A Sustainable Approach to Transforming Mining Waste into Value-Added Products. In K. Randive, S. Pingle, & A. Agnihotri (Eds.), *Innovations in Sustainable Mining: Balancing Environment, Ecology and Economy* (pp. 1–20). Springer International Publishing. https://doi.org/10.1007/978-3-030-73796-2_1

Jiménez-Rivero, A., & García-Navarro, J. (2020). Management of end-of-life gypsum in a circular economy. In *Advances in Construction and Demolition Waste Recycling* (pp. 69–79). Elsevier. https://doi.org/10.1016/b978-0-12-819055-5.00005-x

Ju, J., Feng, Y., Li, H., & Wang, B. (2022). A Novel Approach for Separation and Recovery of Titanium, Scandium, Iron from Acidic Wastewater and Red Gypsum Utilization. *Mining, Metallurgy & Exploration*, *39*(3), 1297–1312. https://doi.org/10.1007/s42461-022-00600-5

Khater, G. A. (2002). The use of Saudi slag for the production of glass-ceramic materials. Ceramics International, 28(1), 59-67.

Khater, G. A., Yue, Y., Abu Safiah, M. O., & Mahmoud, M. A. (2019). Synthesis and Characterization of Anorthite and Magnetite Glass-Ceramics from Basaltic Rocks. *Silicon*, *11*(4), 1763–1774. https://doi.org/10.1007/s12633-018-9991-0

Kim, T. H., Tae, S. H., Chae, C. U., & Choi, W. Y. (2016). The environmental impact and cost analysis of concrete mixing blast furnace slag containing titanium gypsum and sludge in South Korea. *Sustainability (Switzerland)*, *8*(6). https://doi.org/10.3390/su8060502

Kirchherr, J., Reike, D., & Hekkert, M. (2017). Conceptualizing the circular economy: An analysis of 114 definitions. *Resources, Conservation and Recycling*, *127*(April), 221–232. https://doi.org/10.1016/j.resconrec.2017.09.005

Kumar, S., Singh, K.K. & Ramachandrarao, P. Synthesis of cordierite from fly ash and its refractory properties. Journal of Materials Science Letters 19, 1263–1265 (2000). https://doi.org/10.1023/A:1006737932563

Kuntze, R. A. (2009). *Gypsum: Connecting Science and Technology: Vol. ASTM MNL 6* (ASTM Inter).

Kusiorowski, R., Zaremba, T., Gerle, A., Piotrowski, J., Simka, W., & Adamek, J. (2015). Study on the thermal decomposition of crocidolite asbestos. *Journal of Thermal Analysis and Calorimetry*, *120*(3), 1585–1595. https://doi.org/10.1007/s10973-015-4421-7

Kusiorowski, R., Zaremba, T., Piotrowski, J., & Podwórny, J. (2015). Utilisation of cement-asbestos wastes by thermal treatment and the potential possibility use of obtained product for the clinker bricks manufacture. *Journal of Materials Science*, *50*(20), 6757–6767. https://doi.org/10.1007/s10853-015-9231-6

Kyungeun Sung. (2015, April). *A Review on Upcycling: Current Body of Literature, Knowledge Gaps and a Way Forward*.

Jeon, S., Ito, M., Tabelin, C. B., Pongsumrankul, R., Kitajima, N., Park, I., & Hiroyoshi, N. (2018). Gold recovery from shredder light fraction of E-waste recycling plant by flotation-ammonium thiosulfate leaching. Waste management, 77, 195-202

Larson, A. C., & Dreele, R. B. von. (n.d.). *GENERAL STRUCTURE ANALYSIS SYSTEM*. 231.

Leder, N. (2020). *Influential factors for value creation within the Circular Economy_ Framework for Waste Valorisation*. 10.

Legambiente. (2018). *Liberi dall’amianto? I ritardi dei piani regionali, delle bonifiche e delle alternative alle discariche*.

Lemougna, P. N., Yliniemi, J., Ismailov, A., Levanen, E., Tanskanen, P., Kinnunen, P., ... & Illikainen, M. (2019). Recycling lithium mine tailings in the production of low temperature (700–900 C) ceramics: Effect of ladle slag and sodium compounds on the processing and final properties. Construction and Building Materials, 221, 332-344

Liang, B., Li, C., Zhang, C., & Zhang, Y. (2005). Leaching kinetics of Panzhihua ilmenite in sulfuric acid. *Hydrometallurgy*, *76*(3–4), 173–179. https://doi.org/10.1016/J.HYDROMET.2004.10.006

Liu, S., Guan, X., Zhang, S., Xu, C., Li, H., & Zhang, J. (2017). Sintering red mud based imitative ceramic bricks with CO2 emissions below zero. Materials Letters, 191, 222-224.

Loutou, M., Taha, Y., Benzaazoua, M., Daafi, Y., & Hakkou, R. (2019). Valorization of clay by-product from moroccan phosphate mines for the production of fired bricks. Journal of Cleaner Production, 229, 169-179

Ligabue, M. L., Gualtieri, A. F., Lassinantti Gualtieri, M., Malferrari, D., & Lusvardi, G. (2020). Recycling of thermally treated cement-asbestos for the production of porcelain stoneware slabs. *Journal of Cleaner Production*, *247*, 119084. https://doi.org/10.1016/J.JCLEPRO.2019.119084

Martin, M., & Eklund, M. (2011). Improving the environmental performance of biofuels with industrial symbiosis. *Biomass and Bioenergy*, *35*(5), 1747–1755. https://doi.org/10.1016/j.biombioe.2011.01.016

Martins, F. F., & Castro, H. (2020). Raw material depletion and scenario assessment in European Union – A circular economy approach. *Energy Reports*, *6*, 417–422. https://doi.org/https://doi.org/10.1016/j.egyr.2019.08.082

McNulty, G. S. (2007). Production of titanium dioxide. *Proceedings of NORM V International Conference, Seville, Spain*, 169–189.

Meinert, L. D., Robinson, G. R., & Nassar, N. T. (2016). Mineral resources: Reserves, peak production and the future. *Resources*, *5*(1). https://doi.org/10.3390/resources5010014

Misra, K. (2012). *Understanding mineral deposits*. Springer Science & Business Media.

Mohd Tadza, M. Y., Mazelan, N., Yusri, N. F., & Abdullah, A. (2019). Some Geotechnical Properties of Pure and Waste Gypsum for Geoelectrical Grounding Applications. *Civil and Environmental Engineering Reports*, *29*(3), 97–106. https://doi.org/10.2478/ceer-2019-0027

Montanaro, L., Bianchini, N., Rincon, J. M., & Romero, M. (2001). Sintering behavior of pressed red mud wastes from zinc hydrometallurgy. Ceramics international, 27(1), 29-37

Morimoto, N. (1988). Nomenclature of Pyroxenes. *Mineralogy and Petrology*, *39*(1), 55–76. https://doi.org/10.1007/BF01226262

Muralikrishna, I. v, & Manickam, V. (2017). *Chapter Thirteen - Industrial Wastewater Treatment Technologies, Recycling, and Reuse* (I. v Muralikrishna & V. B. T.-E. M. Manickam, Eds.; pp. 295–336). Butterworth-Heinemann. https://doi.org/https://doi.org/10.1016/B978-0-12-811989-1.00013-0

Norme in materia ambientale. GU Serie Generale n. 88 del 14 aprile 2006 - Supplemento Ordinario n. 96, *152* (2006) (testimony of Italian Decree Minister).

Northey, S. A., Mudd, G. M., & Werner, T. T. (2018). Unresolved Complexity in Assessments of Mineral Resource Depletion and Availability. In *Natural Resources Research* (Vol. 27, Issue 2, pp. 241–255). Springer New York LLC. https://doi.org/10.1007/s11053-017-9352-5

OECD. (2015). Material Resources, Productivity and the Environment. In *OECD Green Growth Studies*. OECD. https://www.oecd-ilibrary.org/environment/material-resources-productivity-and-the-environment_9789264190504-en

Pacella, A., Tomatis, M., Viti, C., Bloise, A., Arrizza, L., Ballirano, P., & Turci, F. (2020). Thermal inertization of amphibole asbestos modulates Fe topochemistry and surface reactivity. *Journal of Hazardous Materials*, *398*, 123119. https://doi.org/10.1016/j.jhazmat.2020.123119

Paglietti, F., Malinconico, S., della Staffa, B. C., Bellagamba, S., & de Simone, P. (2016). Classification and management of asbestos-containing waste: European legislation and the Italian experience. *Waste Management*, *50*, 130–150. https://doi.org/10.1016/j.wasman.2016.02.014

Paglionico, M., 2017, I rifiuti contenenti amianto: da problema a risorsa. Geologia dell’Ambiente, Supplemento al n. 4/2017:29–33. ISSN 1591–5352.

Paolini, V., Tomassetti, L., Segreto, M., Borin, D., Liotta, F., Torre, M., & Petracchini, F. (2019). Asbestos treatment technologies. *Journal of Material Cycles and Waste Management*, *21*(2), 205–226. https://doi.org/10.1007/s10163-018-0793-7

Peixin, Z., & Jiaqiang, Y. (2000). Mössbauer and infrared spectroscopy investigation on glass ceramics using red mud. Zeitschrift für Metallkunde, 91

Pol, V. G. (2010). Upcycling: Converting waste plastics into paramagnetic, conducting, solid, pure carbon microspheres. *Environmental Science and Technology*, *44*(12), 4753–4759. https://doi.org/10.1021/es100243u

Ponomarenko, T., Nevskaya, M., & Jonek-Kowalska, I. (2021). Mineral resource depletion assessment: Alternatives, problems, results. *Sustainability (Switzerland)*, *13*(2), 1–15. https://doi.org/10.3390/su13020862

Protano, G., Baroni, D., Bianchi, S., Russo, C., & Salleolini, M. (2020). Assessing the impact on groundwater chemistry of an environmental restoration performed using industrial solid waste from TiO2 production. *Applied Geochemistry*, *120*(May), 104666. https://doi.org/10.1016/j.apgeochem.2020.104666

Qin, J., Cui, C., Cui, X., Hussain, A., Yang, C., & Yang, S. (2015). Recycling of lime mud and fly ash for fabrication of anorthite ceramic at low sintering temperature. Ceramics International, 41(4), 5648-5655.

Rahmani, A. H., Almatroudi, A., Babiker, A. Y., Khan, A. A., & Alsahly, M. A. (2018). Effect of Exposure to Cement Dust among the Workers: An Evaluation of Health Related Complications. *Open Access Macedonian Journal of Medical Sciences*, *6*(6), 1159–1162. https://doi.org/10.3889/oamjms.2018.233

Ramachandran, V. S., & Paroli, R. M. (2002). *Handbook of Thermal Analysis of Andrew Publishing*.

Rathossi, C., & Pontikes, Y. (2010). Effect of firing temperature and atmosphere on ceramics made of NW Peloponnese clay sediments: Part II. Chemistry of pyrometamorphic minerals and comparison with ancient ceramics. Journal of the European Ceramic Society, 30(9), 1853-1866.

Rawlings, R. D., Wu, J. P., & Boccaccini, A. R. (2006). Glass-ceramics: their production from wastes—a review. Journal of materials science, 41(3), 733-761.

Rees, J. (2017). *Natural resources: allocation, economics and policy*. Routledge.

Rietveld, H. M. (1969). A profile refinement method for nuclear and magnetic structures. *Journal of Applied Crystallography*, *2*(2), 65–71. https://doi.org/10.1107/s0021889869006558

Ronchi, E., Leoni, S., Vigni, F., Pettinao, E., Galli, L., Erme, A., Brunori Cutaia, C. L., Rinaldi, C., Scalbi, S., Altamura, P., Ansanelli, G., Beltrani, T., Buttol, P., Cellurale, M., Cerbone, A., Ceruti, F., Chiavetta, C., Cortesi, S., Corrado, S., … Zucaro, A. (2022). *4° RAPPORTO SULL'ECONOMIA CIRCOLARE IN ITALIA-2022 A cura del Circular Economy Network Gruppo di lavoro del Network e della Fondazione per lo sviluppo sostenibile*. www.circulareconomynetwork.it

Rosli, N. A., Aziz, H. A., Selamat, M. R., & Lim, L. L. P. (2020). A mixture of sewage sludge and red gypsum as an alternative material for temporary landfill cover. *Journal of Environmental Management*, *263*(October 2019), 110420. https://doi.org/10.1016/j.jenvman.2020.110420

Rosli, N. A., Aziz, H. A., Selamat, M. R., Lim, L. L. P., & Zawawi, M. H. (2021). Effect of compaction on physical properties of a sewage sludge and red gypsum mixture as intermediate landfill cover. *Construction and Building Materials*, *289*, 123153. https://doi.org/10.1016/J.CONBUILDMAT.2021.123153

Ross, M., & Nolan, R. P. (2003). History of asbestos discovery and use and asbestos-related disease in context with the occurrence of asbestos within ophiolite complexes. In *Ophiolite concept and the evolution of geological thought*. Geological Society of America. https://pubs.geoscienceworld.org/books/book/522/chapter/3801516

Ruiz, A. I., Ortega, A., Fernández, R., Miranda, J. F., López Samaniego, E., & Cuevas, J. (2018). Thermal treatment of asbestos containing materials (ACM) by mixing with Na2CO3 and special clays for partial vitrification of waste. *Materials Letters*, *232*, 29–32. https://doi.org/10.1016/j.matlet.2018.08.061

Sánchez, J., Curt, M. D., Robert, N., & Fernández, J. (2019). Biomass resources. In The role of bioenergy in the bioeconomy (pp. 25-111). Academic Press.

Swainson, I. P., Dove, M. T., Schmahl, W. W., & Putnis, A. (1992). Neutron powder diffraction study of the åkermanite-gehlenite solid solution series. Physics and Chemistry of Minerals, 19(3), 185-195

Saidani, M., Kendall, A., Yannou, B., Leroy, Y., & Cluzel, F. (2019). Closing the loop on platinum from catalytic converters: Contributions from material flow analysis and circularity indicators. *Journal of Industrial Ecology*, *23*(5), 1143–1158. https://doi.org/10.1111/jiec.12852

Sarrigani G.V., Amiri I.S. (2019) Literature Review of Glass-Ceramic and Willemite Production from Waste Materials. In: Willemite-Based Glass Ceramic Doped by Different Percentage of Erbium Oxide and Sintered in Temperature of 500-1100C. SpringerBriefs in Electrical and Computer Engineering. Springer, Cham. https://doi.org/10.1007/978-3-030-10644-7_2

Schindelin, J., Arganda-Carreras, I., Frise, E., Kaynig, V., Longair, M., Pietzsch, T., Preibisch, S., Rueden, C., Saalfeld, S., Schmid, B., Tinevez, J.-Y., White, D. J., Hartenstein, V., Eliceiri, K., Tomancak, P., & Cardona, A. (2012). Fiji: an open-source platform for biological-image analysis. *Nature Methods*, *9*(7), 676–682. https://doi.org/10.1038/nmeth.2019

Scoble, M., Klein, B., & Dunbar, W. S. (2003). Mining Waste: Transforming Mining Systems for Waste Management. In *International Journal of Surface Mining* (Vol. 17, Issue 2).

Selikoff, I. J., Churg, J., & Hammond, E. C. (1965). Relation between Exposure to Asbestos and Mesothelioma. *New England Journal of Medicine*, *272*(11), 560–565. https://doi.org/10.1056/NEJM196503182721104

Selli, D., Tawfilas, M., Mauri, M., Simonutti, R., & di Valentin, C. (2019). Optimizing PEGylation of TiO2 Nanocrystals through a Combined Experimental and Computational Study. *Chemistry of Materials*, *31*(18), 7531–7546. https://doi.org/10.1021/acs.chemmater.9b02329

Shakeel, M., Jabeen, F., Shabbir, S., Asghar, M. S., Khan, M. S., & Chaudhry, A. S. (2016). Toxicity of Nano-Titanium Dioxide (TiO2-NP) Through Various Routes of Exposure: a Review. In *Biological Trace Element Research* (Vol. 172, Issue 1). Humana Press Inc. https://doi.org/10.1007/s12011-015-0550-x

Shanshal, S. A., & Al-Qazaz, H. K. (2020). Consequences of cement dust exposure on pulmonary function in cement factory workers. *American Journal of Industrial Medicine*, ajim.23211. https://doi.org/10.1002/ajim.23211

Silpa Kaza, Lisa Yao, Perinaz Bhada-Tata, and F. V. W. (2018). What a Waste 2.0: A Global Snapshot of Solid Waste Management to 2050 All. In *Uban development series* (Vol. 1, Issue 1). https://doi.org/10.1596/978-1-4648-1329-0

Skinner, H. C. W., Ross, M., & Frondel, C. C. N.-T. A. S. 1988. (1988). *Asbestos and other fibrous materials: mineralogy, crystal chemistry, and health effects*. Oxford University Press.

Smykatz-Kloss, W. (2012). *Differential thermal analysis: application and results in mineralogy* (Vol. 11). Springer Science & Business Media.

Spasiano, D., & Pirozzi, F. (2017). Treatments of asbestos containing wastes. *Journal of Environmental Management*, *204*, 82–91. https://doi.org/10.1016/j.jenvman.2017.08.038

Strohmeier, B. R., Huntington, J. C., Bunker, K. L., Sanchez, M. S., Allison, K., & Lee, R. J. (2010). What is asbestos and why is it important? Challenges of defining and characterizing asbestos. *International Geology Review*, *52*(7–8), 801–872. https://doi.org/10.1080/00206811003679836

Sung, K. (2015). A Review on Upcycling: Current Body of Literature, Knowledge Gaps and a Way Forward. *International Conference on Environmental, Cultural, Economic and Social Sustainability*, *17*(4), 28–40. http://irep.ntu.ac.uk/id/eprint/12706/1/219287_PubSub1825_Sung.pdf

Sutcu, M., Alptekin, H., Erdogmus, E., Er, Y., & Gencel, O. (2015). Characteristics of fired clay bricks with waste marble powder addition as building materials. Construction and Building Materials, 82, 1-8. http://dx.doi.org/10.1016/j.conbuildmat.2015.02.055

Taha, Y., Benzaazoua, M., Mansori, M., Yvon, J., Kanari, N., & Hakkou, R. (2016). Manufacturing of ceramic products using calamine hydrometallurgical processing wastes. Journal of Cleaner Production, 127, 500-510.

Taha, Y., Benzaazoua, M., Hakkou, R., & Mansori, M. (2017). Coal mine wastes recycling for coal recovery and eco-friendly bricks production. Minerals Engineering, 107, 123-138.

Tang, Z., Li, W., Tam, V. W. Y., & Xue, C. (2020). Advanced progress in recycling municipal and construction solid wastes for manufacturing sustainable construction materials. *Resources, Conservation & Recycling: X*, *6*, 100036. https://doi.org/10.1016/J.RCRX.2020.100036

Tayebi-Khorami, M., Edraki, M., Corder, G., & Golev, A. (2019). Re-thinking mining waste through an integrative approach led by circular economy aspirations. In *Minerals* (Vol. 9, Issue 5). MDPI AG. https://doi.org/10.3390/min9050286

Tian, X., Cui, X., Lai, T., Ren, J., Yang, Z., Xiao, M., Wang, B., Xiao, X., & Wang, Y. (2021). Gas sensors based on TiO2 nanostructured materials for the detection of hazardous gases: A review. *Nano Materials Science*, *3*(4), 390–403. https://doi.org/10.1016/J.NANOMS.2021.05.011

Toby, B. H. (2001). EXPGUI, a graphical user interface for GSAS. *Journal of Applied Crystallography*, *34*(2), 210–213. https://doi.org/10.1107/S0021889801002242

Torréns-Martín, D., Fernández-Carrasco, L., & Blanco-Varela, M. T. (2015). Thermal analysis of blended cements. *Journal of Thermal Analysis and Calorimetry*, *121*(3), 1197–1204. https://doi.org/10.1007/s10973-015-4569-1

Tóth Szita, K. (2017). THE APPLICATION OF LIFE CYCLE ASSESSMENT IN CIRCULAR ECONOMY. *Hungarian Agricultural Engineering*, *31*, 5–9. https://doi.org/10.17676/hae.2017.31.5

Trinh, H. B., Lee, J. chun, Suh, Y. jae, & Lee, J. (2020). A review on the recycling processes of spent auto-catalysts: Towards the development of sustainable metallurgy. *Waste Management*, *114*, 148–165. https://doi.org/10.1016/J.WASMAN.2020.06.030

UNEP (2016). Global Material Flows and Resource Productivity. An Assessment Study of the UNEP International Resource Panel. H. Schandl, M. Fischer-Kowalski, J. West, S. Giljum, M. Dittrich, N. Eisenmenger, A. Geschke, M. Lieber, H. P. Wieland, A. Schaffartzik, F. Krausmann, S. Gierlinger, K. Hosking, M. Lenzen, H. Tanikawa, A. Miatto, and T. Fishman. Paris, United Nations Environment Programme

Viti, C. (2010). Serpentine minerals discrimination by thermal analysis. *American Mineralogist*, *95*(4), 631–638. https://doi.org/10.2138/am.2010.3366

Wagner, J. C., Sleggs, C. A., & Marchend, P. (1960). *Diffuse pleural mesothelioma and asbestos exposure in the North Western Cape Province*. *17*(Br J In Med), 260–271.

Wang, Z., Lyu, X., Yao, G., Wu, P., Wang, J., & Wei, J. (2020). Preparation of Ca–Si–Al–Mg porous ceramics by Co-operation of Ca&Mg-contained soda residue and altered rock gold tailings. *Journal of Cleaner Production*, *262*, 121345. https://doi.org/10.1016/J.JCLEPRO.2020.121345

Wegener, C. (2016). Upcycling. In V. P. Glăveanu, L. Tanggaard, & C. Wegener (Eds.), *Creativity — A New Vocabulary* (pp. 181–188). Palgrave Macmillan UK. https://doi.org/10.1057/9781137511805_22

Weir, A., Westerhoff, P., Fabricius, L., Hristovski, K., & von Goetz, N. (2012). Titanium dioxide nanoparticles in food and personal care products. *Environmental Science and Technology*, *46*(4), 2242–2250. https://doi.org/10.1021/es204168d

WEST, R. R., & SUTTON, W. J. (1954). Thermography of Gypsum. *Journal of the American Ceramic Society*, *37*(5), 221–224. https://doi.org/10.1111/j.1151-2916.1954.tb14027.x

Wills, B. A. (2013). Mineral processing technology: an introduction to the practical aspects of ore treatment and mineral recovery. Elsevier.

Winterstetter, A., Laner, D., Rechberger, H., & Fellner, J. (2015). Framework for the evaluation of anthropogenic resources: A landfill mining case study - Resource or reserve? *Resources, Conservation and Recycling*, *96*, 19–30. https://doi.org/10.1016/j.resconrec.2015.01.004

Yarborough, C. M. (2007). The risk of mesothelioma from exposure to chrysotile asbestos: *Current Opinion in Pulmonary Medicine*, *13*(4), 334–338. https://doi.org/10.1097/MCP.0b013e328121446c

Yousif, A. M. (2019). Recovery and then individual separation of platinum, palladium, and rhodium from spent car catalytic converters using hydrometallurgical technique followed by successive precipitation methods. *Journal of Chemistry*, *2019*. https://doi.org/10.1155/2019/2318157

Yvon, Y., & Sharrock, P. (2011). Characterization of Thermochemical Inactivation of Asbestos Containing Wastes and Recycling the Mineral Residues in Cement Products. *Waste and Biomass Valorization*, *2*(2), 169–181. https://doi.org/10.1007/s12649-011-9063-9

Zanelli, C., Conte, S., Molinari, C., Soldati, R., & Dondi, M. (2021). Waste recycling in ceramic tiles: a technological outlook. *Resources, Conservation and Recycling*, *168*, 105289. https://doi.org/10.1016/J.RESCONREC.2020.105289

Zhang, J., Yan, Y., & Hu, Z. (2018). Preparation and characterization of foamed concrete with Ti-extracted residues and red gypsum. *Construction and Building Materials*, *171*, 109–119. https://doi.org/https://doi.org/10.1016/j.conbuildmat.2018.03.072

Zhang, S., Ding, Y., Liu, B., & Chang, C. chi. (2017). Supply and demand of some critical metals and present status of their recycling in WEEE. In *Waste Management* (Vol. 65, pp. 113–127). Elsevier Ltd. https://doi.org/10.1016/j.wasman.2017.04.003

Zhang, X., Chen, J., Jiang, J., Li, J., Tyagi, R. D., & Surampalli, R. Y. (2020). The potential utilization of slag generated from iron- and steelmaking industries: a review. *Environmental Geochemistry and Health*, *42*(5), 1321–1334. https://doi.org/10.1007/s10653-019-00419-y

Zhang, Y., Wang, F., Huang, H., Guo, Y., Li, B., Liu, Y., & Chu, P. K. (2016). Gypsum blocks produced from TiO2 production by-products. *Environmental Technology*, *37*(9), 1094–1100. https://doi.org/10.1080/09593330.2015.1102329

APPENDIX I

On the following pages there are photos of the samples: A) hand-held sample photos; B) stereomicroscope photos with focus on the fibers; C and D) SEM/BSE images of the fibers (chrysotile, crocidolite or synthetic).

TEC 1

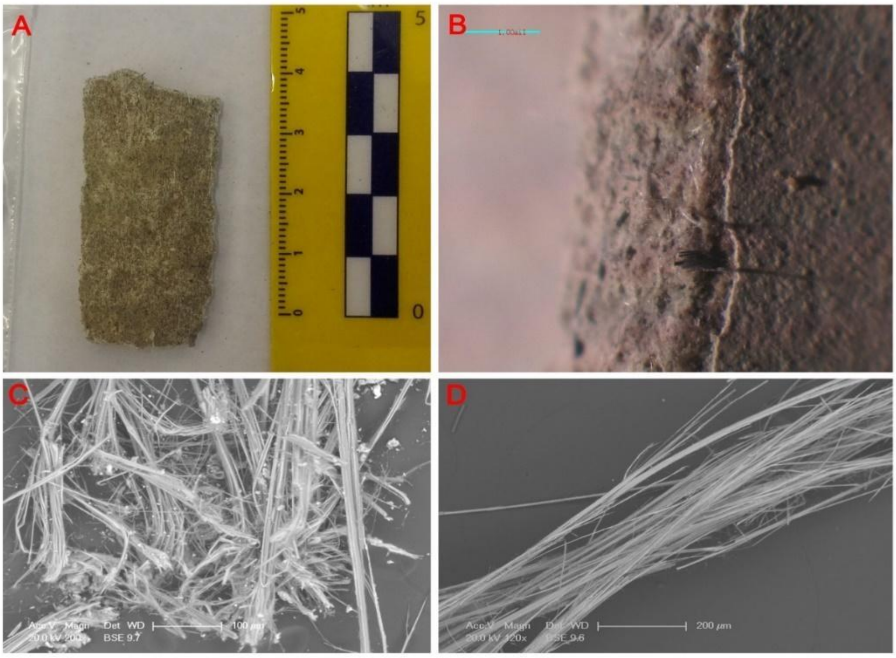

TEC 2

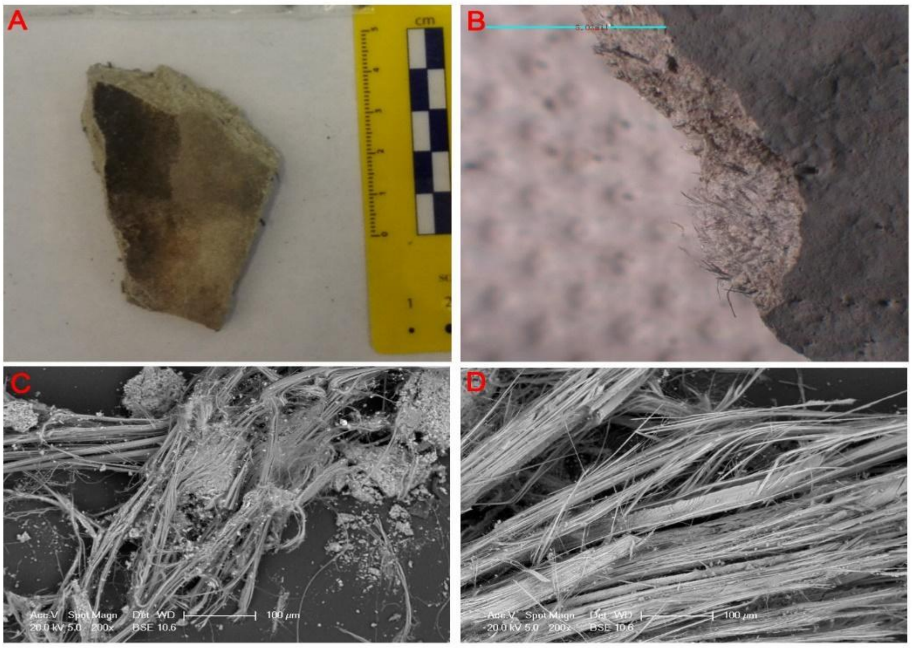

TEC 3

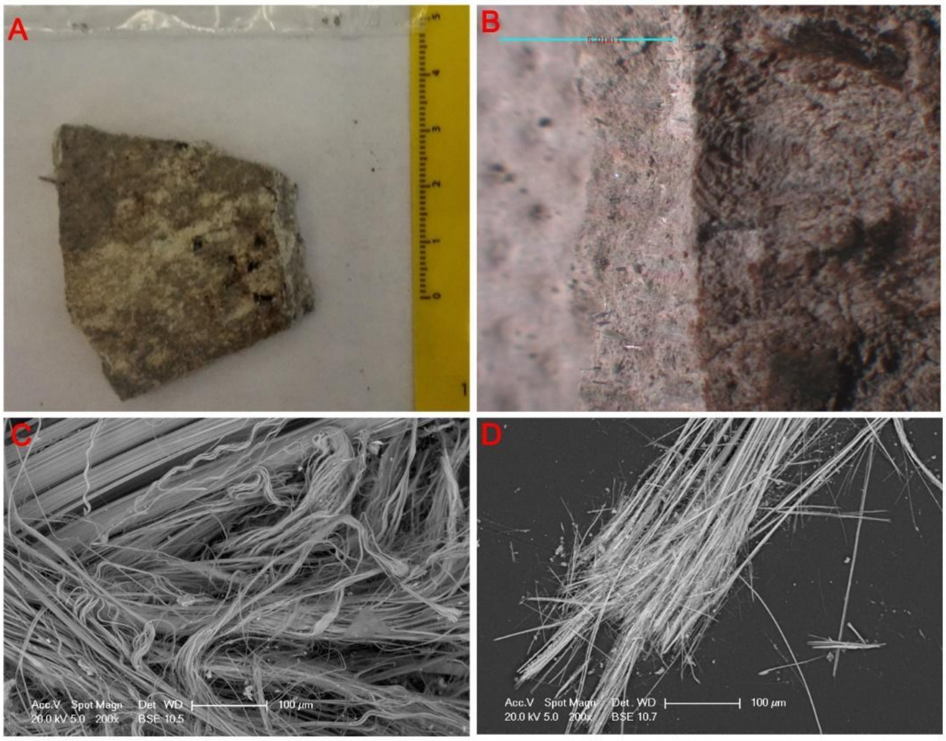
A
B
C
Acc.V Spot Magn Det WD 100 μm
20.0 kV 5.0 200x BSE 10.5
D
Acc.V Spot Magn Det WD 100 μm
20.0 kV 5.0 200x BSE 10.7

TEC 4

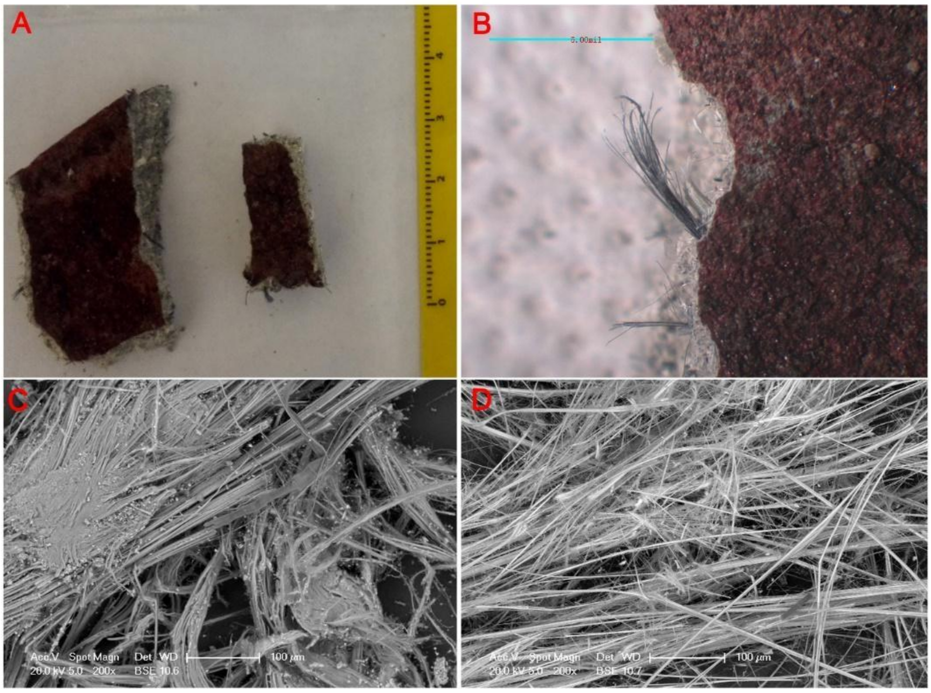
A
B
5.00mil
C
Acc.V Spot Magn Det WD 100 μm
20.0 kV 5.0 200x BSE 10.6
D
Acc.V Spot Magn Det WD 100 μm
20.0 kV 5.0 200x BSE 10.7

TEC 5

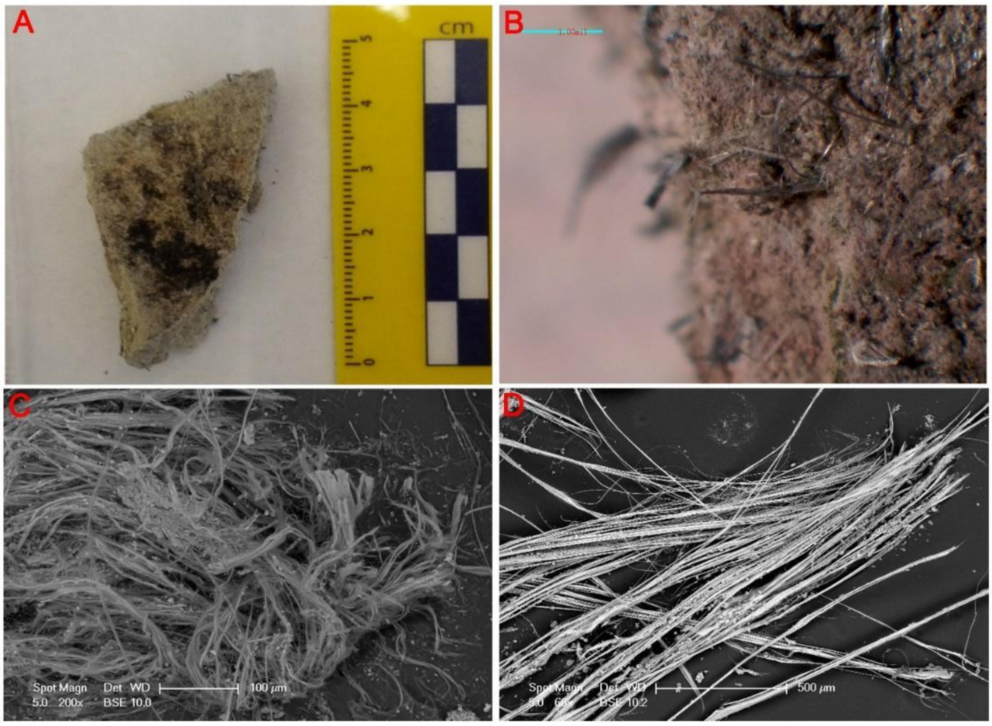
A
cm
0
1
2
3
4
5
B
C
Spot Magn Det WD 100 µm
5.0 200x BSE 10.0
D
Spot Magn Det WD 500 µm
5.0 66x BSE 10.2

TEC 6

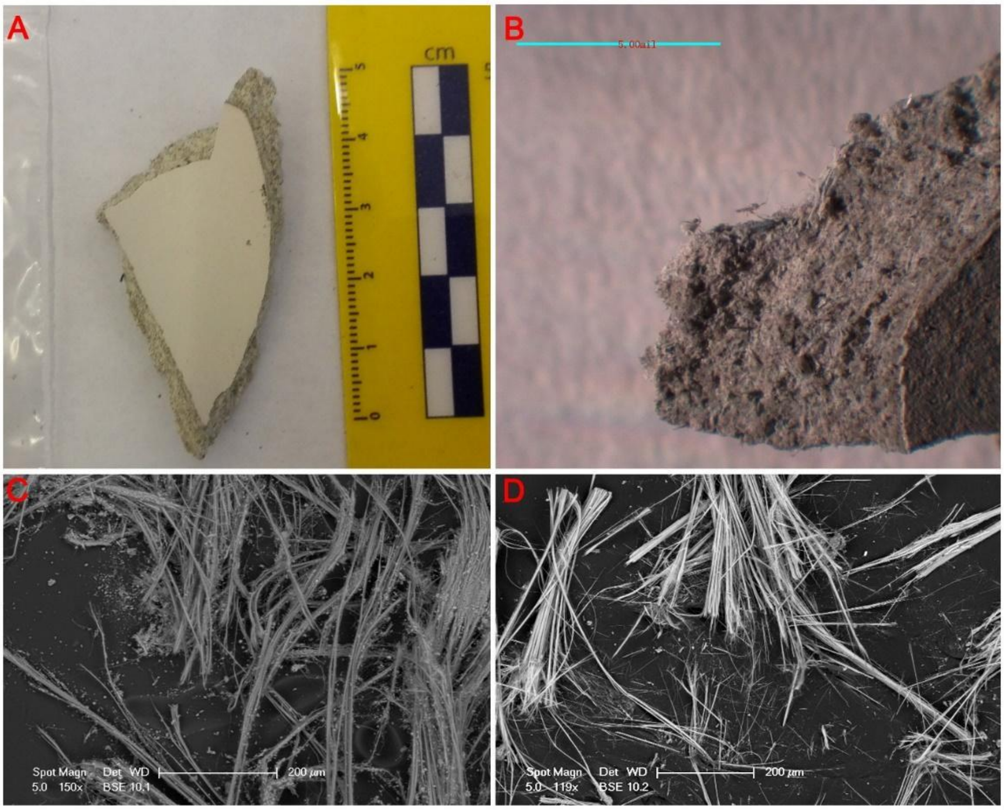
A
cm
0
1
2
3
4
5
B
5.00 mm
C
Spot Magn Det WD 200 µm
5.0 150x BSE 10.1
D
Spot Magn Det WD 200 µm
5.0 119x BSE 10.2

TEC 7

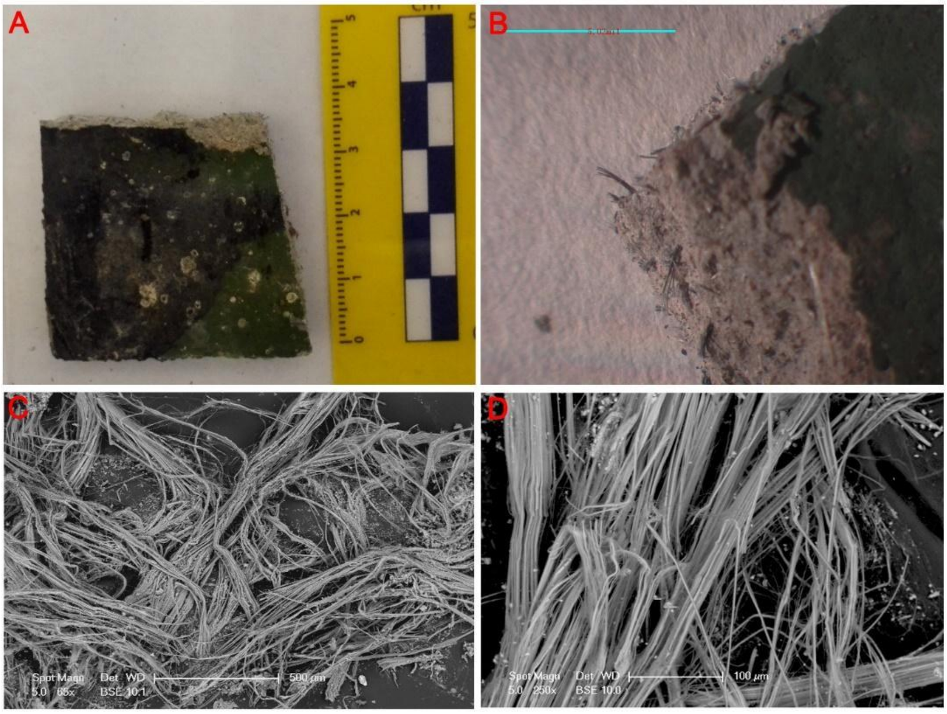
A
cm
B
C
Spot Magn Det WD 500 µm
5.0 65x BSE 10.1
D
Spot Magn Det WD 100 µm
5.0 250x BSE 10.0

TEC 8

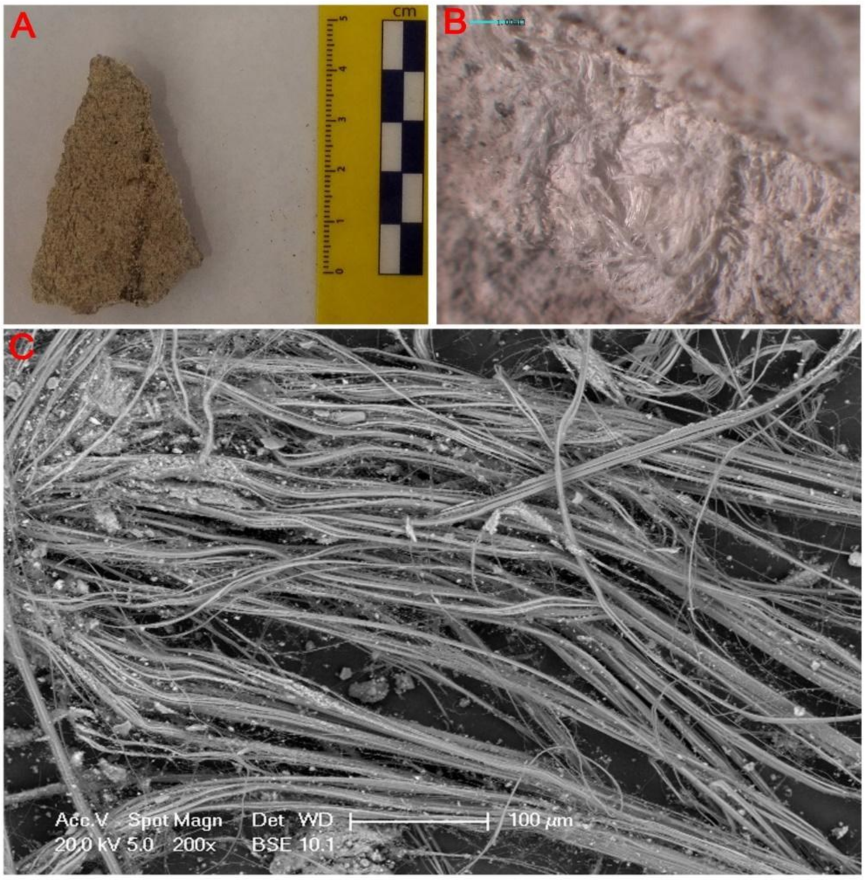
A
cm
B
C
Acc.V Spot Magn Det WD 100 µm
20.0 kV 5.0 200x BSE 10.1

TEC 9

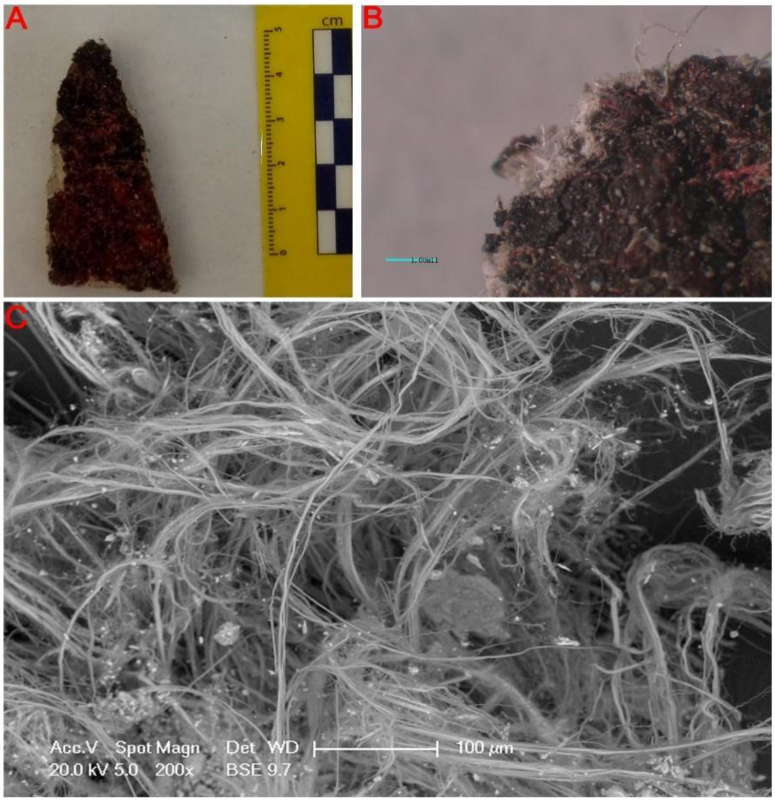
A
cm
B
C
Acc.V Spot Magn Det WD 100 µm
20.0 kV 5.0 200x BSE 9.7

TEC 10

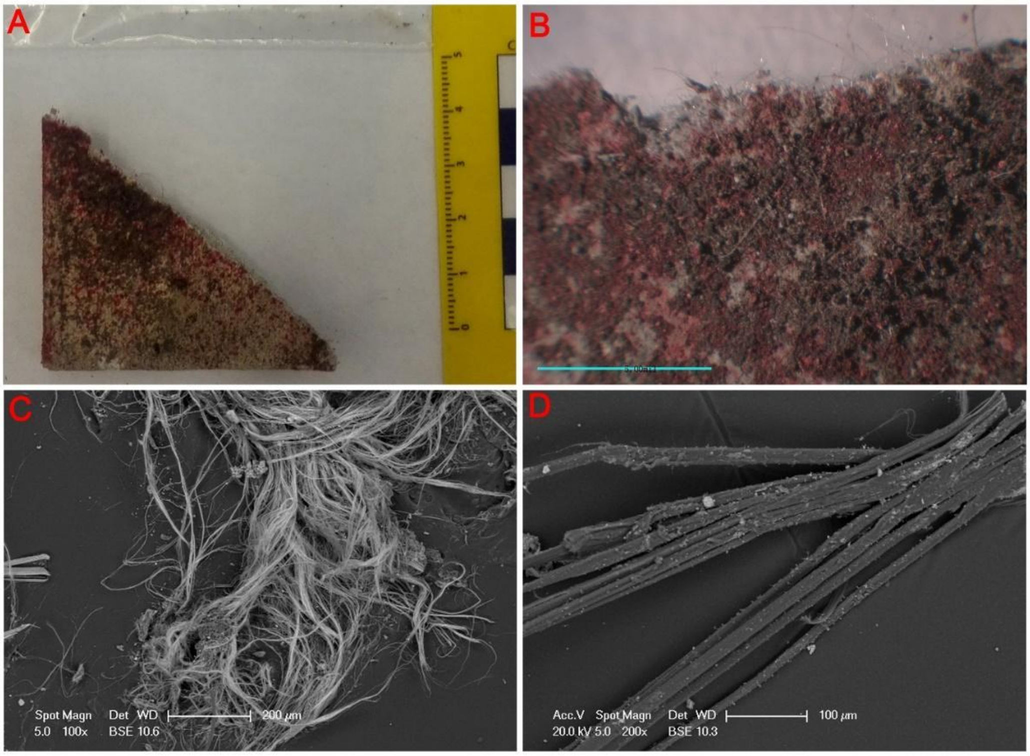
A
B
C
Spot Magn Det WD 200 µm
5.0 100x BSE 10.6
D
Acc.V Spot Magn Det WD 100 µm
20.0 kV 5.0 200x BSE 10.3

TEC 11

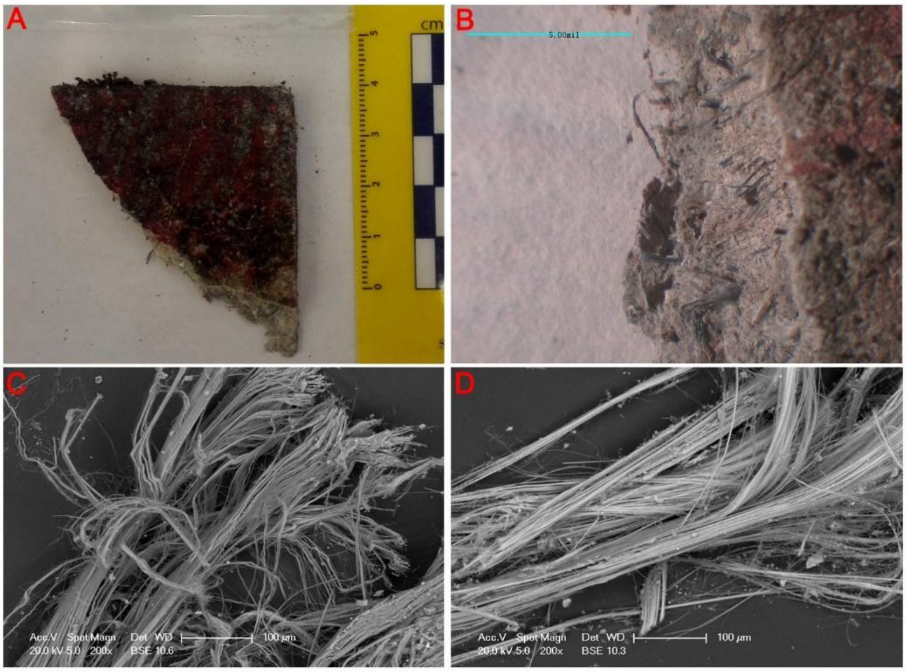
A
cm
B
5.00mil
C
Acc.V Spot Magn Det WD 100 µm
20.0 kV 5.0 200x BSE 10.6
D
Acc.V Spot Magn Det WD 100 µm
20.0 kV 5.0 200x BSE 10.3

TEC 12

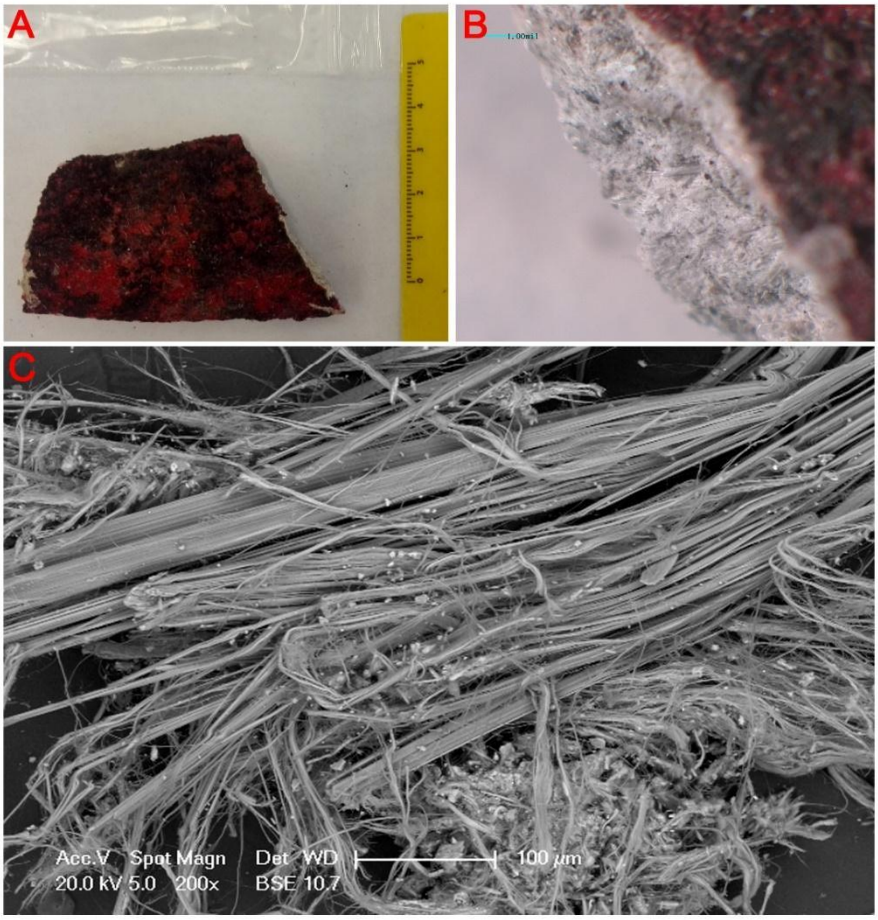
A
B
1.00mil
C
Acc.V Spot Magn Det WD 100 µm
20.0 kV 5.0 200x BSE 10.7

TEC 13

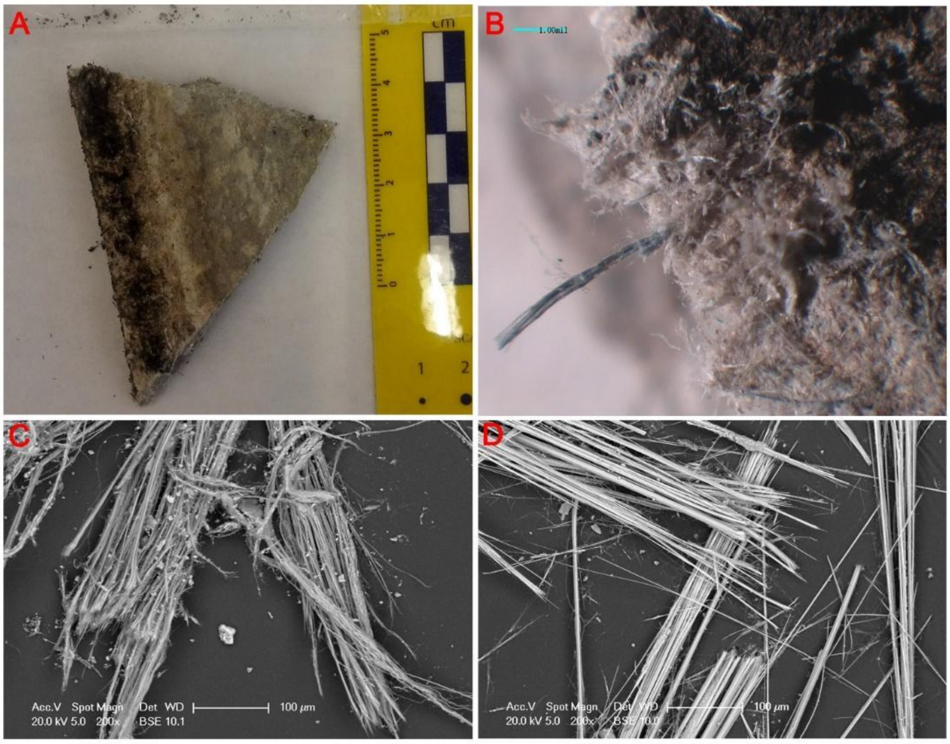
A
cm
B
1.00mil
C
Acc.V Spot Magn Det WD 100 µm
20.0 kV 5.0 200x BSE 10.1
D
Acc.V Spot Magn Det WD 100 µm
20.0 kV 5.0 200x BSE 10.2

TEC 14

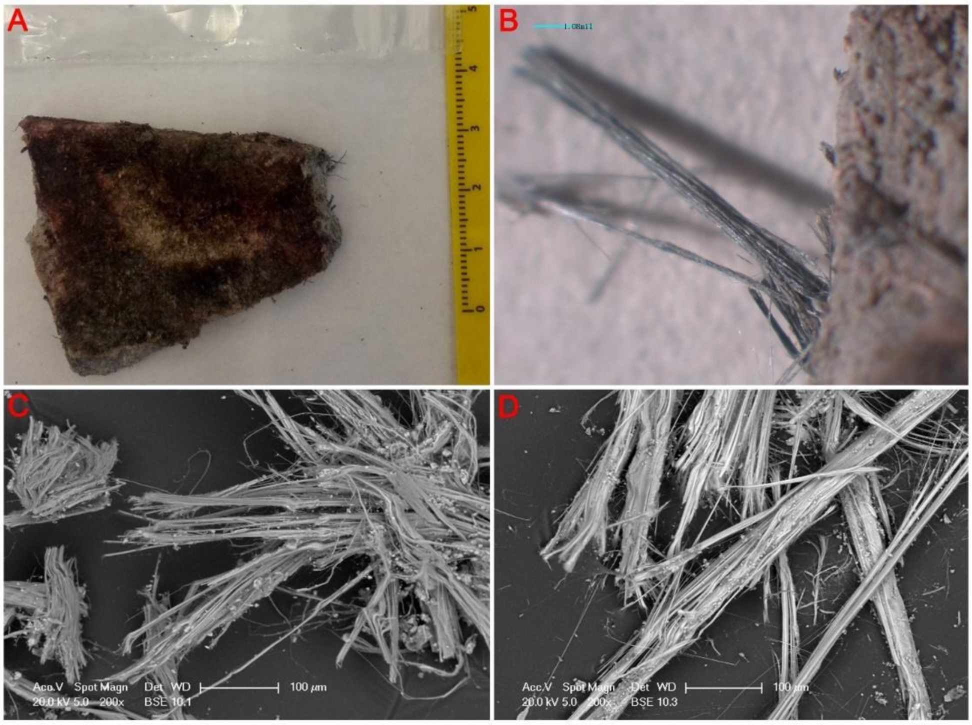
A
B
1.00mil
C
Acc.V Spot Magn Det WD 100 µm
20.0 kV 5.0 200x BSE 10.1
D
Acc.V Spot Magn Det WD 100 µm
20.0 kV 5.0 200x BSE 10.3

TEC 15

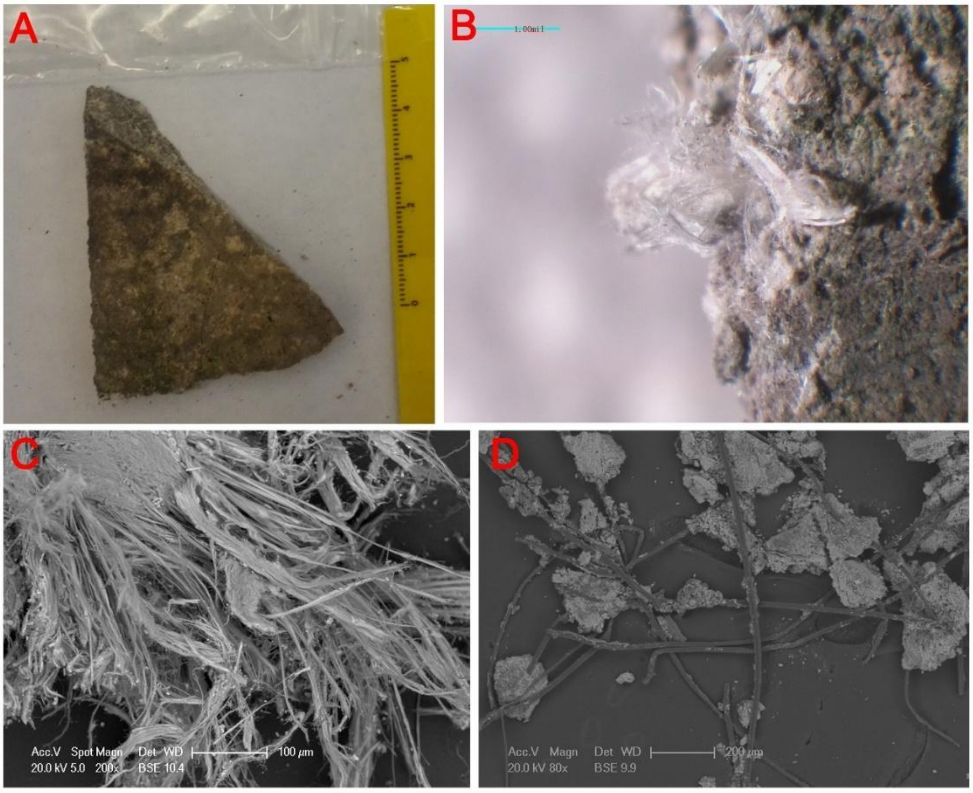
A
B
1.00mil
C
Acc.V Spot Magn Det WD 100 µm
20.0 kV 5.0 200x BSE 10.4
D
Acc.V Magn Det WD 200 µm
20.0 kV 80x BSE 9.9

TEC 16

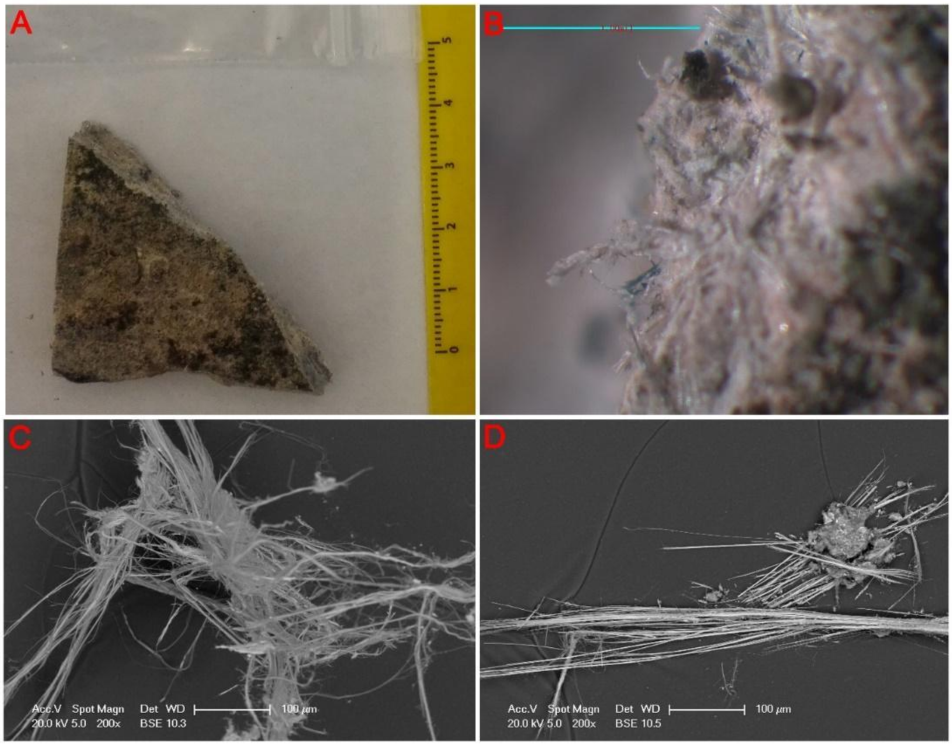
A
B
C
Acc.V Spot Magn Det WD 100 µm
20.0 kV 5.0 200x BSE 10.3
D
Acc.V Spot Magn Det WD 100 µm
20.0 kV 5.0 200x BSE 10.5

TEC 17

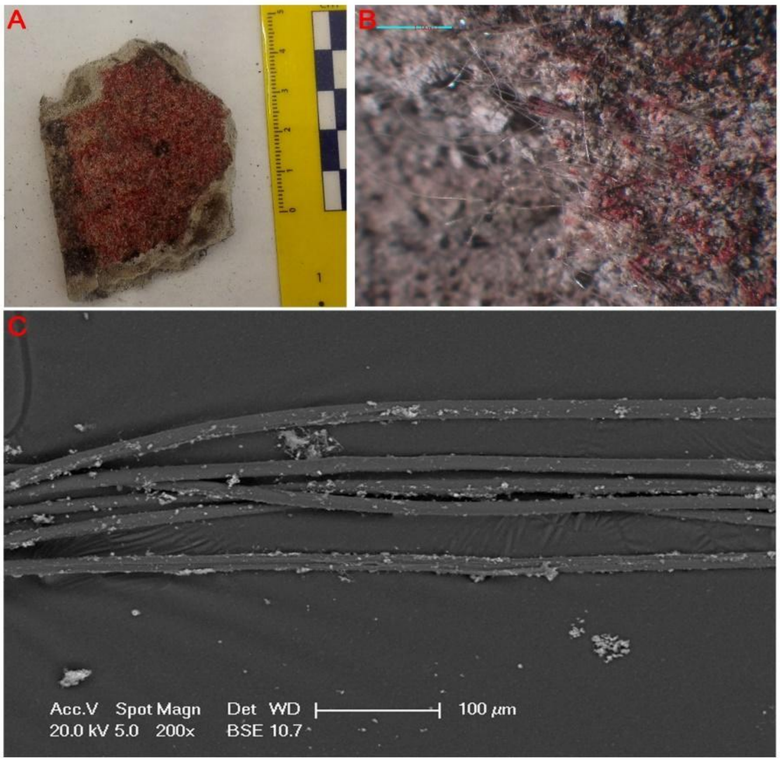
A
B
C
Acc.V Spot Magn Det WD 100 µm
20.0 kV 5.0 200x BSE 10.7

TEC 18

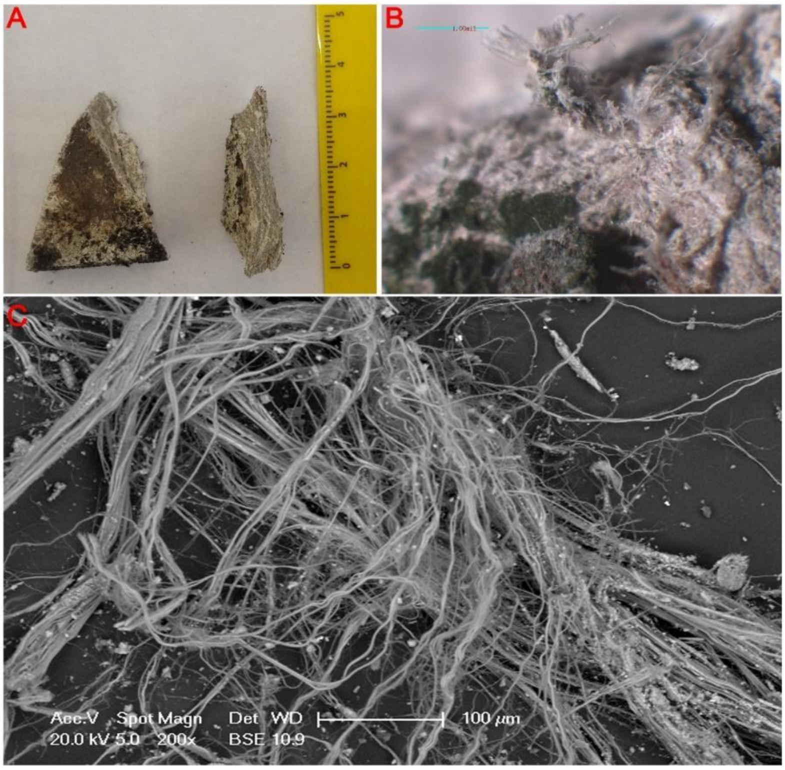
A
B
C
Acc.V Spot Magn Det WD 100 µm
20.0 kV 5.0 200x BSE 10.9

TEC 19

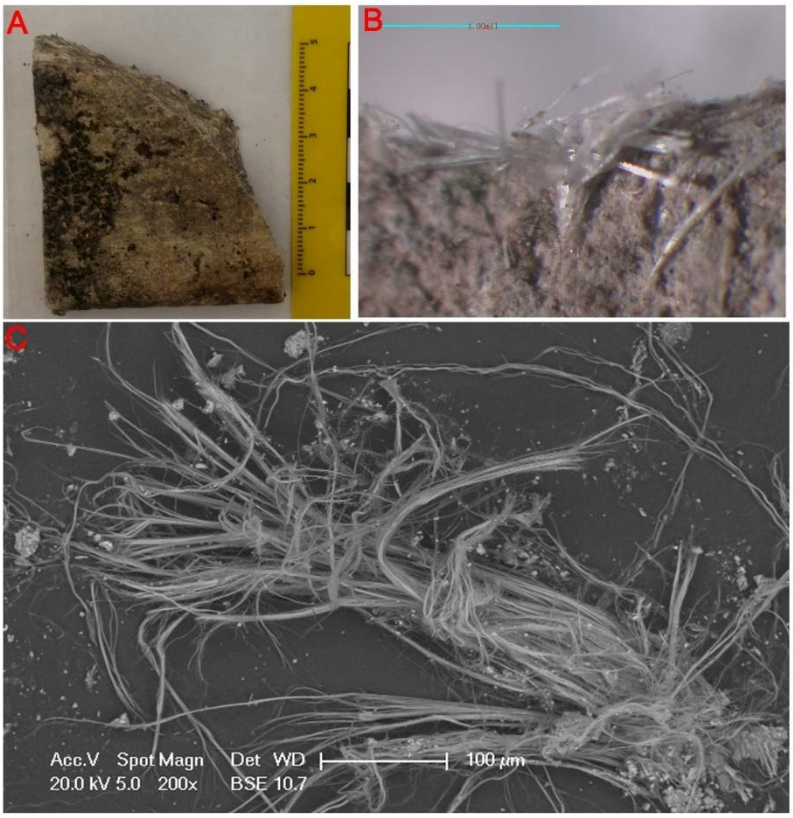
A
B
C
Acc.V Spot Magn Det WD 100 µm
20.0 kV 5.0 200x BSE 10.7

TEC 20

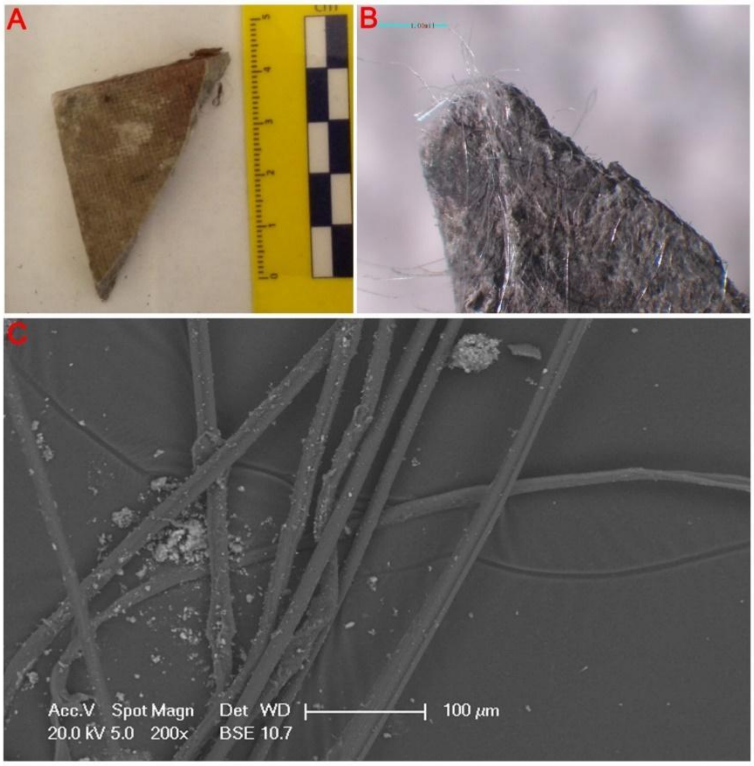
A
B
C
Acc.V Spot Magn Det WD 100 µm
20.0 kV 5.0 200x BSE 10.7

TEC 21

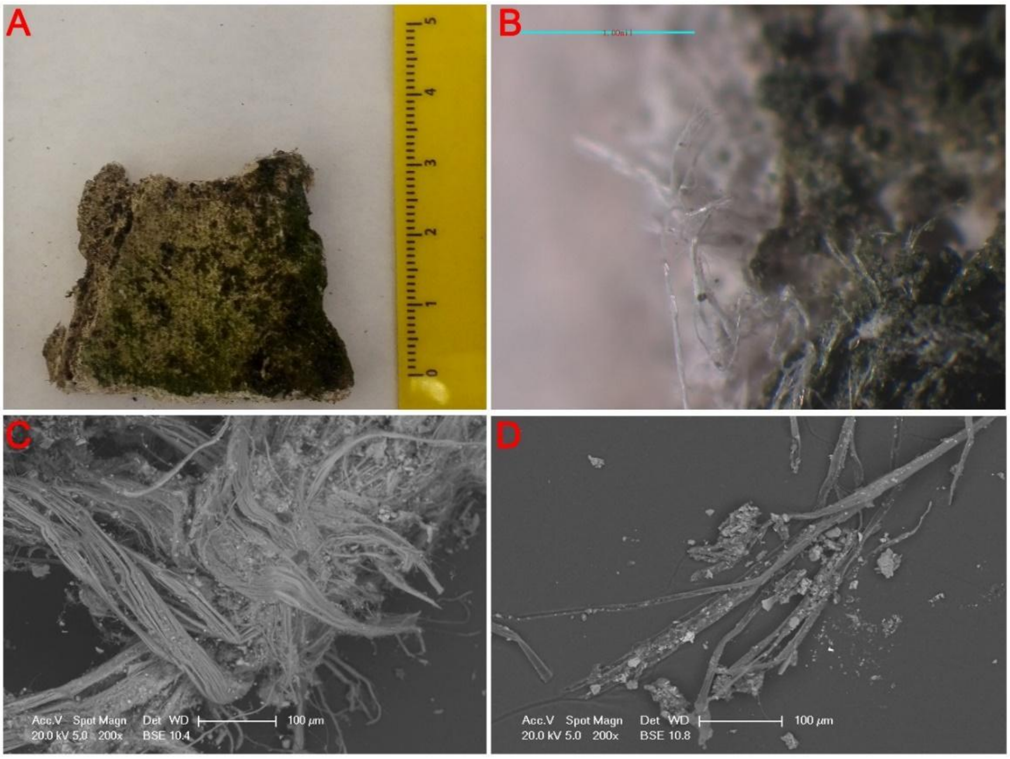
A
B
C
D
Acc.V Spot Magn Det WD 100 µm
20.0 kV 5.0 200x BSE 10.4
Acc.V Spot Magn Det WD 100 µm
20.0 kV 5.0 200x BSE 10.8

TEC 22

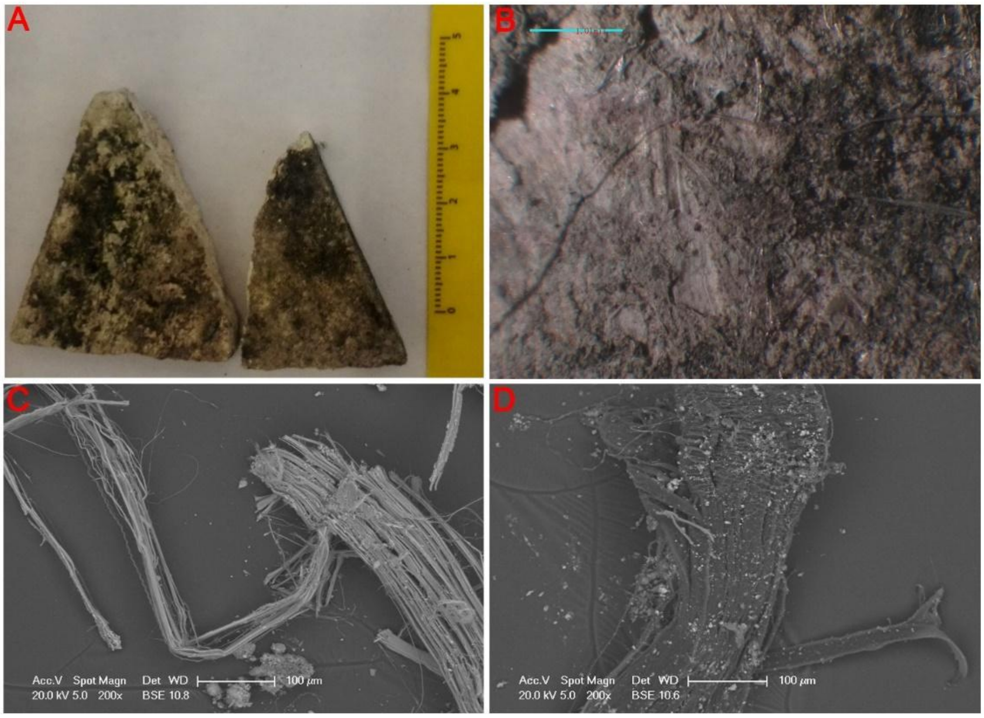
A
B
C
D
Acc.V Spot Magn Det WD 100 µm
20.0 kV 5.0 200x BSE 10.8
Acc.V Spot Magn Det WD 100 µm
20.0 kV 5.0 200x BSE 10.6

ISA 1

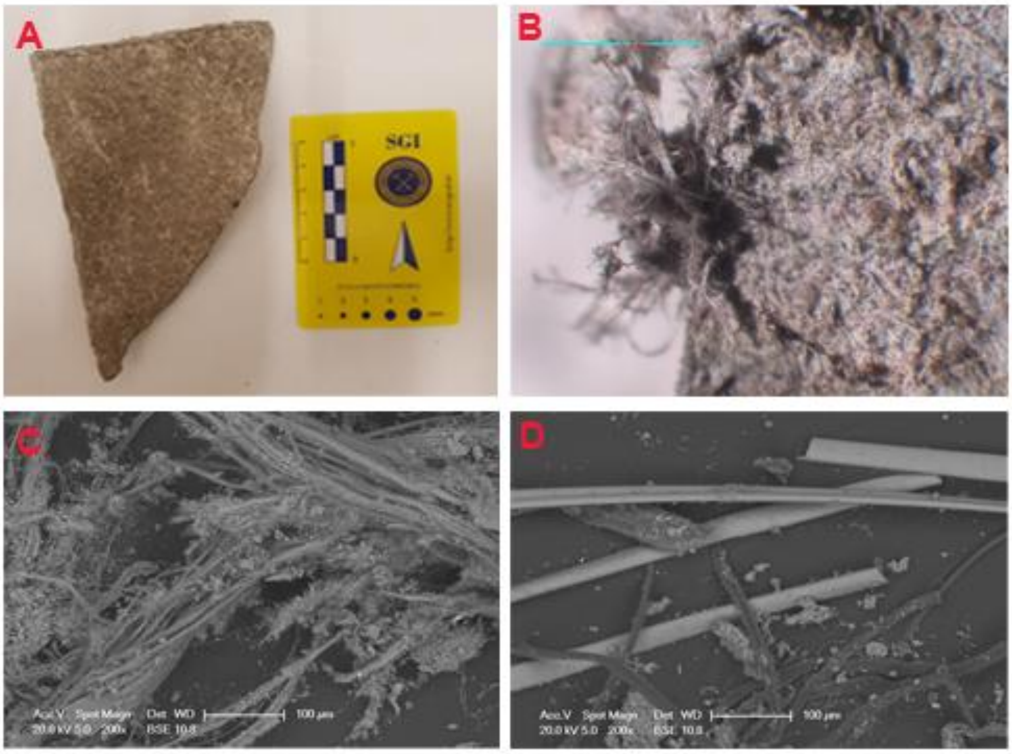
A
SGI
B
C
Acc.V Spot Magn Det WD 100 µm
20.0 kV 5.0 200x BSE 10.8
D
Acc.V Spot Magn Det WD 100 µm
20.0 kV 5.0 200x BSE 10.8

ISA 2

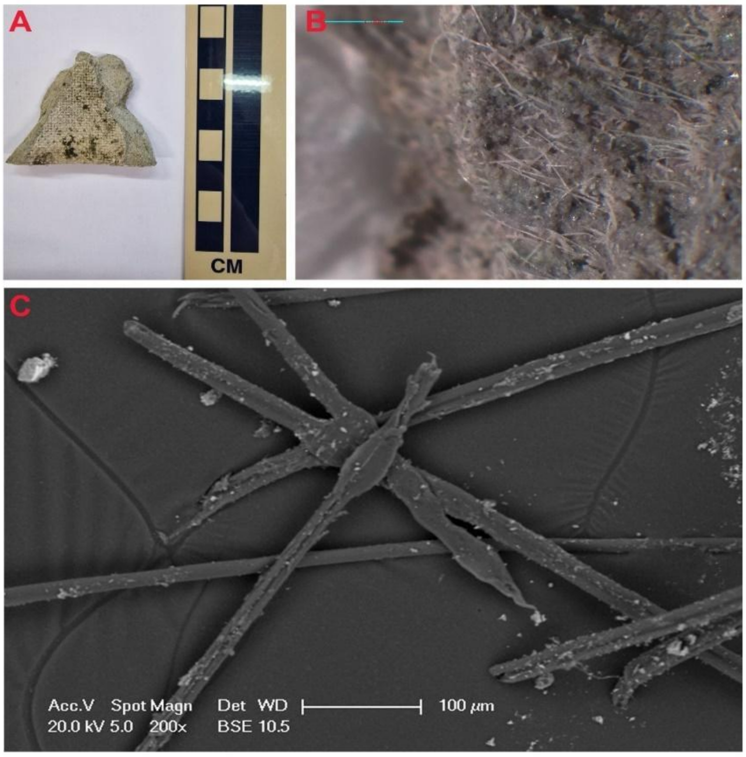
A
CM
B
C
Acc.V Spot Magn Det WD 100 µm
20.0 kV 5.0 200x BSE 10.5

ISA 3

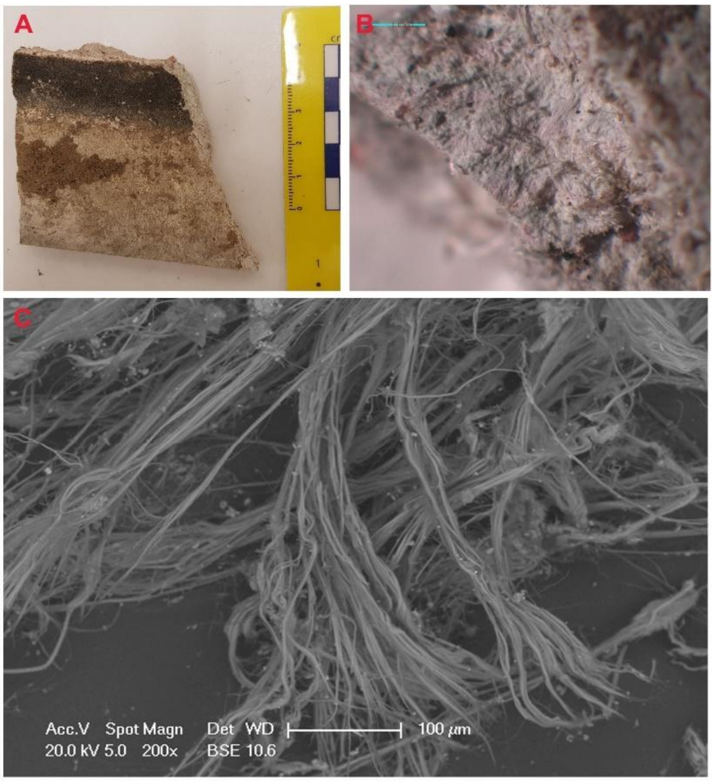
A
cm
B
C
Acc.V Spot Magn Det WD 100 µm
20.0 kV 5.0 200x BSE 10.6

ISA 4

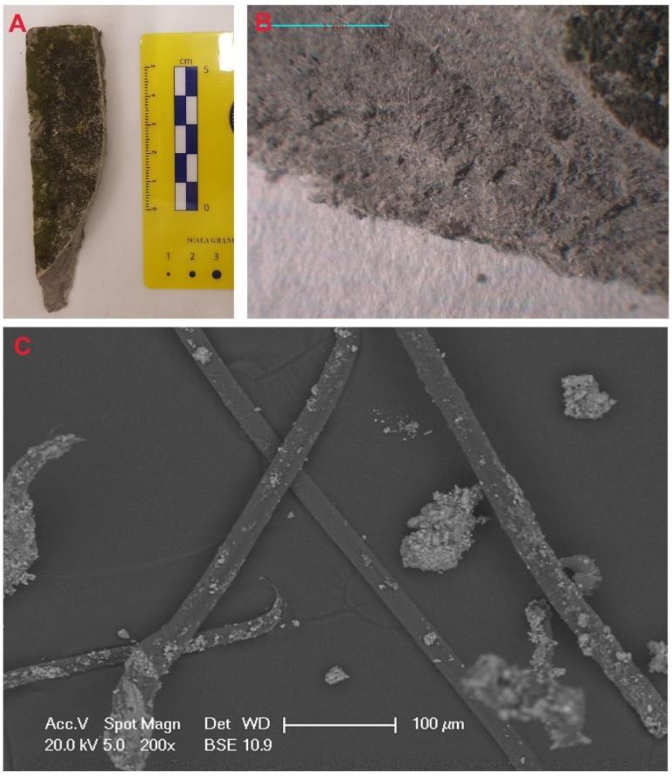
A
cm
B
C
Acc.V Spot Magn Det WD 100 µm
20.0 kV 5.0 200x BSE 10.9

Hereafter I report some EDS analyses made on selected fibers of chrysotile and crocidolite.

An1 Chrysotile

```
Elem    Wt %  Mol % K-Ratio   Z     A     F
-------------------------------------------------------------
MgO   44.23  55.15  0.1047  0.9835  0.5932  1.0043
Al2O3    4.14   2.04  0.0071  0.9546  0.4823  1.0065
SiO2   48.89  40.89  0.0907  0.9824  0.5982  1.0000
FeO    2.75   1.92  0.0130  0.8658  1.0033  1.0000
Total  100.00 100.00

Oxygen By Diff.

Elem    Wt %  Chem K-Ratio   Z     A     F
-------------------------------------------------------------
MgK   26.68   2.66  0.1047  0.9835  0.5932  1.0043
AlK    2.19   0.20  0.0071  0.9546  0.4823  1.0065
SiK   22.85   1.97  0.0907  0.9824  0.5982  1.0000
FeK    2.14   0.09  0.0130  0.8658  1.0033  1.0000
Oxygen  46.15   7.00
```

An2 Crocidolite

```
Elem    Wt %  Mol % K-Ratio   Z     A     F
-------------------------------------------------------------
Na2O    8.84   8.86  0.0141  0.9815  0.2926  1.0024
MgO    3.78   5.84  0.0067  1.0061  0.3852  1.0043
Al2O3    0.54   0.33  0.0011  0.9765  0.5075  1.0083
SiO2   57.13  59.12  0.1260  1.0049  0.6385  1.0005
CaO    0.55   0.61  0.0027  0.9771  0.9231  1.0119
FeO   29.15  25.23  0.1519  0.8886  1.0024  1.0000
Total  100.00 100.00

Oxygen By Diff.

Elem    Wt %  Chem K-Ratio   Z     A     F
-------------------------------------------------------------
NaK    6.55   2.55  0.0141  0.9815  0.2926  1.0024
MgK    2.28   0.84  0.0067  1.0061  0.3852  1.0043
AlK   0.29   0.10  0.0011  0.9765  0.5075  1.0083
SiK   26.71   8.51  0.1260  1.0049  0.6385  1.0005
CaK    0.40   0.09  0.0027  0.9771  0.9231  1.0119
FeK   22.66   3.63  0.1519  0.8886  1.0024  1.0000
Oxygen  41.11  23.00
```

An3 Chrysotile

```
Elem    Wt %  Mol % K-Ratio   Z     A     F
-------------------------------------------------------------
Na2O    1.30   1.04  0.0028  0.9594  0.4330  1.0071
MgO   45.03  55.48  0.1037  0.9835  0.5839  1.0040
Al2O3    1.67   0.81  0.0028  0.9546  0.4746  1.0065
SiO2   48.75  40.29  0.0900  0.9825  0.6005  1.0001
CaO    0.63   0.55  0.0027  0.9535  0.9232  1.0011
FeO    2.63   1.82  0.0123  0.8658  1.0029  1.0000
Total  100.00 100.00

Oxygen By Diff.

Elem    Wt %  Chem K-Ratio   Z     A     F
-------------------------------------------------------------
NaK    0.96   0.10  0.0028  0.9594  0.4330  1.0071
MgK   27.16   2.74  0.1037  0.9835  0.5839  1.0040
AlK    0.88   0.08  0.0028  0.9546  0.4746  1.0065
SiK   22.79   1.99  0.0900  0.9825  0.6005  1.0001
CaK    0.45   0.03  0.0027  0.9535  0.9232  1.0011
FeK    2.04   0.09  0.0123  0.8658  1.0029  1.0000
Oxygen  45.72   7.00
```

An4 Crocidolite

```
Elem    Wt %  Mol % K-Ratio   Z     A     F
-------------------------------------------------------------
Na2O    6.59   6.66  0.0092  0.9846  0.2779  1.0023
MgO    3.55   5.52  0.0056  1.0093  0.3775  1.0041
Al2O3    0.64   0.39  0.0012  0.9796  0.5003  1.0079
SiO2   55.13  57.51  0.1092  1.0081  0.6309  1.0005
CaO    0.70   0.78  0.0032  0.9804  0.9235  1.0136
FeO   33.39  29.13  0.1587  0.8919  1.0023  1.0000
Total  100.00 100.00

Oxygen By Diff.
```

```
Elem    Wt %  Chem K-Ratio   Z     A     F
-----------------------------------------------------------
NaK   4.89   1.94  0.0092  0.9846  0.2779  1.0023
MgK   2.14   0.80  0.0056  1.0093  0.3775  1.0041
AlK   0.34   0.11  0.0012  0.9796  0.5003  1.0079
SiK  25.77   8.36  0.1092  1.0081  0.6309  1.0005
CaK   0.50   0.11  0.0032  0.9804  0.9235  1.0136
FeK  25.96   4.23  0.1587  0.8919  1.0023  1.0000
Oxygen  40.40  23.00
```

An5 Chrysotile

```
Elem    Wt %  Mol % K-Ratio   Z     A     F
-----------------------------------------------------------
Na2O   1.31   1.04  0.0033  0.9585  0.4423  1.0074
MgO   46.35  56.67  0.1271  0.9826  0.5940  1.0040
Al2O3   1.60   0.77  0.0031  0.9537  0.4740  1.0064
SiO2  48.36  39.67  0.1042  0.9816  0.6002  1.0001
CaO    1.10   0.97  0.0055  0.9525  0.9236  1.0005
FeO    1.29   0.88  0.0069  0.8649  1.0026  1.0000
Total  100.00 100.00
Oxygen By Diff.

Elem    Wt %  Chem K-Ratio   Z     A     F
-----------------------------------------------------------
NaK   0.97   0.10  0.0033  0.9585  0.4423  1.0074
MgK  27.95   2.81  0.1271  0.9826  0.5940  1.0040
AlK   0.85   0.08  0.0031  0.9537  0.4740  1.0064
SiK  22.60   1.97  0.1042  0.9816  0.6002  1.0001
CaK   0.79   0.05  0.0055  0.9525  0.9236  1.0005
FeK   1.00   0.04  0.0069  0.8649  1.0026  1.0000
Oxygen  45.84   7.00
```

An6 Crocidolite

```
Elem    Wt %  Mol % K-Ratio   Z     A     F
-----------------------------------------------------------
Na2O   9.12   9.06  0.0130  0.9800  0.2989  1.0024
MgO    3.67   5.61  0.0058  1.0046  0.3912  1.0043
Al2O3   0.62   0.37  0.0011  0.9750  0.5147  1.0083
SiO2  54.55  55.91  0.1057  1.0034  0.6453  1.0009
CaO    6.58   7.22  0.0285  0.9756  0.9276  1.0100
FeO   25.47  21.83  0.1155  0.8872  0.9979  1.0000
Total  100.00 100.00
```

```
Oxygen By Diff.

Elem    Wt %  Chem K-Ratio   Z     A     F
-----------------------------------------------------------
NaK   6.77   2.66  0.0130  0.9800  0.2989  1.0024
MgK   2.21   0.82  0.0058  1.0046  0.3912  1.0043
AlK   0.33   0.11  0.0011  0.9750  0.5147  1.0083
SiK  25.50   8.21  0.1057  1.0034  0.6453  1.0009
CaK   4.70   1.06  0.0285  0.9756  0.9276  1.0100
FeK  19.80   3.20  0.1155  0.8872  0.9979  1.0000
Oxygen  40.70  23.00
```

An7 Crocidolite

```
Elem    Wt %  Mol % K-Ratio   Z     A     F
-----------------------------------------------------------
Na2O   8.20   8.12  0.0124  0.9790  0.3021  1.0027
MgO    5.55   8.45  0.0093  1.0035  0.3985  1.0045
Al2O3   0.72   0.43  0.0013  0.9740  0.5137  1.0086
SiO2  58.23  59.44  0.1177  1.0023  0.6437  1.0005
CaO    1.13   1.23  0.0051  0.9744  0.9230  1.0106
FeO   26.16  22.33  0.1247  0.8860  1.0019  1.0000
Total  100.00 100.00

Oxygen By Diff.

Elem    Wt %  Chem K-Ratio   Z     A     F
-----------------------------------------------------------
NaK   6.09   2.33  0.0124  0.9790  0.3021  1.0027
MgK   3.35   1.21  0.0093  1.0035  0.3985  1.0045
AlK   0.38   0.12  0.0013  0.9740  0.5137  1.0086
SiK  27.22   8.53  0.1177  1.0023  0.6437  1.0005
CaK   0.81   0.18  0.0051  0.9744  0.9230  1.0106
FeK  20.33   3.20  0.1247  0.8860  1.0019  1.0000
Oxygen  41.82  23.00
```

An8 Chrysotile

```
Elem    Wt %  Mol % K-Ratio   Z     A     F
-----------------------------------------------------------
Na2O   0.86   0.70  0.0011  0.9601  0.4236  1.0067
MgO   41.14  51.87  0.0552  0.9842  0.5773  1.0044
Al2O3   3.39   1.69  0.0035  0.9553  0.4873  1.0068
SiO2  50.46  42.68  0.0553  0.9832  0.6061  1.0001
CaO    0.63   0.57  0.0017  0.9542  0.9226  1.0014
FeO    3.51   2.49  0.0100  0.8666  1.0028  1.0000
Total  100.00 100.00
```

```
Oxygen By Diff.

Elem     Wt %  Chem K-Ratio    Z       A       F
------------------------------------------------------------
NaK    0.64   0.07  0.0011  0.9601  0.4236  1.0067
MgK   24.81   2.49  0.0552  0.9842  0.5773  1.0044
AlK    1.80   0.16  0.0035  0.9553  0.4873  1.0068
SiK   23.59   2.05  0.0553  0.9832  0.6061  1.0001
CaK    0.45   0.03  0.0017  0.9542  0.9226  1.0014
FeK    2.73   0.12  0.0100  0.8666  1.0028  1.0000
Oxygen  45.98   7.00
```

Hereafter some SEM/BSE additionally images on the 4 Inert samples with the EDS analises

INERT 1

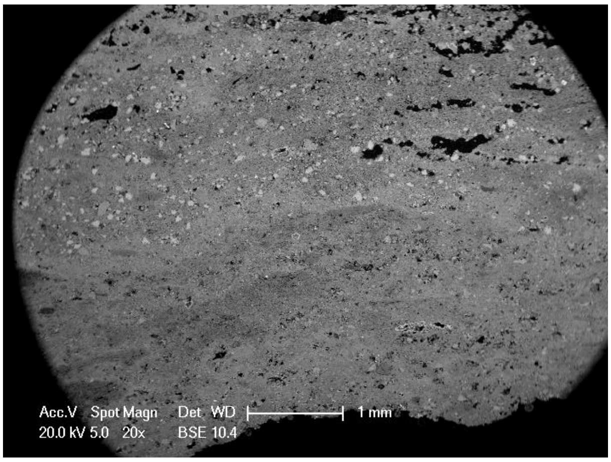

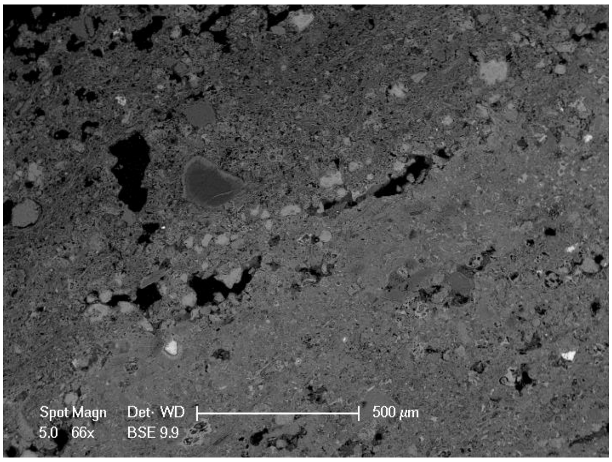

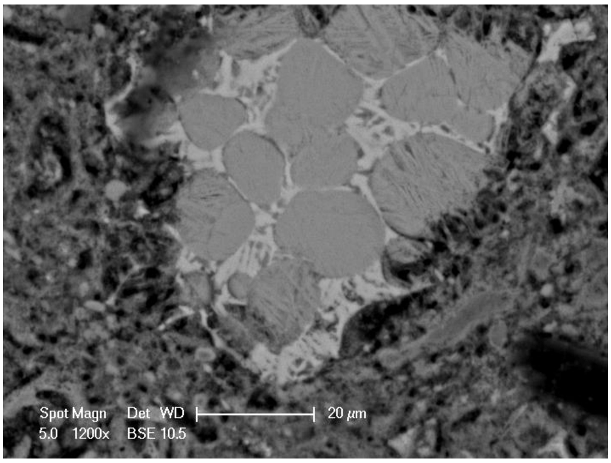

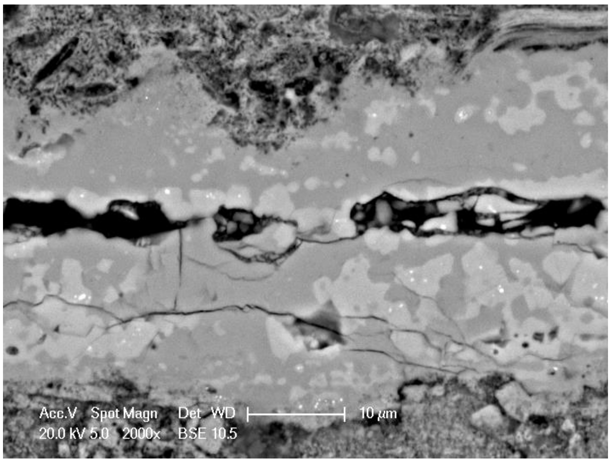

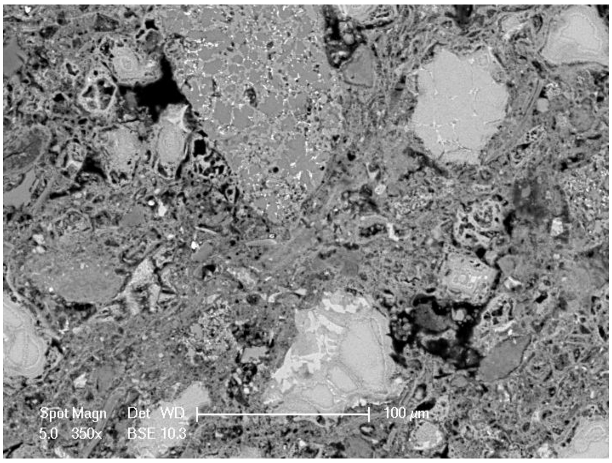

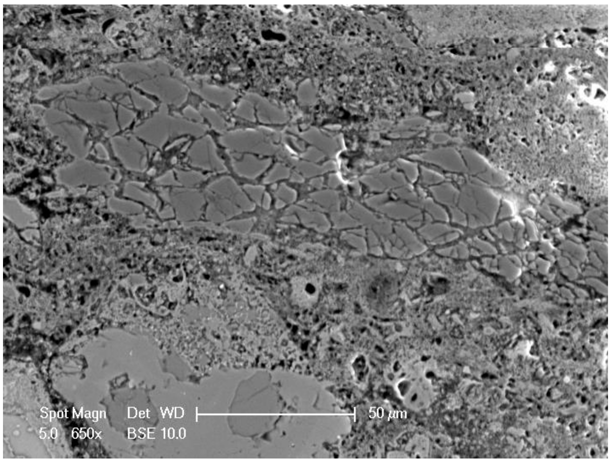

An1 larnite

```
Elem    Wt %  Chem K-Ratio   Z     A     F
MgK   0.52   0.04  0.0009  0.9954  0.4625  1.0047
AlK   1.34   0.09  0.0030  0.9660  0.6064  1.0087
SiK  15.23   0.94  0.0413  0.9941  0.7228  1.0062
K K   0.30   0.01  0.0011  0.9450  0.9453  1.0892
CaK  45.50   1.96  0.1595  0.9670  0.9685  1.0000
Oxygen  37.11   4.00

Elem    Wt %  Chem K-Ratio   Z     A     F
-----------------------------------------------------------
MgK   0.41   0.03  0.0008  0.9954  0.4625  1.0047
AlK   1.27   0.08  0.0030  0.9660  0.6076  1.0088
SiK  15.43   0.95  0.0434  0.9941  0.7245  1.0062
K K   0.43   0.02  0.0017  0.9450  0.9451  1.0884
CaK  45.31   1.95  0.1643  0.9670  0.9677  1.0000
Oxygen  37.15   4.00
```

An2 bulk porous matrix

```
Elem    Wt %  Mol % K-Ratio   Z     A     F
MgO   5.45   8.11  0.0155  0.9964  0.4713  1.0051
Al2O3  11.97   7.04  0.0363  0.9670  0.5885  1.0071
SiO2  32.27  32.22  0.0996  0.9951  0.6608  1.0041
K2O   0.23   0.15  0.0018  0.9455  0.9277  1.0587
CaO  45.44  48.61  0.3008  0.9676  0.9556  1.0015
FeO   4.64   3.87  0.0308  0.8799  0.9693  1.0000
Total  100.00 100.00
```

An3 bulk compact matrix

```
Elem    Wt %  Mol % K-Ratio   Z     A     F
MgO   5.52   7.99  0.0153  0.9980  0.4588  1.0043
Al2O3   7.63   4.37  0.0227  0.9686  0.5765  1.0067
SiO2  25.41  24.69  0.0799  0.9967  0.6712  1.0054
K2O   0.51   0.32  0.0041  0.9474  0.9415  1.0792
CaO  57.45  59.80  0.3846  0.9695  0.9651  1.0011
FeO   3.48   2.83  0.0229  0.8819  0.9608  1.0000
Total  100.00 100.00
```

An4 bulk matrix

```
Elem    Wt %  Mol % K-Ratio   Z     A     F
MgO   7.63  11.16  0.0218  0.9962  0.4729  1.0048
Al2O3  10.63   6.15  0.0317  0.9668  0.5782  1.0069
SiO2  31.04  30.48  0.0954  0.9950  0.6584  1.0041
K2O   0.34   0.21  0.0026  0.9453  0.9289  1.0597
CaO  46.03  48.43  0.3047  0.9675  0.9561  1.0014
FeO   4.35   3.57  0.0288  0.8798  0.9689  1.0000
Total  100.00 100.00
```

An5 glass around ex croc

```
Elem    Wt %  Mol % K-Ratio   Z     A     F
-----------------------------------------------------------
Na2O   3.06   2.95  0.0031  0.9759  0.3064  1.0025
MgO   3.82   5.67  0.0046  1.0003  0.4288  1.0046
Al2O3   2.15   1.26  0.0029  0.9709  0.5543  1.0084
SiO2  45.26  45.01  0.0636  0.9991  0.6764  1.0029
K2O   0.38   0.24  0.0013  0.9494  0.9131  1.0390
CaO  30.69  32.70  0.0927  0.9716  0.9437  1.0050
MnO   0.30   0.26  0.0009  0.8677  0.9696  1.0000
FeO  14.33  11.92  0.0444  0.8837  0.9797  1.0000
Total  100.00 100.00
```

An6 olivine kst

```
Elem    Wt %  Mol % K-Ratio   Z     A     F
-----------------------------------------------------------
Na2O   0.64   0.63  0.0005  0.9849  0.2707  1.0020
MgO   4.02   6.05  0.0034  1.0096  0.3941  1.0036
Al2O3   2.37   1.41  0.0023  0.9798  0.5169  1.0065
SiO2  35.65  35.99  0.0369  1.0082  0.6401  1.0030
K2O   0.00   0.00  0.0000  0.9590  0.9167  1.0434
CaO  31.73  34.32  0.0753  0.9813  0.9480  1.0088
MnO   0.18   0.16  0.0004  0.8767  0.9695  1.0000
FeO  25.40  21.44  0.0606  0.8930  0.9795  1.0000
Total  100.00 100.00

lem    Wt %  Chem K-Ratio   Z     A     F
-----------------------------------------------------------
NaK   0.48   0.04  0.0005  0.9849  0.2707  1.0020
MgK   2.42   0.17  0.0034  1.0096  0.3941  1.0036
AlK   1.26   0.08  0.0023  0.9798  0.5169  1.0065
```

```
SiK  16.66  1.04 0.0369 1.0082 0.6401 1.0030
K K   0.00  0.00 0.0000 0.9590 0.9167 1.0434
CaK  22.68  0.99 0.0753 0.9813 0.9480 1.0088
MnK   0.14  0.00 0.0004 0.8767 0.9695 1.0000
FeK  19.74  0.62 0.0606 0.8930 0.9795 1.0000
Oxygen 36.61  4.00
```

An7 glass ex croc

```
Elem    Wt % Mol % K-Ratio   Z     A     F
-----------------------------------------------------------
Na2O  12.17 12.56 0.0136 0.9793 0.3212 1.0025
MgO   2.00  3.17 0.0024 1.0039 0.4013 1.0046
Al2O3   0.82  0.52 0.0011 0.9743 0.5336 1.0088
SiO2  53.07 56.50 0.0773 1.0027 0.6626 1.0017
K2O   9.65  6.55 0.0339 0.9524 0.8972 1.0076
CaO   3.44  3.92 0.0107 0.9747 0.8966 1.0064
MnO   0.19  0.17 0.0006 0.8703 0.9864 1.0000
FeO  18.65 16.60 0.0624 0.8863 0.9931 1.0000
Total 100.00 100.00
```

An8 px

```
Elem    Wt % Mol % K-Ratio   Z     A     F
-----------------------------------------------------------
Na2O   1.06  1.02 0.0011 0.9762 0.3007 1.0028
MgO   5.36  7.95 0.0067 1.0006 0.4313 1.0048
Al2O3   0.85  0.50 0.0012 0.9711 0.5488 1.0092
SiO2  53.09 52.87 0.0771 0.9994 0.6771 1.0020
K2O   0.43  0.27 0.0015 0.9496 0.9017 1.0264
CaO  20.17 21.53 0.0633 0.9718 0.9347 1.0068
MnO   0.31  0.26 0.0010 0.8678 0.9789 1.0000
FeO  18.74 15.60 0.0607 0.8838 0.9871 1.0000
Total 100.00 100.00

Elem    Wt % Chem K-Ratio   Z     A     F
-----------------------------------------------------------
NaK   0.78  0.08 0.0011 0.9762 0.3007 1.0028
MgK   3.23  0.31 0.0067 1.0006 0.4313 1.0048
AlK   0.45  0.04 0.0012 0.9711 0.5488 1.0092
SiK  24.82  2.06 0.0771 0.9994 0.6771 1.0020
K K   0.35  0.02 0.0015 0.9496 0.9017 1.0264
CaK  14.42  0.84 0.0633 0.9718 0.9347 1.0068
MnK   0.24  0.01 0.0010 0.8678 0.9789 1.0000
FeK  14.56  0.61 0.0607 0.8838 0.9871 1.0000
Oxygen 41.14  6.00
```

An9 olivine

```
Elem    Wt % Mol % K-Ratio   Z     A     F
-----------------------------------------------------------
Na2O   1.45  1.45 0.0013 0.9964 0.2429 1.0020
MgO   9.81 15.16 0.0105 1.0214 0.3524 1.0027
Al2O3   1.00  0.61 0.0012 0.9912 0.4490 1.0052
SiO2  38.59 40.03 0.0509 1.0200 0.5776 1.0008
K2O   1.13  0.75 0.0041 0.9706 0.8917 1.0127
CaO   1.33  1.48 0.0044 0.9931 0.9243 1.0189
MnO   0.51  0.45 0.0017 0.8875 0.9972 1.0000
FeO  46.19 40.07 0.1583 0.9041 1.0016 1.0000
Total 100.00 100.00

Elem    Wt % Chem K-Ratio   Z     A     F
-----------------------------------------------------------
NaK   1.07  0.08 0.0013 0.9964 0.2429 1.0020
MgK   5.91  0.43 0.0105 1.0214 0.3524 1.0027
AlK   0.53  0.03 0.0012 0.9912 0.4490 1.0052
SiK  18.04  1.13 0.0509 1.0200 0.5776 1.0008
K K   0.94  0.04 0.0041 0.9706 0.8917 1.0127
CaK   0.95  0.04 0.0044 0.9931 0.9243 1.0189
MnK   0.39  0.01 0.0017 0.8875 0.9972 1.0000
FeK  35.90  1.13 0.1583 0.9041 1.0016 1.0000
Oxygen 36.26  4.00
```

An10 ex chrysotile

```
Elem    Wt % Mol % K-Ratio   Z     A     F
-----------------------------------------------------------
Na2O   1.17  0.92 0.0019 0.9582 0.4473 1.0076
MgO  48.10 58.43 0.0798 0.9823 0.6005 1.0039
Al2O3   1.65  0.79 0.0020 0.9535 0.4700 1.0062
SiO2  47.18 38.45 0.0613 0.9813 0.5960 1.0001
K2O   0.29  0.15 0.0010 0.9301 0.8851 1.0010
CaO   0.79  0.69 0.0025 0.9522 0.9227 1.0003
MnO   0.00  0.00 0.0000 0.8493 0.9984 1.0000
FeO   0.83  0.56 0.0028 0.8646 1.0027 1.0000
Total 100.00 100.00

Elem    Wt % Chem K-Ratio   Z     A     F
-----------------------------------------------------------
```

NaK	0.86	0.09	0.0019	0.9582	0.4473	1.0076
MgK	29.01	2.92	0.0798	0.9823	0.6005	1.0039
AlK	0.87	0.08	0.0020	0.9535	0.4700	1.0062
SiK	22.05	1.92	0.0613	0.9813	0.5960	1.0001
K K	0.24	0.02	0.0010	0.9301	0.8851	1.0010
CaK	0.56	0.03	0.0025	0.9522	0.9227	1.0003
MnK	0.00	0.00	0.0000	0.8493	0.9984	1.0000
FeK	0.64	0.03	0.0028	0.8646	1.0027	1.0000
Oxygen	45.75	7.00				

INERT 2

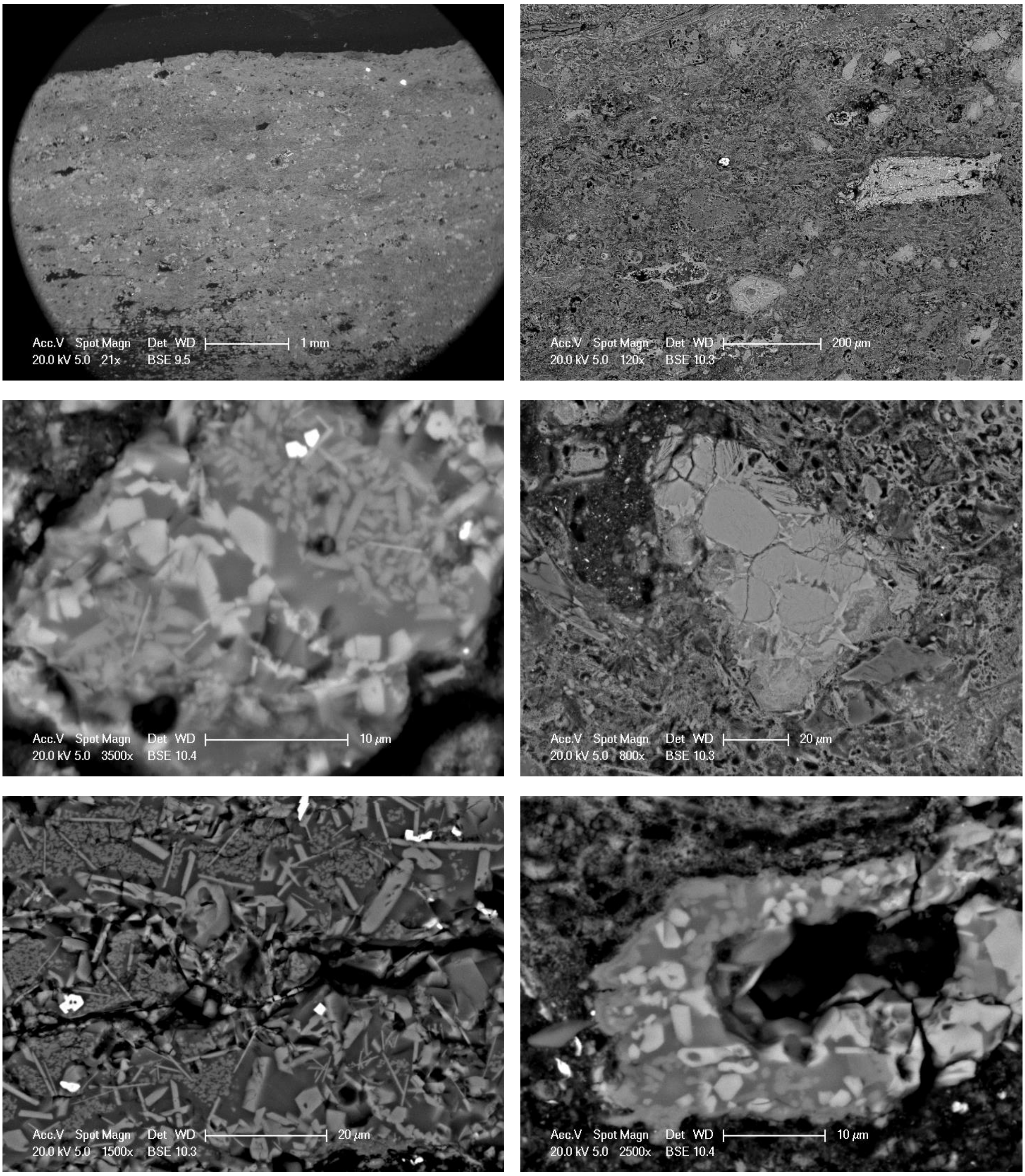
Acc.V Spot Magn Det WD 1 mm
20.0 kV 5.0 21x BSE 9.5
Acc.V Spot Magn Det WD 200 µm
20.0 kV 5.0 120x BSE 10.3
Acc.V Spot Magn Det WD 10 µm
20.0 kV 5.0 3500x BSE 10.4
Acc.V Spot Magn Det WD 20 µm
20.0 kV 5.0 800x BSE 10.3
Acc.V Spot Magn Det WD 20 µm
20.0 kV 5.0 1500x BSE 10.3
Acc.V Spot Magn Det WD 10 µm
20.0 kV 5.0 2500x BSE 10.4

An1 glass matrix

```
Elem    Wt %  Mol % K-Ratio   Z      A      F
-----------------------------------------------------------
Na2O   1.99   2.07  0.0026  0.9799  0.3011  1.0028
MgO   2.77   4.44  0.0043  1.0044  0.4269  1.0053
Al2O3   0.96   0.61  0.0017  0.9748  0.5569  1.0102
SiO2   58.77  63.14  0.1067  1.0032  0.6840  1.0018
K2O   11.93   8.18  0.0500  0.9532  0.8948  1.0063
CaO   1.49   1.71  0.0055  0.9755  0.8866  1.0073
FeO   22.09  19.85  0.0886  0.8872  0.9923  1.0000
Total  100.00 100.00
```

An2 olivine

```
Elem    Wt %  Mol % K-Ratio   Z      A      F
-----------------------------------------------------------
Na2O   0.65   0.66  0.0007  1.0024  0.2296  1.0017
MgO   9.55  14.88  0.0118  1.0275  0.3369  1.0023
Al2O3   0.43   0.26  0.0006  0.9971  0.4336  1.0045
SiO2   34.58  36.16  0.0546  1.0261  0.5637  1.0008
K2O   0.50   0.33  0.0022  0.9768  0.8926  1.0141
CaO   0.70   0.78  0.0028  0.9994  0.9274  1.0226
MnO   3.59   3.18  0.0149  0.8934  0.9988  1.0000
FeO   50.01  43.74  0.2092  0.9101  1.0028  1.0000
Total  100.00 100.00
```

```
Elem    Wt %  Chem K-Ratio   Z      A      F
-----------------------------------------------------------
NaK   0.49   0.04  0.0007  1.0024  0.2296  1.0017
MgK   5.76   0.44  0.0118  1.0275  0.3369  1.0023
AlK   0.23   0.02  0.0006  0.9971  0.4336  1.0045
SiK   16.16   1.06  0.0546  1.0261  0.5637  1.0008
K K   0.41   0.02  0.0022  0.9768  0.8926  1.0141
CaK   0.50   0.02  0.0028  0.9994  0.9274  1.0226
MnK   2.78   0.09  0.0149  0.8934  0.9988  1.0000
FeK   38.87   1.28  0.2092  0.9101  1.0028  1.0000
Oxygen  34.80   4.00
```

An3 ex chrysotile

```
Elem    Wt %  Mol % K-Ratio   Z      A      F
-----------------------------------------------------------
Na2O   0.55   0.45  0.0010  0.9602  0.4289  1.0071
MgO   45.05  56.01  0.0886  0.9843  0.5856  1.0040
Al2O3   3.85   1.89  0.0056  0.9554  0.4753  1.0061
SiO2   46.78  39.02  0.0729  0.9833  0.5925  1.0001
K2O   0.26   0.14  0.0011  0.9321  0.8845  1.0010
CaO   0.17   0.15  0.0006  0.9543  0.9223  1.0014
MnO   0.28   0.20  0.0011  0.8512  0.9990  1.0000
FeO   3.05   2.13  0.0123  0.8666  1.0031  1.0000
Total  100.00 100.00
```

```
Elem    Wt %  Chem K-Ratio   Z      A      F
-----------------------------------------------------------
NaK   0.41   0.04  0.0010  0.9602  0.4289  1.0071
MgK   27.17   2.75  0.0886  0.9843  0.5856  1.0040
AlK   2.04   0.19  0.0056  0.9554  0.4753  1.0061
SiK   21.87   1.91  0.0729  0.9833  0.5925  1.0001
K K   0.22   0.01  0.0011  0.9321  0.8845  1.0010
CaK   0.12   0.01  0.0006  0.9543  0.9223  1.0014
MnK   0.22   0.01  0.0011  0.8512  0.9990  1.0000
FeK   2.37   0.10  0.0123  0.8666  1.0031  1.0000
Oxygen  45.58   7.00
```

An4 ex chrysotile

```
Elem    Wt %  Mol % K-Ratio   Z      A      F
-----------------------------------------------------------
Na2O   1.41   1.14  0.0029  0.9604  0.4319  1.0070
MgO   44.76  55.63  0.0994  0.9845  0.5819  1.0040
Al2O3   2.27   1.12  0.0037  0.9556  0.4747  1.0063
SiO2   46.70  38.94  0.0834  0.9835  0.5982  1.0003
K2O   1.84   0.98  0.0085  0.9324  0.8865  1.0011
CaO   0.42   0.38  0.0018  0.9545  0.9179  1.0011
MnO   0.35   0.24  0.0015  0.8514  0.9973  1.0000
FeO   2.25   1.57  0.0102  0.8668  1.0018  1.0000
Total  100.00 100.00
```

```
Elem    Wt %  Chem K-Ratio   Z      A      F
-----------------------------------------------------------
NaK   1.04   0.11  0.0029  0.9604  0.4319  1.0070
MgK   27.00   2.76  0.0994  0.9845  0.5819  1.0040
AlK   1.20   0.11  0.0037  0.9556  0.4747  1.0063
SiK   21.83   1.93  0.0834  0.9835  0.5982  1.0003
K K   1.53   0.10  0.0085  0.9324  0.8865  1.0011
CaK   0.30   0.02  0.0018  0.9545  0.9179  1.0011
MnK   0.27   0.01  0.0015  0.8514  0.9973  1.0000
FeK   1.75   0.08  0.0102  0.8668  1.0018  1.0000
```

```
Oxygen  45.08   7.00
```

An5 glass

```
Elem     Wt %  Mol % K-Ratio    Z      A      F
-----------------------------------------------------------
Na2O   4.04   4.20  0.0045  0.9830  0.2920  1.0025
MgO   2.67   4.27  0.0035  1.0076  0.4057  1.0048
Al2O3   1.57   0.99  0.0023  0.9779  0.5349  1.0089
SiO2   54.83  58.84  0.0861  1.0064  0.6604  1.0015
K2O   8.84   6.05  0.0334  0.9564  0.8940  1.0078
CaO   1.75   2.02  0.0059  0.9788  0.8972  1.0093
MnO   2.07   1.88  0.0074  0.8741  0.9885  1.0000
FeO  24.24  21.76  0.0876  0.8902  0.9947  1.0000
Total  100.00 100.00
```

An6 olivine

```
Elem     Wt %  Mol % K-Ratio    Z      A      F
-----------------------------------------------------------
Na2O   1.29   1.29  0.0014  0.9988  0.2392  1.0019
MgO  10.79  16.63  0.0140  1.0238  0.3480  1.0025
Al2O3   0.98   0.60  0.0014  0.9935  0.4409  1.0048
SiO2   36.32  37.56  0.0587  1.0224  0.5693  1.0008
K2O   0.50   0.33  0.0022  0.9730  0.8921  1.0133
CaO   0.86   0.96  0.0036  0.9955  0.9270  1.0208
MnO   3.96   3.47  0.0167  0.8898  0.9985  1.0000
FeO  45.30  39.18  0.1925  0.9064  1.0026  1.0000
Total  100.00 100.00

Elem     Wt %  Chem K-Ratio    Z      A      F
-----------------------------------------------------------
NaK   0.95   0.07  0.0014  0.9988  0.2392  1.0019
MgK   6.51   0.48  0.0140  1.0238  0.3480  1.0025
AlK   0.52   0.03  0.0014  0.9935  0.4409  1.0048
SiK  16.98   1.08  0.0587  1.0224  0.5693  1.0008
K K   0.41   0.02  0.0022  0.9730  0.8921  1.0133
CaK   0.62   0.03  0.0036  0.9955  0.9270  1.0208
MnK   3.06   0.10  0.0167  0.8898  0.9985  1.0000
FeK  35.22   1.13  0.1925  0.9064  1.0026  1.0000
Oxygen  35.73   4.00
```

An7 px

```
Elem     Wt %  Mol % K-Ratio    Z      A      F
-----------------------------------------------------------
Na2O   1.80   1.80  0.0021  0.9834  0.2829  1.0027
MgO   6.99  10.75  0.0097  1.0080  0.4042  1.0043
Al2O3   1.70   1.03  0.0026  0.9783  0.5132  1.0081
SiO2  53.44  55.16  0.0869  1.0067  0.6390  1.0010
K2O   2.96   1.95  0.0120  0.9568  0.8899  1.0101
CaO   2.86   3.17  0.0105  0.9792  0.9160  1.0118
MnO   2.92   2.55  0.0111  0.8745  0.9931  1.0000
FeO  27.33  23.59  0.1059  0.8907  0.9984  1.0000
Total  100.00 100.00

Elem     Wt %  Chem K-Ratio    Z      A      F
-----------------------------------------------------------
NaK   1.34   0.14  0.0021  0.9834  0.2829  1.0027
MgK   4.21   0.41  0.0097  1.0080  0.4042  1.0043
AlK   0.90   0.08  0.0026  0.9783  0.5132  1.0081
SiK  24.98   2.10  0.0869  1.0067  0.6390  1.0010
K K   2.46   0.15  0.0120  0.9568  0.8899  1.0101
CaK   2.05   0.12  0.0105  0.9792  0.9160  1.0118
MnK   2.26   0.10  0.0111  0.8745  0.9931  1.0000
FeK  21.24   0.90  0.1059  0.8907  0.9984  1.0000
Oxygen  40.56   6.00
```

An8 glass

```
Elem     Wt %  Mol % K-Ratio    Z      A      F
-----------------------------------------------------------
Na2O   6.73   6.90  0.0094  0.9795  0.3114  1.0027
MgO   3.73   5.88  0.0059  1.0040  0.4160  1.0049
Al2O3   1.63   1.02  0.0029  0.9744  0.5407  1.0092
SiO2   55.60  58.78  0.1042  1.0028  0.6656  1.0015
K2O   8.60   5.80  0.0382  0.9526  0.8943  1.0074
CaO   2.55   2.89  0.0101  0.9749  0.8983  1.0075
MnO   2.12   1.90  0.0088  0.8705  0.9880  1.0000
FeO  19.04  16.84  0.0811  0.8865  0.9944  1.0000
Total  100.00 100.00
```

An9 cpx

```
Elem     Wt %  Mol % K-Ratio    Z      A      F
-----------------------------------------------------------
Na2O   1.02   0.97  0.0014  0.9748  0.3124  1.0031
MgO   9.57  13.96  0.0152  0.9992  0.4461  1.0048
Al2O3   0.82   0.47  0.0014  0.9698  0.5422  1.0090
```

```
SiO2   53.25  52.12  0.0955  0.9980  0.6709  1.0018
K2O    1.42   0.89  0.0061  0.9480  0.8995  1.0217
CaO   16.46  17.26  0.0634  0.9702  0.9293  1.0065
MnO    2.19   1.82  0.0086  0.8663  0.9815  1.0000
FeO   15.27  12.50  0.0614  0.8822  0.9892  1.0000
Total  100.00 100.00

Elem     Wt %  Chem K-Ratio    Z      A      F
------------------------------------------------------------
NaK   0.76   0.08  0.0014  0.9748  0.3124  1.0031
MgK   5.77   0.55  0.0152  0.9992  0.4461  1.0048
AlK   0.43   0.04  0.0014  0.9698  0.5422  1.0090
SiK  24.89   2.04  0.0955  0.9980  0.6709  1.0018
K K   1.18   0.07  0.0061  0.9480  0.8995  1.0217
CaK  11.76   0.68  0.0634  0.9702  0.9293  1.0065
MnK   1.70   0.07  0.0086  0.8663  0.9815  1.0000
FeK  11.87   0.49  0.0614  0.8822  0.9892  1.0000
Oxygen  41.64   6.00
```

An10 olivine

```
Elem     Wt %  Mol % K-Ratio    Z      A      F
------------------------------------------------------------
Na2O    0.97   0.97  0.0010  1.0000  0.2359  1.0019
MgO   10.91  16.81  0.0130  1.0250  0.3445  1.0024
Al2O3    0.83   0.50  0.0011  0.9947  0.4369  1.0046
SiO2   34.92  36.10  0.0520  1.0236  0.5657  1.0008
K2O    0.32   0.21  0.0013  0.9743  0.8928  1.0142
CaO    1.43   1.58  0.0055  0.9968  0.9283  1.0214
MnO    3.79   3.32  0.0148  0.8910  0.9982  1.0000
FeO   46.84  40.50  0.1844  0.9076  1.0024  1.0000
Total  100.00 100.00

Elem     Wt %  Chem K-Ratio    Z      A      F
------------------------------------------------------------
NaK    0.72   0.06  0.0010  1.0000  0.2359  1.0019
MgK    6.58   0.49  0.0130  1.0250  0.3445  1.0024
AlK    0.44   0.03  0.0011  0.9947  0.4369  1.0046
SiK   16.32   1.05  0.0520  1.0236  0.5657  1.0008
K K    0.26   0.01  0.0013  0.9743  0.8928  1.0142
CaK    1.02   0.05  0.0055  0.9968  0.9283  1.0214
MnK    2.94   0.10  0.0148  0.8910  0.9982  1.0000
FeK   36.41   1.18  0.1844  0.9076  1.0024  1.0000
Oxygen  35.31   4.00
```

INERT 3

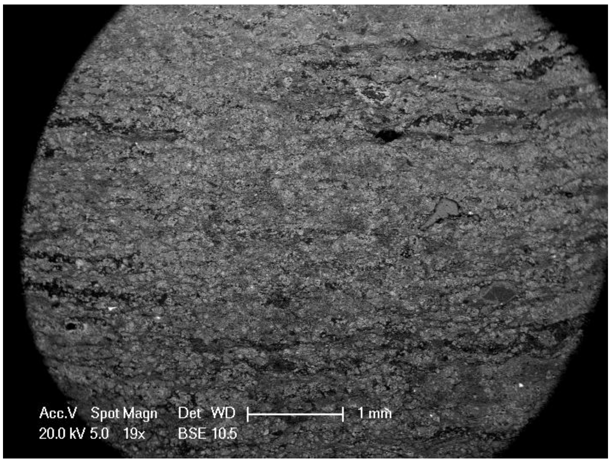
Acc.V Spot Magn Det WD 1 mm
20.0 kV 5.0 19x BSE 10.5

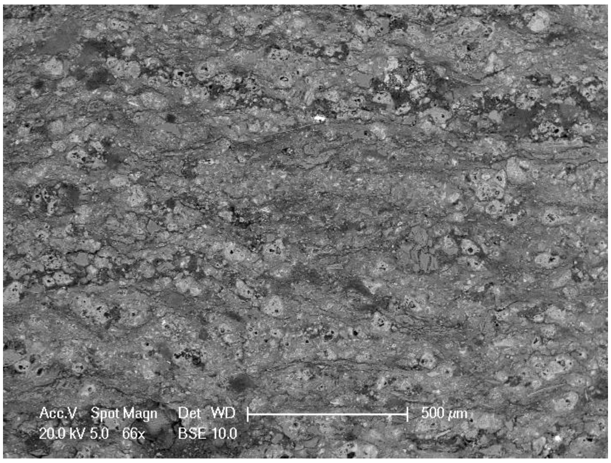
Acc.V Spot Magn Det WD 500 μm
20.0 kV 5.0 66x BSE 10.0

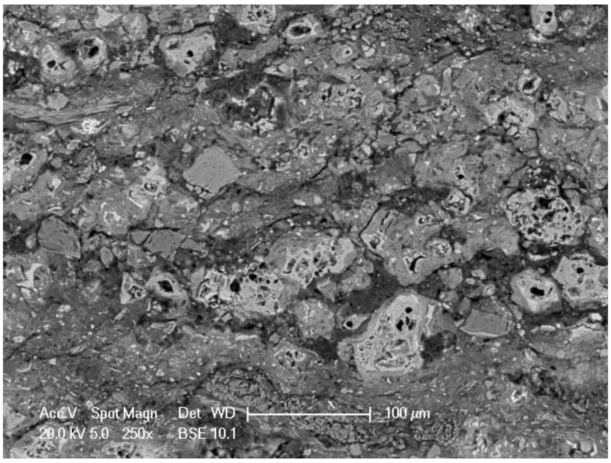
Acc.V Spot Magn Det WD 100 μm
20.0 kV 5.0 250x BSE 10.1

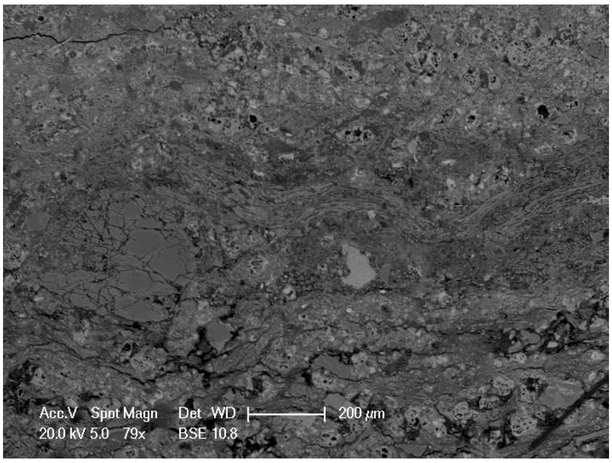
Acc.V Spot Magn Det WD 200 μm
20.0 kV 5.0 79x BSE 10.8

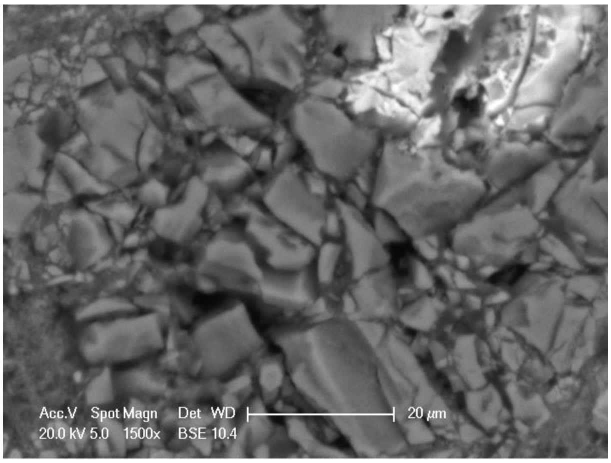
Acc.V Spot Magn Det WD 20 μm
20.0 kV 5.0 1500x BSE 10.4

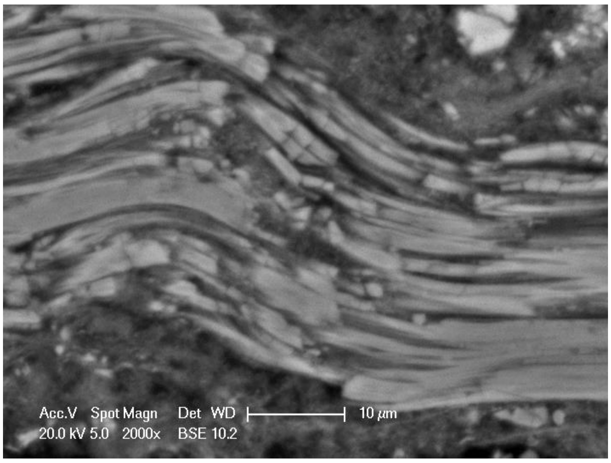
Acc.V Spot Magn Det WD 10 μm
20.0 kV 5.0 2000x BSE 10.2

An1 glass

```
Elem    Wt %  Mol % K-Ratio   Z      A      F
------------------------------------------------------------
Na2O  10.78  10.96  0.0130  0.9764  0.3308  1.0028
MgO   3.50   5.47  0.0045  1.0008  0.4173  1.0050
Al2O3   0.76   0.47  0.0011  0.9714  0.5432  1.0095
SiO2  57.46  60.25  0.0878  0.9997  0.6721  1.0014
K2O   8.53   5.70  0.0309  0.9493  0.8934  1.0059
CaO   2.10   2.35  0.0068  0.9716  0.8979  1.0059
MnO   0.29   0.25  0.0010  0.8674  0.9885  1.0000
FeO  16.58  14.54  0.0577  0.8832  0.9948  1.0000
Total  100.00 100.00
```

An2 olivine

```
Elem    Wt %  Mol % K-Ratio   Z      A      F
------------------------------------------------------------
Na2O   1.54   1.51  0.0015  0.9955  0.2466  1.0022
MgO  14.79  22.22  0.0164  1.0204  0.3570  1.0024
Al2O3   0.76   0.45  0.0009  0.9903  0.4359  1.0046
SiO2  35.89  36.17  0.0481  1.0190  0.5649  1.0007
K2O   0.48   0.31  0.0018  0.9695  0.8911  1.0118
CaO   0.45   0.49  0.0016  0.9920  0.9264  1.0191
MnO   0.23   0.20  0.0008  0.8865  0.9989  1.0000
FeO  45.86  38.65  0.1631  0.9030  1.0029  1.0000
Total  100.00 100.00
Elem    Wt %  Chem K-Ratio   Z      A      F
------------------------------------------------------------
NaK   1.14   0.09  0.0015  0.9955  0.2466  1.0022
MgK   8.92   0.65  0.0164  1.0204  0.3570  1.0024
AlK   0.40   0.03  0.0009  0.9903  0.4359  1.0046
SiK  16.77   1.06  0.0481  1.0190  0.5649  1.0007
K K   0.40   0.02  0.0018  0.9695  0.8911  1.0118
CaK   0.32   0.01  0.0016  0.9920  0.9264  1.0191
MnK   0.18   0.01  0.0008  0.8865  0.9989  1.0000
FeK  35.64   1.13  0.1631  0.9030  1.0029  1.0000
Oxygen  36.21   4.00
```

An 3 px

```
Elem    Wt %  Mol % K-Ratio   Z      A      F
------------------------------------------------------------
Na2O   4.87   4.70  0.0051  0.9745  0.3174  1.0026
MgO   3.81   5.65  0.0046  0.9989  0.4328  1.0047
Al2O3   3.19   1.87  0.0042  0.9695  0.5585  1.0084
SiO2  44.66  44.43  0.0621  0.9977  0.6754  1.0029
K2O   0.45   0.29  0.0016  0.9478  0.9136  1.0390
CaO  31.04  33.09  0.0928  0.9700  0.9439  1.0041
MnO   0.49   0.41  0.0015  0.8662  0.9692  1.0000
FeO  11.49   9.56  0.0353  0.8821  0.9794  1.0000
Total  100.00 100.00

Elem    Wt %  Chem K-Ratio   Z      A      F
------------------------------------------------------------
NaK   3.61   0.38  0.0051  0.9745  0.3174  1.0026
MgK   2.30   0.23  0.0046  0.9989  0.4328  1.0047
AlK   1.69   0.15  0.0042  0.9695  0.5585  1.0084
SiK  20.87   1.80  0.0621  0.9977  0.6754  1.0029
K K   0.38   0.02  0.0016  0.9478  0.9136  1.0390
CaK  22.18   1.34  0.0928  0.9700  0.9439  1.0041
MnK   0.38   0.02  0.0015  0.8662  0.9692  1.0000
FeK   8.93   0.39  0.0353  0.8821  0.9794  1.0000
Oxygen  39.65   6.00
```

An4 olivine

```
Elem    Wt %  Mol % K-Ratio   Z      A      F
------------------------------------------------------------
Na2O   1.28   1.22  0.0013  0.9817  0.2847  1.0024
MgO   9.39  13.68  0.0116  1.0063  0.4096  1.0035
Al2O3   0.83   0.48  0.0011  0.9766  0.5086  1.0066
SiO2  37.84  36.99  0.0551  1.0050  0.6386  1.0026
K2O   0.52   0.33  0.0020  0.9555  0.9130  1.0369
CaO  27.45  28.76  0.0909  0.9777  0.9431  1.0080
MnO   0.55   0.46  0.0018  0.8734  0.9730  1.0000
FeO  22.13  18.09  0.0746  0.8896  0.9823  1.0000
Total  100.00 100.00

Elem    Wt %  Chem K-Ratio   Z      A      F
------------------------------------------------------------
NaK   0.95   0.07  0.0013  0.9817  0.2847  1.0024
MgK   5.66   0.40  0.0116  1.0063  0.4096  1.0035
AlK   0.44   0.03  0.0011  0.9766  0.5086  1.0066
SiK  17.69   1.07  0.0551  1.0050  0.6386  1.0026
K K   0.44   0.02  0.0020  0.9555  0.9130  1.0369
CaK  19.62   0.83  0.0909  0.9777  0.9431  1.0080
MnK   0.43   0.01  0.0018  0.8734  0.9730  1.0000
FeK  17.20   0.52  0.0746  0.8896  0.9823  1.0000
```

```
Oxygen  37.57   4.00
```

An 5 glass matrix

```
Elem     Wt %  Mol % K-Ratio    Z       A       F
------------------------------------------------------------
Na2O   20.02  19.23  0.0265  0.9678  0.3858  1.0026
MgO    0.49   0.73  0.0006  0.9921  0.4224  1.0049
Al2O3    0.62   0.36  0.0009  0.9629  0.5648  1.0094
SiO2   51.05  50.59  0.0789  0.9910  0.6938  1.0023
K2O    0.39   0.25  0.0014  0.9404  0.9092  1.0307
CaO   26.20  27.82  0.0844  0.9626  0.9409  1.0005
MnO    0.34   0.29  0.0011  0.8590  0.9739  1.0000
FeO    0.89   0.74  0.0030  0.8747  0.9832  1.0000
Total  100.00 100.00
```

An6 ex chrysotile

```
Elem     Wt %  Mol % K-Ratio    Z       A       F
------------------------------------------------------------
Na2O    1.18   0.95  0.0018  0.9603  0.4295  1.0070
MgO   45.15  55.91  0.0696  0.9845  0.5810  1.0039
Al2O3    2.49   1.22  0.0029  0.9556  0.4727  1.0062
SiO2   46.74  38.83  0.0582  0.9834  0.5954  1.0002
K2O    0.68   0.36  0.0022  0.9323  0.8855  1.0014
CaO    0.56   0.50  0.0017  0.9545  0.9216  1.0014
MnO    0.56   0.40  0.0018  0.8514  0.9982  1.0000
FeO    2.64   1.83  0.0086  0.8668  1.0026  1.0000
Total  100.00 100.00

Elem     Wt %  Chem K-Ratio    Z       A       F
------------------------------------------------------------
NaK    0.88   0.09  0.0018  0.9603  0.4295  1.0070
MgK   27.23   2.77  0.0696  0.9845  0.5810  1.0039
AlK    1.32   0.12  0.0029  0.9556  0.4727  1.0062
SiK   21.85   1.92  0.0582  0.9834  0.5954  1.0002
K K    0.56   0.04  0.0022  0.9323  0.8855  1.0014
CaK    0.40   0.02  0.0017  0.9545  0.9216  1.0014
MnK    0.44   0.02  0.0018  0.8514  0.9982  1.0000
FeK    2.05   0.09  0.0086  0.8668  1.0026  1.0000
Oxygen  45.28   7.00
```

INERT 4

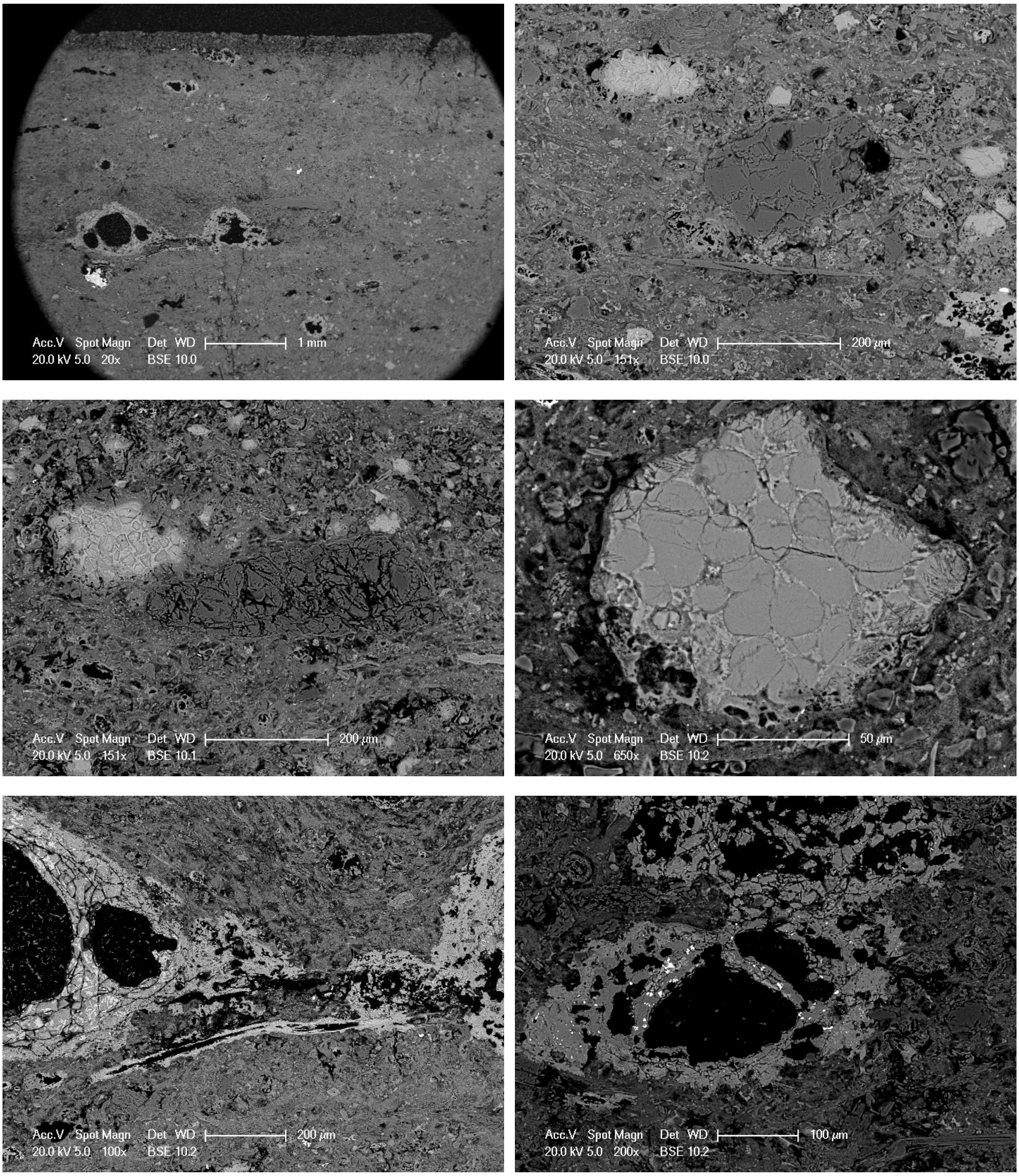

An1 olivine (scheletrica)

```
Elem    Wt %  Mol % K-Ratio   Z     A     F
------------------------------------------------------------
Na2O   1.03  1.04  0.0011  1.0010  0.2311  1.0018
MgO   11.19  17.25  0.0142  1.0261  0.3377  1.0022
Al2O3   0.49  0.30  0.0007  0.9958  0.4289  1.0043
SiO2   33.84  35.01  0.0543  1.0246  0.5585  1.0007
CaO   0.73   0.81  0.0031  0.9980  0.9287  1.0220
FeO  52.71  45.59  0.2253  0.9088  1.0031  1.0000
Total  100.00 100.00
```

```
Elem    Wt %  Chem K-Ratio   Z     A     F
------------------------------------------------------------
NaK   0.77   0.06  0.0011  1.0010  0.2311  1.0018
MgK   6.75   0.51  0.0142  1.0261  0.3377  1.0022
AlK   0.26   0.02  0.0007  0.9958  0.4289  1.0043
SiK  15.82   1.03  0.0543  1.0246  0.5585  1.0007
CaK   0.52   0.02  0.0031  0.9980  0.9287  1.0220
FeK  40.97   1.34  0.2253  0.9088  1.0031  1.0000
Oxygen  34.91   4.00
```

An2 olivine

```
Elem    Wt %  Mol % K-Ratio   Z     A     F
------------------------------------------------------------
Na2O   0.92   0.94  0.0009  1.0033  0.2253  1.0016
MgO   8.19  12.89  0.0100  1.0284  0.3300  1.0022
Al2O3   0.62   0.38  0.0009  0.9980  0.4308  1.0044
SiO2   34.39  36.30  0.0540  1.0269  0.5600  1.0008
CaO   0.56   0.63  0.0023  1.0004  0.9285  1.0231
FeO  55.33  48.85  0.2310  0.9111  1.0032  1.0000
Total  100.00 100.00
```

```
Elem    Wt %  Chem K-Ratio   Z     A     F
------------------------------------------------------------
NaK   0.68   0.05  0.0009  1.0033  0.2253  1.0016
MgK   4.94   0.38  0.0100  1.0284  0.3300  1.0022
AlK   0.33   0.02  0.0009  0.9980  0.4308  1.0044
SiK  16.07   1.06  0.0540  1.0269  0.5600  1.0008
CaK   0.40   0.02  0.0023  1.0004  0.9285  1.0231
FeK  43.01   1.43  0.2310  0.9111  1.0032  1.0000
Oxygen  34.57   4.00
```

An3 glass ex croc

```
Elem    Wt %  Mol % K-Ratio   Z     A     F
------------------------------------------------------------
 Na2O   11.59  11.60  0.0161  0.9756  0.3207  1.0027
MgO   1.88   2.89  0.0028  1.0001  0.4031  1.0051
Al2O3   0.87   0.53  0.0015  0.9707  0.5359  1.0097
SiO2   63.08  65.15  0.1138  0.9989  0.6646  1.0004
CaO   1.37   1.52  0.0054  0.9708  0.9222  1.0086
FeO   21.22  18.32  0.0885  0.8825  1.0015  1.0000
Total  100.00 100.00
```

An4 px

```
Elem    Wt %  Mol % K-Ratio   Z     A     F
------------------------------------------------------------
Na2O   2.87   2.81  0.0036  0.9823  0.2826  1.0027
MgO   8.60  12.96  0.0127  1.0069  0.3989  1.0041
Al2O3   0.86   0.51  0.0014  0.9772  0.5007  1.0078
SiO2   53.76  54.33  0.0932  1.0056  0.6303  1.0007
CaO   3.03   3.28  0.0121  0.9780  0.9249  1.0124
FeO   30.88  26.10  0.1291  0.8896  1.0005  1.0000
Total  100.00 100.00
```

```
Elem    Wt %  Chem K-Ratio   Z     A     F
------------------------------------------------------------
NaK   2.13   0.22  0.0036  0.9823  0.2826  1.0027
MgK   5.19   0.50  0.0127  1.0069  0.3989  1.0041
AlK   0.46   0.04  0.0014  0.9772  0.5007  1.0078
SiK  25.13   2.10  0.0932  1.0056  0.6303  1.0007
CaK   2.16   0.13  0.0121  0.9780  0.9249  1.0124
FeK  24.00   1.01  0.1291  0.8896  1.0005  1.0000
Oxygen  40.93   6.00
```

An5 px

```
Elem    Wt %  Mol % K-Ratio   Z     A     F
------------------------------------------------------------
Na2O   2.63   2.59  0.0033  0.9834  0.2776  1.0025
MgO   7.28  11.03  0.0109  1.0081  0.3938  1.0040
Al2O3   0.79   0.48  0.0013  0.9783  0.5014  1.0077
SiO2   52.41  53.29  0.0936  1.0068  0.6313  1.0008
CaO   5.20   5.66  0.0214  0.9793  0.9267  1.0125
FeO   31.69  26.95  0.1356  0.8909  0.9988  1.0000
Total  100.00 100.00
```

```
Elem    Wt %  Chem K-Ratio   Z      A      F
-----------------------------------------------------------
NaK   1.95  0.20  0.0033  0.9834  0.2776  1.0025
MgK   4.39  0.43  0.0109  1.0081  0.3938  1.0040
AlK   0.42  0.04  0.0013  0.9783  0.5014  1.0077
SiK  24.50  2.07  0.0936  1.0068  0.6313  1.0008
CaK   3.71  0.22  0.0214  0.9793  0.9267  1.0125
FeK  24.64  1.05  0.1356  0.8909  0.9988  1.0000
Oxygen  40.39   6.00
```

An6 olivine

```
Elem    Wt %  Mol % K-Ratio   Z      A      F
-----------------------------------------------------------
Na2O   0.94   0.92  0.0010  0.9882  0.2604  1.0019
MgO    4.79   7.20  0.0064  1.0130  0.3789  1.0032
Al2O3   0.48   0.29  0.0007  0.9831  0.4971  1.0062
SiO2   35.36  35.70  0.0591  1.0116  0.6288  1.0026
CaO   27.61  29.86  0.1066  0.9848  0.9456  1.0109
FeO   30.82  26.02  0.1199  0.8963  0.9827  1.0000
Total  100.00 100.00
Elem    Wt %  Chem K-Ratio   Z      A      F
-----------------------------------------------------------
NaK   0.70  0.05  0.0010  0.9882  0.2604  1.0019
MgK   2.89  0.21  0.0064  1.0130  0.3789  1.0032
AlK   0.25  0.02  0.0007  0.9831  0.4971  1.0062
SiK  16.53  1.05  0.0591  1.0116  0.6288  1.0026
CaK  19.73  0.88  0.1066  0.9848  0.9456  1.0109
FeK  23.96  0.76  0.1199  0.8963  0.9827  1.0000
Oxygen  35.94   4.00
```

An7 ex chrysotile

```
Elem    Wt %  Mol % K-Ratio   Z      A      F
-----------------------------------------------------------
Na2O   1.19   0.95  0.0037  0.9595  0.4357  1.0072
MgO   45.97  56.52  0.1609  0.9837  0.5877  1.0039
Al2O3   1.10   0.54  0.0027  0.9548  0.4727  1.0064
SiO2   47.79  39.42  0.1319  0.9826  0.6009  1.0002
K2O    1.46   0.77  0.0100  0.9315  0.8859  1.0009
CaO    0.40   0.36  0.0025  0.9536  0.9188  1.0008
FeO    2.09   1.44  0.0141  0.8660  1.0020  1.0000
Total  100.00 100.00
```

```
Elem    Wt %  Chem K-Ratio   Z      A      F
-----------------------------------------------------------
NaK   0.88  0.09  0.0037  0.9595  0.4357  1.0072
MgK  27.72  2.82  0.1609  0.9837  0.5877  1.0039
AlK   0.58  0.05  0.0027  0.9548  0.4727  1.0064
SiK  22.34  1.96  0.1319  0.9826  0.6009  1.0002
K K   1.21  0.08  0.0100  0.9315  0.8859  1.0009
CaK   0.29  0.02  0.0025  0.9536  0.9188  1.0008
FeK   1.63  0.07  0.0141  0.8660  1.0020  1.0000
Oxygen  45.35   7.00
```

An8 olivine

```
Elem    Wt %  Mol % K-Ratio   Z      A      F
-----------------------------------------------------------
Na2O   1.48   1.49  0.0014  1.0010  0.2317  1.0017
MgO    9.90  15.38  0.0115  1.0260  0.3370  1.0023
Al2O3   0.97   0.60  0.0013  0.9957  0.4325  1.0044
SiO2   34.02  35.48  0.0502  1.0246  0.5606  1.0008
K2O    0.21   0.14  0.0009  0.9754  0.8923  1.0141
CaO    1.22   1.36  0.0047  0.9979  0.9283  1.0216
FeO   52.21  45.55  0.2046  0.9087  1.0025  1.0000
Total  100.00 100.00

Elem    Wt %  Chem K-Ratio   Z      A      F
-----------------------------------------------------------
NaK   1.09  0.09  0.0014  1.0010  0.2317  1.0017
MgK   5.97  0.45  0.0115  1.0260  0.3370  1.0023
AlK   0.51  0.03  0.0013  0.9957  0.4325  1.0044
SiK  15.90  1.04  0.0502  1.0246  0.5606  1.0008
K K   0.17  0.01  0.0009  0.9754  0.8923  1.0141
CaK   0.87  0.04  0.0047  0.9979  0.9283  1.0216
FeK  40.59  1.33  0.2046  0.9087  1.0025  1.0000
Oxygen  34.89   4.00
```

An9 ex chrysotile

```
Elem    Wt %  Mol % K-Ratio   Z      A      F
-----------------------------------------------------------
Na2O   0.53   0.42  0.0009  0.9592  0.4322  1.0072
MgO   46.44  56.69  0.0844  0.9834  0.5895  1.0039
Al2O3   0.47   0.22  0.0006  0.9545  0.4717  1.0065
SiO2   48.51  39.72  0.0708  0.9823  0.6025  1.0002
K2O    0.42   0.22  0.0016  0.9312  0.8854  1.0018
```

```
CaO    1.19   1.05  0.0042  0.9533  0.9224  1.0010
FeO    2.43   1.66  0.0091  0.8657  1.0022  1.0000
Total  100.00 100.00

Elem     Wt %  Chem K-Ratio    Z       A       F
---------------------------------------------------------------
NaK    0.40   0.04  0.0009  0.9592  0.4322  1.0072
MgK   28.01   2.83  0.0844  0.9834  0.5895  1.0039
AlK    0.25   0.02  0.0006  0.9545  0.4717  1.0065
SiK   22.67   1.98  0.0708  0.9823  0.6025  1.0002
K K    0.35   0.02  0.0016  0.9312  0.8854  1.0018
CaK    0.85   0.05  0.0042  0.9533  0.9224  1.0010
FeK    1.89   0.08  0.0091  0.8657  1.0022  1.0000
Oxygen  45.58   7.00
```

Hereafter are shown some TEM images on the inertized fibers of chrysotile and crocidolite

Ex chrysotile

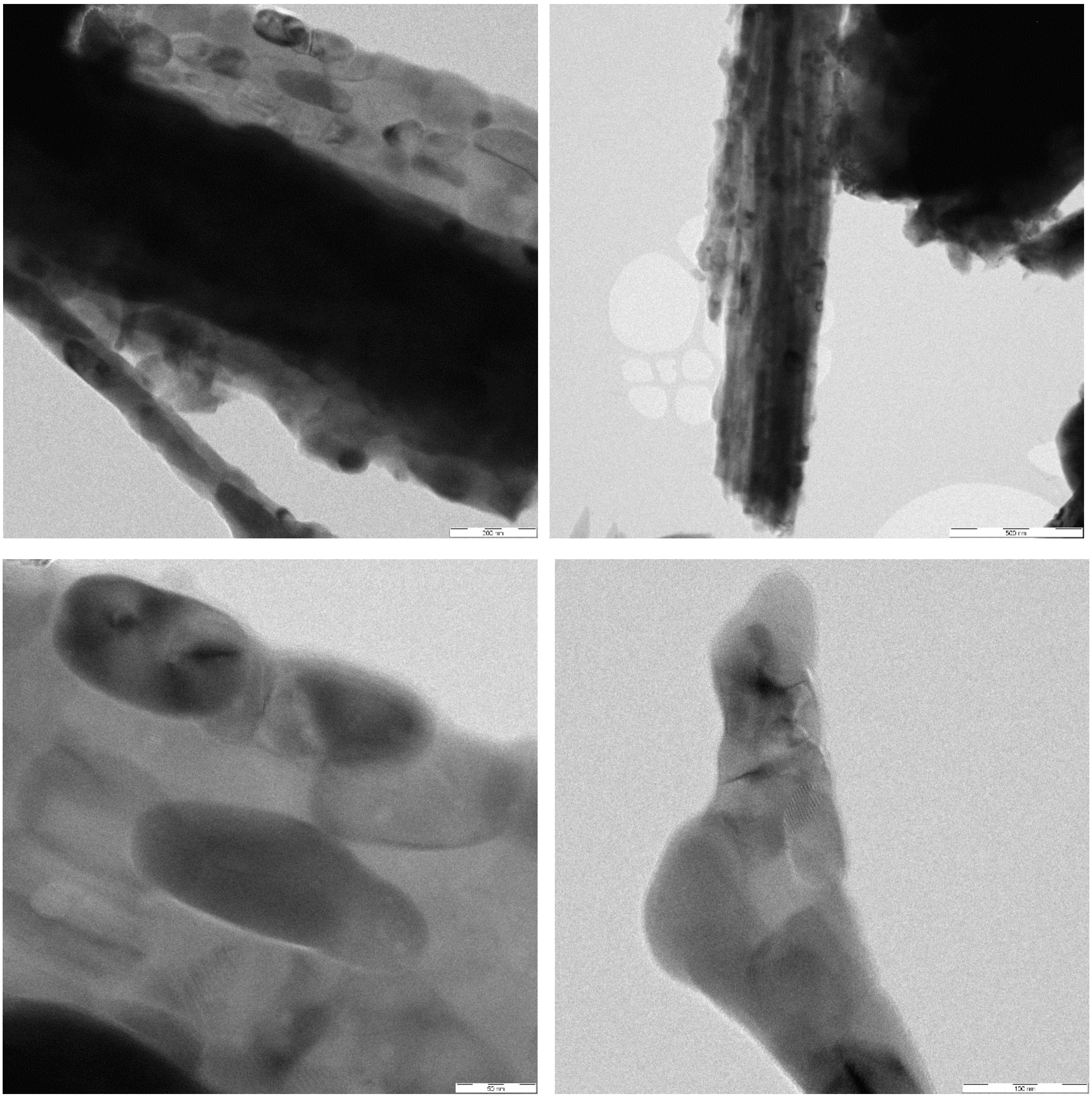

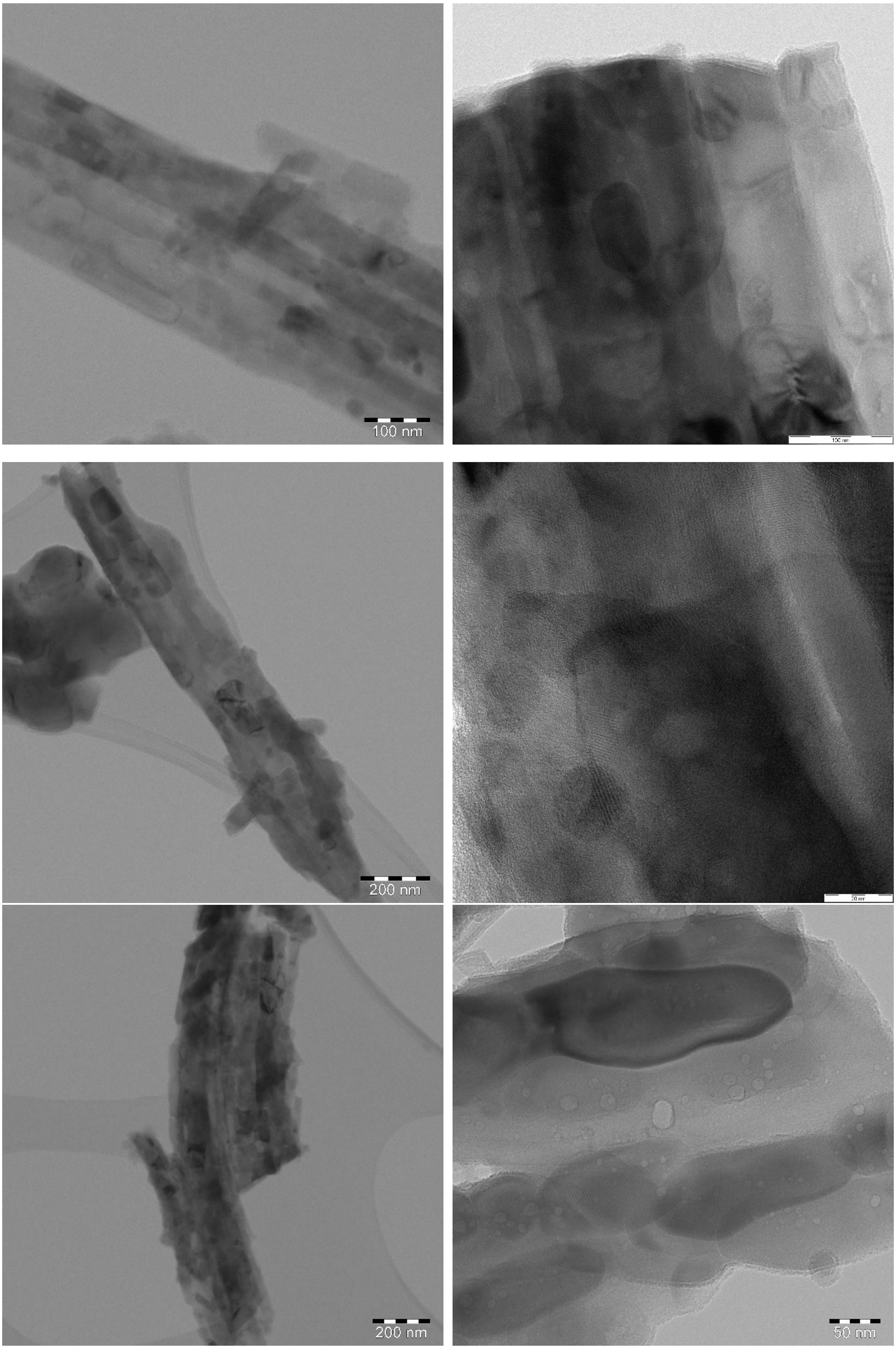
100 nm
100 nm
200 nm
20 nm
200 nm
50 nm

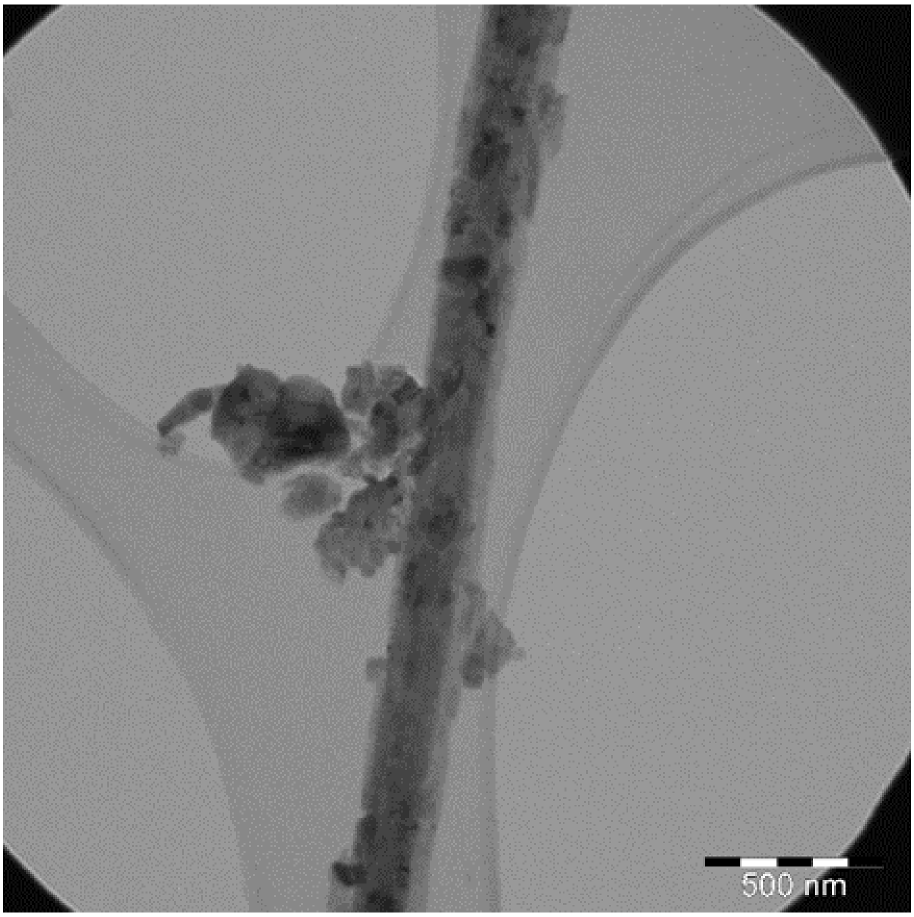
500 nm

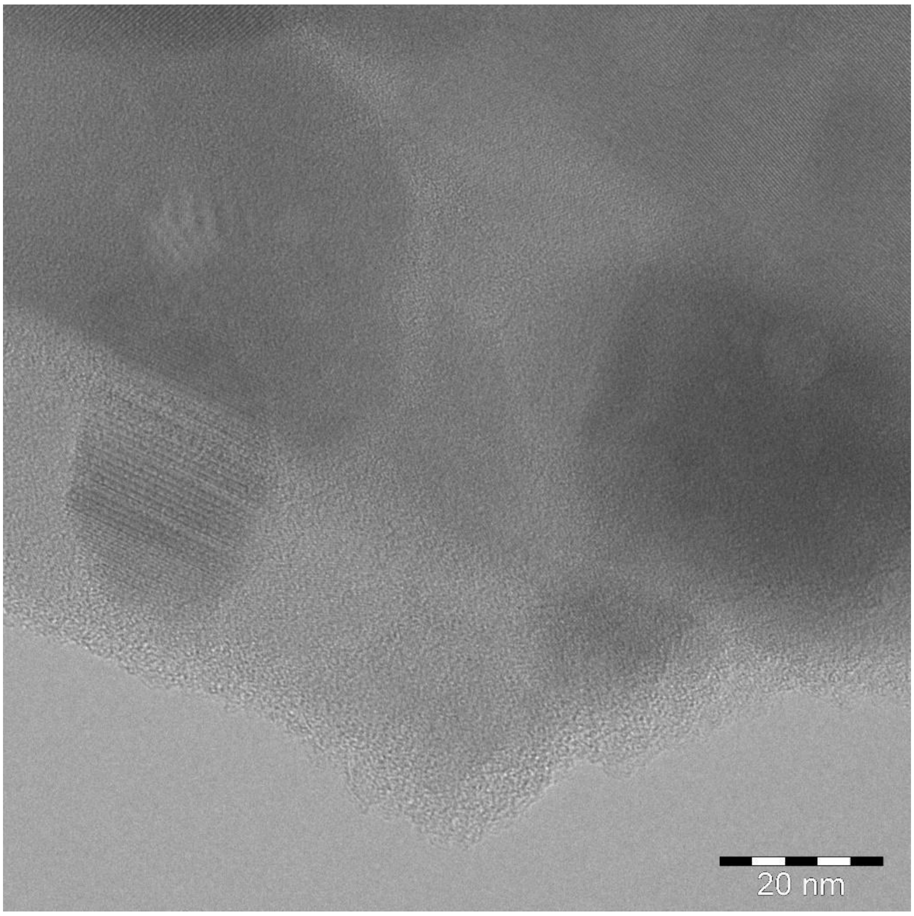
20 nm

Crocidolite

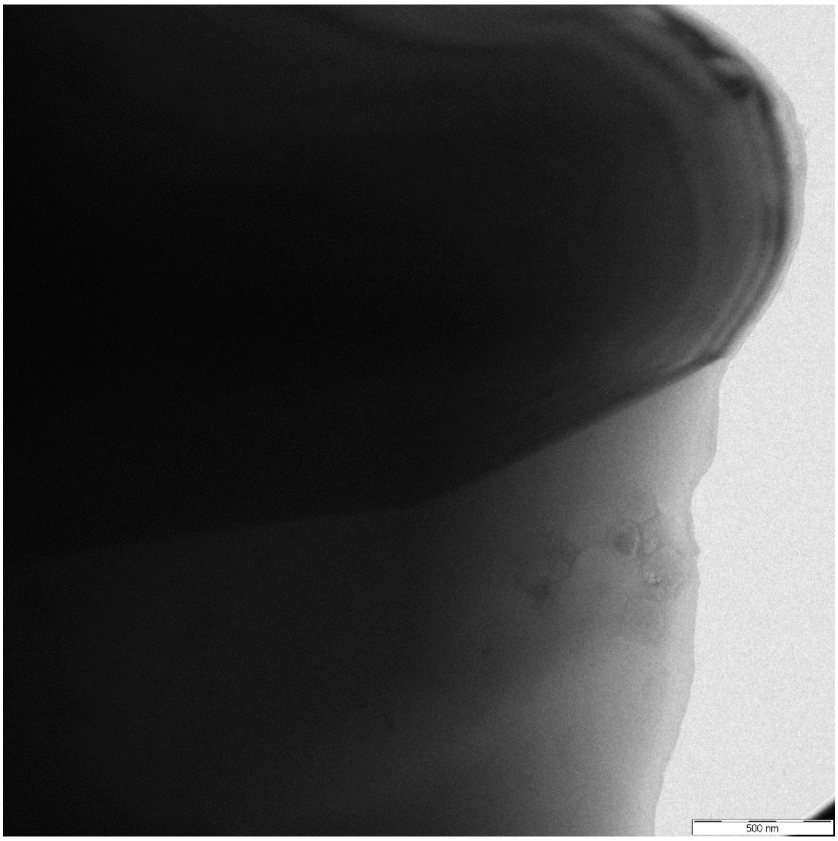

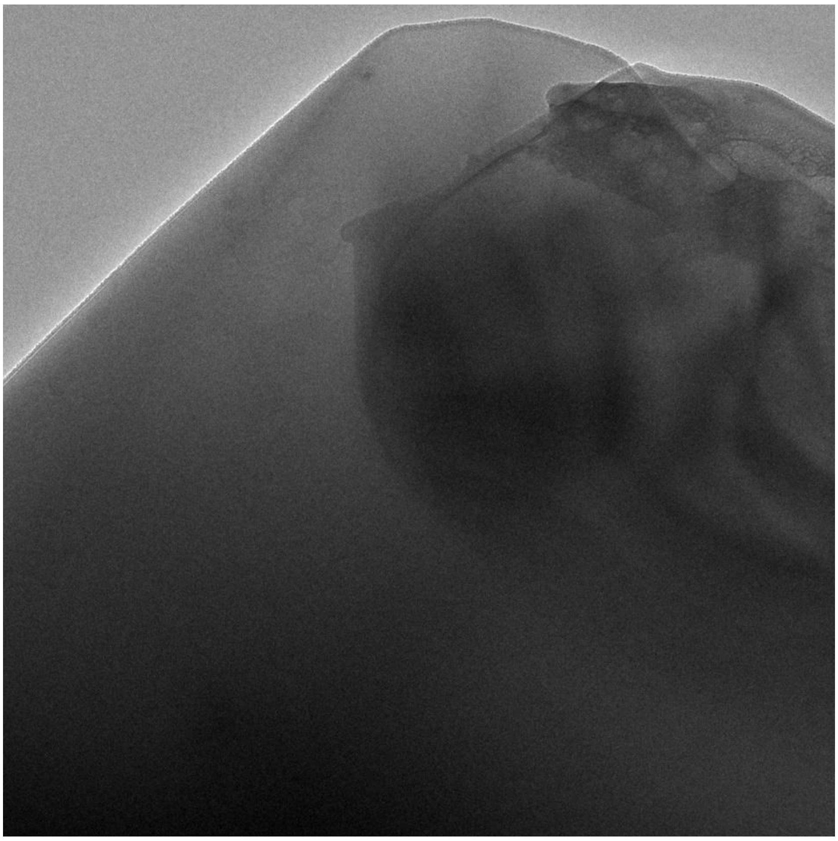

APPENDIX III

Hereafter are reported the supplementary materials of the Red Gypsum work.

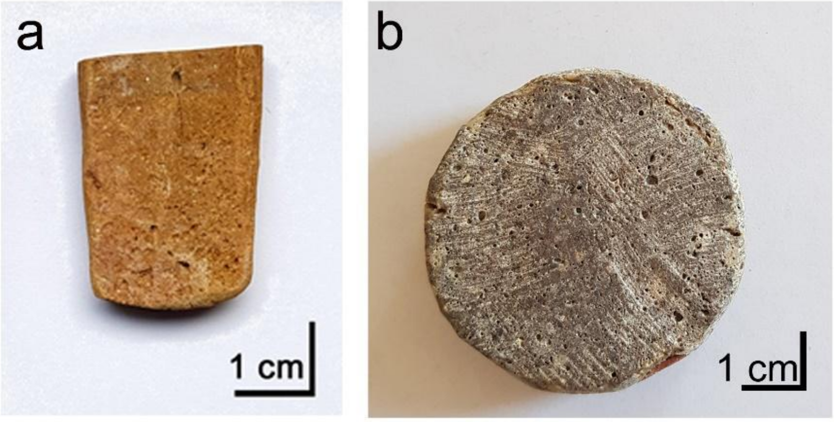

Figure 1S. Ceramic tests obtained using up to 70% of waste gypsum. A) CRG1 B) CRG4.

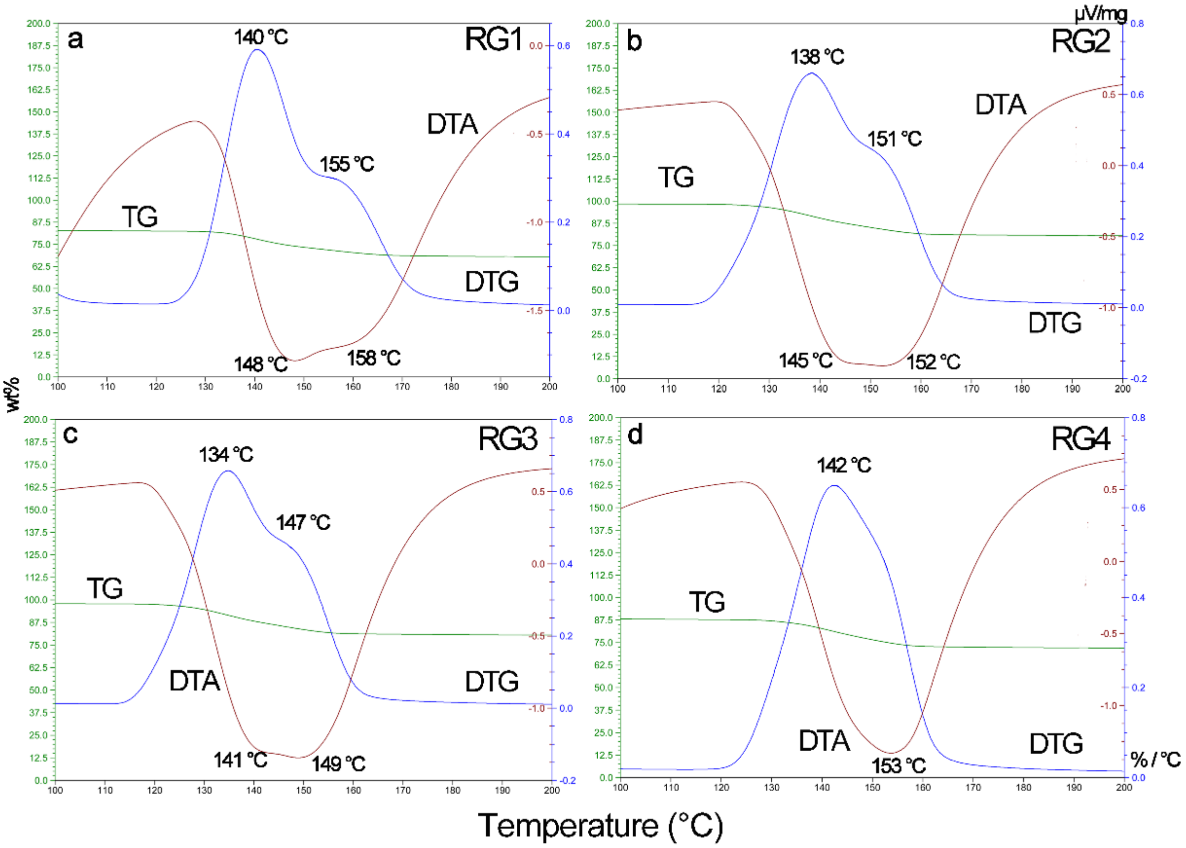

Figure 2S. The image reports the main thermal data TG, DTG, and DTA for the four samples in the temperature range 100°C - 200°C. The figure reports the main DTG/DTA peaks showing the transition from gypsum to hemihydrate and from hemihydrate to anhydrite.

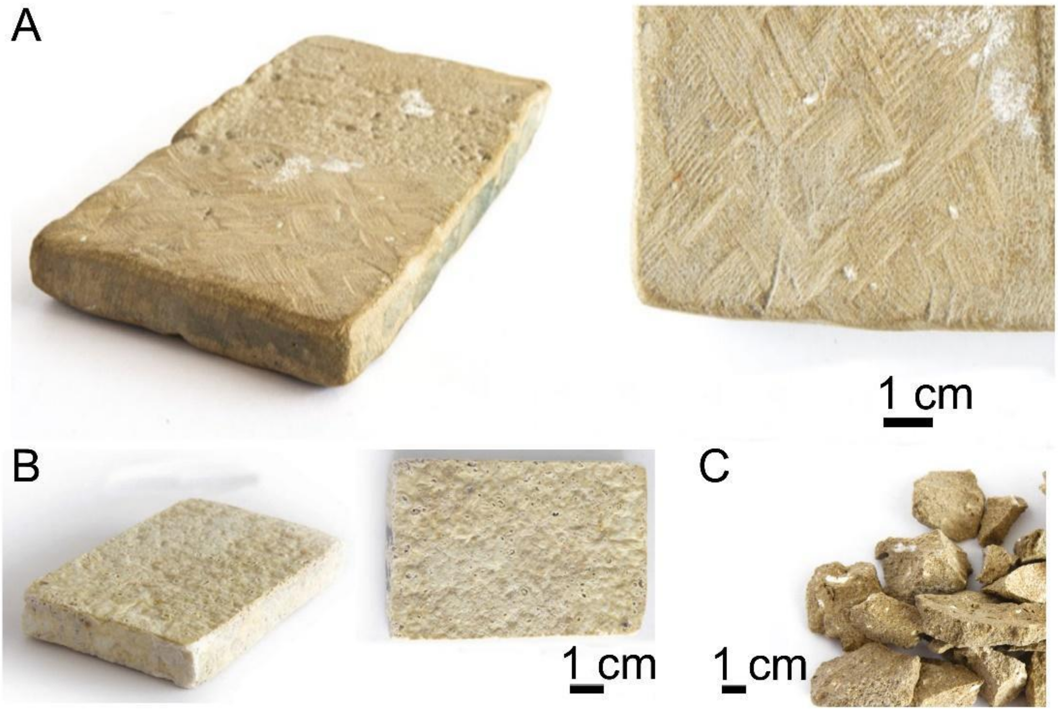

Figure 3S. Other ceramic materials realized with Red Gypsum samples.

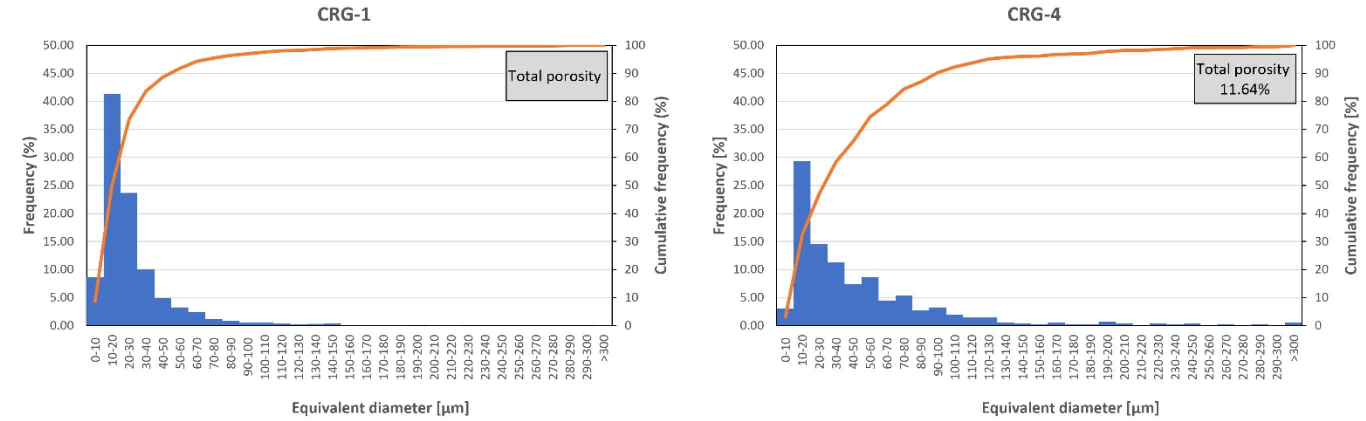

Figure 4S. Pore size distribution for the two ceramic samples CRG1 and CRG4.

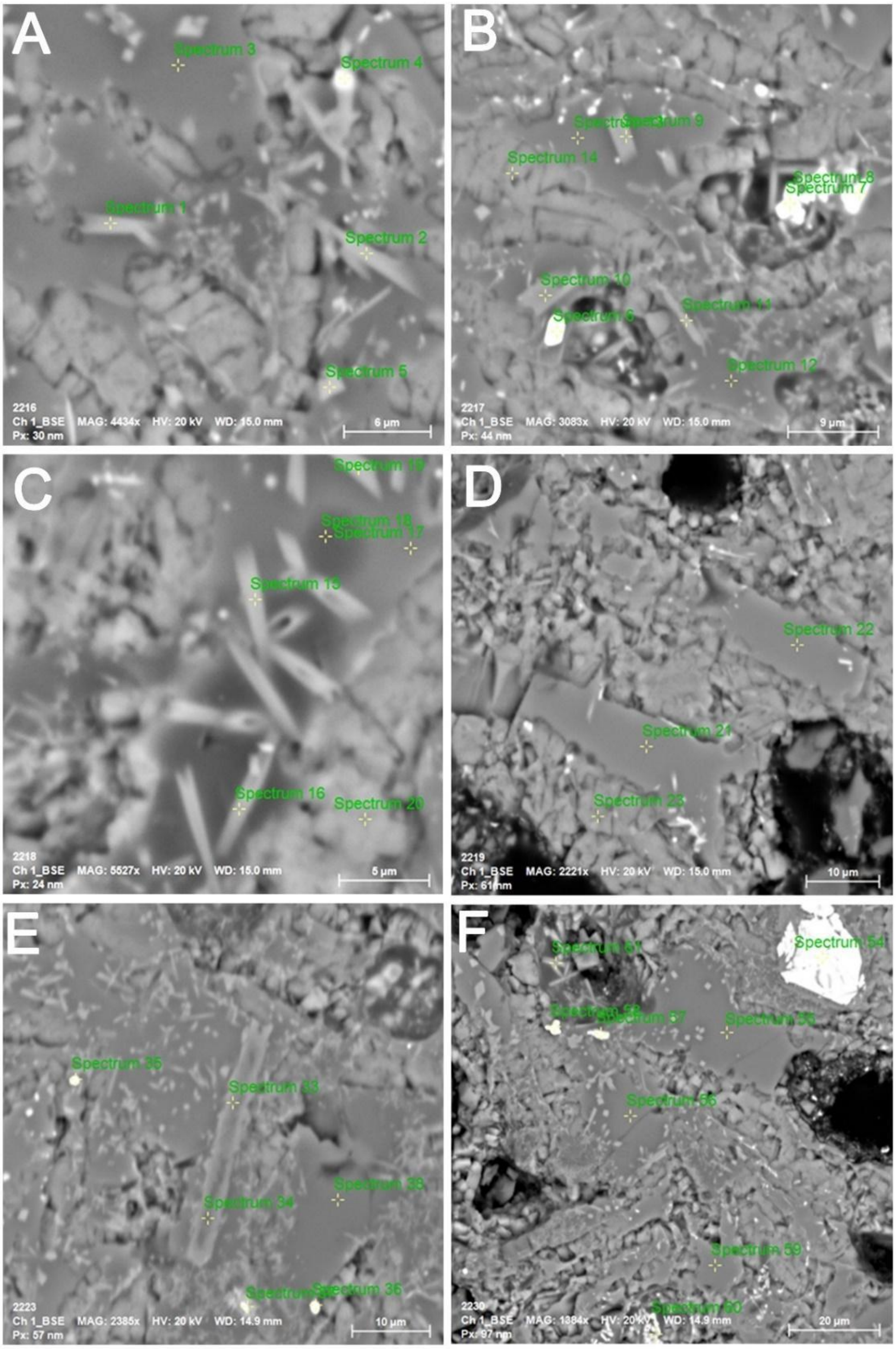

Figure 5S. CRG1 SEM BSE images showing some EDS analyses points

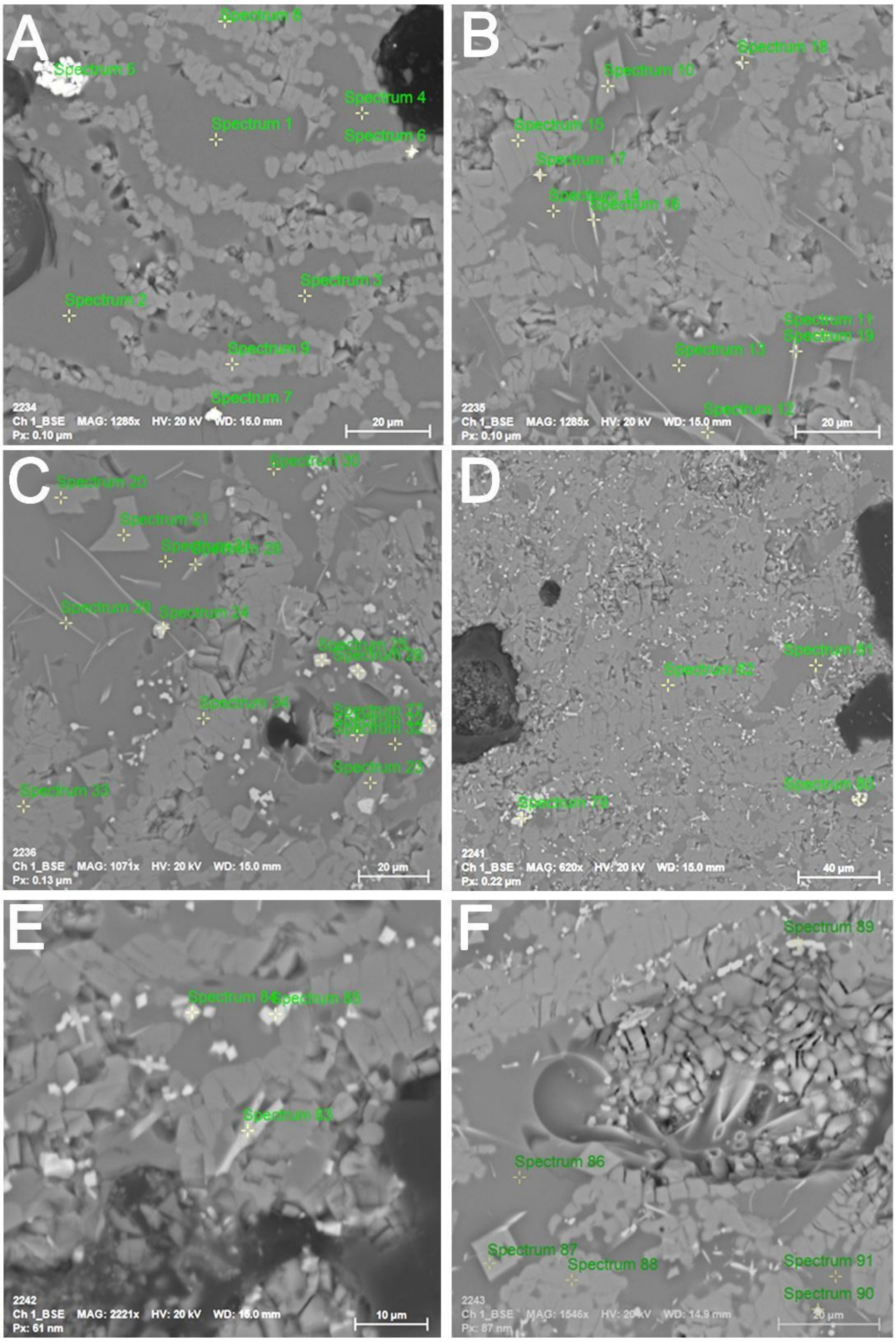

Figure 6S. CRG4 SEM BSE images showing some EDS analyses points.

Table 1S. It is reported the name of the sample, the production year for each one, and the site of sampling

	Year of waste production	**Samplig site**
RG 1	2010	Outside of the industrial plant
RG 2	2016	Industrial sheds
RG 3	June 2021	Industrial sheds
RG 4	July 2021	Outside of the industrial plant

Table 2S. There are reported the parameters used for image analyses and pores distribution for the two CRG samples.

		Roundness	**Equivalent diameter [µm]**	**Aspect ratio**	**Area [µm²]**	**Porosity %**
CRG1	Minimum	0.152	8.12	1	51.84	
	Maximum	1	449.72	6.488	158844.24	
	Mean	0.8534	28.77	1.4806	1382.174	22.22
CRG4	Minimum	0.108	8.13	1	51.96	

	Maximum	1	326.31	16.988	83628.03	
	Mean	0.7994	48.208	1.563	3586.588	11.64

Table 3S. The SEM EDS analyses of the phases composition of the two CRG samples. For each phase it is reported the maximum, minimum and mean values.

Phase	**Glass**							
Sample	**CRG1**				**CRG4**			
Wt% Oxides	***Max value***	***Min value***	***mean***	***mean SdT***	***Max value***	***Min value***	***mean***	***mean SdT***
SiO_2	68.74	42.82	57.90	4.74	68.22	47.29	57.41	3.57
Al_2O_3	15.19	0.43	11.88	3.06	16.70	10.72	13.42	0.82
MgO	43.71	0.41	4.63	5.24	5.02	1.38	2.98	0.57
FeO (tot)	15.80	3.04	4.60	1.12	10.69	1.70	4.24	0.80
Na_2O	7.69	0.00	5.66	1.45	7.43	5.46	6.16	0.30
K_2O	1.92	0.08	1.19	0.39	1.57	0.72	1.04	0.13
CaO	16.39	0.21	8.88	3.33	14.36	4.07	9.29	1.61
TiO_2	2.79	0.00	1.96	0.46	7.51	0.96	2.10	0.45
Cr_2O_3	0.05	0.00	0.01	0.01	0.03	0.00	0.01	0.01
MnO	0.28	0.00	0.09	0.06	0.69	0.01	0.25	0.10
SO_3	13.15	0.34	2.38	1.70	12.03	0.75	2.11	1.35
SnO_2	1.14	0.09	0.49	0.17	1.10	0.05	0.59	0.19
V_2O_3	0.71	0.00	0.36	0.15	1.24	0.08	0.39	0.17
Phase	**Anhydrite**							

Sample	**CRG1**				**CRG4**			
Wt% Oxides	***Max value***	***Min value***	***mean***	***mean SdT***	***Max value***	***Min value***	***mean***	***mean SdT***
SiO_2	3.31	0.29	1.73	0.89	8.12	0.15	1.85	1.42
Al_2O_3	0.80	0.00	0.44	0.23	1.58	0.00	0.36	0.26
MgO	0.20	0.06	0.12	0.05	0.30	0.00	0.07	0.07
FeO (tot)	0.41	0.16	0.24	0.08	0.50	0.00	0.14	0.10
Na_2O	0.68	0.22	0.43	0.12	0.46	0.00	0.12	0.09
K_2O	0.16	0.00	0.04	0.05	0.16	0.00	0.02	0.02
CaO	36.14	32.67	34.16	1.14	36.51	32.04	35.57	0.91
TiO_2	0.32	0.07	0.18	0.10	0.35	0.00	0.10	0.09
Cr_2O_3	0.00	0.00	0.00	0.00	0.03	0.00	0.01	0.01
MnO	0.14	0.00	0.08	0.05	0.18	0.00	0.04	0.03
SO_3	65.46	60.18	62.55	1.33	63.36	56.49	61.69	1.12
SnO_2	0.18	0.00	0.04	0.05	0.19	0.00	0.02	0.03
V_2O_3	0.00	0.00	0.00	0.00	0.04	0.00	0.00	0.00

Phase	**Pyroxene**							
Sample	**CRG1**				**CRG4**			
Wt% Oxides	***Max value***	***Min value***	***mean***	***mean SdT***	***Max value***	***Min value***	***mean***	***mean SdT***
SiO_2	58.04	46.94	52.17	2.23	54.76	45.15	47.77	1.89
Al_2O_3	14.14	2.39	8.39	2.46	17.10	3.72	7.53	3.30
MgO	18.93	0.86	9.57	3.37	13.37	0.00	8.96	4.50
FeO (tot)	9.33	3.18	6.58	1.19	19.56	3.93	10.00	2.14
Na_2O	6.99	0.97	3.89	1.23	7.36	0.54	2.94	2.22
K_2O	1.26	0.00	0.48	0.30	0.93	0.00	0.36	0.38
CaO	23.01	11.67	16.70	2.36	23.19	5.86	17.33	5.91
TiO_2	2.59	0.58	2.01	0.39	14.98	1.47	4.76	3.01

Cr_2O_3	0.08	0.00	0.04	0.02	0.07	0.00	0.03	0.01
MnO	0.47	0.08	0.17	0.05	0.78	0.20	0.33	0.07
SO_3	-	-	-	-	-	-	-	-
SnO_2	-	-	-	-	-	-	-	-
V_2O_3	-	-	-	-	-	-	-	-

Phase	**Ox Fe and Ti**							
Sample	**CRG1**				**CRG4**			
Wt% Oxides	***Max value***	***Min value***	***mean***	***mean SdT***	***Max value***	***Min value***	***mean***	***mean SdT***
SiO_2	29.94	0.13	7.99	7.77	36.33	0.30	12.17	8.96
Al_2O_3	8.45	0.00	2.66	2.27	8.85	0.89	3.38	2.02
MgO	4.21	0.00	1.91	1.38	9.35	0.58	4.20	1.21
FeO (tot)	97.25	31.08	70.67	18.44	87.95	12.34	55.79	22.16
Na_2O	4.16	0.56	1.89	0.97	5.21	0.00	1.61	1.39
K_2O	0.68	0.00	0.16	0.16	0.67	0.00	0.14	0.13
CaO	11.16	0.13	2.42	2.02	15.56	0.31	3.54	2.72
TiO_2	41.65	0.03	8.46	8.97	77.67	2.02	15.21	11.04
Cr_2O_3	1.97	0.00	0.29	0.29	1.03	0.00	0.23	0.18
MnO	0.87	0.22	0.42	0.13	1.31	0.18	0.58	0.20
SO_3	18.34	0.03	2.60	3.10	25.36	0.07	2.40	2.75
SnO_2	0.75	0.00	0.18	0.22	1.44	0.00	0.62	0.40
V_2O_3	1.28	0.00	0.33	0.35	0.57	0.00	0.12	0.12

Phase	**Cassiterite**							
Sample	**CRG1**				**CRG4**			
Wt% Oxides	***Max value***	***Min value***	***mean***	***mean SdT***	***Max value***	***Min value***	***mean***	***mean SdT***
SiO_2	33.14	0.31	9.38	6.51	13.78	0.51	4.90	4.46
Al_2O_3	7.00	0.27	2.69	1.78	3.20	0.05	1.14	1.00
MgO	1.64	0.00	0.63	0.47	0.61	0.00	0.20	0.17

FeO (tot)	2.32	0.13	0.79	0.54	0.62	0.11	0.29	0.15
Na_2O	5.03	0.31	2.11	1.24	2.43	0.00	0.72	0.67
K_2O	0.67	0.20	0.35	0.09	0.42	0.15	0.27	0.07
CaO	9.06	0.08	2.48	1.74	1.55	0.13	0.76	0.38
TiO_2	1.22	0.01	0.34	0.31	0.38	0.00	0.08	0.10
Cr_2O_3	0.03	0.00	0.01	0.01	0.05	0.00	0.01	0.01
MnO	0.01	0.00	0.00	0.00	0.11	0.00	0.02	0.03
SO_3	15.54	0.47	3.60	3.67	2.18	0.03	0.57	0.38
SnO_2	97.83	44.17	77.61	12.42	98.48	77.11	91.02	6.73
V_2O_3	0.11	0.00	0.01	0.02	0.07	0.00	0.01	0.02

In the next images SEM/BSE, RG1-RG2-RG3-RG4 it is possible to observe the microstructure of red gypsum. Here are also reported some EDS analyses.

RG1

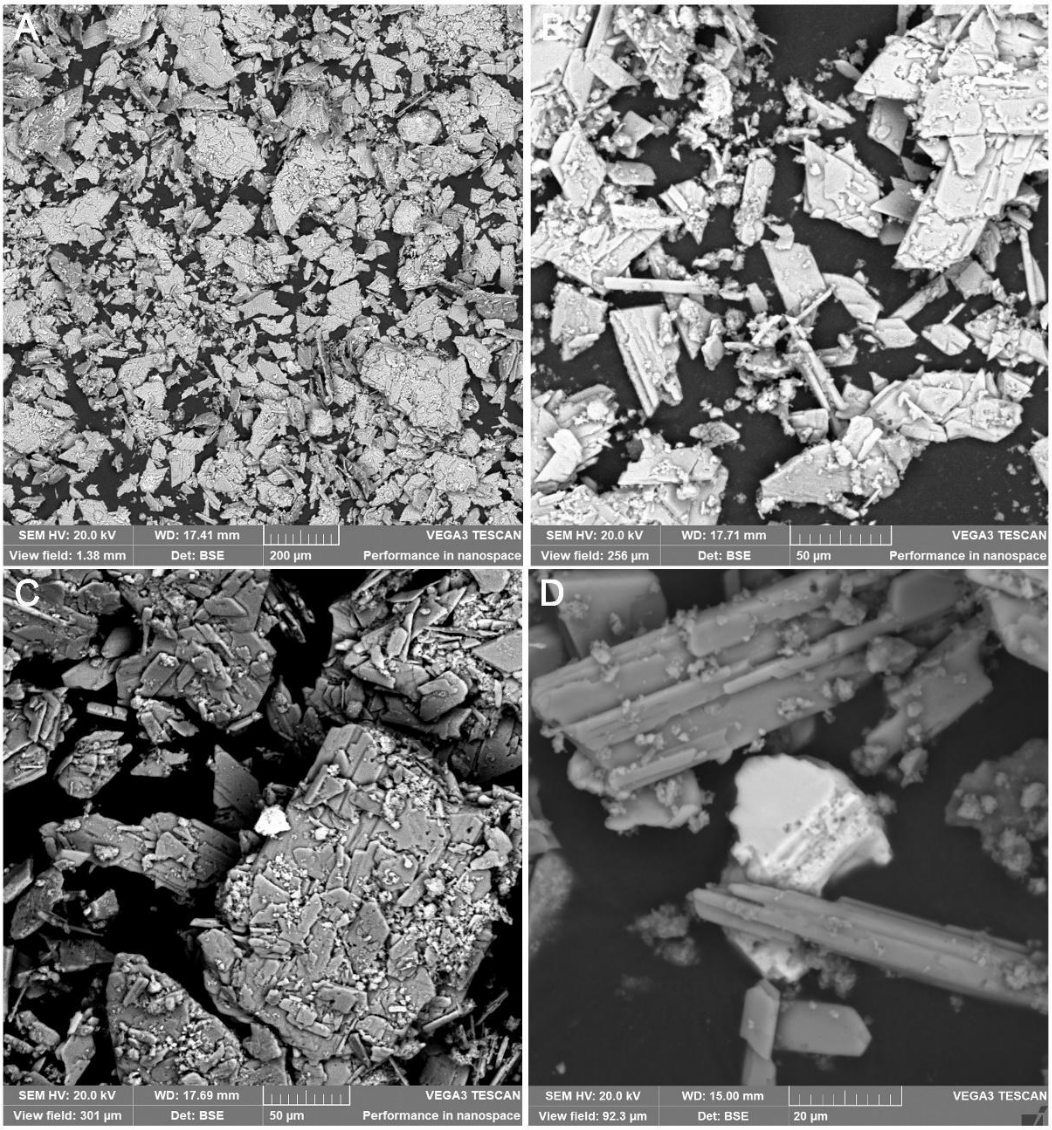

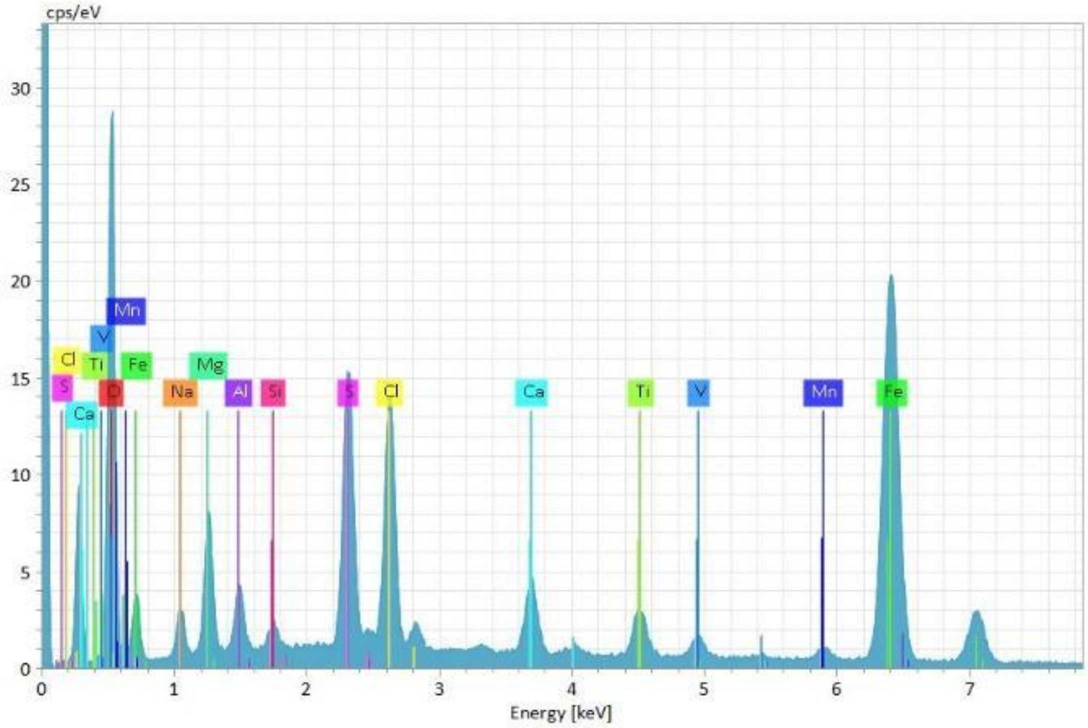
cps/eV
30
25
20
15
10
5
0
Mn
V
Cl
Ti
Fe
Mg
S
O
Na
Al
Si
S
Cl
Ca
Ti
V
Mn
Fe
Ca
0
1
2
3
4
5
6
7
Energy [keV]

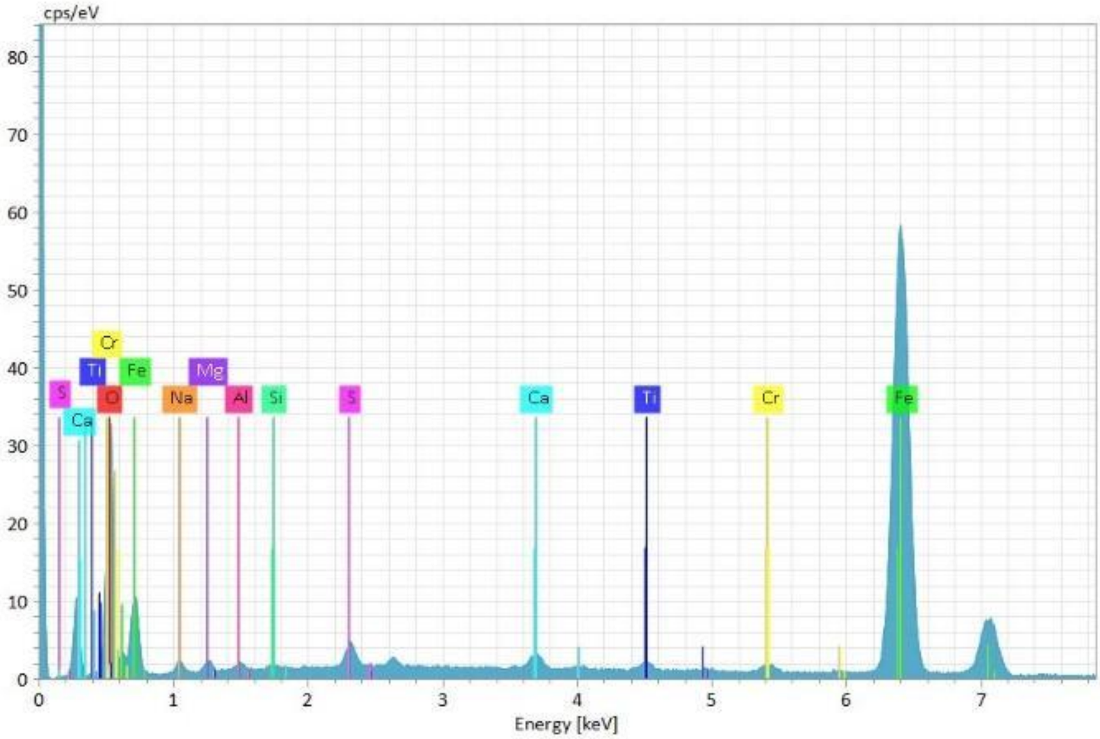
cps/eV
80
70
60
50
40
30
20
10
0
Cr
Ti
Fe
Mg
S
O
Na
Al
Si
S
Ca
Ti
Cr
Fe
Ca
0
1
2
3
4
5
6
7
Energy [keV]

RG2

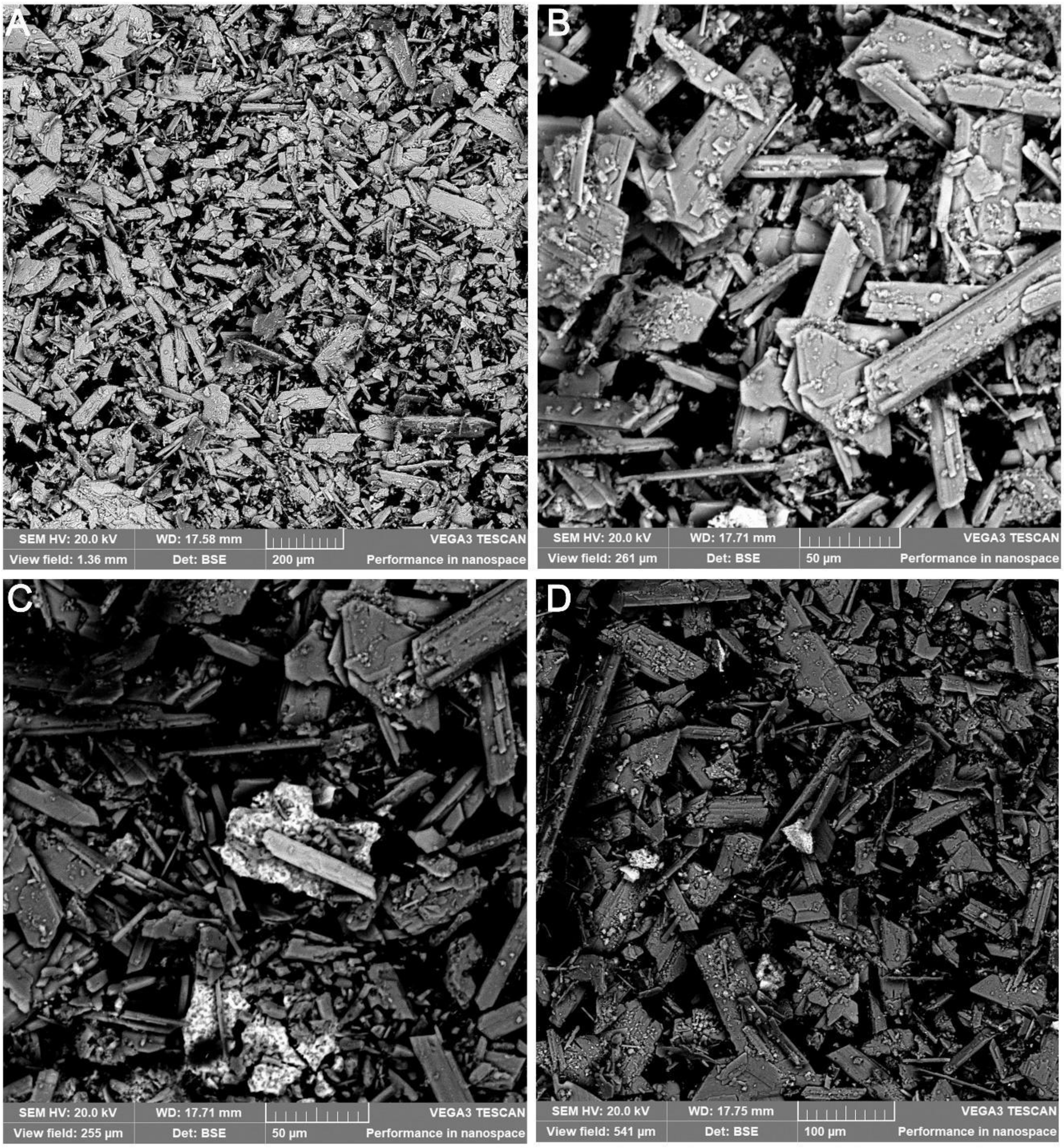
A
SEM HV: 20.0 kV
WD: 17.58 mm
VEGA3 TESCAN
View field: 1.36 mm
Det: BSE
200 µm
Performance in nanospace
B
SEM HV: 20.0 kV
WD: 17.71 mm
VEGA3 TESCAN
View field: 261 µm
Det: BSE
50 µm
Performance in nanospace
C
SEM HV: 20.0 kV
WD: 17.71 mm
VEGA3 TESCAN
View field: 255 µm
Det: BSE
50 µm
Performance in nanospace
D
SEM HV: 20.0 kV
WD: 17.75 mm
VEGA3 TESCAN
View field: 541 µm
Det: BSE
100 µm
Performance in nanospace

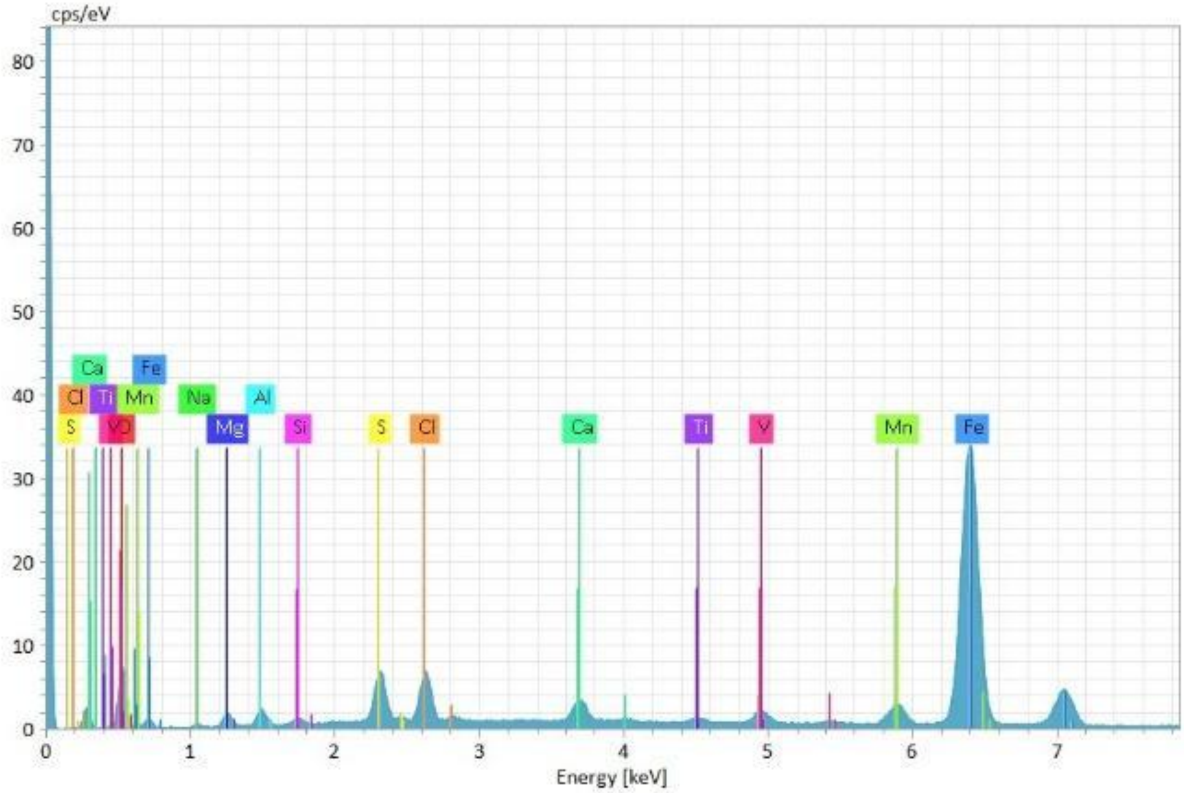
cps/eV
80
70
60
50
40
30
20
10
0
Ca
Fe
Cl
Ti
Mn
Na
Al
S
V
O
Mg
Si
S
Cl
Ca
Ti
V
Mn
Fe
0
1
2
3
4
5
6
7
Energy [keV]

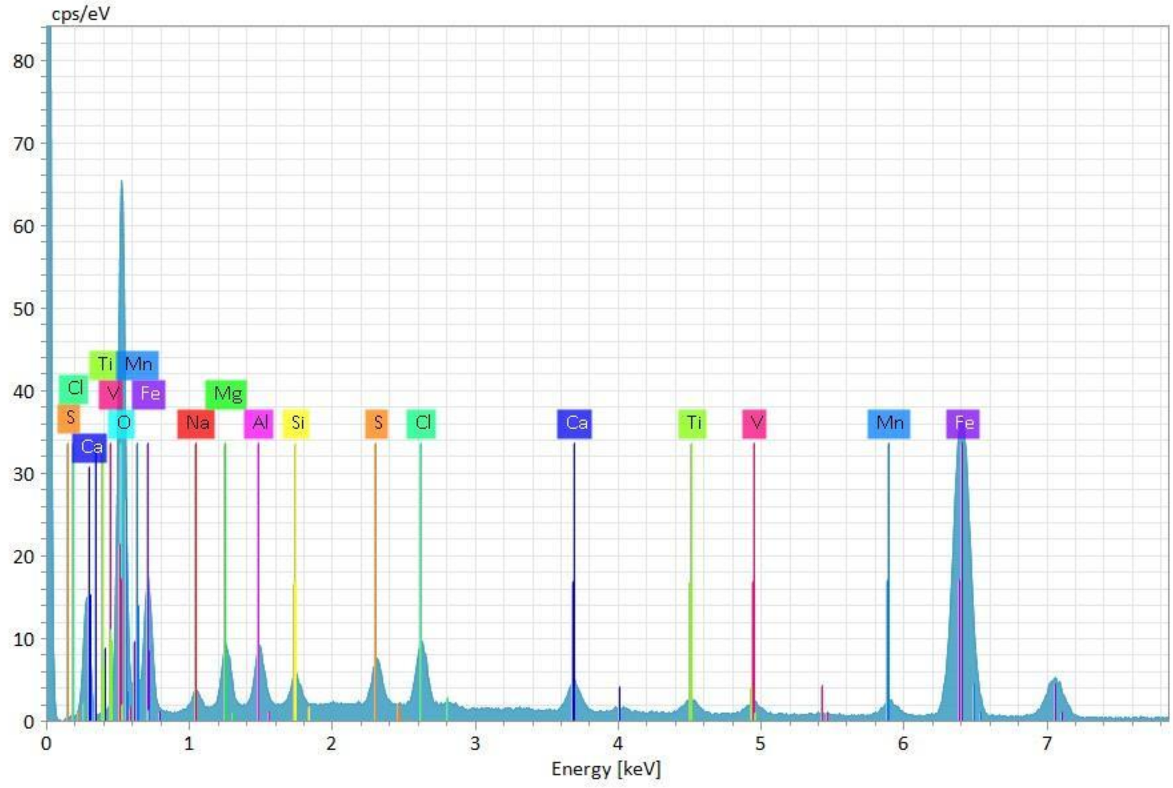
cps/eV
80
70
60
50
40
30
20
10
0
Ti
Mn
Cl
V
Fe
Mg
S
O
Na
Al
Si
S
Cl
Ca
Ti
V
Mn
Fe
Ca
0
1
2
3
4
5
6
7
Energy [keV]

RG3

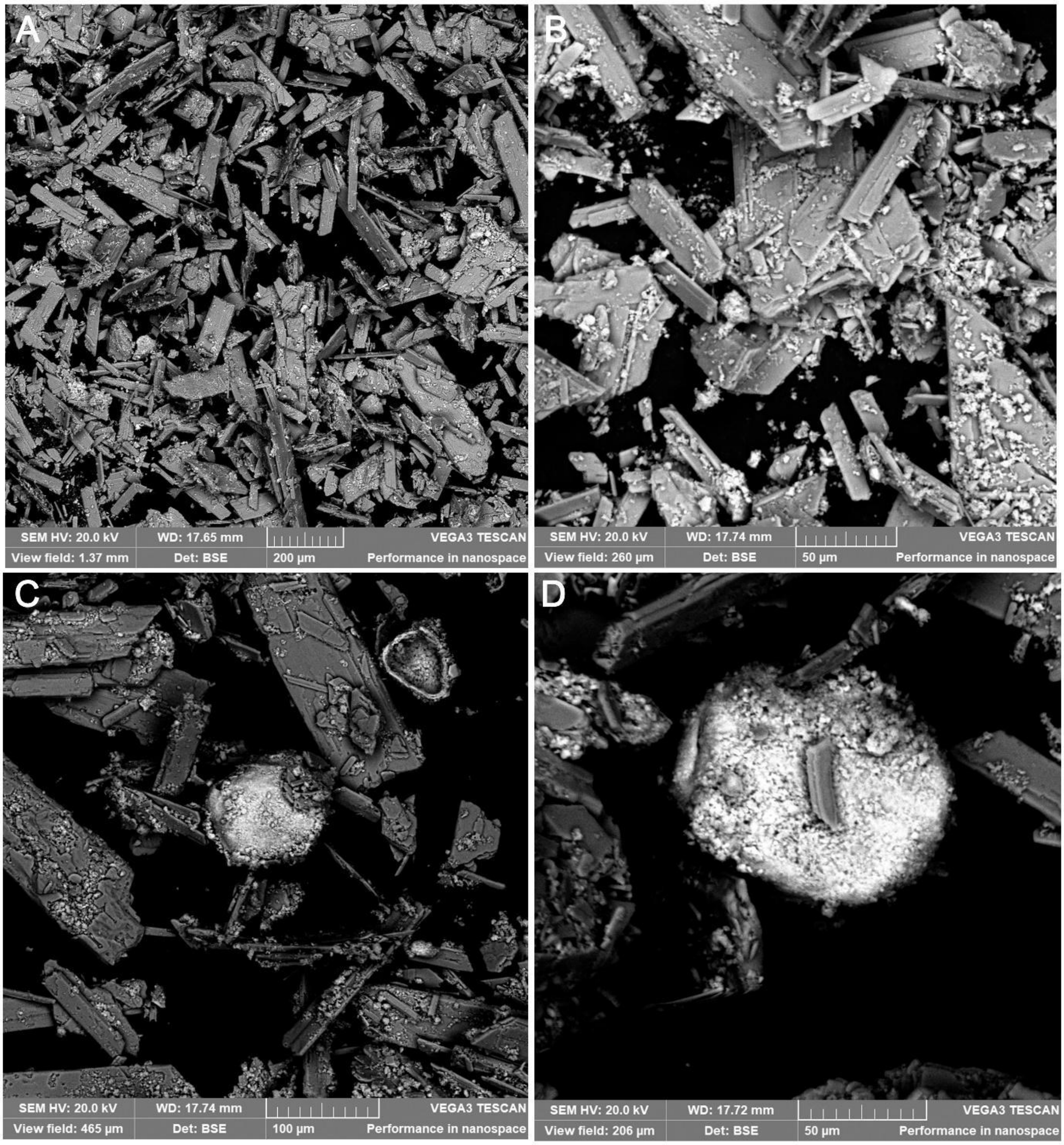
A
SEM HV: 20.0 kV
WD: 17.65 mm
VEGA3 TESCAN
View field: 1.37 mm
Det: BSE
200 μm
Performance in nanospace
B
SEM HV: 20.0 kV
WD: 17.74 mm
VEGA3 TESCAN
View field: 260 μm
Det: BSE
50 μm
Performance in nanospace
C
SEM HV: 20.0 kV
WD: 17.74 mm
VEGA3 TESCAN
View field: 465 μm
Det: BSE
100 μm
Performance in nanospace
D
SEM HV: 20.0 kV
WD: 17.72 mm
VEGA3 TESCAN
View field: 206 μm
Det: BSE
50 μm
Performance in nanospace

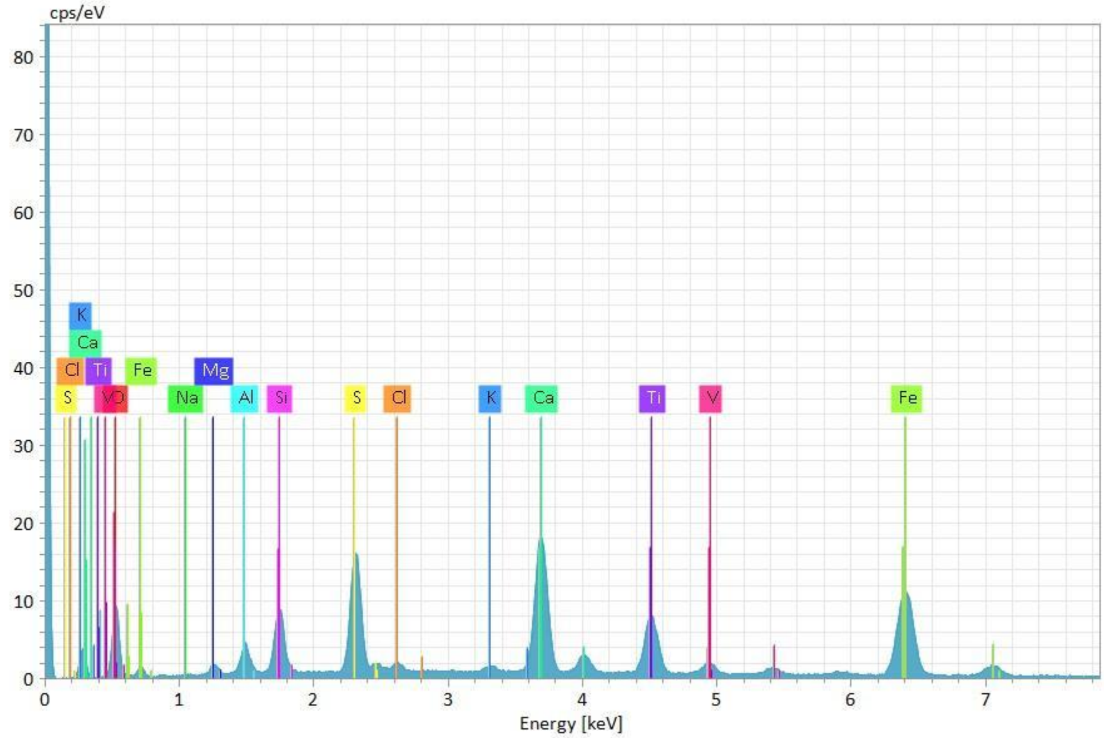
cps/eV
80
70
60
50
40
30
20
10
0
K
Ca
Cl
Ti
Fe
Mg
S
VO
Na
Al
Si
S
Cl
K
Ca
Ti
V
Fe
0
1
2
3
4
5
6
7
Energy [keV]

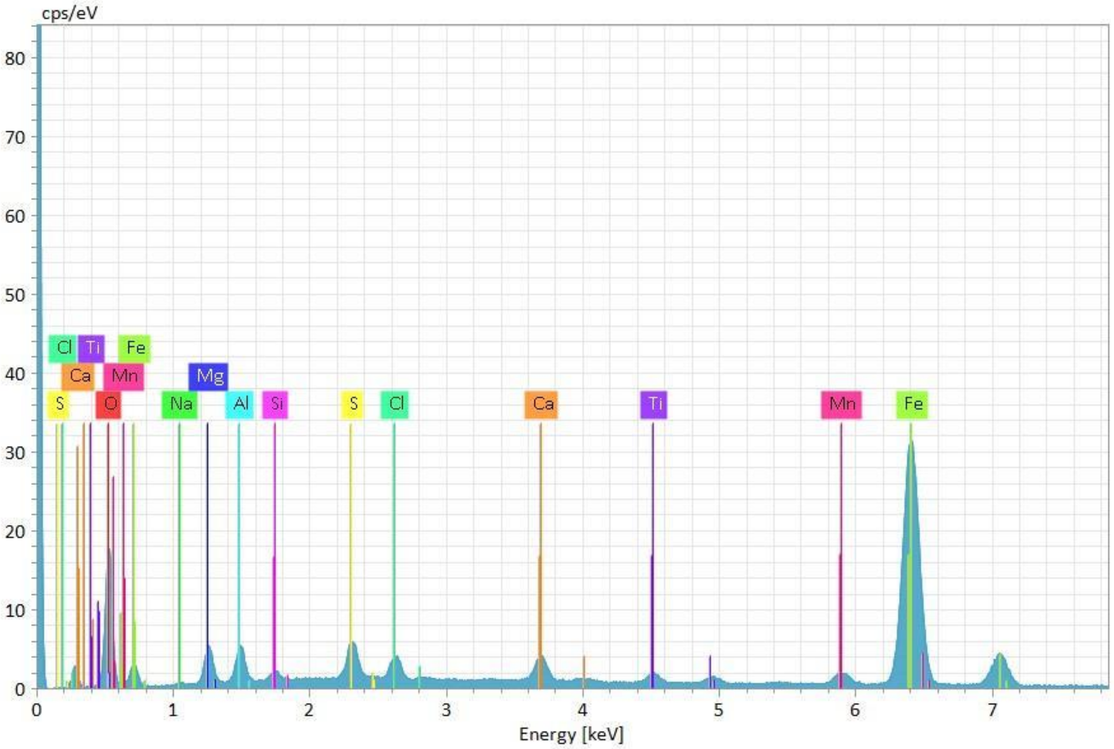
cps/eV
80
70
60
50
40
30
20
10
0
Cl
Ti
Fe
Ca
Mn
Mg
S
O
Na
Al
Si
S
Cl
Ca
Ti
Mn
Fe
0
1
2
3
4
5
6
7
Energy [keV]

RG4

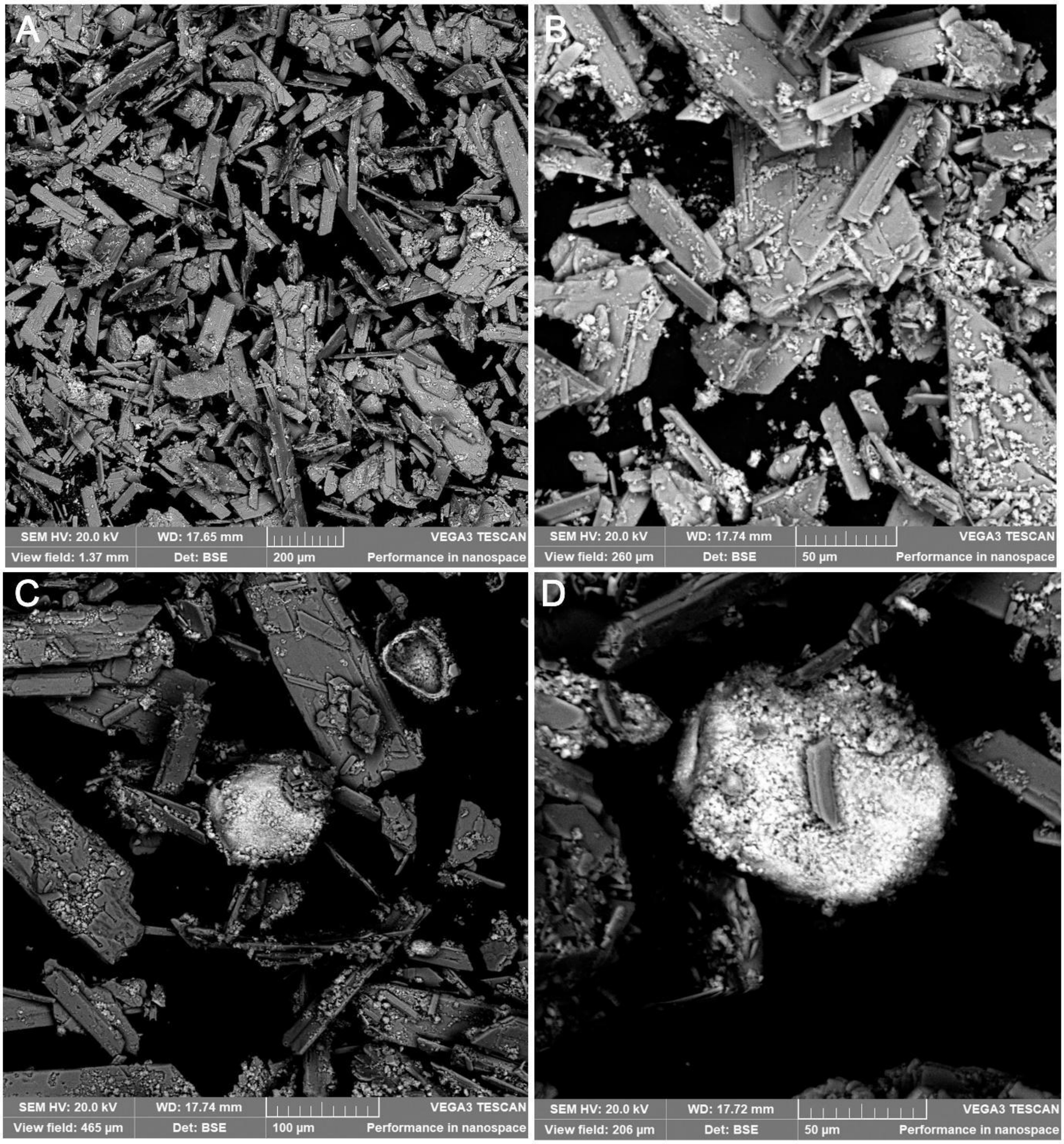
A
SEM HV: 20.0 kV
WD: 17.65 mm
VEGA3 TESCAN
View field: 1.37 mm
Det: BSE
200 µm
Performance in nanospace
B
SEM HV: 20.0 kV
WD: 17.74 mm
VEGA3 TESCAN
View field: 260 µm
Det: BSE
50 µm
Performance in nanospace
C
SEM HV: 20.0 kV
WD: 17.74 mm
VEGA3 TESCAN
View field: 465 µm
Det: BSE
100 µm
Performance in nanospace
D
SEM HV: 20.0 kV
WD: 17.72 mm
VEGA3 TESCAN
View field: 206 µm
Det: BSE
50 µm
Performance in nanospace

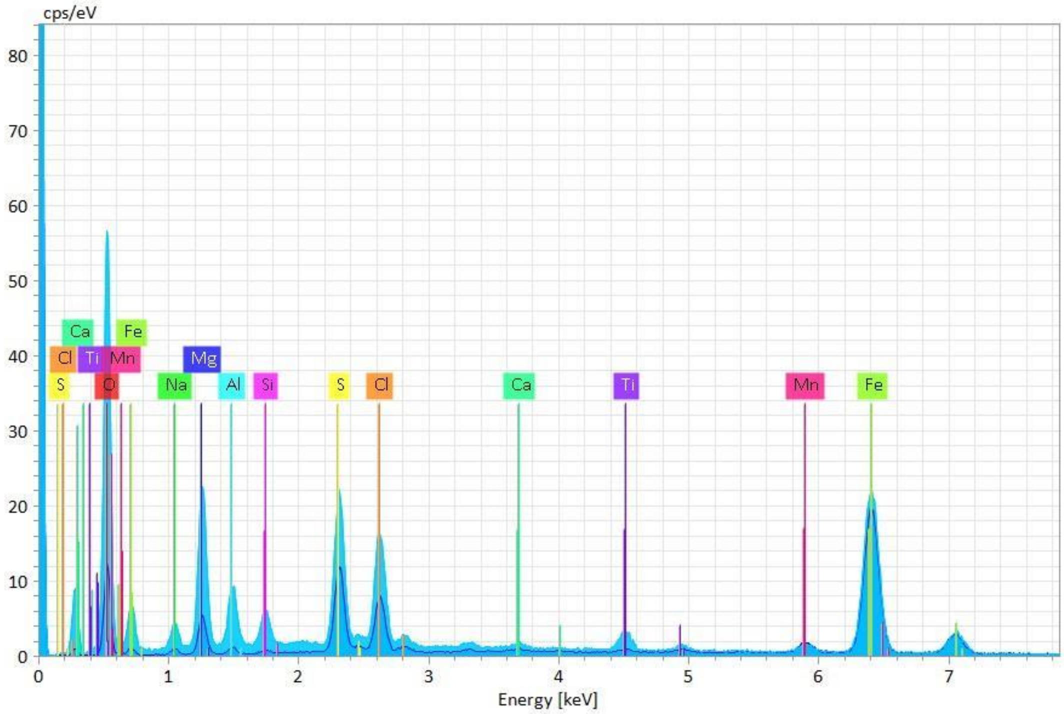
cps/eV
80
70
60
50
40
30
20
10
0
Ca
Fe
Cl
Ti
Mn
Mg
S
O
Na
Al
Si
S
Cl
Ca
Ti
Mn
Fe
0
1
2
3
4
5
6
7
Energy [keV]

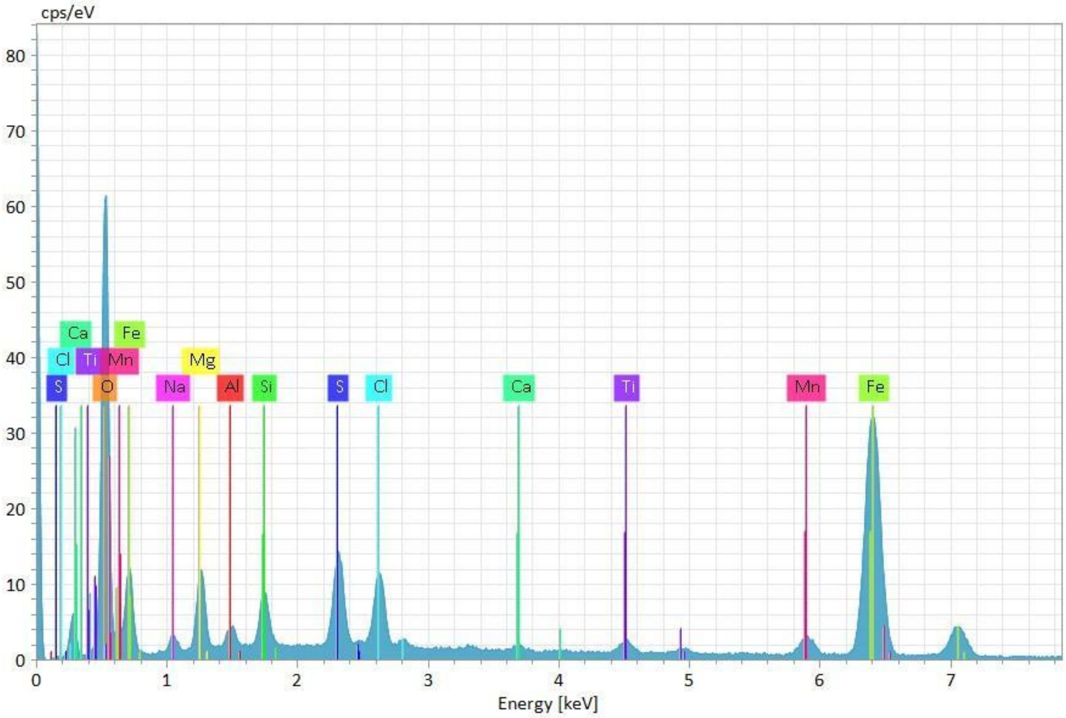
cps/eV
80
70
60
50
40
30
20
10
0
Ca
Fe
Cl
Ti
Mn
Mg
S
O
Na
Al
Si
S
Cl
Ca
Ti
Mn
Fe
0
1
2
3
4
5
6
7
Energy [keV]

Hereafter, some SEM/BSE images of CRG1 and EDS chemical analyses.

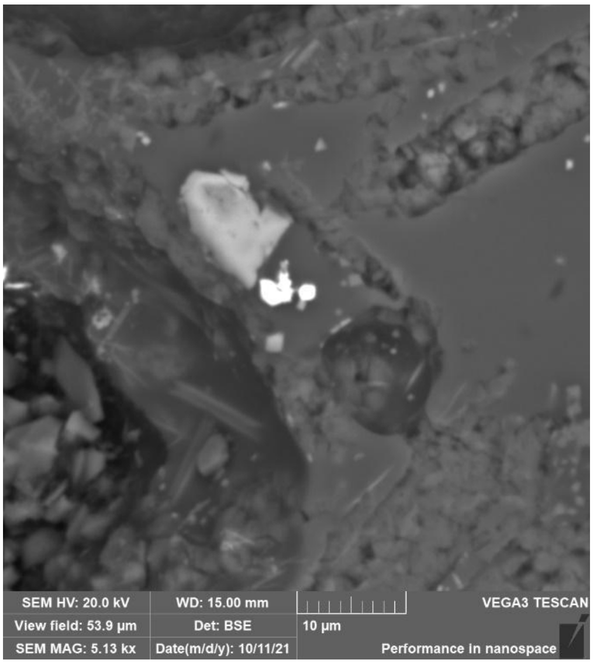

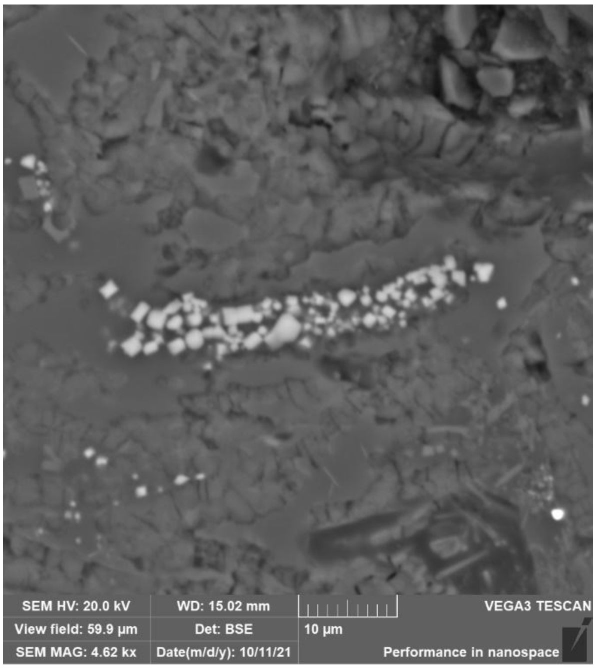

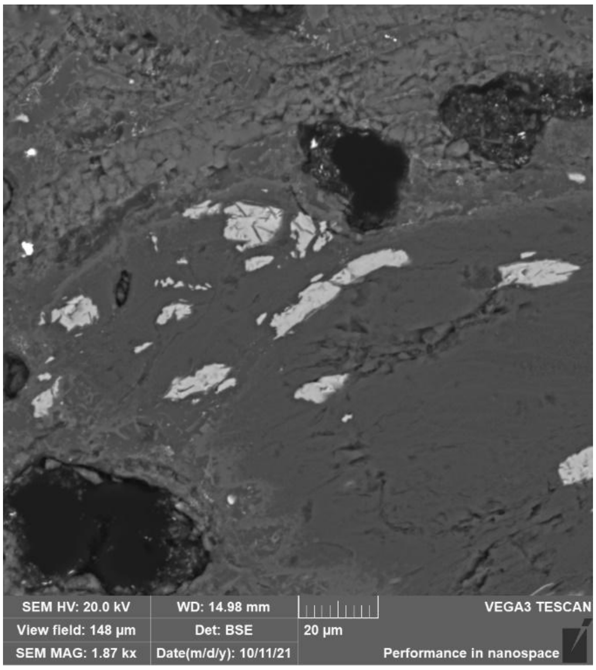

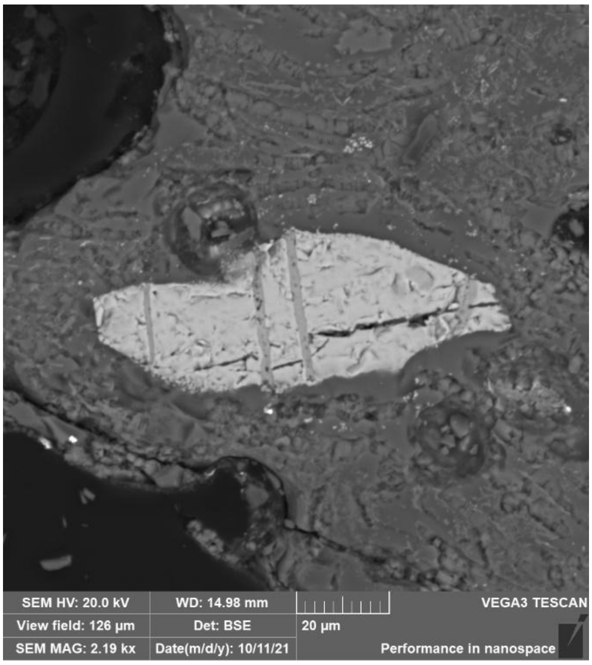

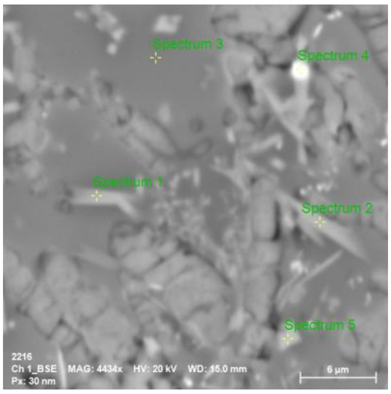
Spectrum 3
Spectrum 4
Spectrum 1
Spectrum 2
Spectrum 5
2216
Ch 1_BSE MAG: 4434x HV: 20 kV WD: 15.0 mm
6 µm
Px: 30 nm

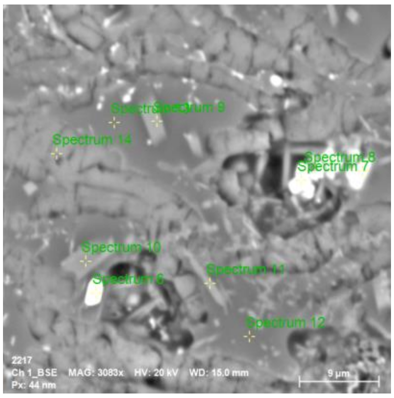
Spectrum 13
Spectrum 9
Spectrum 14
Spectrum 8
Spectrum 7
Spectrum 10
Spectrum 6
Spectrum 11
Spectrum 12
2217
Ch 1_BSE MAG: 3083x HV: 20 kV WD: 15.0 mm
9 µm
Px: 44 nm

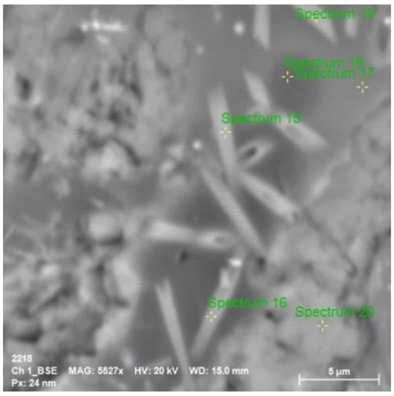
Spectrum 19
Spectrum 18
Spectrum 17
Spectrum 15
Spectrum 16
Spectrum 20
2218
Ch 1_BSE MAG: 5527x HV: 20 kV WD: 15.0 mm
5 µm
Px: 24 nm

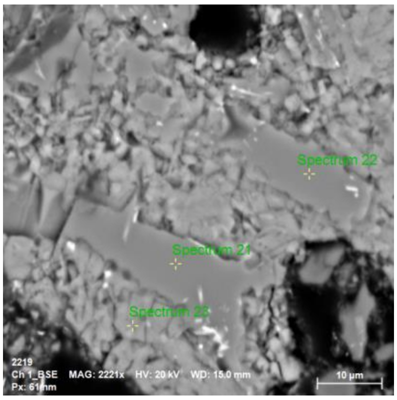
Spectrum 22
Spectrum 21
Spectrum 23
2219
Ch 1_BSE MAG: 2221x HV: 20 kV WD: 15.0 mm
10 µm
Px: 61 nm

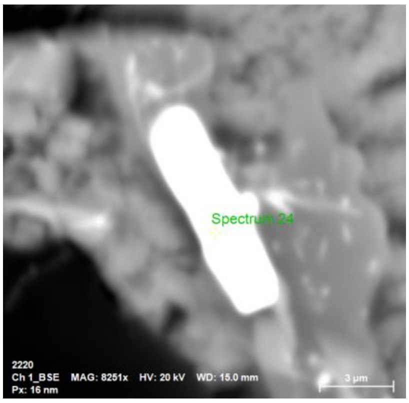
Spectrum 24
2220
Ch 1_BSE MAG: 8251x HV: 20 kV WD: 15.0 mm
3 µm
Px: 16 nm

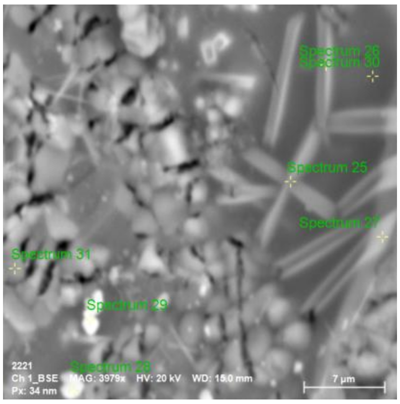
Spectrum 26
Spectrum 30
Spectrum 25
Spectrum 27
Spectrum 31
Spectrum 29
Spectrum 28
2221
Ch 1_BSE MAG: 3979x HV: 20 kV WD: 15.0 mm
7 µm
Px: 34 nm

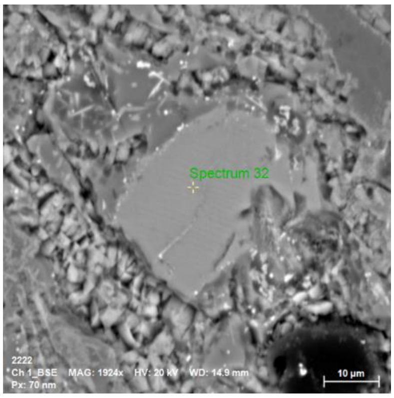
Spectrum 32
2222
Ch 1_BSE MAG: 1924x HV: 20 kV WD: 14.9 mm
10 µm
Px: 70 nm

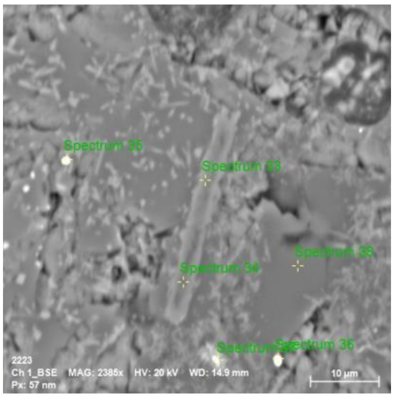
Spectrum 35
Spectrum 33
Spectrum 34
Spectrum 36
Spectrum 37
Spectrum 38
2223
Ch 1_BSE MAG: 2385x HV: 20 kV WD: 14.9 mm
10 µm
Px: 57 nm

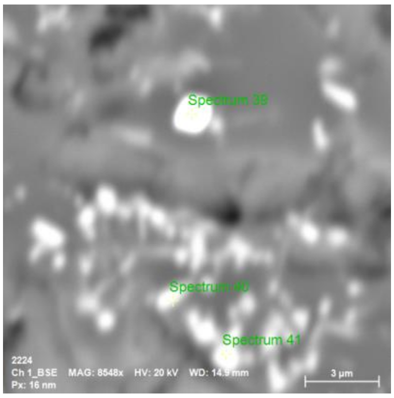
Spectrum 39
Spectrum 40
Spectrum 41
2224
Ch 1_BSE MAG: 8548x HV: 20 kV WD: 14.9 mm
3 µm
Px: 16 nm

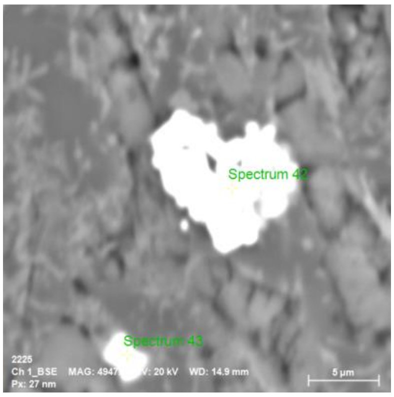
Spectrum 42
Spectrum 43
2225
Ch 1_BSE MAG: 4947x HV: 20 kV WD: 14.9 mm
5 µm
Px: 27 nm

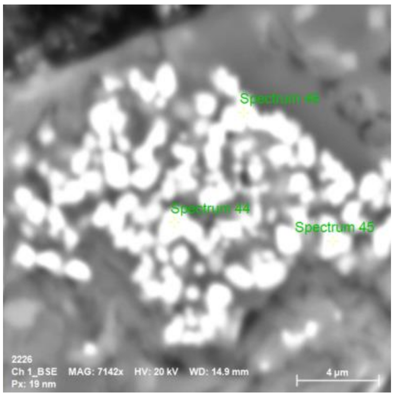
Spectrum 46
Spectrum 44
Spectrum 45
2226
Ch 1_BSE MAG: 7142x HV: 20 kV WD: 14.9 mm
4 µm
Px: 19 nm

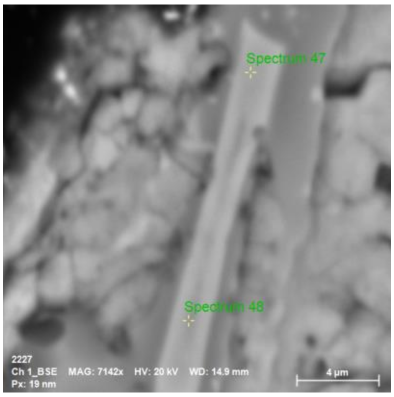
Spectrum 47
Spectrum 48
2227
Ch 1_BSE MAG: 7142x HV: 20 kV WD: 14.9 mm
4 µm
Px: 19 nm

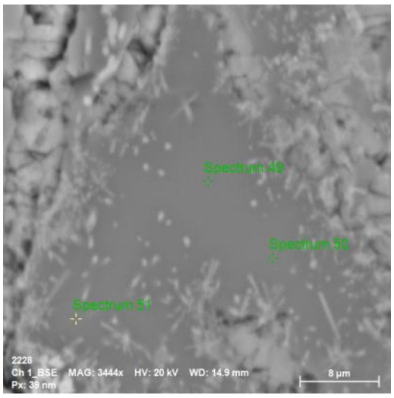
Spectrum 49
Spectrum 50
Spectrum 51
2228
Ch 1_BSE MAG: 3444x HV: 20 kV WD: 14.9 mm
Px: 39 nm
8 µm

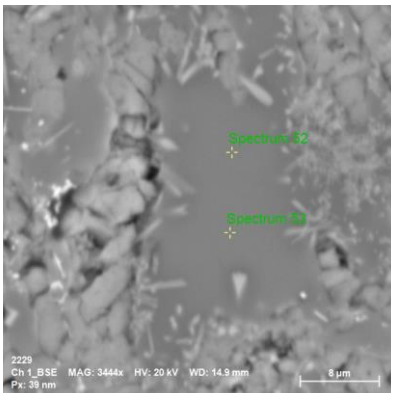
Spectrum 52
Spectrum 53
2229
Ch 1_BSE MAG: 3444x HV: 20 kV WD: 14.9 mm
Px: 39 nm
8 µm

Spectrum	**SiO2**	**Al2O3**	**MgO**	**FeO**	**Na2O**	**K2O**	**CaO**	**TiO2**	**Cr2O3**	**MnO**	**SO3**	**SnO2**	**V2O3**
Spectrum 1	54.36666	10.90363	6.601475	6.590421	4.695075	0.819254	11.78643	2.589375	0.026367	0.064325	0.915698	0.316446	0.324841
Spectrum 2	47.36482	8.542862	7.820494	6.550325	3.677631	0.505292	15.32791	1.992486	0.009054	0.185583	7.226423	0.678832	0.118292
Spectrum 3	62.10594	14.44572	1.262933	3.516357	7.212701	1.619433	5.665573	1.792336	0	0.056053	1.475789	0.488916	0.35824
Spectrum 4	61.85482	6.97019	5.554448	4.084325	4.27225	0.504319	10.11082	1.502486	0	0	4.674781	0.345162	0.126398
Spectrum 5	37.69368	7.134534	6.748269	4.709773	3.690993	0.344872	19.08451	1.511538	0	0.085968	18.38383	0.454529	0.157508
Spectrum 6	2.905665	0.83526	0.14968	0.371048	0.684166	0.198718	1.515014	0.100429	0.000626	0	3.564526	89.67487	0
Spectrum 7	9.338768	4.213263	0.501995	0.317264	3.027618	0.418638	1.229227	0.199276	0	0	1.57157	79.18238	0
Spectrum 8	8.858156	2.952797	0.257496	0.384845	3.024205	0.223061	0.718952	0.10533	0	0	0.656432	82.81873	0
Spectrum 9	49.93404	8.253539	10.03524	7.796628	3.309303	0.540618	16.26409	2.169091	0.01484	0.127151	0.735537	0.819928	0
Spectrum 10	49.03373	3.801382	13.36076	6.439903	1.7716	0.105156	20.46269	1.315839	0.05094	0.113501	2.250512	1.209304	0.084675
Spectrum 11	51.88349	8.469455	8.462876	6.188073	4.834007	0.528017	14.23146	1.723466	0.012613	0.063245	3.07208	0.436164	0.095061
Spectrum 12	62.08468	14.84065	0.647818	3.560654	7.686569	1.61943	5.047321	2.071466	0	0.01911	1.433271	0.668767	0.320266
Spectrum 13	58.36489	14.46259	2.215316	3.540233	7.127681	1.388206	7.992343	1.898412	0	0.019	2.036248	0.678874	0.276206
Spectrum 14	0.287039	0.000924	0.100068	0.158942	0.224117	0	33.36329	0.305109	0	0.101837	65.45867	0	0
Spectrum 15	50.13055	8.870111	6.681244	6.414689	3.828243	0.812622	14.95315	2.179285	0.020838	0.084338	5.249596	0.693172	0.082162
Spectrum 16	49.39258	9.001397	7.480987	6.144614	4.969578	0.644653	13.86729	1.866833	0.019757	0.099904	5.971043	0.404415	0.136954
Spectrum 17	48.49828	11.30287	0.732921	3.301776	6.012968	1.089688	11.49509	1.848652	0.002511	0.143723	14.95444	0.147681	0.4694
Spectrum 18	62.54735	13.72414	0.881428	4.097722	5.188364	1.536341	7.277986	2.38358	0.011251	0.060964	1.194231	0.386619	0.710019
Spectrum 19	54.82815	10.56583	5.813125	6.94615	4.611574	0.983329	11.40711	2.104889	0	0.115041	1.826635	0.47477	0.323395
Spectrum 20	1.536134	0.322024	0.056423	0.173595	0.378962	0	33.43267	0.25484	0	0.131347	63.63774	0.076266	0
Spectrum 21	50.47427	13.72747	4.204381	4.748711	5.767487	0.79764	14.50978	2.535017	0	0.088901	1.773589	0.642637	0.73012
Spectrum 22	51.28566	13.72509	3.836931	4.706462	6.062814	0.810546	13.99971	2.525043	0.015603	0.148559	1.77152	0.466562	0.645502
Spectrum 23	2.050939	0.635553	0.195098	0.190234	0.409543	0.025208	33.18613	0.079635	0	0.032829	63.18023	0.014604	0
Spectrum 24	2.120648	0.802133	0.189443	0.237738	0.956769	0.309538	6.28744	0.011702	0	0	15.50984	73.57475	0
Spectrum 25	48.00113	7.684275	11.07853	7.82635	3.937444	0.193966	16.25394	2.302227	0.064542	0.082361	2.110485	0.38196	0.082788
Spectrum 26	49.17483	8.537289	9.497925	7.829148	4.402163	0.395775	15.42522	2.103563	0.033228	0.036819	1.912164	0.622836	0.029041
Spectrum 27	47.42004	8.460348	9.384225	8.005725	3.948626	0.336244	16.05177	2.502194	0.024696	0.168759	3.20144	0.445528	0.050411
Spectrum 28	21.58866	6.379428	4.209054	38.14356	3.760571	0.304239	8.06733	4.688437	0.680994	0.255843	11.47168	0.434107	0.01609

Spectrum 29	29.93694	8.453648	3.824816	37.50352	4.078155	0.488705	5.542043	4.94075	0.731873	0.315796	3.803705	0.341648	0.038395
Spectrum 30	59.03494	15.18919	1.593864	3.366668	6.70615	1.120601	7.735621	2.165368	0.005851	0.129004	2.112017	0.516114	0.324618
Spectrum 31	3.310808	0.804342	0.203132	0.163154	0.678001	0.164439	32.6689	0.102303	0	0	61.72941	0.175509	0
Spectrum 32	53.47745	0.426864	12.15289	15.79888	0	0.07761	16.38716	0.704317	0	0.282296	0.483169	0.209359	0
Spectrum 33	54.40819	2.363628	18.65669	3.103318	1.420193	0.136201	17.5358	0.565187	0.044825	0.060238	1.354475	0.343192	0.008063
Spectrum 34	56.88379	2.855424	20.01449	3.042635	1.506742	0.145716	13.93402	0.777411	0.039367	0.074515	0.533394	0.092931	0.09956
Spectrum 35	17.82499	5.141381	1.28199	1.907696	3.29293	0.313535	9.057047	1.042016	0	0	15.53844	44.58302	0.016955
Spectrum 36	33.14246	6.99697	1.636347	2.322575	5.030216	0.672424	3.374161	1.221326	0	0	1.432499	44.17102	0
Spectrum 37	24.54333	6.328474	2.473606	46.21534	4.155407	0.537144	2.412476	11.889	0.105743	0.22622	0.698644	0.202465	0.212147
Spectrum 38	68.73587	11.69319	0.784853	3.475245	6.648052	1.915756	3.57546	1.667607	0	0	0.842806	0.478269	0.182899
Spectrum 39	16.04498	4.854075	1.142008	1.071999	3.90095	0.359759	2.139828	0.766937	0	0	2.312772	67.40669	0
Spectrum 40	21.76551	6.633156	3.423205	29.91465	4.340233	0.429084	10.47232	4.371278	0.197155	0.208974	17.70304	0.541397	0
Spectrum 41	18.69517	5.550723	2.752267	28.16512	3.643249	0.476077	12.0667	3.967662	0.201137	0.242142	23.73328	0.362002	0.144475
Spectrum 42	0.314155	0.267949	0	0.318869	0.30906	0.264072	0.083461	0.110311	0.032238	0	0.473501	97.82638	0
Spectrum 43	3.571876	0.899008	0.469983	0.26181	0.972141	0.425875	0.985762	0.080374	0.009711	0	1.456119	90.75812	0.109226
Spectrum 44	9.727533	3.245792	2.647675	70.39665	2.0156	0.219715	3.216014	3.451812	0.051551	0.455663	4.534101	0.029746	0.008152
Spectrum 45	12.63337	4.214435	3.216102	65.70357	3.154407	0.274731	2.685733	3.715543	0.04056	0.41583	3.725026	0	0.220686
Spectrum 46	12.48415	4.282553	3.565176	67.78887	2.74689	0.312474	2.048434	4.261004	0.034053	0.353871	1.854813	0.267717	0
Spectrum 47	50.8933	4.585389	14.61983	5.417337	2.20339	0.118304	19.01083	1.673652	0.071551	0.127954	0.901189	0.178017	0.199253
Spectrum 48	51.28536	3.989868	16.10923	4.738438	1.832836	0.099887	18.66386	1.17549	0.044001	0.210846	1.516836	0.333345	0
Spectrum 49	65.81613	12.53681	0.5744	3.735631	6.485581	1.604934	5.55308	1.81664	0	0.023833	1.216591	0.261559	0.374809
Spectrum 50	64.03736	13.02592	0.411389	3.796319	6.421528	1.471307	6.520523	2.227079	0.011193	0.11376	1.299189	0.296191	0.368244
Spectrum 51	62.06834	13.7867	0.443502	3.887907	6.899488	1.427037	7.09451	2.165948	0	0.022933	1.342057	0.575738	0.285842
Spectrum 52	59.70369	15.18817	1.066938	4.074262	7.39201	1.537768	6.303796	2.086466	0.005077	0.146281	1.458938	0.445317	0.591284
Spectrum 53	60.28733	14.85	1.159089	4.140785	7.335109	1.687977	6.216637	2.198884	0	0.117963	1.323032	0.387655	0.295543
Spectrum 54	0.390017	0.170907	4.161881	92.99609	0.557171	0.057455	0.644621	0.034001	0.292412	0.323603	0.371844	0	0
Spectrum 55	58.05571	14.08588	1.000785	4.741548	6.627321	1.394815	9.207788	2.410264	0.000197	0	1.645897	0.532479	0.29732
Spectrum 56	56.02551	13.94313	1.080437	4.724782	6.502061	1.218416	10.51932	2.789901	0	0.055952	1.824063	0.840639	0.475791
Spectrum 57	6.416916	2.188997	1.69234	80.84314	2.209538	0.010382	1.787857	1.256715	1.973596	0.869737	0.61908	0	0.1317
Spectrum 58	1.577617	0.646287	0.140768	0.131283	0.778883	0.273646	0.650058	0.06252	0.004201	0	1.31316	94.37293	0.048643

Spectrum 59	57.72462	13.79135	1.770037	4.324768	6.660282	1.243561	9.751109	2.116112	0	0.074998	1.50243	0.680197	0.36054
Spectrum 60	18.36964	5.751751	1.54612	36.1483	2.189952	0.679077	11.16294	4.69356	0.370698	0.391243	18.33664	0.104405	0.255675
Spectrum 61	50.1413	10.82375	5.20381	6.946984	4.378868	0.945444	14.60483	2.298063	0	0.079866	3.236118	1.210397	0.13057
Spectrum 62	0.181769	0.224087	0	96.74171	0.904681	0	0.467456	0.133527	0.060228	0.215982	0.047606	0	1.02295
Spectrum 63	0.431909	0.605536	0.377421	63.06512	0.719813	0.04401	0.42286	33.25604	0.015331	0.392098	0.154283	0	0.515581
Spectrum 64	0.200805	0.304828	0.199176	95.25062	1.103456	0	0.413915	0.747626	0.067922	0.361457	0.121654	0	1.22854
Spectrum 65	0.13809	1.098156	0.258754	68.06929	0.869932	0.022281	0.405914	28.1686	0.019736	0.382601	0.049827	0	0.516813

Hereafter, some SEM/BSE images of CRG4 and EDS chemical analyses.

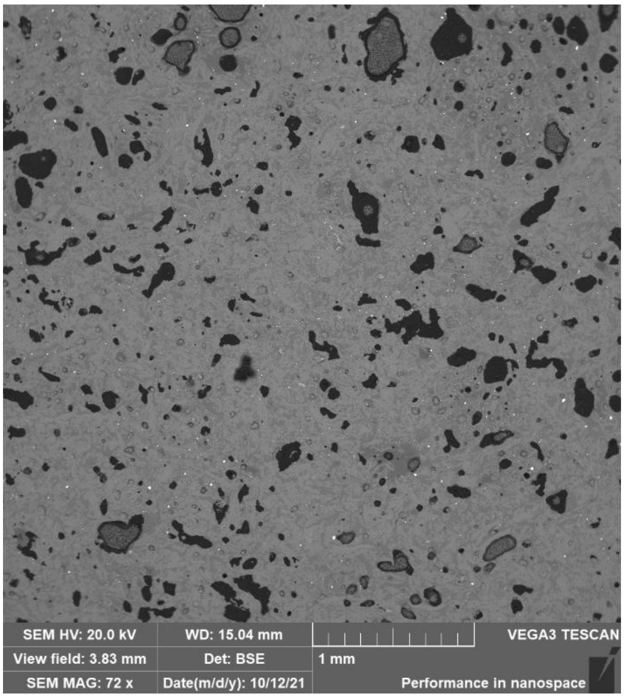

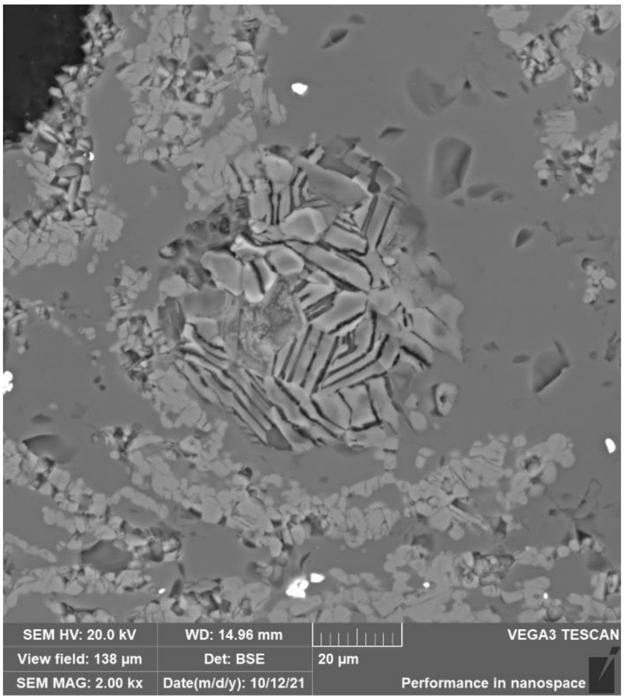

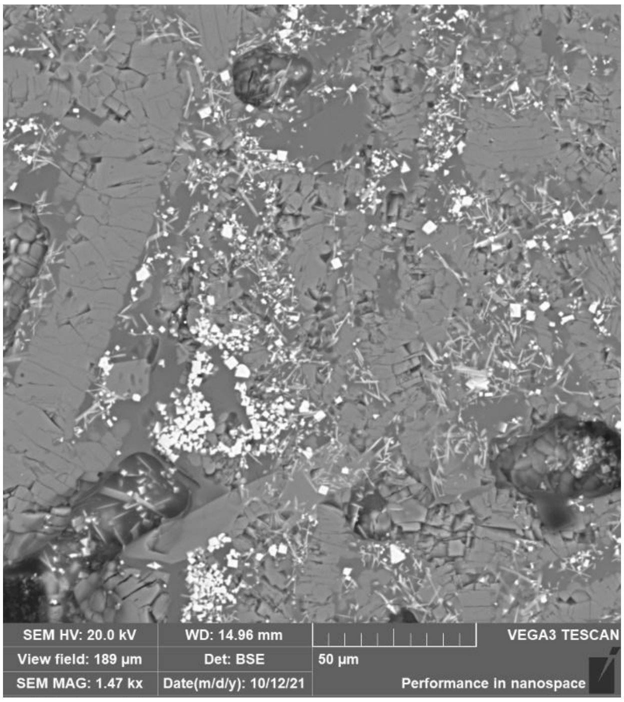

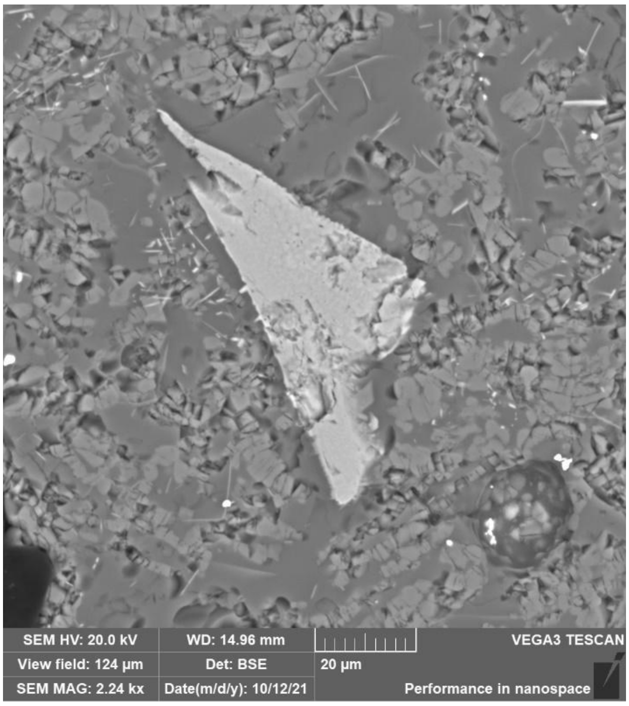

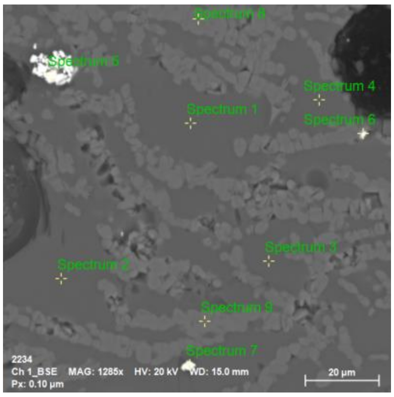
Spectrum 8
Spectrum 5
Spectrum 4
Spectrum 1
Spectrum 6
Spectrum 3
Spectrum 2
Spectrum 9
Spectrum 7
2234
Ch 1_BSE MAG: 1285x HV: 20 kV WD: 15.0 mm
Px: 0.10 µm
20 µm

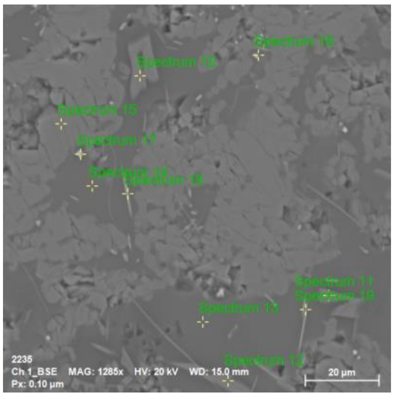
Spectrum 16
Spectrum 10
Spectrum 15
Spectrum 17
Spectrum 14
Spectrum 18
Spectrum 11
Spectrum 19
Spectrum 13
Spectrum 12
2235
Ch 1_BSE MAG: 1285x HV: 20 kV WD: 15.0 mm
Px: 0.10 µm
20 µm

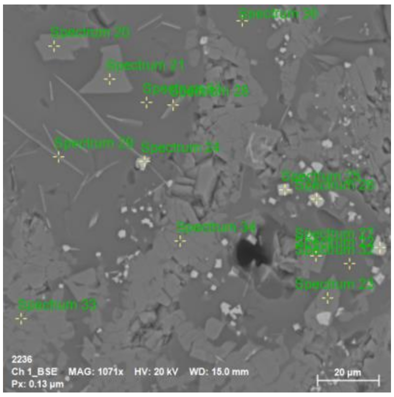
Spectrum 30
Spectrum 20
Spectrum 21
Spectrum 28
Spectrum 29
Spectrum 24
Spectrum 25
Spectrum 26
Spectrum 34
Spectrum 27
Spectrum 23
Spectrum 33
2236
Ch 1_BSE MAG: 1071x HV: 20 kV WD: 15.0 mm
Px: 0.13 µm
20 µm

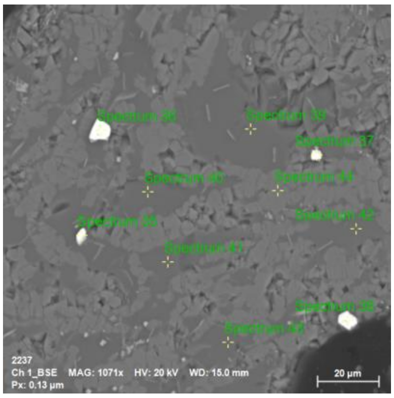
Spectrum 36
Spectrum 39
Spectrum 37
Spectrum 40
Spectrum 44
Spectrum 35
Spectrum 42
Spectrum 41
Spectrum 38
Spectrum 43
2237
Ch 1_BSE MAG: 1071x HV: 20 kV WD: 15.0 mm
Px: 0.13 µm
20 µm

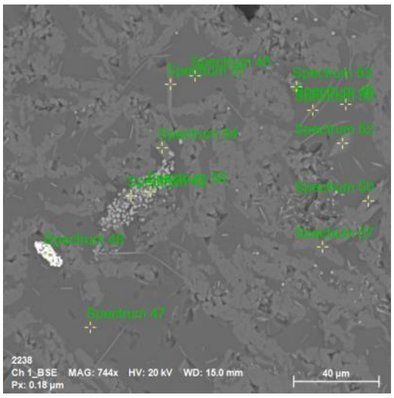
Spectrum 45
Spectrum 51
Spectrum 53
Spectrum 46
Spectrum 54
Spectrum 52
Spectrum 56
Spectrum 50
Spectrum 48
Spectrum 57
Spectrum 47
2238
Ch 1_BSE MAG: 744x HV: 20 kV WD: 15.0 mm
Px: 0.18 µm
40 µm

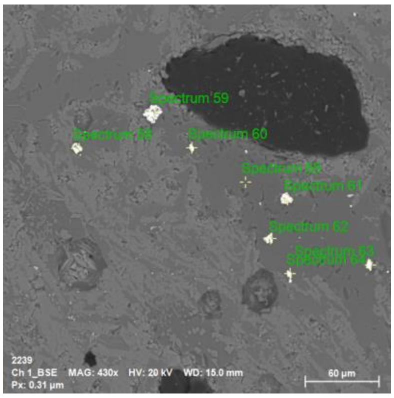
Spectrum 59
Spectrum 58
Spectrum 60
Spectrum 55
Spectrum 61
Spectrum 62
Spectrum 63
Spectrum 64
2239
Ch 1_BSE MAG: 430x HV: 20 kV WD: 15.0 mm
Px: 0.31 µm
60 µm

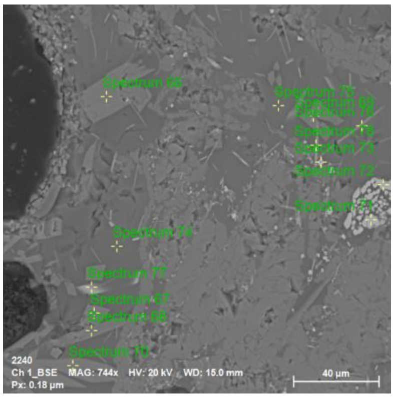
Spectrum 66
Spectrum 75
Spectrum 69
Spectrum 76
Spectrum 78
Spectrum 73
Spectrum 72
Spectrum 71
Spectrum 74
Spectrum 77
Spectrum 67
Spectrum 68
Spectrum 70
2240
Ch 1_BSE MAG: 744x HV: 20 kV WD: 15.0 mm
Px: 0.18 µm
40 µm

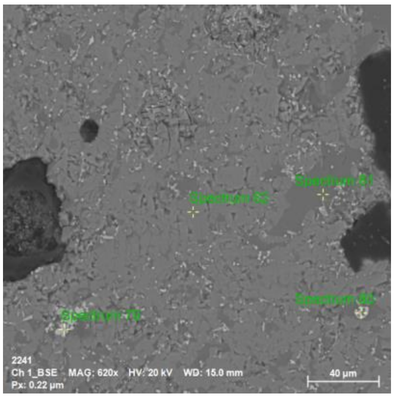
Spectrum 81
Spectrum 82
Spectrum 79
Spectrum 80
2241
Ch 1_BSE MAG: 620x HV: 20 kV WD: 15.0 mm
Px: 0.22 µm
40 µm

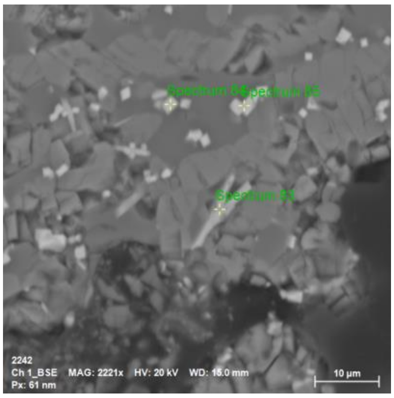
Spectrum 84
Spectrum 85
Spectrum 83
2242
Ch 1_BSE MAG: 2221x HV: 20 kV WD: 15.0 mm
Px: 61 nm
10 µm

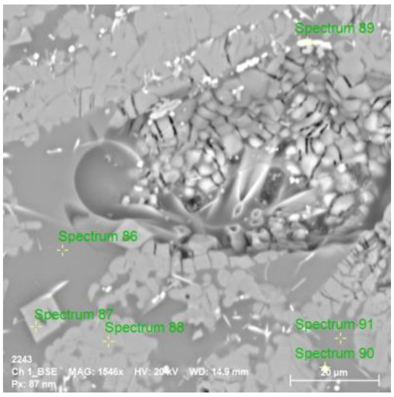
Spectrum 89
Spectrum 86
Spectrum 87
Spectrum 88
Spectrum 91
Spectrum 90
2243
Ch 1_BSE MAG: 1546x HV: 20 kV WD: 14.9 mm
Px: 87 nm
20 µm

Spectrum	**SiO2**	**Al2O3**	**MgO**	**FeO**	**Na2O**	**K2O**	**CaO**	**TiO2**	**Cr2O3**	**MnO**	**SO3**	**SnO2**	**V2O3**
Spectrum 1	62.891	13.240	2.180	3.243	6.103	1.300	7.254	1.773	0.012	0.118	0.961	0.683	0.245
Spectrum 2	62.783	13.628	2.122	3.081	6.128	1.183	7.141	1.763	0.000	0.190	1.141	0.760	0.080
Spectrum 3	63.022	13.585	2.113	3.095	6.326	1.173	6.932	1.847	0.000	0.107	1.021	0.528	0.251
Spectrum 4	61.457	13.429	2.264	3.318	6.206	1.252	7.187	2.014	0.028	0.224	1.296	1.095	0.230
Spectrum 5	0.550	0.060	0.000	0.114	0.000	0.146	0.216	0.000	0.014	0.084	0.335	98.480	0.000
Spectrum 6	12.743	3.202	0.590	0.491	2.435	0.277	1.198	0.150	0.000	0.000	1.018	77.896	0.000
Spectrum 7	2.698	0.772	0.179	0.148	0.386	0.238	0.128	0.011	0.025	0.000	0.345	95.010	0.059
Spectrum 8	1.323	0.341	0.016	0.107	0.033	0.005	35.796	0.267	0.000	0.031	62.080	0.000	0.000
Spectrum 9	0.689	0.143	0.000	0.000	0.000	0.000	36.505	0.059	0.002	0.000	62.602	0.000	0.000
Spectrum 10	46.836	5.045	12.445	8.843	1.434	0.068	20.868	2.841	0.035	0.256	0.514	0.649	0.167
Spectrum 11	46.338	7.041	11.302	8.941	1.877	0.103	20.143	2.587	0.004	0.230	0.625	0.589	0.219
Spectrum 12	45.577	6.611	11.652	8.486	1.636	0.000	22.195	2.515	0.016	0.290	0.499	0.454	0.069
Spectrum 13	58.640	14.389	2.479	4.274	6.731	1.141	7.806	1.933	0.025	0.308	1.304	0.556	0.415
Spectrum 14	58.672	13.058	3.405	4.198	6.029	0.983	9.416	1.853	0.014	0.252	1.245	0.522	0.353
Spectrum 15	0.247	0.000	0.000	0.030	0.045	0.000	36.510	0.027	0.000	0.040	63.101	0.000	0.000
Spectrum 16	36.332	8.784	3.382	21.579	4.554	0.668	5.192	16.149	0.020	0.210	1.748	1.186	0.196
Spectrum 17	31.342	7.791	3.449	36.699	4.711	0.511	5.044	4.903	0.068	0.310	4.412	0.658	0.103
Spectrum 18	17.427	4.731	2.082	26.886	3.389	0.232	15.561	3.509	0.059	0.180	25.357	0.587	0.000
Spectrum 19	42.807	11.790	2.650	16.212	6.044	0.765	5.063	12.518	0.010	0.210	0.837	0.746	0.350
Spectrum 20	44.900	4.638	12.867	9.597	0.869	0.000	22.887	2.938	0.001	0.297	0.244	0.654	0.107
Spectrum 21	45.437	4.161	12.752	9.671	1.076	0.000	22.171	3.300	0.039	0.404	0.322	0.470	0.197
Spectrum 22	45.592	4.677	12.876	9.145	1.050	0.000	21.815	3.505	0.018	0.369	0.332	0.524	0.098
Spectrum 23	45.852	4.428	13.136	8.731	1.068	0.000	22.234	3.167	0.026	0.339	0.414	0.454	0.152
Spectrum 24	4.688	1.614	4.284	75.904	1.024	0.072	0.751	9.410	0.372	0.668	0.224	0.984	0.004
Spectrum 25	2.458	1.195	4.529	77.966	0.274	0.015	1.386	9.537	0.683	0.761	0.572	0.625	0.000
Spectrum 26	1.163	1.073	4.442	79.951	0.242	0.017	0.850	9.894	0.568	0.812	0.388	0.497	0.105
Spectrum 27	0.717	0.893	4.772	79.855	0.184	0.000	1.280	9.723	0.502	0.826	0.424	0.824	0.000

Spectrum 28	45.771	12.166	2.107	13.308	7.239	0.897	5.747	10.794	0.003	0.169	0.894	0.653	0.253
Spectrum 29	45.447	10.807	4.204	12.512	5.747	0.759	8.510	9.505	0.041	0.306	1.282	0.568	0.312
Spectrum 30	52.128	12.846	5.017	5.044	5.461	0.777	13.044	2.528	0.003	0.402	1.678	0.579	0.493
Spectrum 31	56.026	15.232	2.198	3.915	7.006	1.046	9.548	2.076	0.007	0.289	1.892	0.078	0.687
Spectrum 32	55.159	16.703	2.209	2.848	7.428	1.052	9.511	2.088	0.000	0.256	1.659	0.387	0.700
Spectrum 33	0.929	0.161	0.057	0.127	0.068	0.000	36.048	0.000	0.000	0.031	62.543	0.036	0.000
Spectrum 34	2.672	0.329	0.017	0.197	0.003	0.000	34.494	0.023	0.017	0.102	62.145	0.000	0.000
Spectrum 35	2.297	0.591	0.177	0.396	0.434	0.200	1.288	0.028	0.015	0.052	2.177	92.344	0.000
Spectrum 36	0.515	0.117	0.103	0.119	0.044	0.170	0.348	0.243	0.029	0.000	0.467	97.847	0.000
Spectrum 37	0.615	0.194	0.183	0.146	0.205	0.239	0.581	0.000	0.009	0.000	1.331	96.431	0.066
Spectrum 38	1.155	0.052	0.000	0.326	0.000	0.216	0.519	0.010	0.016	0.054	0.616	97.030	0.006
Spectrum 39	59.142	12.908	2.838	4.724	6.089	1.103	8.390	2.232	0.000	0.209	1.399	0.533	0.432
Spectrum 40	59.375	12.874	2.905	4.758	5.673	1.145	8.738	1.808	0.010	0.313	1.230	0.826	0.345
Spectrum 41	60.969	12.517	2.769	4.550	6.055	1.182	7.602	2.141	0.015	0.158	1.020	0.609	0.414
Spectrum 42	57.517	13.453	3.611	4.418	6.143	1.040	9.669	1.709	0.000	0.206	1.365	0.764	0.106
Spectrum 43	47.293	11.275	3.081	3.624	5.689	0.787	13.934	1.325	0.000	0.188	12.034	0.474	0.295
Spectrum 44	3.750	0.644	0.131	0.084	0.154	0.021	34.355	0.346	0.018	0.000	60.426	0.035	0.035
Spectrum 45	58.272	12.745	3.298	4.657	5.835	1.034	9.379	1.916	0.000	0.160	1.596	0.694	0.413
Spectrum 46	57.534	13.008	3.194	4.760	6.192	1.019	9.354	2.113	0.001	0.240	1.628	0.518	0.440
Spectrum 47	59.220	13.332	3.015	4.484	6.233	1.163	8.433	2.071	0.000	0.147	1.101	0.636	0.164
Spectrum 48	10.335	2.361	0.416	0.486	1.076	0.310	1.434	0.380	0.000	0.000	0.367	82.835	0.000
Spectrum 49	4.549	1.845	3.741	77.162	0.925	0.083	1.129	8.204	0.159	0.644	0.432	1.126	0.000
Spectrum 50	46.060	4.855	12.636	9.151	1.099	0.000	22.091	2.624	0.014	0.280	0.368	0.807	0.016
Spectrum 51	48.121	10.826	2.919	13.915	5.443	0.858	5.685	10.194	0.040	0.178	0.903	0.774	0.143
Spectrum 52	46.574	10.394	3.244	13.955	4.739	0.924	7.092	10.466	0.026	0.273	1.078	0.976	0.259
Spectrum 53	46.991	6.089	11.697	8.021	1.982	0.100	21.073	2.493	0.008	0.283	0.508	0.546	0.208
Spectrum 54	46.008	4.095	12.854	9.957	1.207	0.022	21.352	3.019	0.026	0.242	0.439	0.726	0.054
Spectrum 55	50.386	11.772	3.242	10.686	5.960	0.947	6.947	7.507	0.018	0.294	1.180	0.754	0.307
Spectrum 56	13.484	3.195	0.582	69.905	0.000	0.211	1.929	8.271	0.206	0.631	0.386	1.201	0.000

Spectrum 57	2.774	0.706	0.232	0.197	0.123	0.030	35.001	0.111	0.005	0.046	60.773	0.000	0.000
Spectrum 58	13.780	3.109	0.607	0.618	1.878	0.413	1.545	0.216	0.000	0.000	0.721	77.112	0.000
Spectrum 59	10.896	2.494	0.403	0.218	1.945	0.371	1.137	0.000	0.000	0.000	0.231	82.305	0.000
Spectrum 60	1.089	0.399	0.042	0.207	0.018	0.307	0.629	0.015	0.025	0.000	0.351	96.919	0.000
Spectrum 61	9.343	1.938	0.172	0.155	1.551	0.422	0.808	0.021	0.008	0.000	0.212	85.353	0.017
Spectrum 62	2.238	0.646	0.027	0.218	0.432	0.256	0.287	0.039	0.000	0.000	0.028	95.828	0.000
Spectrum 63	0.549	0.048	0.000	0.192	0.000	0.160	0.454	0.022	0.051	0.000	0.394	98.129	0.000
Spectrum 64	1.600	0.482	0.039	0.162	0.337	0.309	0.657	0.000	0.017	0.107	0.228	96.062	0.000
Spectrum 65	68.219	13.796	1.378	1.698	6.450	1.575	4.069	0.958	0.000	0.105	0.754	0.903	0.096
Spectrum 66	45.449	4.258	12.307	10.057	1.066	0.005	22.413	3.369	0.023	0.220	0.093	0.717	0.024
Spectrum 67	46.658	2.228	10.909	11.411	0.000	0.000	23.661	3.354	0.047	0.320	0.329	0.943	0.140
Spectrum 68	47.084	3.907	13.075	9.064	1.254	0.006	22.079	2.360	0.030	0.320	0.190	0.632	0.000
Spectrum 69	42.484	5.072	12.249	11.242	1.303	0.027	20.220	5.940	0.014	0.279	0.376	0.697	0.096
Spectrum 70	46.152	3.698	12.781	10.147	1.138	0.000	21.779	2.782	0.062	0.290	0.210	0.953	0.009
Spectrum 71	1.981	1.114	3.527	80.879	0.265	0.000	0.926	9.135	0.240	0.699	0.370	0.743	0.120
Spectrum 72	1.749	1.149	4.507	79.698	0.341	0.000	0.793	9.295	0.437	0.656	0.257	1.107	0.011
Spectrum 73	6.679	2.205	4.134	69.603	1.147	0.075	2.294	8.342	1.030	0.610	2.695	1.159	0.028
Spectrum 74	54.888	13.760	2.837	4.411	6.464	0.986	10.334	2.373	0.008	0.490	2.133	0.642	0.674
Spectrum 75	55.338	12.791	3.604	4.776	5.973	0.941	11.300	2.151	0.000	0.251	1.596	0.873	0.405
Spectrum 76	47.894	10.753	3.600	10.954	5.476	0.808	9.257	8.545	0.000	0.342	1.344	0.561	0.465
Spectrum 77	20.156	6.527	3.990	31.574	3.795	0.288	2.654	29.103	0.052	0.330	0.393	0.855	0.283
Spectrum 78	46.367	7.911	0.000	18.974	0.649	0.833	7.633	14.637	0.018	0.272	1.452	0.868	0.387
Spectrum 79	2.866	1.411	4.215	75.780	0.513	0.000	2.548	8.301	0.231	0.807	2.090	1.239	0.000
Spectrum 80	12.507	3.474	4.063	65.312	2.260	0.142	1.998	7.586	0.251	0.668	0.556	1.142	0.041
Spectrum 81	47.839	10.720	3.385	3.724	5.575	0.730	14.357	1.416	0.014	0.320	11.256	0.349	0.316
Spectrum 82	0.145	0.043	0.040	0.079	0.103	0.000	36.109	0.029	0.000	0.065	63.358	0.029	0.000
Spectrum 83	9.245	2.510	5.059	40.775	0.000	0.091	2.786	36.986	0.009	0.527	1.790	0.031	0.190
Spectrum 84	15.691	4.524	4.306	60.604	2.822	0.143	2.370	6.887	0.198	0.628	0.797	1.007	0.024
Spectrum 85	5.144	2.166	4.470	74.336	1.489	0.000	1.346	7.834	0.251	0.812	0.715	1.435	0.000

Spectrum 86	58.126	13.418	2.922	4.470	6.198	1.018	9.278	1.795	0.000	0.172	1.490	0.703	0.409
Spectrum 87	45.710	5.082	12.264	9.559	1.472	0.005	21.596	2.650	0.024	0.249	0.520	0.698	0.170
Spectrum 88	0.377	0.074	0.018	0.000	0.078	0.000	36.499	0.053	0.032	0.000	62.870	0.000	0.000
Spectrum 89	22.001	5.550	2.373	44.837	3.264	0.280	6.261	5.149	0.719	0.371	8.326	0.742	0.127
Spectrum 90	34.882	8.847	3.821	35.479	5.210	0.468	4.220	4.510	0.162	0.433	1.451	0.399	0.116
Spectrum 91	57.567	13.033	3.292	4.133	6.216	0.956	9.780	1.988	0.006	0.334	1.578	0.539	0.577

APPENDIX III

The following image is the supplementay material of the article on flotation muds. There are visible the two XRPD patterns

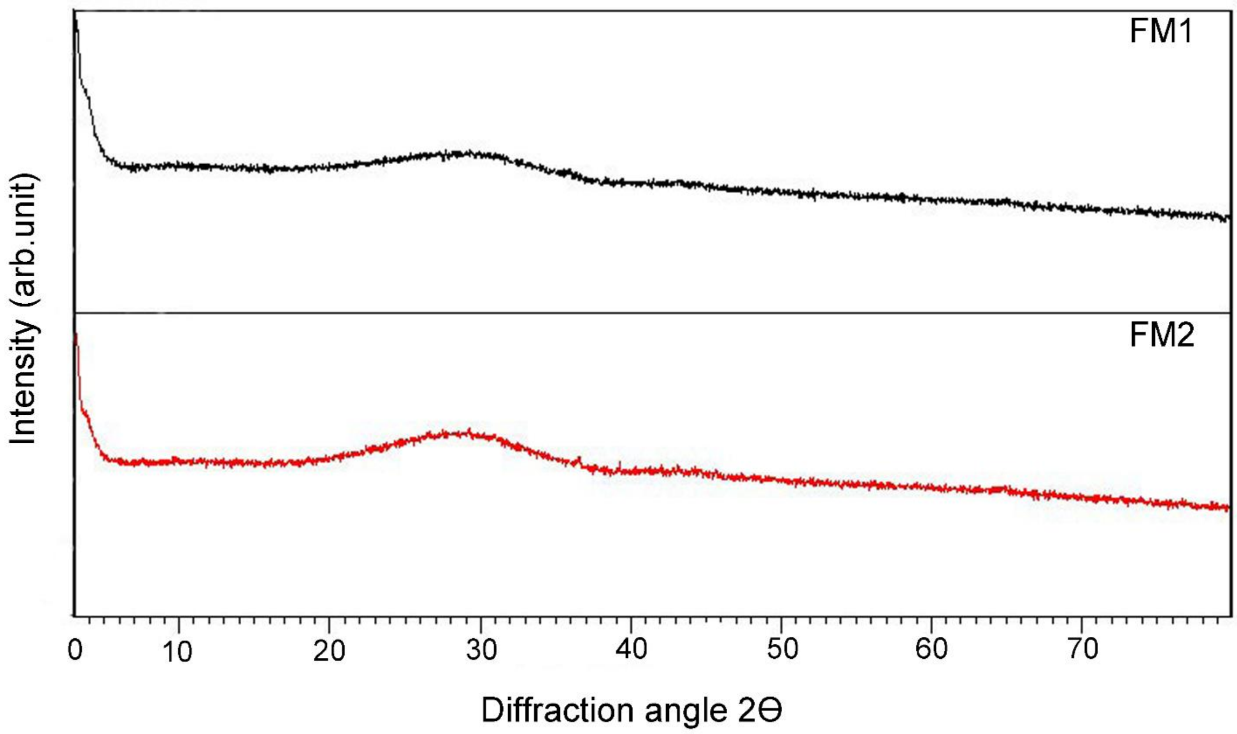

Here after are reported some additional SEM/BSE images of CFM1, and the images where the EDS analyses have been done. Lastly the microanalyses.

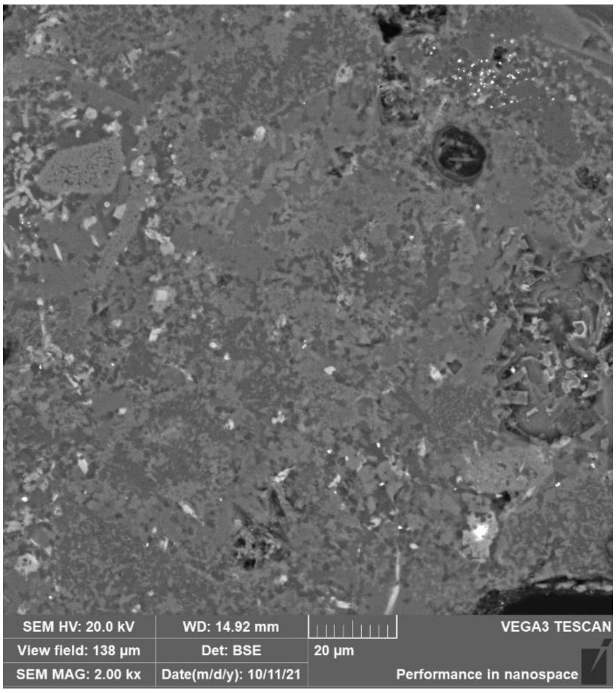

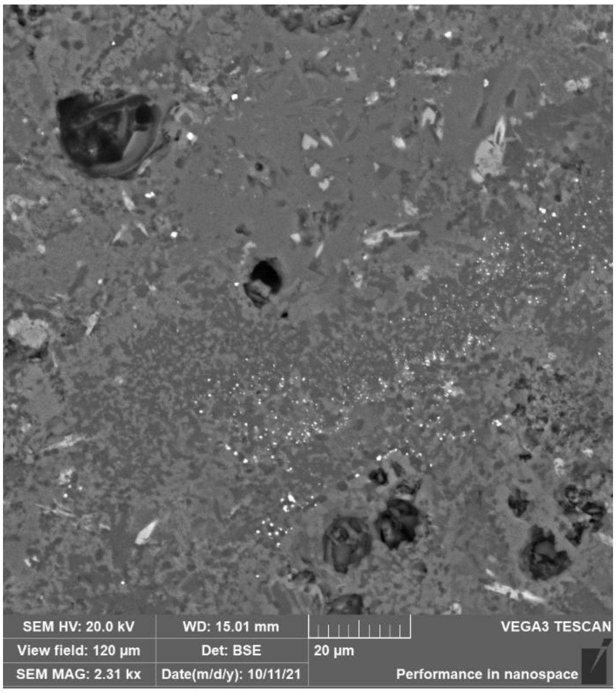

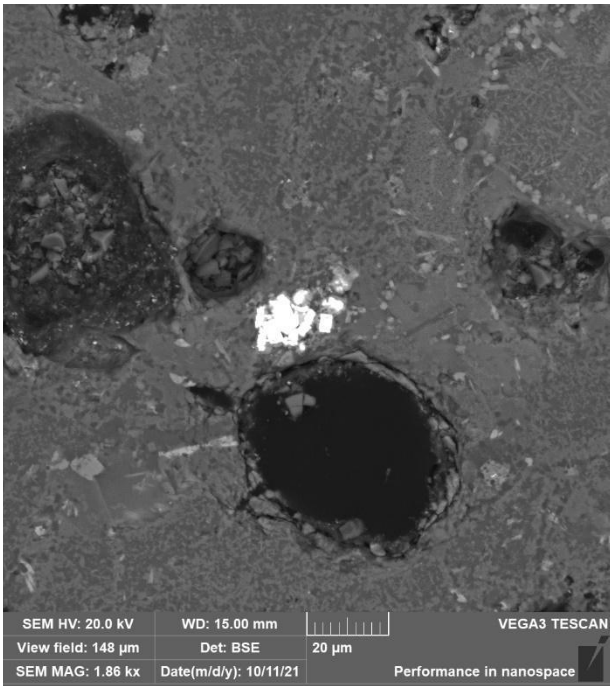

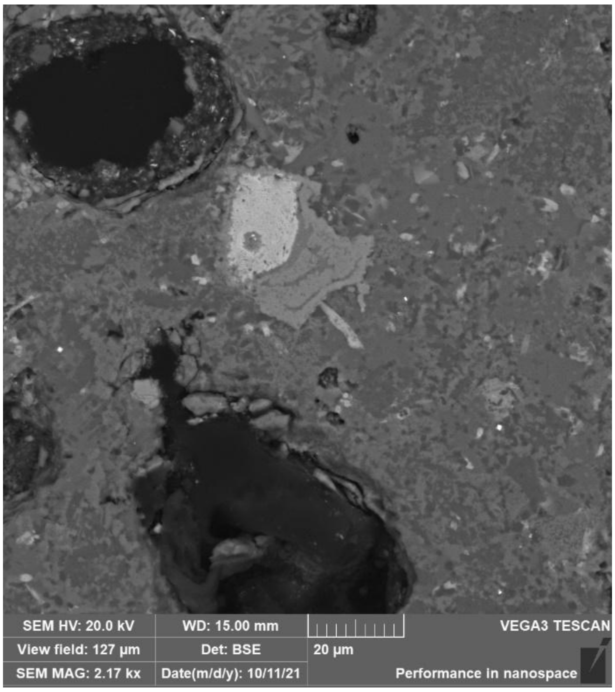

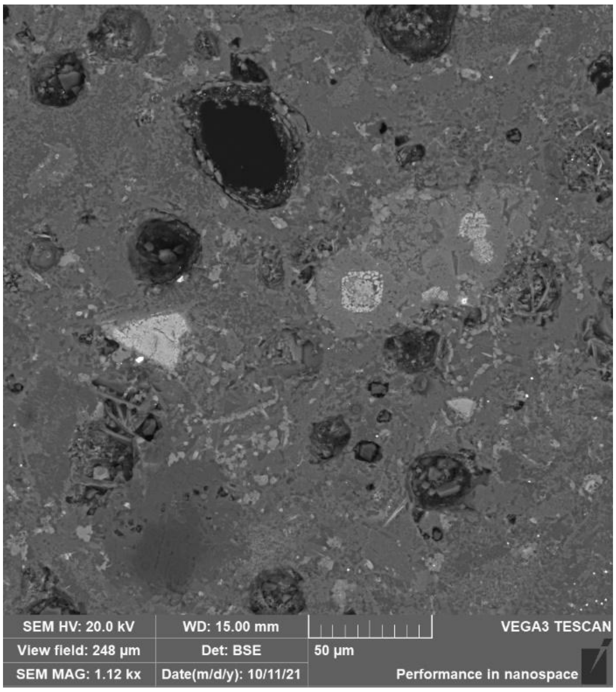
SEM HV: 20.0 kV
WD: 15.00 mm
VEGA3 TESCAN
View field: 248 µm
Det: BSE
50 µm
SEM MAG: 1.12 kx
Date(m/d/y): 10/11/21
Performance in nanospace

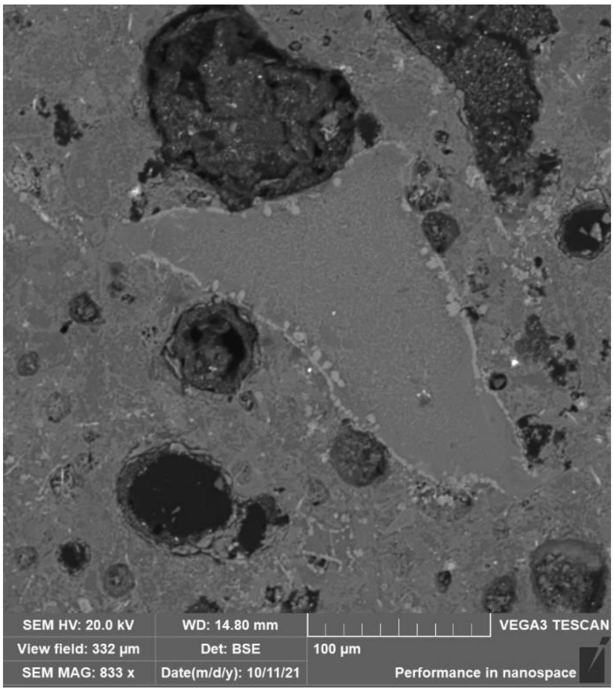
SEM HV: 20.0 kV
WD: 14.80 mm
VEGA3 TESCAN
View field: 332 µm
Det: BSE
100 µm
SEM MAG: 833 x
Date(m/d/y): 10/11/21
Performance in nanospace

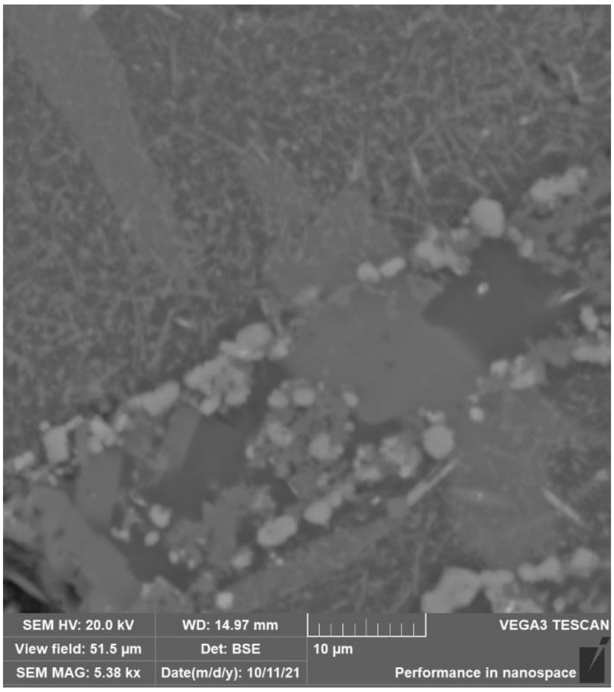
SEM HV: 20.0 kV
WD: 14.97 mm
VEGA3 TESCAN
View field: 51.5 µm
Det: BSE
10 µm
SEM MAG: 5.38 kx
Date(m/d/y): 10/11/21
Performance in nanospace

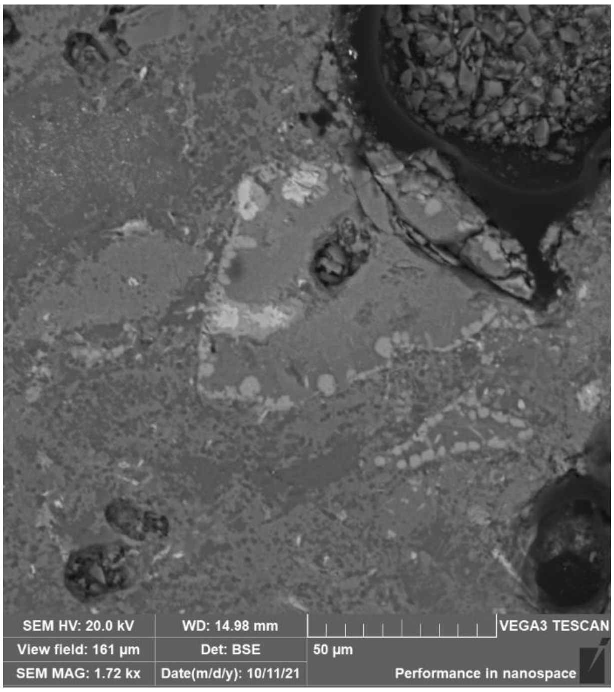
SEM HV: 20.0 kV
WD: 14.98 mm
VEGA3 TESCAN
View field: 161 µm
Det: BSE
50 µm
SEM MAG: 1.72 kx
Date(m/d/y): 10/11/21
Performance in nanospace

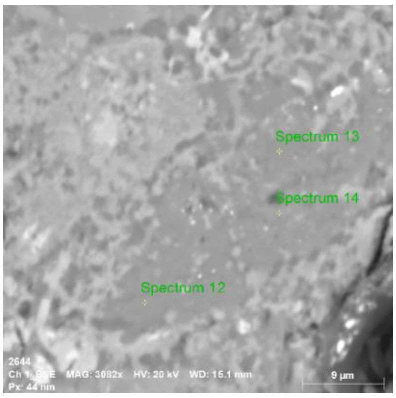
Spectrum 13
Spectrum 14
Spectrum 12
2644
Ch 1_BSE MAG: 3082x HV: 20 kV WD: 15.1 mm
Px: 44 nm
9 µm

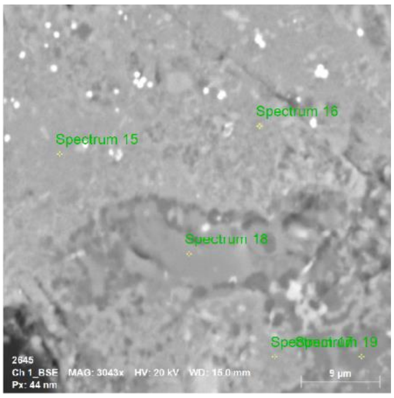
Spectrum 16
Spectrum 15
Spectrum 18
Spectrum 19
2645
Ch 1_BSE MAG: 3043x HV: 20 kV WD: 15.0 mm
Px: 44 nm
9 µm

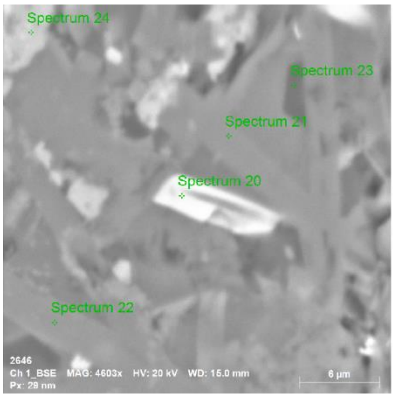
Spectrum 24
Spectrum 23
Spectrum 21
Spectrum 20
Spectrum 22
2646
Ch 1_BSE MAG: 4603x HV: 20 kV WD: 15.0 mm
Px: 29 nm
6 µm

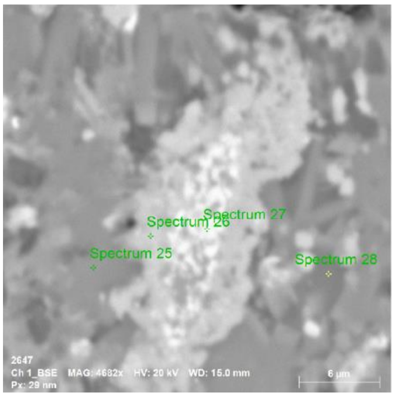
Spectrum 27
Spectrum 26
Spectrum 25
Spectrum 28
2647
Ch 1_BSE MAG: 4682x HV: 20 kV WD: 15.0 mm
Px: 29 nm
6 µm

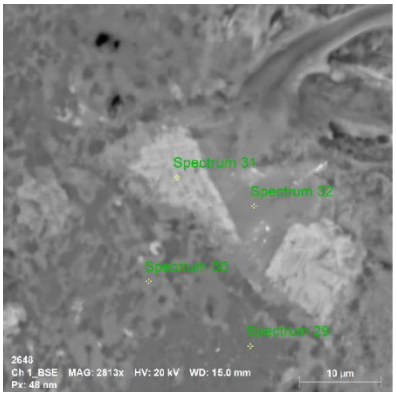
Spectrum 31
Spectrum 32
Spectrum 30
Spectrum 29
2648
Ch 1_BSE MAG: 2813x HV: 20 kV WD: 15.0 mm
Px: 48 nm
10 µm

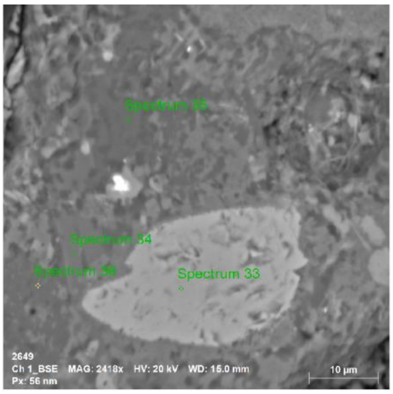
Spectrum 35
Spectrum 34
Spectrum 36
Spectrum 33
2649
Ch 1_BSE MAG: 2418x HV: 20 kV WD: 15.0 mm
Px: 56 nm
10 µm

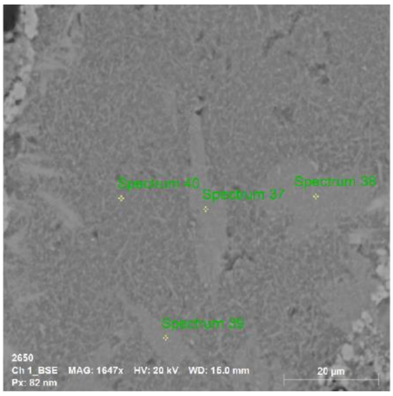
Spectrum 40
Spectrum 37
Spectrum 38
Spectrum 39
2650
Ch 1_BSE MAG: 1647x HV: 20 kV WD: 15.0 mm
Px: 82 nm
20 µm

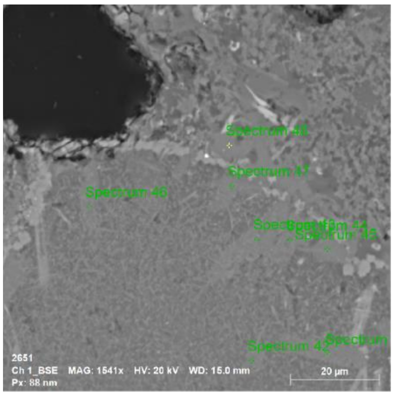
Spectrum 48
Spectrum 47
Spectrum 46
Spectrum 44
Spectrum 45
Spectrum 42
Spectrum
2651
Ch 1_BSE MAG: 1541x HV: 20 kV WD: 15.0 mm
Px: 88 nm
20 µm


Spectrum 49
2652
Ch 1_BSE MAG: 1649x HV: 20 kV WD: 15.0 mm
Px: 82 nm
20 µm

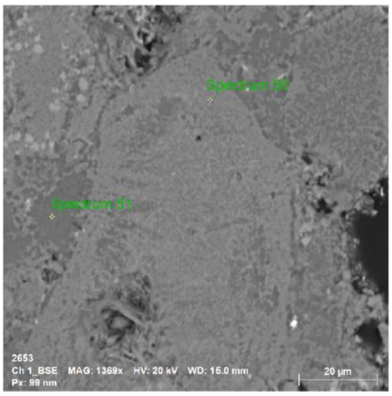
Spectrum 50
Spectrum 51
2653
Ch 1_BSE MAG: 1369x HV: 20 kV WD: 15.0 mm
Px: 99 nm
20 µm

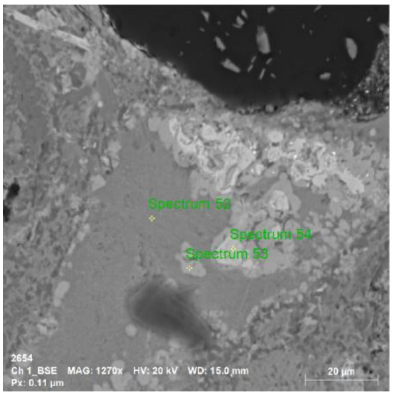
Spectrum 52
Spectrum 54
Spectrum 53
2654
Ch 1_BSE MAG: 1270x HV: 20 kV WD: 15.0 mm
Px: 0.11 µm
20 µm

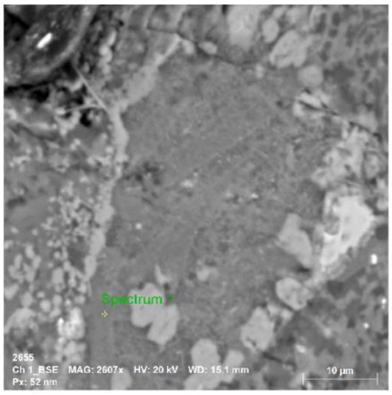
Spectrum 1
2655
Ch 1_BSE MAG: 2607x HV: 20 kV WD: 15.1 mm
Px: 52 nm
10 µm

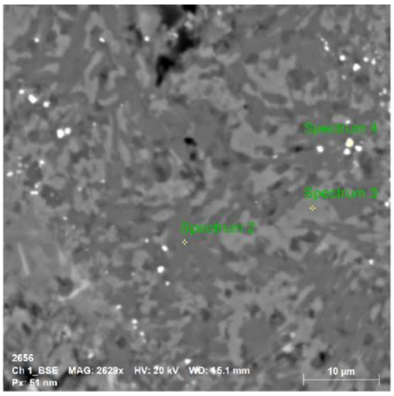
Spectrum 4
Spectrum 3
Spectrum 2
2656
Ch 1_BSE MAG: 2629x HV: 20 kV WD: 15.1 mm
Px: 51 nm
10 µm

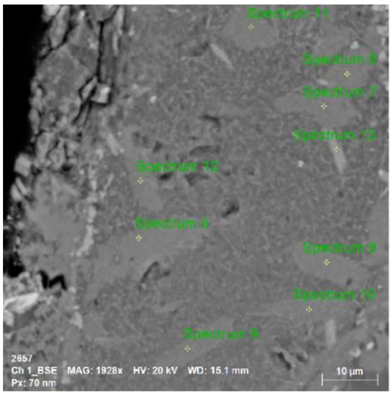
Spectrum 11
Spectrum 6
Spectrum 7
Spectrum 13
Spectrum 12
Spectrum 5
Spectrum 8
Spectrum 10
Spectrum 9
2657
Ch 1_BSE MAG: 1928x HV: 20 kV WD: 15.1 mm
Px: 70 nm
10 µm

Spectrum	Chlorine	Na2O	Al2O3	SiO2	CaO	FeO	MgO	TiO2	K2O	ZnO	ZrO2	Ce2O3	Cr2O3	BaO	NiO	SO3	SnO2
Spectrum 12		1.982	34.814	46.847	16.357												
Spectrum 13		3.878	32.275	48.990	13.888	0.969											
Spectrum 14		1.915	34.987	46.021	16.414	0.663											
Spectrum 15		4.209	14.983	41.206	28.343	6.077	5.181										
Spectrum 16		4.728	17.365	43.925	18.247	7.492	5.097	1.574	1.572								
Spectrum 17		4.565	15.445	41.749	27.693	5.366	5.181										
Spectrum 18		7.826	15.989	41.767	28.877	1.524	3.004			1.014							
Spectrum 19		2.951	30.034	47.012	16.754	1.859	1.390										
Spectrum 20	1.076	2.103	3.743	15.774	28.998				0.604		21.762	25.941					
Spectrum 21		6.707	13.504	42.727	28.244	1.148	5.761		0.456	1.452							
Spectrum 22		6.492	12.742	42.999	30.430	1.401	5.937										
Spectrum 24		0.587	5.927	31.161	28.548	23.940	1.245	4.332			4.260						
Spectrum 25		6.634	13.563	41.652	29.774	1.188	5.957			1.234							
Spectrum 26		0.948	6.507	32.240	28.853	18.660	1.590	5.424			5.779						
Spectrum 27			5.215	11.842	9.289	70.049	1.239	2.063					0.302				
Spectrum 28	0.768	8.241	18.051	37.955	17.636	1.829	1.193		2.564		4.859	4.301		2.603			
Spectrum 29		2.550	35.322	45.744	16.385												
Spectrum 30		4.388	23.949	46.223	19.239	2.763	3.438										
Spectrum 31		1.755	16.412	35.035	20.630	16.643	5.667	1.608			2.252						
Spectrum 32		1.606	11.749	22.275	13.124	33.417	5.103	1.069		2.778	2.113				6.766		
Spectrum 33			27.533			13.896	29.757			14.106			14.710				
Spectrum 34	2.625	9.244	26.209	44.653	9.986	1.092	0.849		1.303		0.973			3.064			
Spectrum 35	1.126	9.943	25.138	39.585	13.594	0.817			0.955		2.365			2.002		4.474	

Spectrum 36	2.430	31.898	46.711	16.032	1.586	1.342										
Spectrum 37	0.903	3.147	52.062	37.243	3.277	3.367										
Spectrum 38	0.981	3.386	51.634	36.800	3.690	3.509										
Spectrum 39	2.195	7.177	49.691	32.803	4.146	3.988										
Spectrum 40	6.445	16.184	47.573	15.904	5.500	5.492	1.403	1.500								
Spectrum 41	0.906	3.657	51.619	37.906	2.695	3.217										
Spectrum 43	0.699	3.815	51.291	37.580	3.074	3.540										
Spectrum 44	2.696	7.576	50.741	33.140	2.702	3.144										
Spectrum 45	7.520	19.873	45.868	15.439	3.869	3.634		2.026					1.772			
Spectrum 46	6.376	18.974	45.486	16.041	4.991	5.365	1.125	1.643								
Spectrum 47	5.454	16.344	45.714	19.627	5.372	4.825	1.259	1.403								
Spectrum 48	0.905	4.307	42.661	34.188	8.236	1.279	2.842			2.437						3.146
Spectrum 49	0.525	2.344	53.299	39.565	1.863	2.403										
Spectrum 50	4.539	14.560	45.049	21.141	6.813	5.551	1.548	0.799								
Spectrum 51	5.792	31.252	47.801	12.866	0.677										1.613	
Spectrum 52	3.249	15.660	37.641	26.437	9.207	4.231				2.529				1.045		
Spectrum 53	5.874	16.648	39.157	18.791	8.705	3.752	2.323	1.166		2.669				0.915		
Spectrum 54		18.090			37.018	11.045			6.410			4.147		23.290		
Spectrum 1	6.313	15.019	42.788	27.098	3.616	4.185			0.981							
Spectrum 2	3.585	32.101	49.582	14.732												
Spectrum 3	1.135	18.914	43.794	19.267	1.964	9.731	1.829			3.367						
Spectrum 4	3.261	28.423	45.049	16.422	0.784						4.837		1.224			
Spectrum 5	1.960	6.386	51.729	35.304	1.894	2.726										
Spectrum 6	0.827	2.561	53.489	38.811	1.553	2.758										
Spectrum 7	1.254	5.554	51.798	35.130	2.596	3.668										

Spectrum 8		0.836	3.797	51.778	38.164	2.138	3.287		
Spectrum 9		3.254	8.821	49.853	31.601	2.552	3.221		0.697
Spectrum 10			2.171	53.022	41.238	1.142	2.426		
Spectrum 11		0.808	3.634	52.112	37.630	2.263	3.553		
Spectrum 12_		7.344	20.052	45.796	15.228	3.783	4.481	1.395	1.919
Spectrum 13_	0.764	6.346	18.342	45.309	17.027	4.249	4.989	1.336	1.638

Here after are reported some additional SEM/BSE images of CFM2, and the images where the EDS analyses have been done. Lastly the microanalyses.

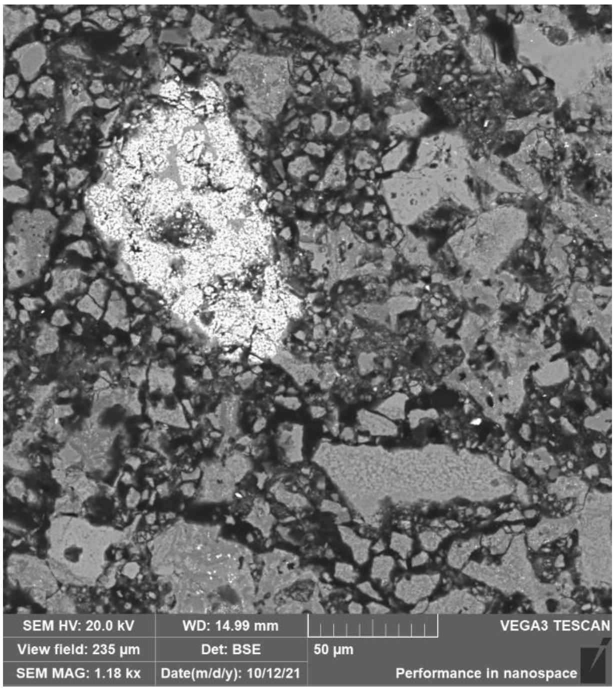

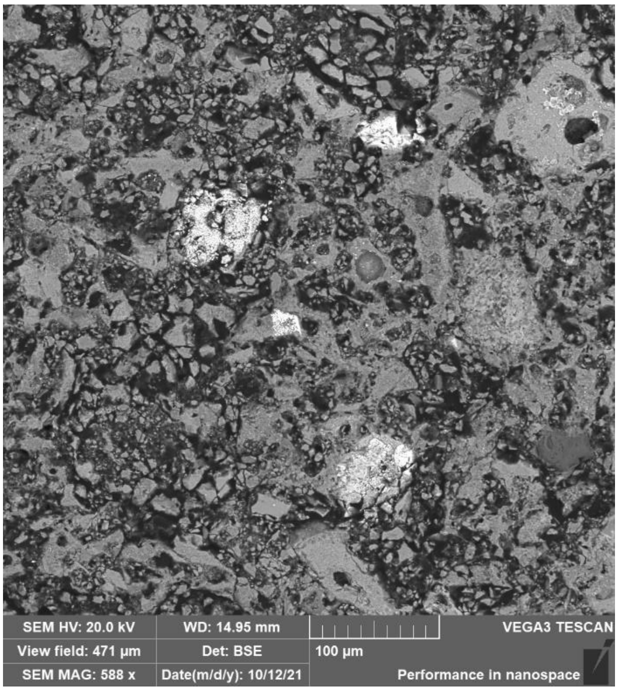

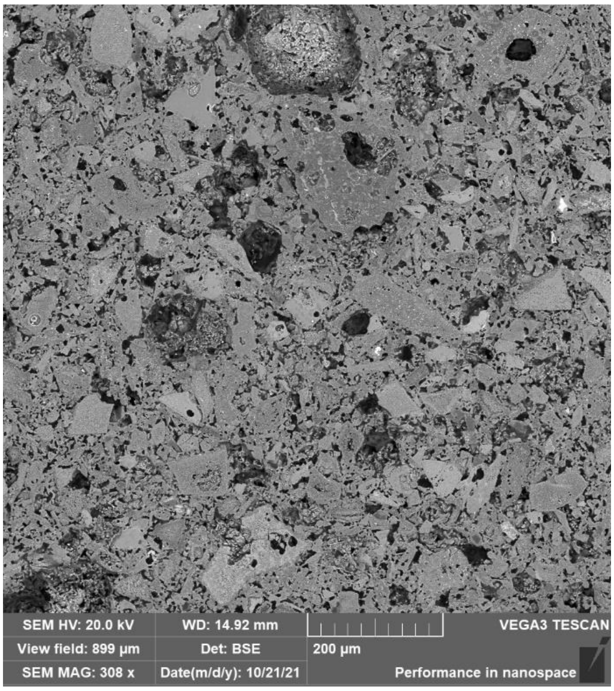

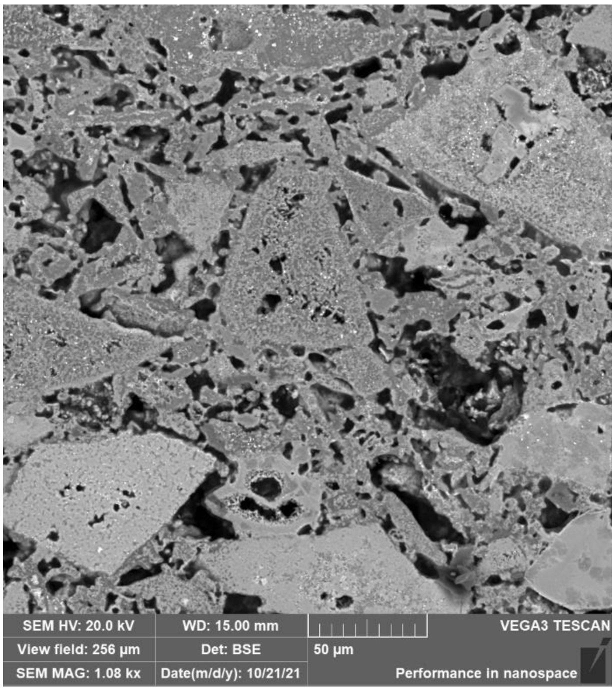

Spectrum	Chlorine	Silver	Na2O	MgO	Al2O3	SiO2	K2O	CaO	FeO	ZnO	ZrO2	BaO	NiO	SnO2	SO3	TiO2	Ce2O3	P2O5
Spectrum 4_			7.763	2.179	7.168	72.924	6.817	3.150										
Spectrum 5_						53.910		46.090										
Spectrum 6_				0.728		54.429		44.844										
Spectrum 7_			1.256	0.759	1.570	56.650	1.124	38.642										
Spectrum 8_			1.857	1.267	2.261	58.619	1.667	34.328										
Spectrum 9_			0.807	18.059	1.250	57.286		22.598										
Spectrum 10_			6.220	1.915	7.812	74.392	6.626	3.034										
Spectrum 1			15.007		34.276	41.843	4.215	3.873	0.786									
Spectrum 2					0.954	97.423	0.691		0.932									
Spectrum 3						100												
Spectrum 4				27.476	71.200				1.323									
Spectrum 5			14.505		34.505	39.955	4.344	6.008	0.682									
Spectrum 6			14.366		35.541	40.015	4.444	4.934	0.699									
Spectrum 7			12.399		27.635	46.551	4.837	6.890	1.689									
Spectrum 8				24.845	68.518				4.928	1.709								
Spectrum 11			4.551	4.447	15.577	40.949	1.917	20.394	8.019		2.636	1.510						
Spectrum 12			2.163	5.034	15.777	37.806	1.666	23.044	8.985		4.334	1.191						
Spectrum 13						100												
Spectrum 14			9.734	7.685	23.419	27.158	2.535	1.208	28.261									
Spectrum 15			7.033		21.094	59.128	8.132	1.666	2.947									
Spectrum 16			2.427	6.174	16.284	35.365	0.789	23.520	8.933		3.866		0.863	1.779				
Spectrum 18			1.337	4.607	17.687	30.771	0.245	22.804	13.380		4.209			0.716	0	1.138	3.106	
Spectrum 19			2.633	5.499	19.518	34.544	0.774	21.432	6.948		3.921					2.069	2.661	
Spectrum 20			13.849		36.511	39.273	4.059	6.308										

Spectrum 21			1.102		3.464	52.934	1.043	41.457										
Spectrum 22			14.827		27.789	43.790	3.574	6.079	1.731						2.211			
Spectrum 23			1.535	0.850	6.728	14.568	1.490	4.107	70.722									
Spectrum 24			2.404	4.203	16.646	34.614	0.597	20.882	18.011		2.644							
Spectrum 26			8.738		23.274	51.506	7.449	7.166	1.866									
Spectrum 27			0.961		2.254	53.348		43.437										
Spectrum 30	2.845					14.248		34.843	0.832		17.432						29.800	
Spectrum 31			9.955		25.016	50.655	7.602	5.209	1.564									
Spectrum 32	0.688		13.138		27.275	43.014	5.165	5.841	0.947						3.932			
Spectrum 33			7.394	4.759	15.051	43.685	1.011	26.232	1.183						0.686			
Spectrum 34		34.195	4.383	2.282	16.672	24.865	2.074	10.431	2.994		1.150					0.955		
Spectrum 35		100.000																
Spectrum 36					3.302	1.123			33.378	4.898			34.067	23.233				
Spectrum 37			2.144	6.437	16.154	35.599	0.508	25.019	7.286		4.002	1.419	1.432					
Spectrum 38			2.350	6.112	15.232	34.294	0.802	23.062	8.348		4.419		1.034	1.729		1.105	1.513	
Spectrum 39			3.085	2.239	29.114	38.566	0.288	22.286	1.881						0.722	1.130		0.688
Spectrum 40				0.862	1.573	0.610		0.789	96.167									